Structural Investigation of Biological and Semiconductor Nanostructures with Nonlinear Multicontrast Microscopy

by

Richard Cisek

A thesis submitted in conformity with the requirements
for the degree of Doctor of Philosophy

Graduate Department of Physics
University of Toronto

Structural Investigation of Biological and Semiconductor Nanostructures with Nonlinear Multicontrast Microscopy

Richard Cisek

Doctor of Philosophy

Graduate Department of Physics
University of Toronto

2012

Abstract

Physical and functional properties of advanced nano-composite materials and biological structures are determined by self-organized atoms and molecules into nanostructures and in turn by microscopic organization of the nanostructures into assemblies of higher structural complexity. Therefore, microscopes are indispensable tools for structural investigations at various levels of organization. In this work, novel nonlinear optical microscopy methods were developed to non-invasively study structural organization at the nanoscopic and microscopic levels. Atomic organization of semiconductor nanowires, molecular organization of amylose biocrystallites in starch granules, and microscopic organization of several photosynthetic organisms was elucidated.

The structure of ZnSe nanowires, key components in many modern nanodevices, was investigated using polarization harmonic generation microscopy. Based on nonlinear optical properties of the different crystal lattices, zinc blende and wurtzite nanowires were differentiated, and the three-dimensional orientation of the zinc blende nanowires could be found. The structure of starch granules, a model biocrystal, important in food as well as health sciences, was also investigated using polarization harmonic microscopy. The study was combined with *ab initio*

calculations using the crystal structures of amylose A and B, revealing that second harmonic signals originate from the hydroxide and hydrogen bonds in the starch granules. Visualization of several photosynthetic organisms including the green algae, *Chlamydomonas reinhardtii*, two species of cyanobacteria, *Leptolyngbya* sp. and *Anabaena* sp., aggregates of light-harvesting pigment-protein complexes as well as chloroplasts from green plants were also explored, revealing that future nonlinear microscopy applications could include structural studies of cell walls, the *Chlamydomonas* eyespot, and photosynthetic membranes.

In this study, several nonlinear optical microscopy modalities were developed for quantitative structural investigations of nano and micro-sized architectures. Non-invasive extraction of crystallographic information in microscopic samples will have a number of potential benefits, for example, in clinical applications, allowing observations of disease states inside tissues without the need for biopsy. Industrial nanotechnology will benefit from fast determination of nanostructures with nonlinear microscopy that will improve quality of nanodevices.

Acknowledgments

Thanks to my loved one, to my friends, and especially to my family, for their unwavering support, I could not have done it without all your help and encouragement. Thanks to the entire Barzda Lab family, past and present. Thanks to the UTM community; it is an honor and a privilege to work amongst you.

Throughout my PhD I have been helped by many great people. Thanks Prof. Arkady Major and Prof. Donatas Zigmantas for building, and maintaining, really great lasers. Thanks to Leigh Spencer for NW as well as photosynthetic structure imaging. Thanks to Nehad Hirmiz for PIPO NW imaging. I'm greatful to Prof. Harry Ruda and his amazing group for the NW project: Ankur Saxena did HRTEM of NWs, Dr. Alex Shik did great NW theory work, and Dr. Usha Philipose performed NW synthesis. Thanks to Prof. Espie for photosynthetic samples and great discussions. Thanks to Prof. D Popov for emailing me the structure of amylose A. Thanks to Serguei Krouglov for SHG theory work. Thanks to Danielle Tokarz for good discussions, help with hyperpolarizability calculations, as well as edits to this thesis. Thanks to Adam Tuer for good discussions, microscope building/aligning work, as well as for PIPO microscopy: visualization and implementation could not have happened without you. Thanks to Nicole Prent for microscope programming, the birefringence PIPO formula and good discussions. Thanks to Daaf Sandkuijl for KGW laser maintenance. Thanks to Catherine Greenhalgh for teaching me LabVIEW, and good discussions. Thanks to Andrew Veglio for microelectronics support. Thanks very much also to Peter Duggan, Rob Dick and Paul Milne for machine shop work. The final thanks goes to Virginijus Barzda, for what student-supervisor relationships should be.

Thanks also to the multitude of scientists, past and present, for bringing us into an age of knowledge, photonics and technology. Thanks to University of Toronto for providing funding and thanks to Canada for providing a safe haven to perform scientific endeavors. Such a highly technology driven thesis topic could not be performed without all these elements.

Table of Contents

List of Tables

List of Figures

Thesis Outline

Many structures in biological organisms consist of highly ordered molecules arranged in symmetric configurations, aka biocrystals, which have high nonlinear optical properties sufficient for probing with a nonlinear optical microscope. Nonlinear optical signals can reveal structural information about the microscopic sample, and can be used to visualize the distribution of biocrystallinity within biological tissue. Structural studies of subcellular biological assemblies are important for increasing the understanding of fundamental physiological processes of morphogenesis. Investigations of physiological processes have many applications in health sciences and the biomedical industry such as; improved drug development to overcome human disease, as well as, improvements in biological product manufacturing including biodegradable materials to reduce garbage or for increase in efficiency of biofuel production and to reduce our need for fossil fuel.

The main tools that are currently used to probe the distribution of crystallographic organization in microscopic structures have serious limitations complicating *in vivo* biological imaging. X-ray diffractometers (XRD) coupled to synchrotron radiation sources are the main tool for obtaining detailed structural information about small crystalline samples (Imberty, Buleon et al. 1991; Liu, Yan et al. 2004; Xia, Dai et al. 2006)), commonly achieving sub-angstrom scale resolution crystal structures of low molecular weight compounds. The resolution of polymer crystal structures which have higher molecular weight, is still a major challenge because it requires a number of intuitive guesses along with trial and error methods (Popov, Buleon et al. 2009). The limitation occurs due to complications in generating sufficiently large polymer crystals, and therefore studies commonly rely on XRD of crystalline fibers, which contain large numbers of small polymer crystals which are well aligned in the fiber direction, but have reduced alignment in the perpendicular direction, taking up a semi-cylindrical symmetry. Selected area electron diffraction (SAED) is another technique commonly used on individual micro crystals, to help deconvolute the fiber X-ray structures and ascertain structural parameters obtained from X-ray studies of crystalline fibers (Imberty, Buleon et al. 1991). Complications arise *in vivo* due to damaging X-ray radiation and the low damage threshold of live tissue for even low intensity electron beams, the need for high vacuum for electron microscopes as well as, the requirement of sample thin sectioning. Therefore, while the achieved resolution of crystal

structures of large polymers using recent techniques is quite amazing, where as an example, a recent study of amylose A achieved 1.3 Å resolution (Popov, Buleon et al. 2009), there is still a lack of non-invasive tools capable of investigating structural properties of *in vivo* biological structures without incurring sample alterations or artifacts.

Nonlinear optical microscopy is a beneficial and complementary technique to XRD, allowing structural investigations of heterogeneous *in vivo* biological assemblies while minimizing invasiveness. The parametric light-matter interactions in nonlinear optical microscopy do not induce molecular excitations within the sample, therefore no photochemical reactions occur, and no heat is deposited into the biological system, if laser radiation outside of linear and nonlinear absorption is used, allowing for long duration functional *in vivo* studies. Since nonlinear optical microscopy does not require any additives or dyes, and can be performed in the epi direction, it is considered a non-invasive investigation technique which is highly beneficial for clinical applications of disease diagnosis via visualization of tissues without the need for biopsies. With current laser technology tissues up to 0.5 mm thick have been probed in 3D without thin sectioning due to the inherent optical sectioning capability of nonlinear microscopy. Additionally nonlinear optical microscopy does not require that the biological sample be purely crystalline in a large area to obtain quantitative crystallographic information. Nonlinear optical microscopy is a complementary technique to XRD because while *in vivo* structural investigations are possible, the technique is mainly limited by optical resolution. The focal volume diameter of a nonlinear optical microscope, which has several hundreds of nm, is similar compared to SAED and XRD probe spot sizes, however it is much surpassed by the angstrom resolution of high resolution transmission electron microscopy (HRTEM) imaging. Therefore nonlinear optical microscopy has the advantage of being a non-invasive, long duration *in vivo* 3D scanning technique, and should be considered as an additional tool to aid in the research of microscopic biological structures and synthetic nanomaterials.

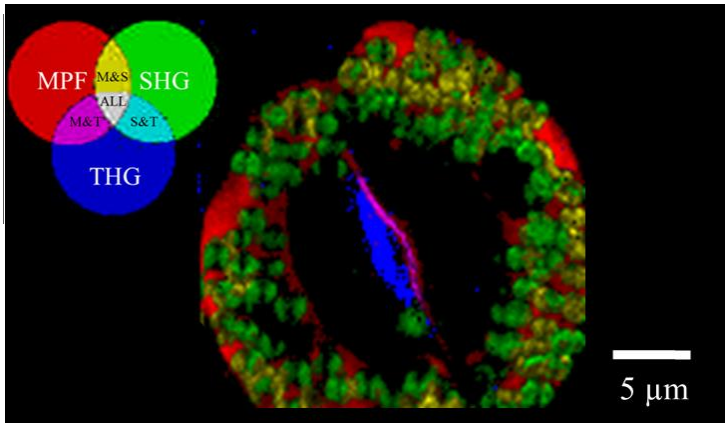

Fig. 0-1: Example of *in vivo* nonlinear microscopy of a stoma in *Clivia mineata* leaf.

A nonlinear microscopic image of a stoma is shown via multiphoton fluorescence (MPF), second harmonic generation (SHG) and third harmonic generation (THG) nonlinear contrast mechanisms. The color coding scheme is presented in the inset: Red shows uncorrelated MPF, green shows uncorrelated SHG, blue shows uncorrelated THG, magenta shows correlated MPF and THG but not SHG, cyan shows correlated SHG and THG but not MPF, yellow shows correlated MPF and SHG but not THG, and white shows correlation of all three signals. Figure reprinted with permission from (Cisek, Spencer et al. 2009).

While not all microscopic biological structures generate nonlinear optical signals, the technique has tremendous potential because many interesting biological structures do generate very intense nonlinear signals which could be used to determine *in vivo* structural characteristics for the study of physiological processes. The Fig. 0-1 demonstrates that nonlinear microscopy can be used *in vivo* for three dimensional (3D) imaging using optical sectioning to visualize various microscopic features in a biological sample. It shows an example of imaging a thick (~0.5 mm) section of a stoma in a *Clivia mineata* leaf; the guard cells of the stoma are visualized in the center (blue/cyan), and a ring of starch granules (green) and chloroplasts (red) are visualized in a circle around the guard cells. The cell walls of the guard cells are visualized with third harmonic nonlinear signals due to a boundary effect, allowing good contrast for visualization with the nonlinear optical microscope. The origin of nonlinear signals from chloroplasts, starch granules and cell walls is from the biocrystallinity of these structures, and therefore they can be structurally probed with nonlinear microscopy. Plants are not unique in having subcellular structures that generate nonlinear optical signals; in animals collagenous connective tissues as well as myosin in muscle tissues generate intense nonlinear signals, which can be probed to reveal different structural characteristics, therefore, this research can also be applied to a variety of subcellular structures in biology and medicine.

While the power of nonlinear microscopy stems from the fact that it can be used for quantitative structural analysis, such studies are only just emerging, and therefore development of experimental tools and methods is needed. A major part of this thesis was dedicated to the design, construction, and software engineering of a nonlinear optical microscope for imaging biological structures *in vivo.* The microscope hardware as well as a new protocol and analysis method was developed to measure the polarization of the outgoing harmonic generated signal, so that quantitative structural analysis of biological samples could be performed. In order to test and verify the capability of the microscope and polarization protocol for quantitative structural imaging, a detailed nonlinear optical microscopic investigation of semiconductor nanowires (NWs) was performed. ZnSe NWs were chosen because they generate intense nonlinear signals, have no absorption near the fundamental or second harmonic laser wavelengths and are crystallographically very well understood. Therefore the nonlinear signals from NWs can easily be related to the structural properties of the nanomaterial. Nanotechnology would particularly benefit from structural measurements of nanomaterials during manufacturing, in order to improve device quality as well as efficiency. Furthermore, the crystallinity of NWs is similar to that of common biological crystals including starch, collagen and myosin, and therefore results from this investigation can be applied to biological studies.

The third part of this thesis is a detailed nonlinear microscopy investigation of starch granules. Starch granules appear in many plants and can aid in the functional study related to photosynthesis research and studies of energy storage in photosynthetic organisms. Furthermore, starch granules represent one of the most studied biocrystals, having two crystalline types that generate intense nonlinear signals, and therefore serve as a good model system to develop an understanding of how nonlinear microscopy can be used to determine structural properties of a biocrystalline sample. Additionally, the source of the optical nonlinearity in starch granules is currently not well understood, and therefore, this thesis aims to answer this fundamental question, which is important for interpreting the crystallographic information observed in starch granules using nonlinear microscopy. In the last section, the initial results of imaging more complex biological structures using nonlinear microscopy is presented including isolated light-harvesting complexes from higher plants, chloroplasts, unicellular alga *Chlamydomonas reinhardtii* and cyanobacteria *Leptolyngbya* sp. and *Anabaena* sp. The aim of the thesis is to develop tools and understanding required in order to study the more complex biological

structures. It is anticipated that future scientists in the field will take advantage of the novel nonlinear microscopy methods and developed knowledge for structural investigations of complex biological structures.

Nonlinear microscopy is at an early stage of development and detailed quantitative studies of biological structures are only just emerging. In order to put nonlinear microscopy in proper context, Chapter 1 will feature a brief history of the optical microscope, followed by a history of the development of the nonlinear optical microscope. The contrast mechanisms pertinent in this thesis that have emerged in nonlinear optical microscopy and some of their applications will be reviewed. The chapter will conclude that in order to further quantitative studies of complex biological structures with nonlinear microscopy we first need to develop quantitative investigation methods using simpler structures, where full crystalline data is available.

Chapter 2 outlines the theory of the three main nonlinear contrast modalities used in this thesis, multiphoton excitation fluorescence, second harmonic generation and third harmonic generation. There is a focus on the second harmonic generation from different types of crystals, as well as theoretical analysis of polarization-in-polarization-out (PIPO) measurements that are possible using this technique, which can reveal details of crystalline structures and their orientations. There is also an explanation of the computational methods used to model the second harmonic generation properties of molecules in this thesis.

Chapter 3 outlines the details of the nonlinear optical microscopy setup. It will carefully review the components of a nonlinear optical microscope, discussing the optics, the scanning and detection system, as well as the laser source. A section is devoted to explaining the analysis of quantitative measurements of ZnSe nanowires and starch granules using PIPO optical microscopy, a new type of microscopy developed in this thesis. Aspects of microscope programming are explained, as well as data analysis using three channel image cross correlation is presented.

Chapter 4 contains a detailed study of second harmonic generation polarization microscopy of solid state nanocrystals. Different types of ZnSe NWs are characterized with polarization SHG microscopy revealing that the method is ideally suited for structural

differentiation of nanocrystals. It forms the basis of the understanding of how nonlinear microscopy behaves in an ideal situation where the structures are known *a priori*, and how to interpret the nonlinear optical signals in a quantitative manner.

Chapter 5 is a detailed investigation of nonlinear microscopy of a model biocrystalline structure, the starch granule. Starch granules have very well studied crystalline ultrastructures, however they contain more disorder than their solid state counterparts. Additionally, since they are composed of polymers, their available crystal structures have reduced resolution as compared with solid state structures such as NWs. Therefore to understand and explain the nonlinear microscopy of these structures the study combines experimental data with numerical calculations. The second harmonic susceptibility of maize and potato starch granules are experimentally obtained by polarization second harmonic generation nonlinear microscopy. Theoretical calculations of second harmonic hyperpolarizability were performed using crystallographic data of amylose starch crystals, and the results were used to attribute the second harmonic generation properties of starch granules to hydrogen and hydroxide bonds from oriented water molecules contained within the starch crystals.

A qualitative study of imaging complex photosynthetic biological structures is presented in Chapter 6, in order to demonstrate the origins of nonlinear signals in more complex biological structures. Several photosynthetic structures were chosen for the study including isolated light-harvesting complexes from higher plants, chloroplasts, unicellular alga *Chlamydomonas reinhardtii* and cyanobacteria *Leptolyngbya* sp. and *Anabaena* sp. The investigation shows examples of simultaneous multiphoton excitation fluorescence, second harmonic generation as well as third harmonic generation imaging of the photosynthetic structures, and was performed to investigate the next steps that research may benefit using nonlinear microscopy methods.

Chapter 1
History of Optical Microscopy

1.1 Optical Microscopes

Small biological structures have been primarily investigated with optical microscopy for 400 years. During this century however, the microscope has evolved from an observational instrument to an analytical and spectroscopic tool with subdiffraction limited spatial and picosecond temporal resolution, capable of examining molecular properties and their macrostructural organization as well as functional dynamics in living cells. Other microscopy techniques have also evolved, such as electron microscopy and atomic force microscopy, which provide higher resolution; however the visualization of structural dynamics inside a living cell remains a prerogative of optical microscopy. Structural visualization can be achieved via a large variety of optical microscopy techniques using different image contrast mechanisms.

Optical microscopes form images based on the spatial variation of light intensity. Characterization of structural visibility against the image background is obtained by its contrast, which is expressed as the intensity difference between the brightest and the darkest pixel normalized to the average pixel intensity in the image. Therefore for the same signal variation, a higher contrast is obtained with lower background intensity. In order for the human eye to resolve structural details, image contrast of at least a few percent is needed (Campbell and Green 1965). High image contrast can be obtained by three main strategies: (i) manipulation of the properties of the excitation light and detection schemes implemented in various optical microscope designs, (ii) labeling and staining the samples, and (iii) image manipulation and analysis techniques that extract useful information from the background. This thesis focuses on the first and the third strategy, which will be described in later chapters.

1.1.1 Brief history of the optical microscope

The optical microscope was invented at the end of the 16th century, and has since remained an indispensible research tool. Experimentation with lenses from spectacles, or eyeglasses, led to the discovery that lenses made from high curvature glass balls produced large magnified images when observed at a close distance. These single lens “simple” microscopes were perfected by Dutch self–educated investigator Antoni van Leeuwenhoek (1632-1723), who achieved greater

than 270 times magnification, the highest available at that time (Leeuwenhoek 1695; Hall 1988). Van Leeuwenhoek used the simple microscope to discover protozoa and the streaming of red blood corpuscles as well as bacteria and other unicellular organisms (Klopsteg 1960; Gest 2004).

Hans and Zaccharias Janssen of the Netherlands likely invented the compound microscope in about 1590 by placing two lenses at a distance inside a tube (Hogg 1867; Ealand 1921; Klopsteg 1960). The first lens produced a magnified intermediate image, which was further magnified by the second lens. The objective of today's microscopes evolved from the first lens, while the second lens became the eyepiece. Galileo Galilei, after he heard about the famous Dutch invention, converted a telescope to a microscope 20 years later (Klopsteg 1960). Robert Hooke further elaborated the compound microscope in his fundamental work Micrographia, presenting numerous imaging applications including cork, a plant tissue that resembled a honeycomb like structure consisting of small "cells", therefore coining the term (Hooke 1665). The compound microscope was further improved by introducing achromatic lenses, flattening the field of view, as well as perfecting the illumination source (Carpenter and Smith 1856; Hogg 1867; Manten 1969). Until the mid-19th century, microscope manufacturing was more of an art than a science, lacking a theoretical basis. The theory of image formation in a compound microscope was developed by Ernst Abbe, who showed that observations of small details are limited not only by the magnification, but by the microscope resolution, which is proportional to the wavelength of imaging light and inversely proportional to the numerical aperture (NA) of the objective (Abbe 1873; Ealand 1921). Reproducible manufacturing of high quality optical microscopes was finally obtained in the early 20th century by the cooperation of Carl Zeiss, Ernst Abbe and glass material manufacturer Otto Schott, and reached standards comparable to today's microscopes.

While early microscope developers were primarily concerned with increasing microscope resolution, field flatness and eliminating aberrations, starting from the beginning of the 20th century more efforts focused on improving image contrast in bright field microscopy and creating new contrast mechanisms based on linear and nonlinear light-matter interactions in specimens.

1.1.2 Wide-field microscopy techniques

In a wide-field microscope the image of an object is formed by microscope optics without scanning. The image is magnified and projected onto a 2-dimensional array detector, either the retina of an eye, or a camera. Although there are many interesting contrast mechanisms for wide-field microscopy, in this section bright field, polarization, and fluorescence contrast mechanisms will be discussed.

In bright field microscopy, absorption, scattering and reflection of illumination light in the sample induces variations in light intensity at the detector giving high background intensity, making unstained subcellular structures difficult to observe. A large variety of staining methods have been developed which allow selective labeling of various structures, for example, early research in the discovery of grana (Strugger 1950) used rhodamine dye as a counterstain to the naturally occurring chlorophyll, while iodine proved to be a good staining method to identify starch ((Buleon, Colonna et al. 1998) and references therein).

Polarization contrast can be used in a wide field microscope using linearly or circularly polarized light to image linear and circular birefringence, respectively. Two crossed linear polarizers, or left and right circular polarizers are used with one polarizer in the illumination path, and the other, called an analyzer after the objective, which converts the changes in polarization to changes in light intensity for detection with typical light detectors. In the absence of birefringence in a sample, the field of view appears to be dark. However, when birefringent objects are introduced into the microscope, rotation of the polarization by the sample allows some of the light to pass through the crossed analyzer, therefore highlighting birefringent structures. In the 19th century, starch granules were already known to exhibit a large birefringence (Hogg 1867), with the observation of the characteristic “Maltese cross” pattern (see Fig. 5.3-4 (c)) in the polarization microscope, distinguishing them from other structures (Carpenter and Smith 1856; Hogg 1867). A circular polarization microscope was also used to image starch granules revealing the dark centrosymmetric hilum in the homogeneously lit birefringent starch granule (Frohlich 1986). The birefringent eye spot in *Chlamydomonas reinhardtii* is also a distinct structure highlighted by the polarization microscope (Yang and Tsuboi 1999).

Fluorescence is one of the most frequently used contrast methods in brightfield microscopy. The popularity of fluorescence contrast arises from high sensitivity and specificity obtained by imaging naturally pigmented or artificially labeled structures. A very high sensitivity; up to the single molecule detection level can be achieved in fluorescence microscopy (Bopp, Jia et al. 1997; van Oijen, Ketelaars et al. 1999). A large variety of fluorophores is available for specific labeling of biological structures including autofluorescing molecules, regular dyes, fluorescent immunostains, quantum dots and genetically encoded fluorescent proteins (Goldman and Spector 2005; Haugland, Spence et al. 2005). Currently, most cellular structures can be specifically highlighted with fluorescent proteins such as the green fluorescent protein (GFP) and structural dynamics can be followed over extended time periods (Dixit, Cyr et al. 2006). Fluorescence imaging microscopy can be easily implemented by isolating the excitation light from the detected fluorescence, usually accomplished using optical color filters. Several contrast mechanisms can be combined into a multicontrast microscope, where cellular structures are visualized with bright field or polarization microscopy and colocalized with the fluorescing structures in the same image (Laclaire 1987; Oida, Sako et al. 1993).

In wide field microscopy, out of focus signals largely contribute to the images. Axial resolution in fluorescence as well as regular bright field microscopy is relatively low, and therefore, submicron resolution images in thicker specimens cannot be obtained in most cases. The axial resolution can be dramatically improved by using confocality or nonlinear signals in scanning microscopy, which will be discussed in the following sections.

1.1.3 Scanning microscopy

Scanning microscopes focus a beam of light into a tiny focal spot on the sample. The focal spot represents a volume with diffraction limited lateral resolution reaching down to several hundred nanometers for the highest numerical aperture oil immersion objectives. The size of the focal volume along the principle propagation direction of the beam (axial direction) depends on the microscope setup. For confocal and nonlinear microscopy, it is roughly three times longer than in the lateral directions forming an ellipsoidal shape (explained in detail in section 3.2.1). The focal volume is scanned over the sample by translating the sample stage or by raster scanning the beam, while signal detection is performed by a single element detector, such as, a photomultiplier tube or an avalanche photodiode. An image can be constructed by assigning the

signal strength value from the detector for each pixel of the image. The position coordinates of the pixels are derived from the scanner. Therefore, the scanning microscope is a single beam device and shares many features common with spectroscopic devices. The scanning method can be advantageous over the wide-field method when confocal or nonlinear excitation is used for optical sectioning of thick specimens (Denk, Strickler et al. 1990; Hepler and Gunning 1998), or when using excitation modulation with lock-in detection for very small variations of the signal on a background with high intensity (Tinoco, Mickols et al. 1987; Finzi, Bustamante et al. 1989), as well as for using spectrally resolved detection with a dispersive element such as a prism or a grating (Vacha, Adamec et al. 2007). The following section discusses the differences in optical sectioning performed by confocal microscopes.

1.1.4 Confocal microscopy

Confocal microscopy was invented by Marvin Lee Minsky (Minsky 1988) in the 1950's, and is advantageous because it provides optical images of thin sample slices (optical slices) inside thicker samples, known as optical sectioning. The introduction of confocality in the fluorescence microscope has revolutionized *in vivo* imaging, since it improves image quality by avoiding light emanating above and below the desired focal plane (Brakenhoff, Vandervoort et al. 1984; Shotton and White 1989), a troublesome problem in imaging biological samples. Confocality is achieved via a confocal pinhole which is placed in the conjugate plane with the sample and with the excitation pinhole, therefore, the detected fluorescence originates from the focal volume at the sample, while out of focus fluorescence gets blocked (Davidovits and Egger 1969; Paddock 1999; Muller 2006; Pawley 2006). With the advent of fast scanners and the increase in the availability of differently colored lasers, laser scanning confocal microscopes have gained popularity in the biological imaging field and they are now routinely used in imaging biological organisms (Cox 1993; Gilroy 1997; Fricker, Runions et al. 2006).

The images recorded by confocal microscopy show a fluorescence intensity distribution map of the sample. The fluorescence intensity is proportional to the concentration of the fluorophores, but it also depends on the fluorescence lifetime, which in turn depends on the local molecular environment (Barzda, de Grauw et al. 2001; Ulrich, Fischer et al. 2004; Cisek, Aus der Au et al. 2005). Confocal microscopy suffers from signal bleaching since molecules absorb photons, and that can induce photo-oxidation reactions. While non-invasive imaging can be

performed by detecting fluorescence from endogenous chromophores, the endogenous chromophores often have low fluorescence yield, and suffer from a lack of specificity, therefore external labels are commonly used for imaging. In the next chapter, nonlinear microscopy is qualitatively described, where inherent confocality is obtained without using a confocal pinhole, and where signal contrast is generated due to nonlinear light-matter interactions and specific structural organization in the samples. The nonlinear imaging modality is quite different from the previously mentioned linear optical microscopy contrast techniques.

1.2 Nonlinear Optical Microscopy

1.2.1 Brief history of nonlinear microscopy

Nonlinear light-matter interactions can be successfully applied as novel visualization contrast mechanisms in optical microscopy. Although the first nonlinear microscope was introduced in 1973 for imaging ZnSe with second harmonic generation (SHG) (Hellwarth and Christensen 1974), the nonlinear microscopy renaissance did not occur until 1990 when the multi-photon excitation fluorescence (MPF) microscope was invented (Denk, Strickler et al. 1990). Rekindled interest in nonlinear microscopy was triggered by two technological advancements; the introduction of stable solid-state Ti:Sapphire femtosecond pulsed lasers, as well as computer technology (Cisek, Spencer et al. 2009). Many other nonlinear contrast mechanisms simultaneously came about for microscopy during the 1990s and early 2000s including; third harmonic generation (THG) (Barad, Eisenberg et al. 1997), non-degenerate sum frequency generation microscopy (Florsheimer 1999), optical Kerr effect microscopy (Potma, de Boeij et al. 2001), coherent anti-Stokes Raman scattering (CARS) microscopy (Duncan, Reintjes et al. 1982; Zumbusch, Holtom et al. 1999) and multiphoton acousto-optic microscopy (AOM) (Wang, Pang et al. 2003; Zhang, Maslov et al. 2006) to name a few. Several nonlinear responses can be generated simultaneously with the same ultra-short laser pulse; therefore, multicontrast imaging microscopy schemes with parallel detection of MPF, SHG, and THG signals have been successfully implemented (Campagnola, Wei et al. 1999; Chu, Chen et al. 2001; Barzda 2005; Sun 2005; Cisek, Prent et al. 2009). The parallel images can be compared and correlated, giving rich information about the structural architecture and molecular distribution in the sample (Barzda 2005; Greenhalgh, Cisek et al. 2005; Cisek, Spencer et al. 2009). In the following sections, several nonlinear contrast mechanisms are qualitatively described, namely second

harmonic generation, third harmonic generation and multiphoton excitation fluorescence. For detailed quantitative description of these processes see Chapter 2.

1.2.2 Second harmonic generation microscopy

Second harmonic generation (SHG) occurs when two electric fields interact with matter to produce a single resultant field (Boyd 2008). Only media with non-central (non-inversion) symmetry can sustain second harmonic generation, therefore, asymmetric molecules or asymmetric microcrystalline structures are required for SHG. Since the laser focal volume is much larger than individual SHG emitters, central symmetry could also occur from centrosymmetrically aligned or randomly oriented emitters. Therefore, liquids with randomly oriented molecules do not produce significant SHG signal (Giordmaine 1965). Interfaces between different materials can break inversion symmetry, providing a powerful tool for studying second-order hyperpolarizabilities of molecules adsorbed onto surfaces (Bloembergen and Pershan 1962). In addition to the symmetry and structural constraints, phase matching conditions have to be met for efficient SHG to occur in bulk media (Armstrong, Bloembergen et al. 1962). The propagation speed of light depends on the wavelength dependent refractive index of the material. This creates a phase shift between the fundamental laser light and the generated second harmonic, diminishing SHG. Phase matching conditions are for example achieved by employing uniaxial nonlinear crystals that have different refractive indices along the ordinary and extraordinary crystal axes (Boyd 2008). At a certain orientation of the crystal, both waves propagate at the same speed leading to the efficient conversion of the nonlinear signal. Due to the wide angle cone of light produced with a high NA microscope objective, phase matching conditions are usually satisfied for at least some of the incoming rays. The efficiency of SHG depends on the structural arrangement of the sample. The presence of multilayer structures, macro-chirality, and proper orientation of structural axes with respect to the direction of the laser polarization largely determines the efficiency of microscopic SHG (Verbiest, Van Elshocht et al. 1998; Campagnola, Wei et al. 1999; Chu, Chen et al. 2004; Kolthammer, Barnard et al. 2005).

Biological membranes are good candidates for SHG at an interface. The two leaflets of a lipid bilayer have to be asymmetrically arranged to produce SHG (Moreaux, Sandre et al. 2000). Often this appears to be the case, since cellular membranes have different lipid and protein

contents in the two sides. However, two adhered oppositely arranged membranes form a centrosymmetric structure, therefore canceling the SHG signal (Moreaux, Sandre et al. 2000).

Sometimes SHG in biological specimens appears from microcrystalline structures, for example, calcite in the pineal gland of the human brain (Baconnier and Lang 2004), muscle tissue (Chu, Chen et al. 2004; Greenhalgh, Prent et al. 2007), collagen (Freund and Deutsch 1986; Stoller, Reiser et al. 2002), aggregates of light-harvesting pigment protein complexes (LHCII) (Barzda 2008) and starch granules (Mizutani, Sonoda et al. 2000). The SHG from those structures is generated in a similar way as in nonlinear crystals. Highly organized birefringent biological structures can provide phase matching conditions for effective bulk second harmonic generation. By measuring SHG at different sample orientations, the tensor elements of the nonlinear optical susceptibility can be deduced describing the structural organization of molecules in a three dimensional array (Chu, Chen et al. 2004). The technique is extended in this thesis to include measurements of the polarization of the outgoing SHG, as will be seen in polarization-in-polariztion-out (PIPO) microscopy of ZnSe crystals and starch granules in Chapter 4 and Chapter 5, respectively. In most cases, bulk generated SHG signals appear to be stronger than surface SHG, due to larger amounts of coherently phased molecules present in a focal volume compared to the excited molecules at an interface. SHG microscopy has been reviewed in several publications (Zipfel, Williams et al. 2003; Barzda 2008; Cisek, Prent et al. 2009).

1.2.3 Third harmonic generation microscopy

Third harmonic generation (THG) is a third-order nonlinear process, which occurs when three incident photon fields interact, producing one resultant THG photon. In nonlinear optical (NLO) microscopes THG is generated under different conditions than SHG, and does not require non-central symmetry, but rather, highlights sample regions which contain interfaces between different refractive indices or third-order NLO susceptibilities. Multilayer structures can enhance the far-field THG intensity provided the right periodicity matching for the excitation wavelength is achieved (Tsang 1995; Kolthammer, Barnard et al. 2005). THG is sensitive to the orientation of the interface with respect to the principal direction of propagation of the laser beam (Muller, Squier et al. 1998). Fig. 2.1-4 demonstrates the interface orientation effect on THG in the imaging of polystyrene beads. A uniform bead larger than the laser focal volume generates THG

only from the top and bottom edge of the structure, where the laser encounters interfaces, and no signal is produced in the middle of the structure, or at the sides of the structure where the laser is oriented parallel to the interface (see Fig. 2.1-4 (a)).

THG can be used to image various biological structures including biological membranes (Muller, Squier et al. 1998), cell walls (Squier, Muller et al. 1998; Cox, Moreno et al. 2005) and multilayer structures such as grana of chloroplasts (Muller, Squier et al. 1998; Millard, Wiseman et al. 1999; Chu, Chen et al. 2001), aggregates of LHCII (Prent, Cisek et al. 2005), and cristae in mitochondria (Barzda 2005). THG was also observed in rhizoids from green algae (Squier, Muller et al. 1998), erythrocytes (Millard, Wiseman et al. 1999), cultured neurons and yeast cells (Yelin and Silberberg 1999), glial cells (Barille, Canioni et al. 2001), myocytes (Chu, Chen et al. 2004; Barzda 2005), *Drosophila* embryos (Supatto, Debarre et al. 2005), sea urchin larval spicules (Oron, Tal et al. 2003) and hemozoin crystals in malaria infected blood cells (Belisle, Costantino et al. 2008). THG was also recently used for imaging human cornea (Olivier, Aptel et al. 2010) as well as nucleoli in hematoxylin stained histological tissues (Tuer, Tokarz et al. 2010). Since THG efficiency depends on the third-order NLO susceptibility of the material, biological samples containing molecules with high third-order nonlinearities, such as chlorophylls and carotenoids (Marder, Torruellas et al. 1997), are one of the best candidates for imaging with THG, and therefore photosynthetic biological structures are prime candidates for nonlinear THG imaging, see Chapter 6.

1.2.4 Multiphoton excitation fluorescence microscopy

The processes of two- and three-photon excitation were first experimentally demonstrated in the optical range in the 1960's (Kaiser and Garrett 1961; Singh and Bradley 1964). Multiphoton absorption occurs when the energy of a molecular transition from the ground electronic state to an excited electronic state matches the combined energy of two or three photons. When the nonlinear excitation process of the molecules is not clearly determined, the resulting fluorescence signal is commonly denoted as multiphoton excitation fluorescence (MPF). Two-photon excitation fluorescence is the most frequently used NLO contrast mechanism in today's microscopic investigations due to the commercial availability of two-photon excitation laser scanning microscopes. MPF contrast in microscopy is based on the NLO excitation of molecules and the subsequent emission of a photon either by the same or by a sensitized neighboring

molecule. A major benefit of MPF microscopy is the possibility to excite molecules within a tiny focal volume due to the nonlinearity of the excitation. Besides providing inherent optical sectioning, without the use of a confocal pinhole in the setup, the nonlinear confinement of excitation reduces out of focus photobleaching in microscopic samples, which was demonstrated already in the initial study on MPF microscopy (Denk, Strickler et al. 1990). MPF microscopy has been described in several reviews (for example see (Konig 2000; So, Dong et al. 2000; Diaspro 2002; Zipfel, Williams et al. 2003)).

Chapter 2
Theory of Nonlinear Optical Microscopy

A theoretical explanation of NLO microscopic contrast mechanisms of second harmonic generation, third harmonic generation and multiphoton excitation fluorescence is presented. Interactions between light and matter can generate significant nonlinear optical signals in a nonlinear microscope determined by the material properties of the sample, i.e. nonlinearity tensors, (section 2.1). A microscope is only as good as the information it can provide, therefore, in order to efficiently utilize microscopic signals quantitatively to determine material properties, the remaining sections (2.2 - 2.6) of the chapter are focused on the description of the second harmonic generation nonlinearity tensor; its basic properties in different types of media and the information that can be gathered using polarization-in-polarization-out microscopy (sections 2.3 and 2.4), the visualization of the tensor (section 2.5), as well as, theoretical calculations of the tensor (section 2.6).

2.1 The Light-Matter Interaction

2.1.1 Induced polarization

Light-matter interactions can be described via an induced polarization, i.e., the induced dipole moment per unit volume. Ultrafast laser pulses, which are used in laser scanning microscopes, have sufficient intensity to induce a nonlinear polarization in various materials. For an intense optical electric field vector ***E***, the polarization vector ***P*** can be expanded in the power series

$$\mathbf{P}(\omega) = \chi^{(1)} : \mathbf{E} + \chi^{(2)} : \mathbf{EE} + \chi^{(3)} : \mathbf{EEE} + \chi^{(4)} : \mathbf{EEEE} + \chi^{(5)} : \mathbf{EEEEE} + \ldots \qquad 2.1\text{-}1$$

where $\chi^{(1)}$ is the linear susceptibility tensor representing effects such as linear absorption and refraction, $\chi^{(2)}$ is the second-order NLO susceptibility tensor, $\chi^{(3)}$ is the third-order NLO susceptibility tensor, and so on. Note that ":" in the Eq. 2.1-1 represents tensor multiplication, and is not specific to the tensor rank. Second harmonic generation is a second-order process, whereas two-photon excitation fluorescence and third harmonic generation are both third-order processes. Eq. 2.1-1 shows that the same excitation source can induce several nonlinear effects simultaneously. Nonlinear effects are characterized by new components of the electric field generated from the acceleration of charges as the nonlinear polarization $\boldsymbol{P}^{NL}$ (second, third, and

higher terms in Eq. 2.1-1) drives the electric field. If we assume that the medium is lossless and dispersionless, the induced polarization at time *t* depends only on the instantaneous value of the electric field, and the equation 2.1-1 can be re-written as a function of time (Boyd 2008):

$$\mathbf{P}(t) = \chi^{(1)} : \mathbf{E} + \chi^{(2)} : \mathbf{EE} + \chi^{(3)} : \mathbf{EEE} + \chi^{(4)} : \mathbf{EEEE} + \chi^{(5)} : \mathbf{EEEEE} + ... \qquad 2.1\text{-}2$$

The laser wavelengths in nonlinear microscopy are purposely chosen to be away from resonance bands to decrase photodamage to *in vivo* structures, as will be discussed in section 3.2.3. When linear absorption is negligible, the nonlinear polarization drives waves with amplitude ***E'*** described by the inhomogeneous wave equation

$$\nabla^2 \mathbf{E}' - \frac{n^2}{c^2}\frac{\partial^2 \mathbf{E}'}{\partial t^2} = \frac{1}{\varepsilon_0 c^2}\frac{\partial^2 \mathbf{P}^{NL}}{\partial t^2} \qquad 2.1\text{-}3$$

where *n* represents the linear refractive index, *c* is the speed of light in vacuum, *t* is time, and ε_0 is the permittivity of free space.

2.1.2 Second harmonic generation

When the optical electric field is sufficiently intense and the second-order susceptibility $\chi^{(2)}$ is non-zero, the second-order polarization $\boldsymbol{P}^{(2)}$ is induced.

$$\mathbf{P}^{(2)} = \chi^{(2)} : \mathbf{EE} \qquad 2.1\text{-}4$$

If a monochromatic electric field ***E(t)*** has frequency ω, the nonlinear polarization becomes

$$\begin{aligned} \mathbf{P}^{(2)}(t) &= \left(\chi^{(2)} : \mathbf{EE}\right)\cos^2 \omega t \qquad 2.1\text{-}5 \\ &= \frac{1}{2}\left(\chi^{(2)} : \mathbf{EE}\right)\left(\cos 2\omega + 1\right) \end{aligned}$$

where the 2ω contribution leads to emission of light at the second harmonic frequency, shown schematically in Fig. 2.1-1: Two photons each at frequency ω nonlinearly scatter inducing the emission of a single photon at the double frequency. SHG proceeds via an intermediate virtual level (dotted lines in Fig. 2.1-1 which has less energy than the electronic resonance, and therefore, no absorption of the fundamental laser wavelength occurs. For fields with different

frequency components, the second harmonic can be generated from each of the fields separately, while the combined fields result in sum- and difference-frequency generation.

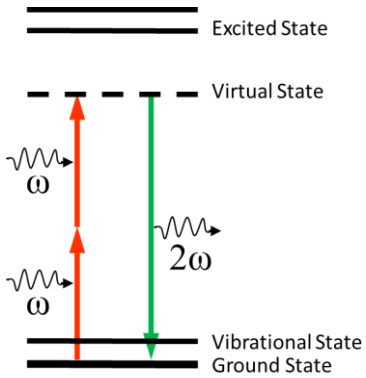

Fig. 2.1-1: Schematic of second harmonic generation.

According to time independent perturbation theory, which assumes no absorption or dispersion in the material, the second harmonic generation tensor is equivalent to the octupole moment of the electron ground state distribution. Notably it also depends on the difference between permanent dipole moment between the ground and excited states. However if the fundamental or SHG frequency is close to a molecular resonance, then the single or two-photon transition dipole moment dominates the $\chi^{(2)}$ (Boyd 2008).

Second harmonic generation is only possible in media with non-central symmetry. A simple proof can be shown by using the contradictory assumption that there exists a centrally symmetric media with $\chi^{(2)} \neq 0$ (Boyd 2008). Since the material is centrally symmetric, reversing the sign of the electric field results in reversed induced polarization, leading to:

$$\begin{aligned} -\mathbf{P}^{(2)}(t) &= \chi^{(2)} : (-\mathbf{E}(t))(-\mathbf{E}(t)) \\ &= \chi^{(2)} : \mathbf{E}(t)\mathbf{E}(t) \end{aligned} \qquad 2.1\text{-}6$$

The contradiction shown in comparing Eq. 2.1-6 and Eq. 2.1-4 proves that $\chi^{(2)} = 0$ in media with central symmetry. This conclusion has serious implications on structural imaging using SHG, since it implies that central symmetry at any scale, from molecular to macromolecular will yield no SHG, and forms the basis for structural studies using the SHG contrast mechanism.

There is an exception to the above conclusion, and in fact a centrally symmetric material can induce SHG due to the electric field, which is discussed in the next section.

2.1.3 SHG from enhancement of the electric field

A classical treatment of a dielectric cylinder is briefly presented in order to explain results from nonlinear optical imaging of semiconductor ZnSe nanowires (NWs). The analysis could also apply to biological structures which also often assemble into fibrillar structures with diameters ranging from tens to hundreds of nm, and tens to hundreds of μm long. Size quantization effects are not commonly observed for nanowire diameters 50-100 nm, since this is well beyond the quantum confinement size of 9 nm for ZnSe (Kumbhojkar, Mahamuni et al. 1998).

An electric field parallel to a dielectric cylinder $E_{0||}$ results in an electric field inside the dielectric cylinder $E_{||}$ of equal magnitude (Landau and Lifshitz 1984):

$$\mathbf{E}_{||} = E_{o||} \qquad 2.1\text{-}7$$

When the incident electric field is perpendicular to the cylinder $E_{0\perp}$, and under the assumption that the cylinder radius *a* remains much less than the wavelength of light λ, the electric field within the cylinder $E_{\perp}$ is diminished due to a surface effect according to (Eq. 8.4 in (Landau and Lifshitz 1984)):

$$\mathbf{E}_{\perp} = \frac{2E_{0\perp}}{1+\varepsilon_r} \qquad 2.1\text{-}8$$

where $\varepsilon_r = \varepsilon/\varepsilon_0$. ε and ε_0 are the dielectric constants of the cylinder and surrounding material, respectively. The reduced internal electric field perpendicular to the cylinder results in a diminished induced polarization of the dielectric material, hence this effect is often referred to as depolarization. When the nanowire radius is comparable to the light wavelength, another approach is used (Ruda and Shik 2006) showing a strong oscillatory dependence of the internal electric field on the frequency of the optical electric field.

Regardless of the symmetry of the media, a non-uniform spatial distribution of the optical electric field can induce SHG. The second-order polarization from isotropic structures governing emission at a frequency *2ω* can be determined by the formula (Bloembergen, Chang et al. 1968):

$$\mathbf{P}(2\omega) = \eta \nabla \bullet \mathbf{E}(\omega)^2 + \zeta \mathbf{E}(\omega)\left(\nabla \bullet \mathbf{E}(\omega)\right) \qquad 2.1\text{-}9$$

where η and ξ are phenomenological coefficients, such that $\eta = -2\xi$ for isotropic and cubic structures, and ***E*** is the laser electric field. While the first term corresponds to a volume effect, having a dipole emission pattern, the second term corresponds to a surface effect having a quadrupole emission pattern, see Fig. 2.1-2 (a) and (b), respectively. The two distinct physical effects give rise to different angular dependencies.

SHG induced by an electric field parallel to the dielectric cylinder $E_{\parallel}$ can be written as the radiation of an effective dipole parallel to the light wave vector with the Poynting vector $S_{\parallel}$ as (Barzda, Cisek et al. 2008)

$$S_{\parallel} = A \frac{E_{\parallel}^4 \left(1 + \sqrt{\varepsilon_r}\right)^2}{\left(\varepsilon_r + 1\right)^2} \sin^2 \varphi \qquad 2.1\text{-}10$$

and SHG caused by the perpendicular electric field to a dielectric cylinder $E_{\perp}$ has a quadrupole character with

$$S_{\perp} = A \frac{E_{\perp}^4 \left(\varepsilon_r - 1\right)^2}{\left(\varepsilon_r + 1\right)^2} \sin^2 2\varphi \qquad 2.1\text{-}11$$

where the factor A is identical for both formulas and φ is the angle between the excitation light vector and the direction to the point of observation, as shown in Fig. 2.1-2 (a) and (b).

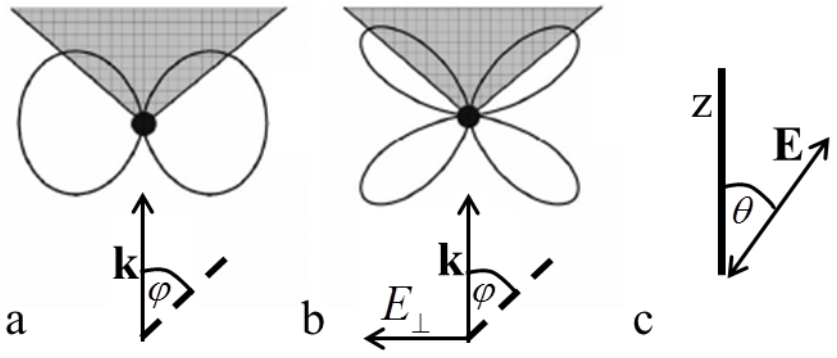

Fig. 2.1-2: Schematic angular distribution of the SHG intensity in a dielectric cylinder.
SHG emission pattern is shown for (a) dipole mode and (b) quadrupole mode where k depicts the wave vector of laser excitation. The axis of the cylinder is perpendicular to the page in (a) and (b). The orientation of the optical electric field E is perpendicular to the page in (a) and lies in the page plane in (b). The photodetector collects SHG radiation emitted in the forward direction (up), within a cone, defined by the angle φ and shown in the shaded area in (a) and (b). Panel (c) shows the angle θ is between the cylinder axis (z) and the optical electric field ***E***. Panels (a) and (b) reprinted with permission from (Barzda, Cisek et al. 2008), Copyright 2008, American Institute of Physics.

The Fig. 2.1-2 (a) and (b) show that while the volume and surface effects, respectively, generate radiation at dipole and quadrupole patterns, the signal collection is ultimately a function of the collection cone angle of the microscope objective, which in our case has numerical aperture of 0.75, and therefore, has a collection cone angle of 97.2° (see Eq. 3.2-1). This cone angle is taken into account via integrating Eq. 2.1-10 and Eq. 2.1-11 over the angle -49°<φ<49°, and letting the laser polarization be an angle θ from the cylinder axis shown in Fig. 2.1-2 (c), and using the electric field for the dielectric cylinder Eq. 2.1-7 and Eq. 2.1-8, the SHG intensity can be written as (Barzda, Cisek et al. 2008):

$$I_{SHG} \propto E_0^4 \left(\cos^4\theta + \frac{10.3\left(\varepsilon_r - 1\right)^2}{\left(\varepsilon_r + 1\right)^4 \left(1 + \sqrt{\varepsilon_r}\right)^2} \sin^4\theta \right) \qquad 2.1\text{-}12$$

2.1.4 Third harmonic generation

Third harmonic generation (THG) is similar to SHG, although in this case, 3 photons of frequency ω are converted to one photon at frequency 3ω, which is shown schematically in Fig. 2.1-3. The expansion of the third-order polarization for a field of a single frequency can be described by:

$$\begin{aligned}\mathbf{P}^{(3)}(t) &= \left(\chi^{(3)} : \mathbf{EEE}\right)\cos^3 \omega t \\ &= \left(\chi^{(3)} : \mathbf{EEE}\right)\left(\frac{1}{4}\cos 3\omega t + \frac{3}{4}\cos \omega t\right)\end{aligned} \qquad 2.1\text{-}13$$

The component containing 3ω is evident in the first term of this expansion, and represents the third harmonic polarization. According to time independent perturbation theory, under nonresonant conditions $\chi^{(3)}$ is a function of the hexadecimal pole and the quadrupole moment of the ground state electron distribution. If on the other hand the fundamental, second or third harmonic frequencies are near a molecular absorption band, than $\chi^{(3)}$ can be dominated by the linear absorption coefficient, the two photon absorption coefficient or the three photon absorption coefficient (Boyd 2008). As was the case for the second-order polarization, applied fields with multiple frequency components could generate additional third-order processes including four wave mixing processes such as coherent anti-Stokes Raman scattering (CARS) and the optical Kerr effect. CARS requires that the difference in frequency between the pump and the Stokes beam is equal to a Raman vibrational frequency, while, the optical Kerr effect depends on the frequency dependent dispersion of the material which is a resonance effect.

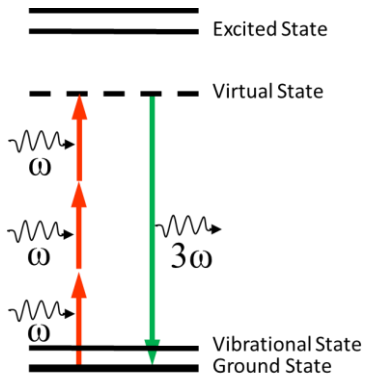

Fig. 2.1-3: Schematic of third harmonic generation

Efficient THG in a microscope requires media with inhomogeneous properties. Although THG can be generated in homogeneous media since it is dipole allowed (Boyd 2008), under tight focusing conditions the THG vanishes when the media has normal dispersion. However, when the focal symmetry is broken by focusing the beam at the entrance window of a gas cell, THG signal can be obtained (Ward and New 1969). This effect constitutes the basis for the THG contrast mechanism in microscopy, giving contrast to interfaces in microscopic structures

(Barad, Eisenberg et al. 1997). The loss of THG under tight focusing can be described via considering the paraxial wave equation assuming slow spatial variation of electric field amplitudes along the beam propagation direction (y direction). The solution for the paraxial wave equation for the amplitude of the third harmonic $A_{3\omega}$ can be written (Boyd 2008)

$$A_{3\omega}(y) = \frac{i6\pi}{nc}\chi^{(3)}A_{\omega}^{3}W_{3\omega} \qquad 2.1\text{-}14$$

where A_{ω} is the amplitude of the fundamental electric field, and the phase matching integral $W_{3\omega}$ is

$$W_{3\omega}(\Delta k, y_0, y) = \int_{y_0}^{y} \frac{e^{i\Delta k y'}}{\left(1+2i\frac{y'}{b}\right)} dy' \qquad 2.1\text{-}15$$

where b is the confocal parameter (see Eq. 3.2-3), $\Delta k = 3k_{\omega} - k_{3\omega}$ is the wave vector mismatch and y_0 is the value of y at the entrance of the nonlinear medium. $W_{3\omega}$ can be solved analytically in the case of a tightly focused Gaussian beam in a homogenous medium, where the limits of integration are replaced by $-\infty$ to ∞, and the solution can be expressed as:

$$W_{3\omega}(\Delta k, y_0, y) = \begin{cases} 0 & \Delta k \le 0 \\ \frac{1}{2}\pi b^2 \Delta k e^{-\frac{b\Delta k}{2}} & \Delta k > 0 \end{cases} \qquad 2.1\text{-}16$$

Therefore in materials that are normally dispersive, the amplitude of the integral, and therefore THG equals zero, even under the condition of perfect phase-matching $(\Delta k = 0)$.

The cancellation of THG in the far field under tight focusing conditions can be understood from consideration of the Gouy phase anomaly that any beam undergoes when passing through a focus (Gouy 1890). The fundamental beam undergoes a phase shift of π rad, and therefore the THG wave generated before the focus is out of phase with the THG wave generated after the focus, resulting in THG cancellation in the far field (Ward and New 1969; Boyd 2008). THG is observed only if the laser focal volume is at an interface of two materials with different refractive indices or third-order nonlinear susceptibilities. Although THG can only

be visualized at an interface, it is a volume effect since it is generated by the bulk media on each side of the interface (Saeta and Miller 2001).

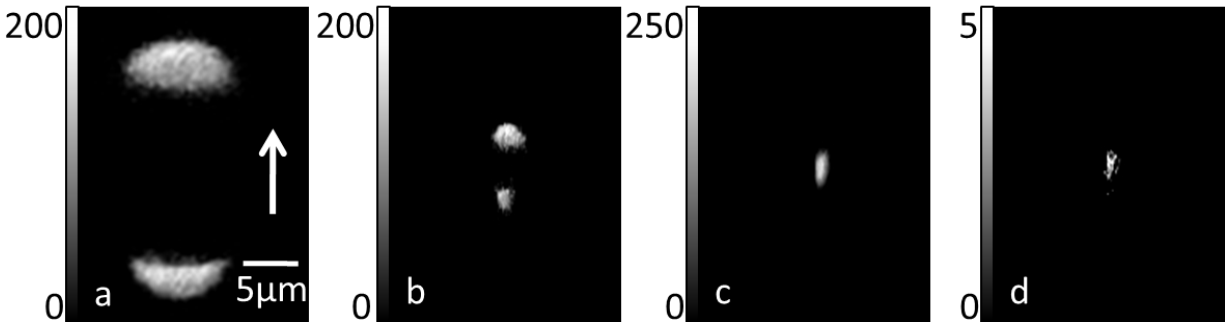

Fig. 2.1-4: Axial views of polystyrene beads of different sizes imaged with THG.
The bead sizes are 10, 3, 1, and 0.1 μm, for (a)-(d), respectively. The laser propagation direction is indicated by the arrow. Figure reprinted with permission from (Carriles, Schafer et al. 2009), Copyright 2009, American Institute of Physics.

In order to demonstrate that THG depends on the size of the object and orientation of the interfaces with respect to the laser beam propagation, several different sized polystyrene beads were imaged in 3D. The image stacks were rendered in 3D and are presented in the axial view in Fig. 2.1-4 where the laser enters from the bottom with respect to the images, and the signal is collected above the beads. The axial point spread function (PSF) of a 1028 nm laser focused by a 1.3 NA oil immersion objective is about 1 μm for THG, as calculated via Eq. 3.2-3. Therefore, the two beads shown in panels (a) and (b) of Fig. 2.1-4 with diameters of 10 and 3 μm, respectively, are larger than the laser PSF, while beads equal or smaller than the PSF are shown in panels (c) and (d) for 1 and 0.1 μm beads, respectively.

It is important to understand typical images produced with THG and relate them to the actual structure of the imaged object. Fig. 2.1-4 shows that beads larger than the PSF ((a) and (b)) generate THG only from the top and bottom interface, where the laser focal volume experiences a change in index of refraction between the surrounding matrix and the polystyrene material. The bottom interface, where the laser enters, is more compact, while the top interface appears larger due to distortion of the beam as it goes through the structure, and results in a larger PSF. It is important to note that no signal originates from the middle of the large beads, since the laser focal volume experiences homogenous polystyrene media. The sides of the bead also do not produce THG because the interfaces appear parallel to the laser propagation direction; therefore breaking of the longitudinal beam symmetry of the focal volume is almost

negligible. Thus it is noteworthy that objects larger than the PSF may produce THG from the two opposite interfaces, but not in the middle, hence they could be misinterpreted as two distinct objects, and therefore discrimination between the two situations may not always be possible.

For the polystyrene beads that are smaller or comparable to the axial PSF of the microscope (1 μm and 0.1 μm beads in (c) and (d), respectively), the third harmonic reveals a continuous volume comparable in size to the PSF. Interestingly, even for the 1 μm bead (Fig. 2.1-4 (c)), the bottom side appears to be narrower with better defined border than the top of the bead. This indicates that some beam distortion occurs over one micron of the bead structure. A 0.1 μm bead was imaged in THG (Fig. 2.1-4 (d)), and showed very weak signal, at least 1 order of magnitude weaker than the larger beads. Since THG is generated in the bulk, therefore, it is a volume dependent effect. A 0.1 μm bead has a very small volume; therefore it provides only a small contribution to the difference in THG between the bead and the surrounding media.

The THG image of the 0.1 μm diameter bead (Fig. 2.1-4 (d)) does not appear significantly smaller than the image of the 1 μm bead (Fig. 2.1-4 (c)) even though there is an order of magnitude difference in size between them. This example of bead imaging shows that structures smaller than diffraction limited resolution appear in THG images as solid objects comparable in size to the PSF. THG imaging of small particles has the same selection rules as for larger particles. Therefore sub-wavelength spatial heterogeneities could serve to enhance the THG in certain systems i.e. the multilayer structure common to many biological systems may strengthen the THG signal (Tsang 1995; Kolthammer, Barnard et al. 2005). The THG signal strength also depends on the difference in the refractive index between the structure and the surrounding media, as well as on the second hyperpolarizabilities of the molecules and their ordering in the structure. Third harmonic generation from different structural arrangements has been modeled by conducting numerical integration of the phase-matching integral (Eq. 2.1-16) (Naumov, Sidorov-Biryukov et al. 2001; Schins, Schrama et al. 2002). THG microscopy was recently reviewed (Squier and Muller 2001; Sun 2005; Barzda 2008; Carriles, Schafer et al. 2009; Cisek, Prent et al. 2009).

In addition to THG, the third-order NLO susceptibility tensor also governs two photon excitation, which is commonly used to image fluorescent biological structures. The multiphoton excitation fluorescence contrast is discussed in the following section.

2.1.5 Multiphoton excitation fluorescence

Multiphoton excitation fluorescence (MPF) is a multistep process consisting of molecular absorption of two or more photons followed by emission of a fluorescence photon. Fluorescence is not a coherent optical response in contrast to SHG or THG; therefore, phase matching and interference effects are not observed in MPF. This simplifies the interpretation of microscopic images where the fluorescence can be directly related to the presence of fluorophores in the sample.

The process of two and three-photon excitation fluorescence is depicted schematically in Fig. 2.1-5, showing the absorption of two or three photons, followed by emission of a fluorescence photon. Two- and three-photon excitation is described by the imaginary components of the third and fifth-order NLO susceptibilities, respectively (see Eq. 2.1-1). The transition rate for two-photon absorption R depends on the square of the laser intensity, I, as follows (Boyd 2008),

$$R = \frac{\sigma^{(2)} I^2}{\hbar\omega} \qquad 2.1\text{-}17$$

where, $\sigma^{(2)}$ is the two-photon absorption cross section and ω is the frequency of the excitation photons. The quadratic dependence of absorption or fluorescence on the excitation intensity can be used to determine whether a sample is excited via two-photon excitation. Two- or three-photon absorption occurs when the energy of a molecular transition matches the combined energy of two or three photons, as depicted in Fig. 2.1-5 (a) and (b) respectively. Quantum mechanically, the absorption probability of two photons is proportional to the two-photon transition moment M_{ng} from the ground state g to the excited state n via intermediate state m, and can be expressed as follows (Boyd 2008):

$$M_{ng} = \sum_{m(\neq n,\neq g)} \left[2\frac{(\boldsymbol{\mu}_{nm}\cdot\mathbf{E})(\boldsymbol{\mu}_{mg}\cdot\mathbf{E})}{\hbar\omega - \hbar\omega_{mg}} \right] - 2\frac{(\Delta\mathbf{p}_{ng}\cdot\mathbf{E})(\boldsymbol{\mu}_{ng}\cdot\mathbf{E})}{\hbar\omega} \qquad 2.1\text{-}18$$

where, μ_{nm}, μ_{mg}, and μ_{ng} are the transition dipole moments between the n and m, m and g, and n and g states, respectively. The term $\Delta\boldsymbol{p}_{ng}=\boldsymbol{p}_{nn}-\boldsymbol{p}_{gg}$ is the change in the static dipole moment between the final n and initial g states. $\hbar\omega_{mg}$ is the energy difference between the states m and g.

Eq. 2.1-18 has two distinct terms: (i) the first term describes the two-photon excitation process via one photon excitation to a virtual state *m* and subsequent excitation to the final electronic state *n*; (ii) the second term expresses direct two-photon excitation to the final state via change in the static dipole moment between the *n* and *g* states. According to the first process, the ground and the final excited states have the same symmetry; therefore the excitation is one-photon forbidden and two-photon allowed. This situation usually appears for non-polar molecules. For polar molecules, two-photon absorption can proceed via the second mechanism, if a large change in the dipole moment occurs during excitation. In this case, the two-photon transition dipole moment is proportional to the one-photon transition dipole, thus two-photon absorption bands will be similar to the linear absorption. The two-photon absorption spectrum of molecules may have similar bands as linear absorption, but new bands may appear and some bands might be missing. The transition probability M_{ng} (Eq. 2.1-18) is proportional to the two-photon absorption cross section and is related to the imaginary part of $\chi^{(3)}$ according to the first term, and depends on the linear absorption coefficient according to the second term.

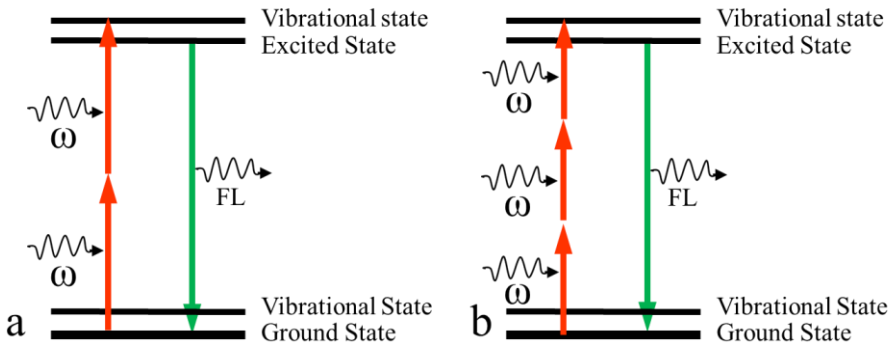

Fig. 2.1-5: Schematic diagram of (a) two and (b) three-photon fluorescence.

Following nonlinear absorption, the dynamics of excitation relaxation proceed as if the excited state was populated via linear absorption. Therefore the fluorescence photon is red-shifted due to the Stokes shift, enabling simple practical differentiation between harmonics and fluorescence via optical bandpass filters.

2.2 Properties of the Second Harmonic Generation Tensor

2.2.1 Introduction to the hyperpolarizability tensor

The hyperpolarizability tensor β is the molecular version of the bulk second-order nonlinear optical susceptibility tensor, $\chi^{(2)}$, and describes the property of the molecule to produce second-order polarization from electric fields according to Eq. 2.1-4. The hyperpolarizability tensor has 3 indices, the first representing the direction of the output field, and the latter two represent the two input fields. Second harmonic generation is degenerate sum-frequency generation where the input waves have identical frequencies, so the last two indices of the tensor can be freely permuted enabling a simplification of the rank-3 tensor which naturally has 27 elements into the matrix d_{il} which has 18 elements via the following convention (Boyd 2008):

$$\begin{array}{cccccccc} jk: & 11 & 22 & 33 & 23,32 & 13,31 & 12,21 \\ l: & 1 & 2 & 3 & 4 & 5 & 6 \end{array} \qquad \text{2.2-1}$$

So that we can refer to the hyperpolarizability matrix, which is defined as:

$$d_{il} = \beta_{ijk} \qquad \text{2.2-2}$$

where β_{ijk} is the hyperpolarizability tensor for individual SHG emitters, such that the hyperpolarizability of the bulk, where all the molecules are aligned, such as in a crystal, is a function of the number of SHG emitters N and their individual hyperpolarizability.

$$\chi_{ijk} \propto N\beta_{ijk} \qquad \text{2.2-3}$$

In this convention the induced polarization is found via:

$$\begin{pmatrix} P_x \\ P_y \\ P_z \end{pmatrix} = 2\varepsilon_0 \begin{pmatrix} d_{11} & d_{12} & d_{13} & d_{14} & d_{15} & d_{16} \\ d_{21} & d_{22} & d_{23} & d_{24} & d_{25} & d_{26} \\ d_{31} & d_{32} & d_{33} & d_{34} & d_{35} & d_{36} \end{pmatrix} \begin{pmatrix} E_x^2 \\ E_y^2 \\ E_z^2 \\ 2E_yE_z \\ 2E_xE_z \\ 2E_xE_y \end{pmatrix} \qquad \text{2.2-4}$$

where ε_0 is the permittivity of free space. To understand the symmetry properties of rank-3 tensors the rotations of tensors in Cartesian space are reviewed in the following section.

2.2.2 Rank-3 tensor rotation in Cartesian space

Rotation in 3D Cartesian space is accomplished by a general rotation matrix *R*:

$$R = \begin{pmatrix} Rxx & Rxy & Rxz \\ Ryx & Ryy & Ryz \\ Rzx & Rzy & Rzz \end{pmatrix} \qquad 2.2\text{-}5$$

To perform the rotation with a rank-3 tensor, the following formulation is used;

$$\beta'_{abc} = \sum_i \sum_j \sum_k R_{ai} R_{bj} R_{ck} \beta_{ijk} \qquad 2.2\text{-}6$$

where β'_{abc} is a component of the rotated tensor, with the variables *a*, *b*, *c* each representing Cartesian components, and the summations are across x, y and z. Substituting Eq. 2.2-5 into Eq. 2.2-6 gives the following generalized expression for individual rotated tensor elements of rank-3 tensors β'_{abc}:

$$\begin{aligned}
\beta'_{abc} &= \sum_i \sum_j R_{ai} R_{bj} \left(R_{cx}\beta_{ijx} + R_{cy}\beta_{ijy} + R_{cz}\beta_{ijz} \right) \\
&= \sum_i R_{ai} \begin{bmatrix} R_{bx}\left(R_{cx}\beta_{ixx} + R_{cy}\beta_{ixy} + R_{cz}\beta_{ixz} \right) + R_{by}\left(R_{cx}\beta_{iyx} + R_{cy}\beta_{iyy} + R_{cz}\beta_{iyz} \right) \\ + R_{bz}\left(R_{cx}\beta_{izx} + R_{cy}\beta_{izy} + R_{cz}\beta_{izz} \right) \end{bmatrix} \\
&= R_{ax} \begin{bmatrix} R_{bx}\left(R_{cx}\beta_{xxx} + R_{cy}\beta_{xxy} + R_{cz}\beta_{xxz} \right) + R_{by}\left(R_{cx}\beta_{xyx} + R_{cy}\beta_{xyy} + R_{cz}\beta_{xyz} \right) \\ + R_{bz}\left(R_{cx}\beta_{xzx} + R_{cy}\beta_{xzy} + R_{cz}\beta_{xzz} \right) \end{bmatrix} + \\
&\quad R_{ay} \begin{bmatrix} R_{bx}\left(R_{cx}\beta_{yxx} + R_{cy}\beta_{yxy} + R_{cz}\beta_{yxz} \right) + R_{by}\left(R_{cx}\beta_{yyx} + R_{cy}\beta_{yyy} + R_{cz}\beta_{yyz} \right) \\ + R_{bz}\left(R_{cx}\beta_{yzx} + R_{cy}\beta_{yzy} + R_{cz}\beta_{yzz} \right) \end{bmatrix} + \\
&\quad R_{az} \begin{bmatrix} R_{bx}\left(R_{cx}\beta_{zxx} + R_{cy}\beta_{zxy} + R_{cz}\beta_{zxz} \right) + R_{by}\left(R_{cx}\beta_{zyx} + R_{cy}\beta_{zyy} + R_{cz}\beta_{zyz} \right) \\ + R_{bz}\left(R_{cx}\beta_{zzx} + R_{cy}\beta_{zzy} + R_{cz}\beta_{zzz} \right) \end{bmatrix}
\end{aligned} \qquad 2.2\text{-}7$$

To illustrate the use of the rotation formula, the general formula for the β'_{zzz} tensor element under an arbitrary rotation of θ around the x axis is calculated, using the following standard matrix which rotates around the x axis:

$$R_x(\theta) = \begin{pmatrix} 1 & 0 & 0 \\ 0 & \cos\phi & -\sin\phi \\ 0 & \sin\phi & \cos\phi \end{pmatrix} \qquad 2.2\text{-}8$$

Substituting Eq. 2.2-8 into Eq. 2.2-7 reveals:

$$\begin{aligned} \beta'_{zzz} &= -\sin\theta\left[-\sin\theta\left(-\sin\theta\beta_{yyy}+\cos\theta\beta_{yyz}\right)+\cos\theta\left(-\sin\theta\beta_{yzy}+\cos\theta\beta_{yzz}\right)\right]+ \\ &\cos\theta\left[-\sin\theta\left(-\sin\theta\beta_{zyy}+\cos\theta\beta_{zyz}\right)+\cos\theta\left(-\sin\theta\beta_{zzy}+\cos\theta\beta_{zzz}\right)\right] \\ &= -\sin^3\theta\beta_{yyy}+\sin^2\theta\cos\theta\beta_{yyz}+\sin^2\theta\cos\theta\beta_{yzy}-\sin\theta\cos^2\theta\beta_{yzz} \\ &+\sin^2\theta\cos\theta\beta_{zyy}-\sin\theta\cos^2\theta\beta_{zyz}-\cos^2\theta\sin\theta\beta_{zzy}+\cos^3\theta\beta_{zzz} \end{aligned} \qquad 2.2\text{-}9$$

Using Eq. 2.2-7 all the components of the tensor can be obtained for any rotation. To obtain arbitrary rotations we note the rotation matrices around y and z axes:

$$R_y(\phi) = \begin{pmatrix} \cos\sigma & 0 & \sin\sigma \\ 0 & 1 & 0 \\ -\sin\sigma & 0 & \cos\sigma \end{pmatrix} \qquad 2.2\text{-}10$$

$$R_z(\psi) = \begin{pmatrix} \cos\psi & -\sin\psi & 0 \\ \sin\psi & \cos\psi & 0 \\ 0 & 0 & 1 \end{pmatrix} \qquad 2.2\text{-}11$$

Arbitrary rotations can be performed by a sequential multiplication of rotation matrices of simple rotations using Eq. 2.2-11, Eq. 2.2-10 and Eq. 2.2-8.

2.3 SHG from Cubic Crystals

2.3.1 Hyperpolarizability tensor under cubic symmetry

With the aim of describing the SHG from cubic crystals, the hyperpolarizability tensor for a cubic material is reviewed. While cubic symmetry commonly appears in semiconductors, it is a fundamental symmetry, and therefore important to review.

A cubic medium is centrally symmetric along cubic faces, therefore the only nonzero terms of the hyperpolarizability tensor are β_{ijk} such that $i \neq j \neq k$ (Boyd 2008). We will additionally limit the discussion to cubic symmetry T_d where there is only one unique element, since this is a common symmetry in materials with zinc blende structure, including but not limited to ZnSe and ZnO, therefore $\beta_{xyz} = \beta_{xzy} = \beta_{yxz} = \beta_{yzx} = \beta_{zxy} = \beta_{zyx} = k$ (Wagner, Kühnelt et al. 1998). In order to create the hyperpolarizability with the cubic [1 1 1] axis oriented along the *z* direction (to coincide with the geometry of a nanowire) we will create a rotation matrix, which will be the product of a rotation around the *z* axis by $\psi = \pi/4$, rotating the [1 1 1] direction into the z-y plane, and then around the *x* axis by $\phi = \cos^{-1}\left(1/\sqrt{3}\right)$ which rotates the [1 1 1] cubic axis into the z-axis using Eq. 2.2-11 and Eq. 2.2-8, respectively. A third rotation is performed with another rotation matrix around the *z* axis (Eq. 2.2-11) by an angle -δ, giving a rotation parameter of the cubic structure around its [1 1 1] axis, resulting in the product rotation matrix *R* in the form:

$$R = R_z(-\delta) R_x\left(\cos^{-1}\frac{1}{\sqrt{3}}\right) R_z\left(\frac{\pi}{4}\right) \qquad 2.3\text{-}1$$

Rotation of the hyperpolarizability tensor using the rotation matrix Eq. 2.3-1 is accomplished via the Eq. 2.2-6, which results in the following nonzero hyperpolarizability tensor values:

$$\begin{aligned} d_{11} &= -d_{12} = -d_{26} = k\sqrt{\frac{2}{3}}\sin 3\delta \\ d_{16} &= d_{21} = -d_{22} = k\sqrt{\frac{2}{3}}\cos 3\delta \\ d_{15} &= d_{23} = d_{24} = d_{31} = d_{32} = \frac{-d_{33}}{2} = -\frac{k}{\sqrt{3}} \end{aligned} \qquad 2.3\text{-}2$$

The hyperpolarizability matrix for a cubic structure with its [1 1 1] axis along the z-axis can then be written using the values in Eq. 2.3-2 as:

$$d_{ij} = \begin{pmatrix} d_{11} & -d_{11} & 0 & 0 & d_{15} & d_{16} \\ d_{16} & -d_{16} & d_{15} & d_{15} & 0 & -d_{11} \\ d_{15} & d_{15} & -2d_{15} & 0 & 0 & 0 \end{pmatrix} \qquad \text{2.3-3}$$

Substituting the cubic hyperpolarizability matrix into Eq. 2.2-4 the induced polarization components ($P^{(2)}{}_x$ and $P^{(2)}{}_z$) are found. Note that $E_y=0$ is assumed to coincide with the experimental approximation that the axial polarization component of the focused laser beam is negligible. The polarizability components are:

$$\begin{aligned} P_x^{(2)} &\propto d_{11}E_x^2 + 2d_{15}E_xE_z \\ P_z^{(2)} &\propto d_{15}\left(E_x^2 - 2E_z^2\right) \end{aligned} \qquad \text{2.3-4}$$

2.3.2 SHG from cubic crystals with linearly polarized excitation

We assume the layout shown in Fig. 2.3-1 where the laser wave vector $\boldsymbol{k}$ is directed into the page, the cubic crystal has growth direction along [1 1 1] and is oriented along z, at a rotation orientation δ around the cubic [1 1 1] axis (which in this case corresponds to z), and the linear polarization of the laser represented by the electric field vector $\boldsymbol{E}$ is oriented at an angle θ from the cubic axis in the z-x plane. Note that the analyzer orientation along $\boldsymbol{A}$ an angle κ from the cubic axis (also in z-x plane) is shown in this figure however, it is intended for Section 2.3.3, and is not included in this analysis.

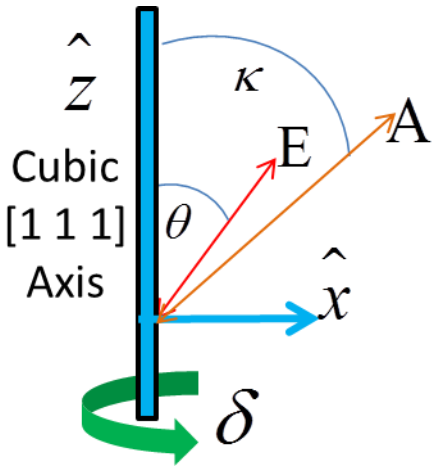

Fig. 2.3-1: Schematic of the geometry for SHG of cubic crystals.

The microscope focal plane is (z-x) where the cubic crystal with growth along [1 1 1] is oriented along the z-axis, the laser is directed into the page, with polarization in the lane of the page, along ***E***, an angle θ from the cubic axis, an analyzer is oriented along ***A***, an angle κ from the cubic axis, and the cubic crystal rotates about its own [1 1 1] axis an angle δ.

According to the geometry, and ignoring the complex conjugates of the electric field, the electric field components can be written as;

$$\begin{aligned} E_x &= E\sin\theta \\ E_z &= E\cos\theta \end{aligned} \qquad \text{2.3-5}$$

where E is the magnitude of the laser electric field. The induced polarization components of a cubic crystal oriented with [1 1 1] axis along the z axis, at a rotation angle δ can be found via substituting the field components Eq. 2.3-5 into Eq. 2.3-4 and using the terms in Eq. 2.3-2:

$$\begin{aligned} P_x^{(2)} &\propto \frac{1}{\sqrt{3}}\left(\sqrt{2}\sin 3\delta \sin^2\theta - \sin 2\theta\right) \\ P_z^{(2)} &\propto \frac{1}{\sqrt{3}}(2\cos^2\theta - \sin^2\theta) \end{aligned} \qquad \text{2.3-6}$$

The SHG intensity is then found as the squared sum of the polarization components, $I_{SHG} = \left(P_x^{(2)}\right)^2 + \left(P_z^{(2)}\right)^2$. Eq. 2.3-6 reveals that the SHG intensity is independent of the cubic crystal rotation parameter δ when $\theta = 0$, but at all other angles, a dependence is expected. In order to further explore this dependence, we will develop polarization-in-polarization-out equations for the cubic crystal in the next section.

2.3.3 Polarization of SHG from cubic crystals

In this section we develop equations that describe the polarization of SHG from cubic NWs that have growth direction along the [1 1 1] cubic axis. While the polarization of the outgoing SHG can simply be calculated by the inverse tangent of the induced polarizations in Eq. 2.3-6, in a microscope, the polarization measurement is performed by placing a polarizer (analyzer) in the signal collection path before the detector and recording the resulting intensities at different orientations of the analyzer. Therefore we assume the analyzer is oriented along $\boldsymbol{A}$ at an angle κ from the cubic [1 1 1] axis, see Fig. 2.3-1. The effect of an analyzer in the detection path can be represented by a Jones matrix with κ as the angle in the optical plane between the helical axis (z) and the analyzer axis:

$$J = \begin{pmatrix} \sin^2\kappa & \sin\kappa\cos\kappa \\ \sin\kappa\cos\kappa & \cos^2\kappa \end{pmatrix} \qquad 2.3\text{-}7$$

Then the resulting SHG (I_{SHG}) intensity can be found via

$$I_{SHG} = \left| J\mathbf{P}_{SHG} \right|^2 \qquad 2.3\text{-}8$$

Using the polarization components, Eq. 2.3-6, the dependence of the analyzer angle can be included in the SHG intensity via Eq. 2.3-8 giving:

$$I_{SHG} \propto \frac{1}{3}\left(\cos\kappa\left(1-3\cos^2\theta\right)+\sin\kappa\left(\sin 2\theta-\sqrt{2}\sin 3\delta\sin^2\theta\right)\right)^2 \qquad 2.3\text{-}9$$

This equation shows the relationship between the SHG intensity, the angle of laser polarization to the cubic [1 1 1] axis θ, the analyzer angle κ, and the different values of rotation of the cubic crystal around the [1 1 1] axis, δ.

2.4 SHG from Hexagonal Crystals

2.4.1 Hyperpolarizability tensor under hexagonal symmetry

In this section, materials with hexagonal symmetry will be considered. This symmetry is very common for nanocrystals, applying to starch, muscle as well as collagenous tissues. In addition, ZnSe NWs also exhibit this type of symmetry. When a material has hexagonal symmetry, the

hyperpolarizability tensor is simplified allowing measurement of a crystal specific nonlinearity ratio value which can characterize particular hexagonally crystalline materials. The reason hexagonal symmetry has this parameter is fundamental: a hexagonal crystal is characterized by the width of the hexagon, and the length of the crystal, while a cubic crystal must remain square. A hexagonal material oriented with its axis along z has the following nonzero hyperpolarizability tensor elements: β_{zzz}, $\beta_{zxx}=\beta_{zyy}$, $\beta_{xzx}=\beta_{xxz}=\beta_{yzy}=\beta_{yyz}$, $\beta_{xyz}=-\beta_{yxz}$, $\beta_{zxy}=-\beta_{zyx}$, $\beta_{xzy}=-\beta_{yzx}$. Additionally if the material is dispersionless, $\beta_{xyz}=\beta_{yxz}=\beta_{zxy}=\beta_{zyx}=\beta_{xzy}=\beta_{yzx}=0$ and $\beta_{zxx}=\beta_{xxz}$ (Kleinman 1962; Boyd 2008), however we shall keep two variables, β_{zxx} and β_{xxz} separate and define $\beta_{zxx}/\beta_{xxz}=d_{31}/d_{15}$ as the Kleinman parameter in order to test whether fits to data reveal that the Kleinman condition holds, a common practice in recent publications of hyperpolarizabilities of hexagonally ordered biological materials (Tiaho, Recher et al. 2007; Psilodimitrakopoulos, Amat-Roldan et al. 2010). To model the situation where the hexagonal fibers are tilted into the laser direction (*y*), a rotation around the x axis, by angle ϕ from the z-axis into the y-axis is performed, thus the rotation matrix Eq. 2.2-8 is substituted into the general rotation formulation Eq. 2.2-7, and using the convention Eq. 2.2-1 with Eq. 2.2-2 results in the following rotated hyperpolarizability components $d_{ij}^{'}$ of a hexagonal crystal:

$$
\begin{aligned}
d_{15}^{'} &= d_{15}\cos\phi \\
d_{16}^{'} &= d_{15}\sin\phi \\
d_{21}^{'} &= d_{31}\sin\phi \\
d_{31}^{'} &= d_{31}\cos\phi \\
d_{23}^{'} &= \sin\phi\left(d_{31}\sin^2\phi-\cos^2\phi\left(2d_{15}-d_{33}\right)\right) \\
d_{32}^{'} &= \cos\phi\left(d_{31}\cos^2\phi-\sin^2\phi\left(2d_{15}-d_{33}\right)\right) \\
d_{33}^{'} &= \cos\phi\left(d_{33}\cos^2\phi+\sin^2\phi\left(2d_{15}+d_{31}\right)\right) \\
d_{22}^{'} &= \sin\phi\left(d_{33}\sin^2\phi+\cos^2\phi\left(2d_{15}+d_{31}\right)\right) \\
d_{24}^{'} &= \cos\phi\left(\sin^2\phi\left(d_{33}-d_{31}-d_{15}\right)+d_{15}\cos^2\phi\right) \\
d_{34}^{'} &= \sin\phi\left(\cos^2\phi\left(d_{33}-d_{31}-d_{15}\right)+d_{15}\sin^2\phi\right)
\end{aligned}
\qquad \text{2.4-1}
$$

Therefore the rotated hyperpolarizability in matrix form is:

$$d_{ij}^{'} = \begin{pmatrix} 0 & 0 & 0 & 0 & d_{15}^{'} & d_{16}^{'} \\ d_{21}^{'} & d_{22}^{'} & d_{23}^{'} & d_{24}^{'} & 0 & 0 \\ d_{31}^{'} & d_{32}^{'} & d_{33}^{'} & d_{34}^{'} & 0 & 0 \end{pmatrix} \qquad 2.4\text{-}2$$

Substituting the rotated hyperpolarizability matrix (Eq. 2.4-2 with values from Eq. 2.4-1) into the polarization Eq. 2.2-4 reveals the components of induced polarization ($P^{(2)}{}_x$ and $P^{(2)}{}_z$):

$$\begin{aligned} P_x^{(2)} &\propto 4d_{15}^{'}E_xE_z \\ P_z^{(2)} &\propto 2E_x^2d_{31}^{'} + 2E_z^2d_{33}^{'} \end{aligned} \qquad 2.4\text{-}3$$

2.4.2 SHG from hexagonal crystals with linearly polarized excitation

Assuming the schematic shown in Fig. 2.4-1 where the laser has ***k*** orientation vector along the y axis, and is linearly polarized along ***E*** in the z-x plane, an angle θ from the z axis, and that the hexagonal structures have axis in the z-y plane, an angle ϕ from the z axis.

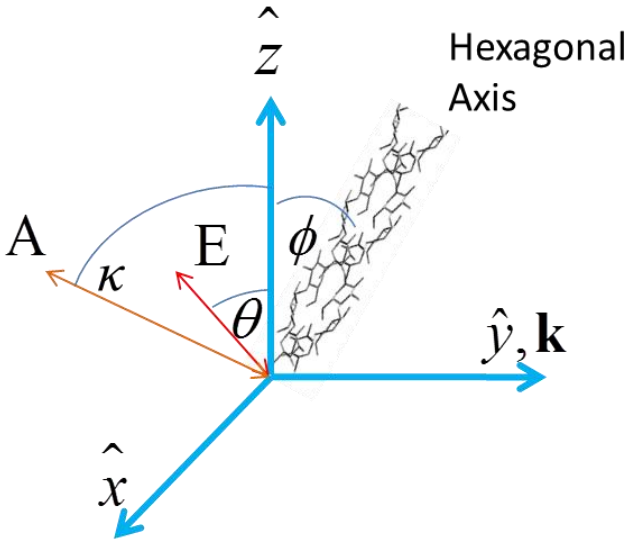

Fig. 2.4-1: Schematic of the geometry for SHG of hexagonal crystals.
The laser is directed along the y-axis, with polarization (E) in the z-x plane an angle θ from the z-axis, analyzer (A) in the z-x plane an angle κ from the z axis, and the hexagonal axis is oriented in the z-y plane an angle ϕ from the z-axis.

According to the geometry laid out in Fig. 2.4-1, the laser electric field components can be expressed as

$$E_x(t) = E\left(e^{-i\omega t} + e^{i\omega t}\right)\sin\theta = 2E\cos\omega t\sin\theta$$
$$E_z(t) = E\left(e^{-i\omega t} + e^{i\omega t}\right)\cos\theta = 2E\cos\omega t\cos\theta \qquad 2.4\text{-}4$$

where E is the magnitude of the electric field, ω is the frequency and t is time. Note that in this instance, the time-dependency is carried forward because the numerical pre-factor is of interest. We can find induced polarization components by substitution of Eq. 2.4-4 into Eq. 2.4-3, giving:

$$P_x^{(2)} \propto 8E^2 d_{15}^{'}\cos^2\omega t\sin 2\theta$$
$$P_z^{(2)} \propto 8E^2\cos^2\omega t\left(d_{31}^{'}\sin^2\theta + d_{33}^{'}\cos^2\theta\right) \qquad 2.4\text{-}5$$

Substituting the rotated SHG tensor elements Eq. 2.4-1 into Eq. 2.4-5 the induced polarization components as a function of angle of polarization of the laser in the z-x plane *(θ)* and tilt of the hexagonal structure into the laser direction in the *z-y* plane *(ϕ)* are obtained:

$$P_x^{(2)} \propto 8E^2 d_{15}\cos^2\omega t\cos\phi\sin 2\theta$$
$$P_z^{(2)} \propto 8E^2\cos^2\omega t\left(d_{31}\cos\phi\sin^2\theta + \left(d_{33}\cos^2\phi + \sin^2\phi\left(2d_{15} + d_{31}\right)\right)\cos^2\theta\right) \qquad 2.4\text{-}6$$

Since interest lies in the components at the double frequency, the following relation is applied; $2\cos^2\omega t = \cos 2\omega t + 1$ into Eq. 2.4-6 and ignoring the time-independent terms since they do not radiate, one obtains (Erikson, Ortegren et al. 2007):

$$P_x^{(2)} \propto 4E^2 d_{15}\left(\cos 2\omega t\right)\cos\phi\sin 2\theta$$
$$P_z^{(2)} \propto 4E^2\left(\cos 2\omega t\right)\left(d_{31}\cos\phi\sin^2\theta + \left(d_{33}\cos^2\phi + \sin^2\phi\left(2d_{15} + d_{31}\right)\right)\cos^2\theta\right) \qquad 2.4\text{-}7$$

Next performing a time-average over one period *(T)*, since the integration time during the measurement is very long compared to the laser frequency,

$$A_{avg}(t) = \frac{\int_0^T A(t)dt}{T} \qquad 2.4\text{-}8$$

and using the fact that if a is a constant then

$$\int_0^T \sin^2(at)dt = \frac{T}{2} - \frac{\sin(2aT)}{4a} \qquad 2.4\text{-}9$$

$$\int_0^T \cos^2(at)dt = \frac{T}{2} + \frac{\sin(2aT)}{4a} \qquad 2.4\text{-}10$$

This is applied to Eq. 2.4-7 where the square of the polarization components are:

$$\left(P_x^{(2)}\right)^2 \propto 8E^4 d_{15}^2 \cos^2\phi \sin^2 2\theta \qquad 2.4\text{-}11$$

$$\left(P_z^{(2)}\right)^2 \propto 8E^2 \cos^2\phi \left(d_{31}\sin^2\theta + \left(d_{33}\cos^2\phi + \sin^2\phi\left(2d_{15}+d_{31}\right)\right)\cos^2\theta\right)^2$$

Finally the SHG intensity due to linearly polarized excitation light (I_{Lin}) can be shown under the assumption that only x and z components of the polarization can be detected (Zhuo, Liao et al. 2010):

$$\begin{aligned} I_{Lin} &= \left(P_x^{(2)}\right)^2 + \left(P_z^{(2)}\right)^2 \\ &\propto 8E^4 \cos^2\phi \left(\left(\cos^2\theta\left(d_{33}\cos^2\phi + \sin^2\phi\left(2d_{15}+d_{31}\right)\right) + d_{31}\sin^2\theta\right)^2 + d_{15}^2 \sin^2 2\theta\right) \end{aligned} \qquad 2.4\text{-}12$$

If the hexagonal fibers are in the x-z plane, $(\phi = 0)$ then Eq. 2.4-12 reduces to the usual equation for hexagonal fibers located in the optical plane (Roth and Freund 1981; Freund, Deutsch et al. 1986).

$$I_{Lin} \propto 8E^4 d_{15}^2 \left(\left(\sin 2\theta\right)^2 + \left(\frac{d_{31}}{d_{15}}\sin^2\theta + \frac{d_{33}}{d_{15}}\cos^2\theta\right)^2\right) \qquad 2.4\text{-}13$$

If the polarization is parallel to the hexagonal axis $(\theta = 0)$, then Eq. 2.4-12 becomes:

$$I_{Lin} \propto 8E^4 \cos^2\phi \left(d_{33}\cos^2\phi + \sin^2\phi\left(2d_{15}+d_{31}\right)\right)^2 \qquad 2.4\text{-}14$$

Eq. 2.4-14 shows that as the hexagonal crystals are tilted into the laser axial direction with angle ϕ, the SHG intensity approaches 0.

2.4.3 Polarization of SHG from hexagonal crystals

The polarization of emitted SHG can be readily measured in the microscope using an analyzer after the collection objective before the detector in the beam path, and can reveal important characteristics about the hexagonal crystal. The polarizability vector of a hexagonal structure oriented in the *x*-*z* plane $(\phi = 0)$ can be represented as the vector (see Eq. 2.4-3):

$$\mathbf{P}^{(2)} \propto \begin{pmatrix} 2d_{15}E_x E_z \\ d_{31}E_x^2 + d_{33}E_z^2 \end{pmatrix} \qquad 2.4\text{-}15$$

where E_x and E_z are components of the laser electric field polarized along the *x* and *z* directions. Similar to the case for cubic crystals, the analyzer axis is defined in the optical (z-x) plane an angle κ from the helical (as opposed to cubic) axis (z) (see Fig. 2.4-1). Then using Eq. 2.3-8 and Eq. 2.4-15, the SHG intensity *I* becomes:

$$I \propto d_{15}^2 E^4 \left(\frac{d_{33}}{d_{15}} \cos\kappa \cos^2\theta + \frac{d_{31}}{d_{15}} \cos\kappa \sin^2\theta + \sin\kappa \sin 2\theta \right)^2 \qquad 2.4\text{-}16$$

This expression is used to fit polarization-in-polarization-out (PIPO) data from starch granules. It is notable that for samples that do not have absorption peaks at the fundamental or second harmonic wavelengths, the parameter d_{31}/d_{15} tends to 1 (Kleinman 1962).

2.4.4 SHG from hexagonal crystals with circularly polarized excitation

Left handed circularly polarized light ($\mathbf{E_L}$) in the z-*x* plane can be represented as:

$$\mathrm{E}_L = E\left(\frac{\hat{z} + i\hat{x}}{\sqrt{2}}\right)e^{-i\omega t} + E\left(\frac{\hat{z} - i\hat{x}}{\sqrt{2}}\right)e^{i\omega t} \qquad 2.4\text{-}17$$

where *E* is the magnitude of the electric field ω is the field frequency and *t* is time. This electric field can be decomposed into *x* and *z* components:

$$\begin{aligned} \left(E_L\right)_x &= \frac{E}{\sqrt{2}}\left(ie^{-i\omega t} - ie^{i\omega t}\right) \\ \left(E_L\right)_z &= \frac{E}{\sqrt{2}}\left(e^{-i\omega t} + e^{i\omega t}\right) \end{aligned} \qquad 2.4\text{-}18$$

Substitution of these components into Eq. 2.4-7 is performed to solve for induced polarization components:

$$P_x^{(2)} \propto 2d_{15}^{'}E^2 i\left(e^{-2i\omega t}+e^{2i\omega t}+2\right)$$
$$P_z^{(2)} \propto E^2\left(d_{31}^{'}\left(-e^{-2i\omega t}-e^{2i\omega t}+2i\right)+d_{33}^{'}\left(e^{-2i\omega t}+e^{2i\omega t}+2\right)\right) \quad \text{2.4-19}$$

Disregarding the constant terms as they do not radiate:

$$P_x^{(2)} \propto 2d_{15}^{'}E^2 e^{i\pi/2}\left(e^{-2i\omega t}+e^{2i\omega t}\right)=4d_{15}^{'}E^2\sin\left(2\omega t\right)$$
$$P_z^{(2)} \propto 2E^2\cos\left(2\omega t\right)\left(d_{33}^{'}-d_{31}^{'}\right) \quad \text{2.4-20}$$

Explicitly replacing the SHG tensor values by the values in the rotated coordinate system, to simulate the SHG resulting from fibers tilted into the laser, substituting in Eq. 2.4-1:

$$P_x^{(2)} \propto 4E^2 d_{15}\cos\phi\sin\left(2\omega t\right)$$
$$P_z^{(2)} \propto 2E^2\cos\left(2\omega t\right)\left(3d_{31}\cos\phi\sin^2\phi+d_{33}\cos^3\phi-d_{31}\cos\phi\right) \quad \text{2.4-21}$$

Then the SHG intensity due to circularly polarized excitation light (I_{Cir}) becomes

$$I_{Cir}=\left(P_x^{(2)}\right)^2+\left(P_z^{(2)}\right)^2 \propto E^4\begin{pmatrix}16\sin^2\left(2\omega t\right)\left(d_{15}\cos\phi\right)^2\\+4\cos^2\left(2\omega t\right)\left(3d_{31}\cos\phi\sin^2\phi+d_{33}\cos^3\phi-d_{31}\cos\phi\right)^2\end{pmatrix} \quad \text{2.4-22}$$

Applying the time-average by integrating the intensity over one SHG period, using Eq. 2.4-8, 2.4-9 and 2.4-10 in 2.4-22 gives:

$$I_{Cir} \propto 2E^4\left(4\left(d_{15}\cos\phi\right)^2+\left(3d_{31}\cos\phi\sin^2\phi+d_{33}\cos^3\phi-d_{31}\cos\phi\right)^2\right) \quad \text{2.4-23}$$

Eq. 2.4-23 is the general SHG intensity collected only from the z-x polarizations resulting from circularly polarized light in the z-x plane inducing polarization of hexagonal fibers that are located off the z-x plane an angle ϕ from the z axis (see Fig. 2.4-1). Although the expression was derived assuming left-handed circular polarized electric field, the result is the same when starting with right handed circular polarization. Eq. 2.4-23 shows that as the fibers tilt into the laser direction *(y)* the intensity goes to 0 with circularly polarized excitation.

2.4.5 SHG ratio from circularly versus linearly polarized light

If the hexagonal crystals are in the z-x plane, which is the usual situation obtained experimentally, an interesting result can come about from the SHG intensity ratio between excitation with circular and linearly polarized light. This ratio is found by dividing the circular polarization expression Eq. 2.4-23 with the expression for SHG intensity from linearly polarized light parallel to the helical axis Eq. 2.4-13, both in the optical plane at $\phi = 0$, giving the expression:

$$\frac{I_{Cir}(\phi=0)}{I_{Lin}(\phi=0)} \propto \frac{\left(4+\left(\frac{d_{33}}{d_{15}}-\frac{d_{31}}{d_{15}}\right)^2\right)}{4\left(\sin^2 2\theta+\left(\frac{d_{31}}{d_{15}}\sin^2\theta+\frac{d_{33}}{d_{31}}\cos^2\theta\right)^2\right)} \qquad 2.4\text{-}24$$

If we let the linear polarization be along the helical axis ($\theta = 0$), and if we use values for the hyperpolarizability parameters of $\frac{d_{33}}{d_{31}} = 5, \frac{d_{15}}{d_{31}} = 1$, then

$$\frac{I_{Cir}}{I_{Lin}(\phi=0)} = 0.20 \qquad 2.4\text{-}25$$

The Fig. 2.4-2 graphing Eq. 2.4-24 for $\theta = 0$ shows that the SHG intensity ratio resulting from circular polarized excitation versus linearly polarized excitation parallel to the helical axis can be used in imaging of hexagonal crystals to predict the hyperpolarizability ratio d_{33}/d_{15} most sensitively in the region $1 \le d_{33}/d_{15} \le 3$, while at a value above 4 the ratio converges to a value of 0.2. The additional effect of the variance of the Kleinman or cylindrical ratio d_{31}/d_{15} has a significant effect on the interpretation of the circular to linear intensity ratio, therefore care should be taken to independently measure this parameter.

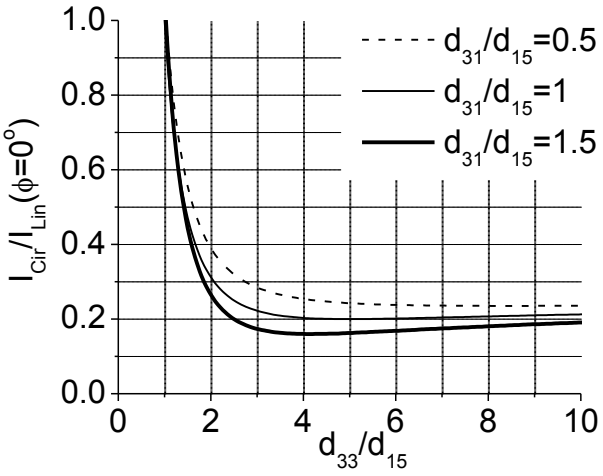

Fig. 2.4-2: SHG intensity ratio between imaging with circularly versus linearly polarized light.
The linearly polarized light is parallel to the helical axis. The SHG intensity ratio is shown as a function of the hyperpolarizability ratio d_{33}/d_{15} for three common values of the Kleinman ratio d_{31}/d_{15}.

2.4.6 The role of birefringence in SHG from hexagonal crystals

In this section how material birefringence can affect the SHG is reviewed. This analysis was not performed for cubic crystals since they do not possess birefringence. A hexagonal lattice on the other hand can have different indices of refraction along the c-axis, termed the ordinary index of refraction n_o and extraordinary index of refraction n_e, such that the birefringence is $\Delta n = n_0 - n_e$. The birefringence induces a phase delay between the two orthogonal electric field components, so that Eq. 2.3-5 can be re-written as;

$$\begin{aligned} E_x &= E\sin\theta \\ E_z &= Ee^{-i\Delta\xi_\omega}\cos\theta \end{aligned} \qquad \text{2.4-26}$$

where

$$\xi_\omega = \frac{2\pi\Delta n l_\omega}{\lambda} \qquad \text{2.4-27}$$

is the phase delay of the fundamental laser at frequency $\omega = c/\lambda$ through a path length l_ω. Substitution of Eq. 2.4-26 and Eq. 2.4-27 into Eq. 2.4-3 gives the polarizability as:

$$P_x(2\omega) \propto d_{15} e^{-i\Delta\xi_\omega} \sin 2\theta$$
$$P_z(2\omega) \propto d_{31} \sin^2\theta + d_{33} e^{-2i\Delta\xi_\omega} \cos^2\theta \qquad \text{2.4-28}$$

We assume that the resultant emitted SHG electric field, $\boldsymbol{E_{2\omega}}$, also experiences a phase delay due to birefringence $\Delta n_{2\omega}$ at wavelength λ/2 across a path length $l_{2\omega}$, which can be written

$$\xi_{2\omega} = \frac{4\pi\Delta n_{2\omega} l_{2\omega}}{\lambda} \qquad \text{2.4-29}$$

and can be incorporated into Eq. 2.4-28 giving:

$$P_x(2\omega) \propto d_{15} \sin 2\theta$$
$$P_z(2\omega) \propto e^{-i\xi_{2\omega}} \left(d_{31} e^{-i\xi_\omega} \sin^2\theta + d_{33} e^{i\xi_\omega} \cos^2\theta \right) \qquad \text{2.4-30}$$

When an analyzer is present in the detection path an angle κ from the z axis in the z-x plane (see Fig. 2.4-1), the SHG intensity can be calculated from the use of the Jones matrix for the analyzer, Eq. 2.3-7, which is combined with the induced polarizations in the following formula:

$$I_{2\omega} \propto \left| P_x(2\omega) \sin\kappa + P_z(2\omega) \cos\kappa \right|^2 \qquad \text{2.4-31}$$

Combining Eq. 2.4-31 with Eq. 2.4-30 yields:

$$I_{2\omega} \propto \sin^2\kappa \sin^2 2\theta + \cos^2\kappa \left(a^2 \sin^4\theta + b^2 \cos^4\theta + \frac{1}{2} ab \sin^2 2\theta \cos 2\xi_\omega \right)$$
$$+ \sin 2\kappa \sin 2\theta \left(a \sin^2\theta \cos\left(\xi_\omega - \xi_{2\omega}\right) + b \cos^2\theta \cos\left(\xi_\omega + \xi_{2\omega}\right) \right) \qquad \text{2.4-32}$$

where the susceptibilities are expressed as two distinct ratios $a = d_{31}/d_{15}$ and $b = d_{33}/d_{15}$. When the birefringence is 0 $\left(\xi_\omega = \xi_{2\omega} = 0\right)$ Eq. 2.4-32 simplifies to Eq. 2.4-16. If the medium is dispersionless in the frequency range 2ω to ω, Kleinman symmetry applies (a=1), and the birefringence is wavelength independent $\Delta n_\omega = \Delta n_{2\omega}$ (Kleinman 1962; Aït-Belkacem, Gasecka et al. 2010).

The derived formulae are useful for analysis of SHG intensity data of different nanostructures. The Eq. 2.1-12 is interesting because it shows that a surface depolarization phenomenon explains SHG emission from thin cylinders, and shows the relation of SHG intensity with the orientation of linear polarization of the laser electric field, and the difference in dielectric constant between the cylinder and its environment. This relation is used in section 4.3.6 to explain that deviation of the hyperpolarizability ratio d_{33}/d_{15} can occur due to this phenomenon. Eq. 2.3-9 relates the SHG intensity to the orientation of a cubic crystal grown along the [1 1 1] axis, with respect to the laser polarization, and the rotation angle of the crystal about its own axis. It is used for polarization SHG data analysis of zinc blende type ZnSe nanowires in sections 3.4.4 and 4.3.3. For hexagonal crystals the equation Eq. 2.4-16 gives the relation between the SHG intensity, the orientation of linear polarization of the laser, and the orientation of an analyzer placed before the detector in the signal detection path. It is used to analyze ZnSe nanowires that have hexagonal symmetry, including twinned zinc blende as well as wurtzite nanowires, in sections 4.3-3 and 4.3-4, respectively. This equation was also used for a qualitative explanation of SHG granule visualization when the polarization is parallel to the hexagonal crystal, and when the analyzer angle is perpendicular, resulting in cross-polarized SHG imaging, in section 5.3.7. When a hexagonal structure is birefringent and sufficiently large, such as a starch granule, the induced retardance of the laser polarization as well as the polarization of the SHG signal become important factors, and Eq. 2.4-32 is a modification of Eq. 2.4-16 which takes this into account. This equation is subsequently used for analysis of starch granule polarization SHG data in sections 5.3.9 and 5.3.10. The equation Eq. 2.4-23 relates SHG intensity of a hexagonal crystal imaged with a circularly polarized laser with its tilt angle out of the image plane, and is used for a qualitative explanation of 3D visualization of starch granules in section 5.3.4. The Eq. 2.4-24 gives the SHG intensity ratio between imaging a hexagonal crystal with linearly polarized light parallel to the crystal axis, and circularly polarized light, and relates this value to hyperpolarizability ratio d_{33}/d_{15}. In section 5.3.3 this equation is used to give a lower bound on the hyperpolarizability ratio in a starch granule. Although many equations were presented that relate SHG intensity to different structural parameters, it is nonetheless useful to visualize the entire hyperpolarizability tensor in order to understand the relationship between a molecule and its resulting hyperpolarizability, which is performed in the following section.

2.5 Visualization of SHG using the Unit Sphere Representation

2.5.1 The unit sphere representation of the hyperpolarizability

Visualization of the first hyperpolarizability tensor was achieved using visualization software (ParaView, Kitware Inc.) The unit sphere visualization of the hyperpolarizability tensor was used in this thesis, details of which can be found in our publication (Tuer, Krouglov et al. 2010). The unit sphere visualization technique has the benefit of no loss of information, as compared with representations of SHG via a single vector, as in the bond additivity model, or as in NLOPredict software (Moad, Moad et al. 2007), which uses only polarization-in effects. Visualization of the SHG tensor is possible by utilizing an effective SHG dipole vector defined as:

$$\boldsymbol{\beta}_{eff} = \beta : \hat{\mathbf{E}}(\theta,\phi)\hat{\mathbf{E}}(\theta,\phi) \qquad 2.5\text{-}1$$

where β is the first hyperpolarizability tensor, and $\hat{\mathbf{E}}(\theta,\phi)$ is the unit vector incident electric field defined in spherical coordinates (θ,ϕ), where ϕ is the zenith angle from the *z*-axis and θ is the azimuthal angle rotating around z in the x-y plane, visualized in Fig. 2.5-1.

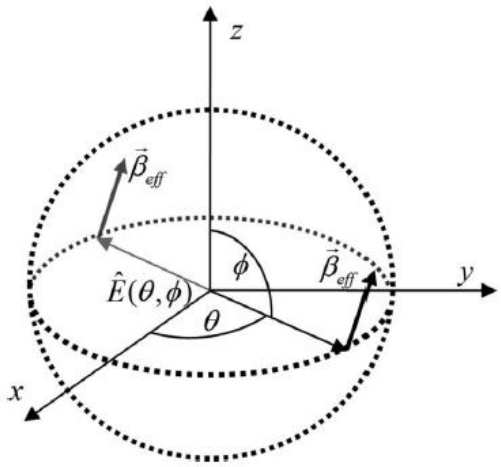

Fig. 2.5-1: Schematic of the unit sphere representation.
The (θ,ϕ) position on the sphere corresponds to the polarization of *E*, whereas the β_{eff} arrow at (θ,ϕ) on the unit sphere provides information about the polarization and magnitude of the generated second harmonic. Figure reprinted with permission from (Tuer, Krouglov et al. 2010).

Performing the vector product Eq. 2.5-1 to solve for individual effective hyperpolarizability vector dipole components, where the index *i* corresponds to Cartesian coordinates x, y and z:

$$\left(\beta_{eff}\right)_i = \beta_{ixx}\cos^2\phi\sin^2\theta + \beta_{ixy}\sin 2\phi\sin^2\theta + \beta_{ixz}\cos\phi\sin 2\theta + \beta_{iyy}\sin^2\phi\sin^2\theta + \beta_{iyz}\sin\phi\sin 2\theta + \beta_{izz}\cos^2\theta \qquad 2.5\text{-}2$$

This visualization technique is unique in that the orientation and magnitude of induced polarization is visualized for each input polarization.

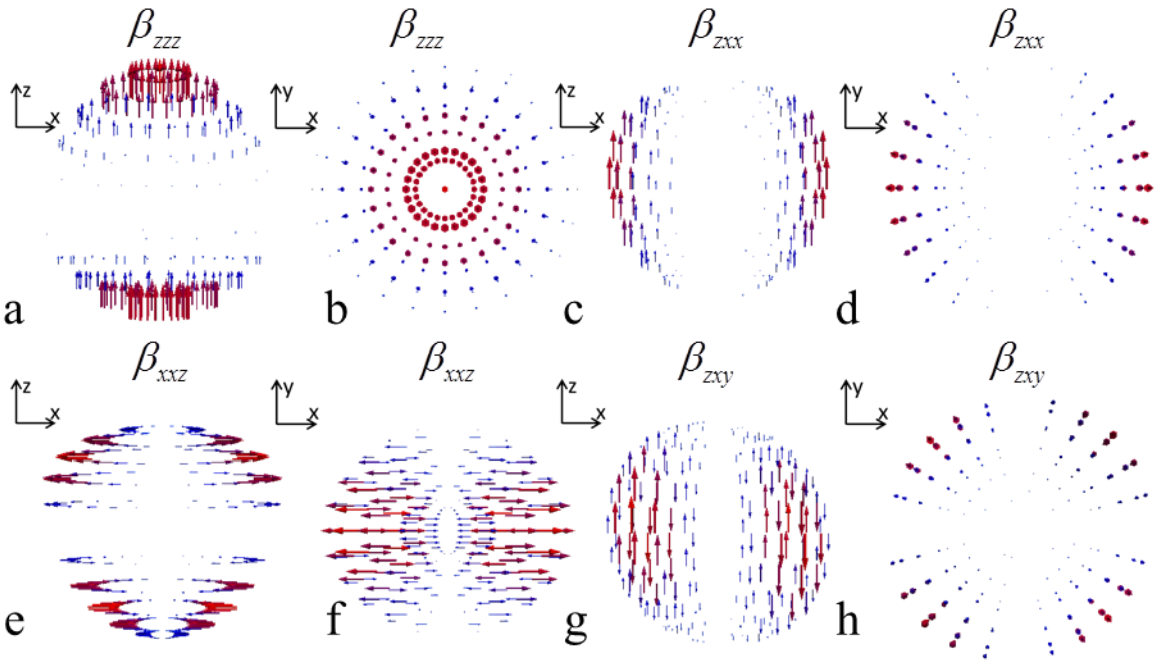

Fig. 2.5-2: Unit sphere representations of different hyperpolarizability terms.
Images are viewed from the top (a,c,e,g) and the side (b,d,f,h), with nonzero hyperpolarizability term indicated above each image.

Fig. 2.5-2 explicitly shows examples of unit spheres corresponding to different individual hyperpolarizability terms. The location of the arrow on the unit sphere describes the input polarization orientation coinciding with the radial vector of the sphere, while the directionality of the arrow and its magnitude describes the orientation of the induced hyperpolarizability dipole and its magnitude, respectively. For example see Fig. 2.5-2 (a) and (b) which show, respectively, the side (z-x) and top (y-x) views of a unit sphere representing a hyperpolarizability where only the β_{zzz} term is nonzero; the arrows are largest at the top of the sphere, where $(\theta,\phi)=(0,0)$, showing that an input polarization oriented along the *z*-axis will induce polarization of the largest magnitude, and since the arrows are parallel to the *z*-axis they show that this induced polarization will be directed also along the *z*-axis. If the component had reversed sign (i.e. $\beta_{zzz}=-1$) then the

arrows would point down, which is sensible considering second-order polarization has inherent directionality which is responsible for SHG signal cancellation upon loss of non-central symmetry. This unit sphere also shows that when the electric field is polarized perpendicular to *z*, $(\phi = 90°)$ no arrows are visible, and therefore, no induced polarization is expected.

Fig. 2.5-2 (c) and (d) show the unit sphere representation of the hyperpolarizability component $\beta_{zxx} = 1$. This component is maximal when input polarization is $(\phi = 90°)$, however since the arrows point along *z*, it shows the output polarization can be perpendicular to the input polarization thanks due to this type of cross term. The β_{xxz} term is also important since it is equal to β_{zxx} in Kleinman symmetry (Kleinman 1962), however it has a unique visualization in the unit sphere representation. Fig. 2.5-2 (e) and (f) show that this β_{xxz} term has maximum amplitude when the input polarization is at 45° to the z axis, with arrows pointing out above the equator, and in below it. Therefore, when considering structures with Kleinman symmetry, where $\beta_{xxz} = \beta_{zxx}$ it is important to know that a combination of the glyph vectors Fig. 2.5-2 (c) and (e) will occur in the visualization.

For completeness a chiral β_{zxy} hyperpolarizability is visualized in Fig. 2.5-2 (g) and (h). Although it is not heavily used in this thesis, it has an interesting counter intuitive unit sphere appearance that can help in understanding more complicated molecular hyperpolarizabilities.

2.5.2 SHG unit spheres for hexagonal and cubic crystals

SHG unit sphere representations of common crystals are beneficial to understand how sample symmetries effect the symmetry and directionalities of SHG. Many basic crystal types were modeled in our publication (Tuer, Krouglov et al. 2010). In this section we limit the focus to visualizations of hexagonal and cubic crystals. The Fig. 2.5-3 shows unit spheres for hexagonal crystals with their unique axis directed along the z-axis (a-d), as well as unit spheres representing cubic crystals with [1 1 1] direction along the z-axis in (e-g).

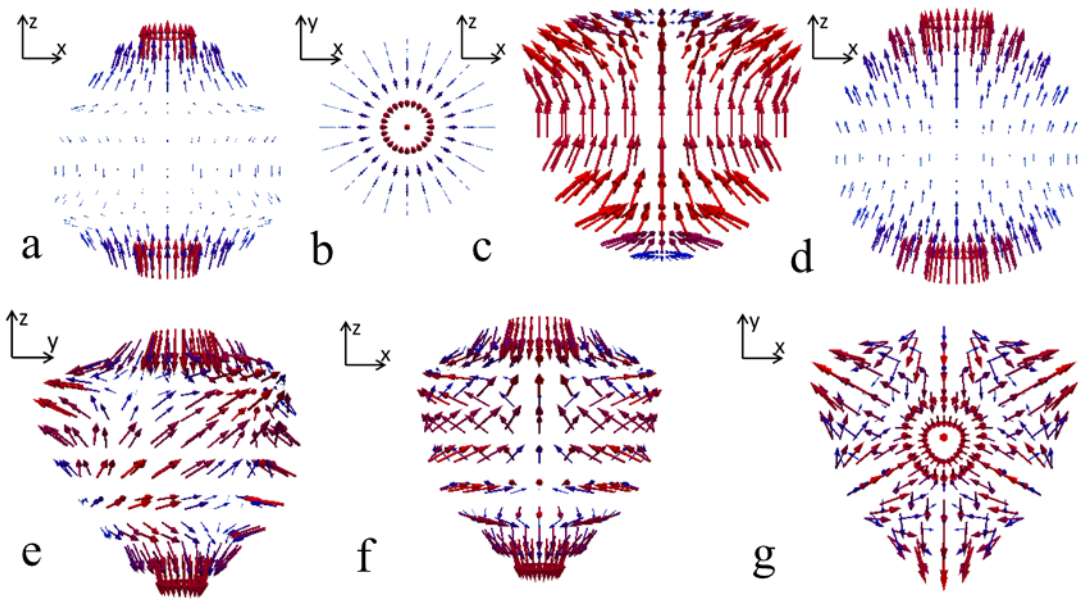

Fig. 2.5-3: Model unit spheres for hexagonal (a-d) and cubic (e-g) crystals.

Crystals are aligned with hexagonal axis along z, and shown with d_{31}/d_{15}=1 and d_{33}>0. Panels (a) and (b) show the side (z-x) and top (y-x) view of a hexagonal crystal with d_{33}/d_{15}= -4. Panels (c) and (d) show hexagonal crystals from the side (z-x) with d_{33}/d_{15}= 0 and 4 respectively. Panels (e-g) show unit sphere representation of a cubic crystal with its [1 1 1] axis oriented along z; the z-y view is shown in (e), the z-x view in (f) and the top (y-x) view in (g).

The unit sphere representation of the hyperpolarizability is useful for understanding the symmetry properties of crystal species based on their symmetry since it summarizes all the possible SHG polarizations based on any input orientation of laser polarization within a single image. Hexagonal crystals are symmetric about the (z) axis, as visualized in Fig. 2.5-3 (a) and (b), which show, respectively, the side (z-x) and top (y-x) view of a unit sphere representation of a hexagonal crystal with hyperpolarizability ratio d_{33}/d_{15}= -4. In order to relate these data to the model contour plots for hexagonal crystals, Fig. 3.4-9, unit spheres at two additional values of the hexagonal hyperpolarizability ratio are shown: d_{33}/d_{15}= 0 in (c) and d_{33}/d_{15}= 4 in (d). Indeed the arrows in the unit sphere representation in (a), (c) and (d), respectively match well with the contour plots of Fig. 3.4-9 (c1),(c3) and (c5).

Fig. 2.5-3 (e) and (f) show two perpendicular orientations of a unit sphere representing a cubic crystal aligned with its [1 1 1] axis along the z direction, while panel (g) shows the top view of the crystal. It is easily observable in (g) that cubic crystals with z along [1 1 1] have a 120° symmetry about their *z* axis, corresponding to rotation of δ in the Eq. 2.3-9. This symmetry is also shown in Fig. 3.4-6 showing the unique range of $-30° \le \delta \le 30°$.

2.6 Hartree-Fock Calculations of Molecular Hyperpolarizabilities

Calculations of molecular hyperpolarizabilities are now possible with the current software and computational power available, however, to understand the results and limitations of the calculations a basic review of electronic structure theory is presented. This section features a very basic overview of Hartree-Fock theory that will be used in subsequent subsections in this chapter, as well as in section 5.4, to theoretically explain the molecular origin of hyperpolarizabilities. The subject matter requires a deep understanding of molecular electronic theory, primarily based in quantum mechanics and quantum field theory, along with an explanation of computer algorithm efficiency to properly understand the different choices of algorithms and options that can be used in computer calculations of real molecular systems. The scope of this section is much more narrow; it will begin with a basic review of the assumptions required for Hartree-Fock theory, followed by several sections of examples of using the procedure to calculate hyperpolarizabilities of basic molecules. Then the SHG bond additivity model is introduced and used to deduce the hyperpolarizabilities of bonds important to starch crystals including C-O, C-H and O-H.

2.6.1 Introduction to electronic structure

The time dependent equation governing the behavior of a one particle single dimensional system was postulated in 1926 by Erwin Schrödinger and bears his name;

$$H(\mathrm{x})\Psi(\mathrm{x},t) = i\hbar\frac{\partial\Psi(\mathrm{x},t)}{\partial t} \qquad 2.6\text{-}1$$

where $H(\boldsymbol{x})$ is the energy function operator of the system at coordinates $\boldsymbol{x}$, $\hbar = h/2\pi$ where h is Planck's constant, t is time, and $\Psi(\boldsymbol{x},t)$ is the wave or state function which describes different possible electronic time dependent configurations; postulated by Max Borne shortly after the discovery of the Schrodinger equation was the idea that the probability $P(\boldsymbol{x},t)$ of finding an electron at position $\boldsymbol{x}$ during time t can be written as:

$$P(\mathrm{x},t) = \left|\Psi(\mathrm{x},t)\right|^2 \qquad 2.6\text{-}2$$

For a multi-electron system with M nuclei and N electrons, many energy terms can be considered in the Hamiltonian (H), with one possible form as:

$$H(r,R) = -\frac{\hbar^2}{2m_e}\sum_{i=1}^{N}\nabla_i^2 - \frac{\hbar^2}{2}\sum_{i=1}^{M}\frac{\nabla_i^2}{m_j} - \sum_{j=1}^{M}Z_j\sum_{k=1}^{N}\frac{e^2}{|r_k - R_j|} + \sum_{j<k=1}^{M}\frac{Z_j Z_k e^2}{|R_k - R_j|} + \sum_{j<k=1}^{N}\frac{e^2}{|r_k - r_j|} + \sum_{k=1}^{N} e\mathbf{r}_k \bullet \mathbf{E} \qquad 2.6\text{-}3$$

where r_i is the position of the i'th electron, m_e is the mass of an electron, e is the charge on an electron, R_i is the position of the i'th nucleus, Z_i is the atomic number of the i'th nucleus, m_i is the mass of the i'th nucleus and $\boldsymbol{E}$ is the induced electric field vector. The first two terms in the Hamiltonian contain kinetic energy, of electrons and of nuclei, respectively. Terms 3-5 of Eq. 2.6-3 contain, from left to right; a coulomb attraction between electrons and nuclei, a coulomb repulsion between nuclei, and a coulomb repulsion between electrons. Many more energies could be additionally considered here, such as magnetic fields, spin-orbit interactions, but they are omitted since they are not considered in calculations. The topic of this section is described in great detail in the literature (Simons and Nichols 1997; Levine 2000; Simons 2011).

The first approximation made is termed the Born-Oppenheimer, and it allows neglecting the effects of the second term in the Hamiltonian, Eq. 2.6-3, describing the kinetic energy of nuclei. This approximation, also termed the clamped Hamiltonian approximation, is justified under the consideration that nuclear motions occur on a much slower timescale than electronic motions.

Another important approximation is made when we assume the wave function is separable:

$$\Psi(\mathrm{x},t) = f(t)\psi(\mathrm{x}) \qquad 2.6\text{-}4$$

which using $f(t) = e^{-iEt/\hbar}$ leads to the simplified time-independent Schrodinger equation.:

$$-\frac{\hbar}{2m}\frac{\partial^2\psi(x)}{\partial x^2} + V(x,t)\psi(x) = E\psi(x) \qquad 2.6\text{-}5$$

In this equation $\psi(x)=\psi_1(x)\psi_2(x)\psi_3(x)...$ describes time independent (stationary) states, known as molecular states, having corresponding energies E_n, giving the interesting result that the probability of finding the electron is:

$$P(x,t)=\left|\Psi(x,t)\right|^2=\left|\psi(x)\right|^2 \qquad 2.6\text{-}6$$

These discoveries together with numerous experimental and theoretical studies of atomic and molecular orbitals have led to the development of vast libraries of basis functions which mimic the geometry of atomic orbitals in real atomic systems *(ψ(x))*, by comparing predicted energies with experimentally derived atomic and molecular spectra, and can be found in such databases as the environment molecular sciences library basis set exchange (Feller 1996).

The pairwise interaction between electrons, the second to last term in the Hamiltonian, Eq. 2.6-3, is problematic because it is not separable. The electron-electron coulomb repulsion interaction is not additive electron by electron, and hence cannot be converted to Eq. 2.6-5 via separation of variables. Therefore the Hartree approximation is made, which supposes separation of variables can be performed on the electron-electron repulsion energy, by assuming each electron responds to the mean field of all the other electrons in the system, rather than to each electron. Furthermore, the calculations assume this effective Hartree potential of all the electrons together affecting one electron can be adequately approximated by a function of the radius *r* only. Another pairwise electron interaction can be considered with the idea of Pauli's exclusion principle, that electrons should be antisymmetric in an atomic orbital, i.e. having opposite spin. In order to account for this, the Hartree-Fock method makes use of anti-symmetrized spin-orbitals, which do not permit electrons of the same spin to reside in proximity to one another. The implication of using this method gives the restriction that only closed shell systems (neutral molecules) can be calculated, otherwise these Fock orbitals become more complicated due to having to calculate exchange integrals where the surface of a wave function crosses another wave function.

The calculation proceeds to find the optimal wave functions, and is known as the Hartree self-consistent field (SCF) method. An initial guess of the wave functions is made, in the form:

$$\psi_n^m(r,\theta,\phi)=R_{nl}(r)Y_l^m(\theta,\phi) \qquad 2.6\text{-}7$$

where *R(r)* is a function of the radius, and $Y_l^m(\theta,\phi)$ is a spherical harmonic and a function of spherical coordinates (θ,ϕ). An energy calculation using the time-independent and clamped nucleus Schrödinger equation is subsequently performed, followed by iterative adjustment of the functions $\psi_n^m(x)$ until the energy E_n is minimized.

Calculation of the molecular hyperpolarizability in the quasi-static limit (Born Oppenheimer approximation) is equivalent to a geometrical calculation of the octopole of the ground state electron distribution (Boyd 2008). Recently the HONDO implementation of frequency dependent hyperpolarizability calculations is used in many software packages, including Gaussian and GAMESSUS, and has been described in detail (Sekino and Bartlett 1986; Karna and Dupuis 1991).

2.6.2 GAMESSUS Implementation of the HONDO algorithm on SciNet

The GAMESSUS software package (Gordon Group, Purdue University) which runs on the University of Toronto SciNet supercomputing cluster is a powerful tool that allows many different types of calculations on molecular systems including time dependent Hartree-Fock calculations. GAMESSUS (Schmidt, Baldridge et al. 1993) implements the HONDO algorithm (Karna and Dupuis 1991), and has the advantage over other more popular packages in that it has built in many basis sets into one easy to use package, with multi-CPU capability which was easily supported on a unix cluster. The restriction with using GAMESSUS on the SciNet supercomputing cluster is the time restriction of 48 hours per calculation, since this implementation of TDHF calculations of hyperpolarizabilities cannot be restarted, limiting the number of atoms to fewer than ~80 in the 6-311G**++ basis. Additionally since the algorithm requires neutral molecules, all bonds have to be saturated, therefore, a large number of hydrogen atoms typically needed for organic molecules, severely limits the size or number of molecules that can be calculated. This is especially a nuisance when considering an organic crystal such as amylose A, which would normally be continuous, and instead, must be cleaved and saturated with hydrogen bonds.

2.6.3 The bond additivity model and the hyperpolarizable unit

Estimations of hyperpolarizabilities of molecules based on the additivity of hyperpolarizabilities of individual bonds have proven to be inadequate in molecules containing large atoms and

complex bonds, however, it has in certain cases been relatively accurate for simple organic molecules (Levine and Bethea 1975; Tuer, Krouglov et al. 2011). In the assumed quasi-static limit of TDHF calculations, the hyperpolarizability of a molecule is equal to the octopole moment of the ground state electron distribution (Boyd 2008), and hence is a geometrical function of the wave functions, therefore, although bond additivity does not accurately reproduce the geometry, it can be used as a guide in discussions of THDF calculations of more complex molecular structures. To more accurately describe crystals, larger molecular segments, i.e. hyperpolarizable units, are beneficial to calculate, and these are being increasingly used in the literature of organic molecules including collagen and cellulose (Moad and Simpson 2005; Perry, Moad et al. 2005; Gualtieri, Haupert et al. 2008; Loison and Simon 2010).

In the bond additivity model, the hyperpolarizability of a molecule is calculated by addition of the hyperpolarizabilities of each bond. Each bond is treated as having cylindrical symmetry with only one hyperpolarizability tensor component, β_{zzz}, oriented along the bond direction. In order to perform the addition of hyperpolarizabilities of bonds, the respective hyperpolarizabilities must be oriented the same way as in the larger molecule, or, for each bond, rotated hyperpolarizability tensor elements must be obtained via Eq. 2.2-6, with a proper rotation matrix found independently by measuring the angle between the bonds (or hyperpolarizable units).

2.6.4 Hyperpolarizability of simple molecules and bonds

The hyperpolarizabilities of several simple molecules have been determined using TDHF calculations on the SciNet cluster. Hyperpolarizability estimates for individual bonds including C-O, C-H and O-H were subsequently performed using the bond additivity model.

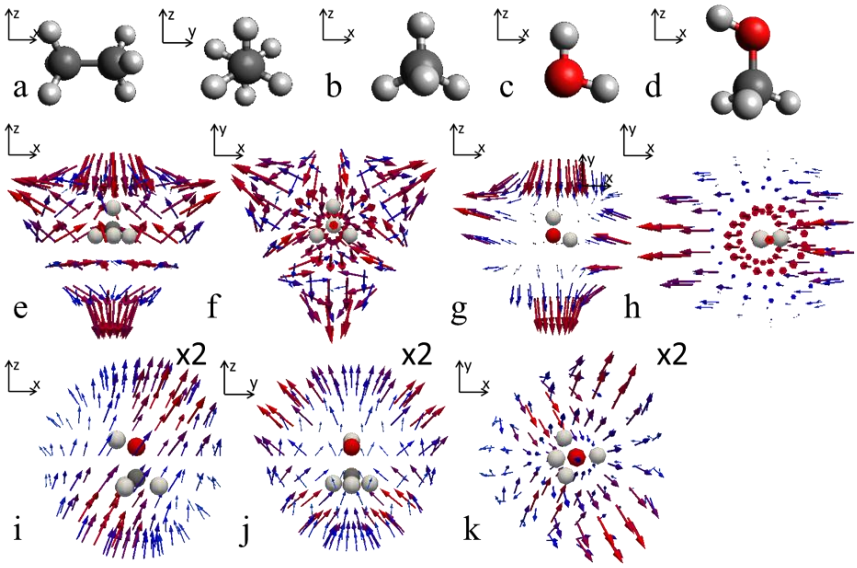

Fig. 2.6-1: Unit sphere representations of TDHF calculated hyperpolarizabilities for simple molecules.
The centrosymmetric molecule ethane is shown at two projections (a), while the non-centrosymmetric molecules methane, water and methanol are shown in (b), (c) and (d), respectively. The hyperpolarizability for ethane was 0 while the corresponding unit spheres of calculated hyperpolarizabilities are shown at two orientations for methane in (e),(f), water in (g),(h) and at three orientations for methanol in (i),(j),(k).

Ethane had $\beta=0$ since it is centrosymmetric, see Fig. 2.6-1 (a), while the other non-centrosymmetric molecules including methane (b), water (c), and methanol (d) had nonzero hyperpolarizabilities in (e-f), (g-h) and (j-k), respectively. As expected, the hyperpolarizabilities of methane (e,f), water (g,h) and methanol (i,j,k) correspond to their molecular symmetries. The unit sphere representing the hyperpolarizability of methane (e,f) visualizes four SHG dipole components oriented along H-C bonds, with three effective SHG dipoles visible from the top view (f) and the last one is horizontal in (e). The hyperpolarizability unit sphere calculated for water shows two SHG dipoles, each oriented along the H-O direction visualized in (g). The unit sphere for methanol (i,j,k) appears to be a combination of hyperpolarizabilities from water and methane, where contributions from the x-oriented hydroxyl bond has partially cancelled the contribution from the –x oriented C-H bond (see (i) and (k)), while the two remaining C-H bond contributions are clearly visualized in (j).

The hyperpolarizabilities that were calculated for simple molecules were used to deduce hyperpolarizabilities for individual bonds C-H, O-H and C-O under the assumption that each bond had a single hyperpolarizability tensor component along the bond orientation. Hyperpolarizabilities with only β_{zzz} nonzero were fit to the *ab initio* calculations for the

hyperpolarizability for water and methane to obtain hyperpolarizabilities for O-H and C-H bonds, respectively. These values were then subsequently used to fit the bonds in methanol to obtain an estimate for the hyperpolarizability of the C-O bond. The results for bond hyperpolarizabilities are listed in Table 2.6-1, and reveal that the directionality of the bond always occurs from the less electronegative to the more electronegative atom, i.e. H to C, H to O and C to O, as well, all three bonds have a very similar magnitude to one another. The similar magnitudes are not unexpected; although the atoms in the C-O bond are larger than in H-C and H-O, and therefore a larger hyperpolarizability would be expected since hyperpolarizability generally scales as L^7 where L is the size of the molecule (see pg. 259 in (Boyd 2008)), the H-O and H-C bonds are much shorter than the O-C bond. The results of bond hyperpolarizabilities will be used in section 5.4.1 of this thesis for calculation of the theoretical hyperpolarizability of starch granules using the bond additivity model.

Bond	**β_{zzz} (au)**
C-H	-33.2
O-H	-26.6
C-O	30

Table 2.6-1: Hyperpolarizabilities for individual bonds of C-H, O-H and C-O.
Hyperpolarizabilities were deduced from TDHF calculations of water, methane and methanol molecules.

Chapter 3
Instrumentation and Measuring Methods of Nonlinear Optical Microscopy

The specialized instrumentation as well as analysis methods for nonlinear optical microscopy which can simultaneously induce and efficiently detect multiphoton excitation fluorescence (MPF), second harmonic generation (SHG), as well as third harmonic generation (THG) is described in this chapter. Section 3.1 gives a brief introduction to the nonlinear optical microscope while section 3.2 gives details of the hardware components of a nonlinear optical microscope. Section 3.3 includes details of programming the microscope software for the interested reader. Section 3.4 describes the imaging methods of nonlinear optical microscopy, including polarization-in-polarization-out (PIPO) microscopy, which is subsequently used for quantitative imaging of ZnSe nanowires and starch granules in Chapter 4 and Chapter 5, as well as image analysis methods used in the thesis, including generation of correlated images, which are shown in Chapter 6, as well as methods used to analyze PIPO microscopy data.

3.1 Introduction to the Instrumentation of a Nonlinear Optical Microscope

The nonlinear optical microscope is a unique combination of novel technologies which has emerged as a powerful research tool over the past 30 years. Nonlinear laser scanning microscopes share many features with confocal laser scanning microscopes. The major novelty of nonlinear optical microscopes is the ultrafast pulsed laser source; the continuous wave (CW) lasers used in confocal microscopes do not have enough power to efficiently drive nonlinear light-matter interactions. A sufficiently high peak power for nonlinear optical signal generation can be obtained using pulsed lasers, which have ultra-short duration pulses in the picosecond and femtosecond time regime. NLO microscopes focus the peak power in small focal volumes through the use of high numerical aperture (NA) microscope objectives. In contrast to confocal microscopy, where optical sectioning is achieved by removing out-of-focus signal via a spatial filter, the confocality in nonlinear microscopes is achieved as a direct result of the nonlinear intensity dependence of the signal; focusing a pulsed laser beam provides enough intensity to achieve nonlinear interactions and provides optical sectioning with high spatial resolution. By scanning the focal volume in the xy plane, where the beam propagation direction is defined to be

along the z-axis, 2D images can be created by synchronizing the signal detection with the position of scanning mirrors. In addition, different positions along the z-axis can be sampled enabling construction of 3D images. A 3D volume can be visualized by combining 2D slices into a single volume and rendering with 3D visualization software.

Depending on the desired nonlinear interaction, a nonlinear laser scanning microscope can involve more than one laser beam. For example, second and third harmonic generation imaging can be accomplished with a single laser beam, while coherent anti-Stokes Raman (CARS) and non-degenerate sum frequency generation require two beams with different wavelengths. In principle, the setup can be extended to three laser beams of different wavelengths for non-degenerate four-wave mixing microscopy. In addition, the application of multiple beams of the same wavelength can be used to produce multiple foci, which could decrease image acquisition times and provide simultaneous imaging at different depths (Amir, Carriles et al. 2007). Single beam setups, however, are always easier to implement and are typically more robust when used in clinical or biology lab environments.

This chapter focuses on single laser beam systems. The functionality of nonlinear microscopes can be enhanced by implementing a multicontrast detection system. Traditionally, three parallel detection channels have been used in confocal and two-photon excitation fluorescence microscopes, where the emission signal is usually divided into different spectral ranges by dichroic mirrors and optical filters, or by separating the signal with a dispersive optical element. Similarly, spectral separation can be applied for detecting different nonlinear optical responses. Parallel images acquired simultaneously at different wavelengths, corresponding to different nonlinear contrast mechanisms, carry complementary information about the same sample structure. Multicontrast detection methods provide the possibility of making a direct correlation of parallel images on a pixel-by-pixel basis. In addition, a simultaneous detection scheme eliminates the problem of artifacts from signal bleaching or movement of the sample occurring during imaging. Since multiphoton excitation fluorescence is emitted isotropically in randomly oriented chromophores, it can be collected in either the forward or backward direction. Conveniently, backward fluorescence detection (epi-fluorescence) uses the excitation objective for collecting the emitted fluorescence photons. Many research groups implement nonlinear excitation fluorescence imaging by coupling femtosecond lasers into a confocal microscope and using a non-descanned port for efficient signal detection (see discussion by (Zipfel, Williams et

al. 2003)). Harmonic signals are generated more efficiently in the forward direction; therefore, they are usually detected in transmission mode. Larger modifications of a confocal microscope are required for implementing transmission mode detection. The easiest way of building a harmonic microscope is by using a high NA condenser and transmission detector that exists on some models of laser scanning confocal microscopes (see for example (Millard, Campagnola et al. 2003; Cox, Moreno et al. 2005)). In addition, three-channel detection requires extensive modifications to a commercial microscope (Sun 2005) or making a home-built microscope setup (Barzda 2005). Further information on the instrumentation of nonlinear microscopes can be found in several extensive reviews (Squier and Muller 2001; Sun 2005; Barzda 2008; Carriles, Schafer et al. 2009).

3.2 Nonlinear Optical Microscope Setup

Nonlinear microscopes have three main functional parts: the optical setup of the microscope, the synchronized laser scanning and signal detection system, and the femtosecond laser source. In the following sections, a detailed description of each of these functional units is provided.

3.2.1 Optical setup of the nonlinear microscope

This section describes the optical setup of a three-channel multicontrast nonlinear optical microscope built in our laboratory. Fig. 3.2-1 depicts a typical scheme for the setup of a nonlinear optical laser scanning microscope, with the laser traversing the x-y plane. The setup shares some common features with the confocal laser scanning microscope. The laser is directed through an optical isolator (Conoptics model 715), shown in Fig. 3.2-1, in order to keep the back reflections of the microscope optics from interfering with the laser modelocking. Two mirrors, M1 and M2, direct the laser into the microscope box through a filter which blocks the outside light (FEL750, Thorlabs). During regular maintenance of the femtosecond laser, the outgoing beam can shift slightly, thus the two mirrors are necessary at the entrance of the microscope to ensure proper beam re-alignment. The filter set, shown schematically by F1 also contains neutral optical density filters, which are used to attenuate the laser intensity for optimal imaging conditions.

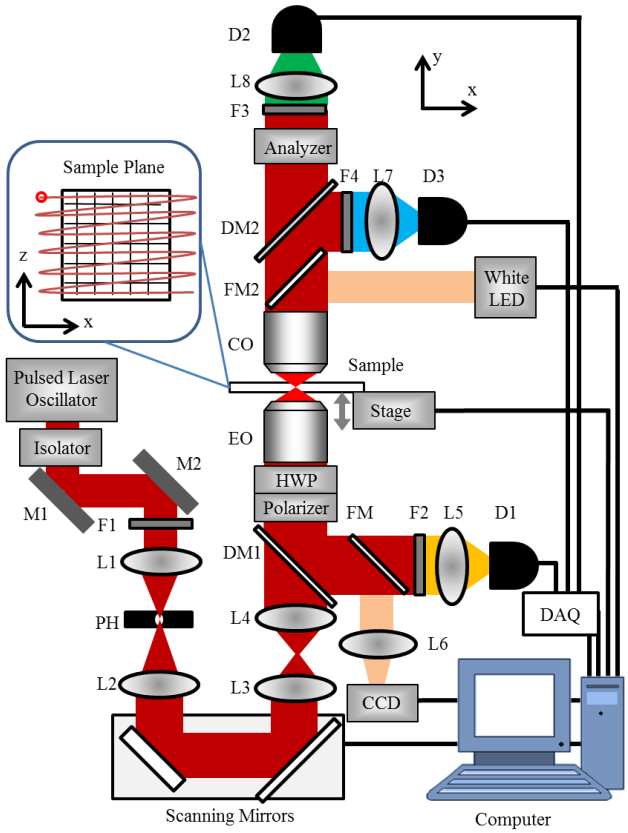

Fig. 3.2-1: Schematic diagram of the nonlinear optical microscope.

The components are as follows: F: optical filters, L: lenses, PH: pinhole, DM: dichroic mirrors, FM: flipping mirrors, CCD: white light camera, D: photon counting detectors, EO: excitation microscope objective, CO: collection microscope objective, DAQ: data acquisition card, LED: light emitting diode white light source. The inset on the top left shows the sample plane z-x showing the raster scan pattern of laser scanning. Images not to scale. Figure reprinted with permission from (Cisek, Spencer et. al. 2009).

The beam then is focused through a pinhole (PH), 30μm in diameter (Thorlabs Inc.), which is placed at the focus of a 1:2 telescope (lenses L1 and L2). While the pinhole (PH) is used as a spatial filter to produce a circular mode of the laser beam, the telescope is additionally used to magnify the beam to match the size of the scanning mirrors. For alignment, the pinhole is usually placed on an XYZ translation stage, so that the optimal position of the focus can be found. 10 mm scanning mirrors are used (SC2000 controller with two MiniSax amplifiers and VM1000 galvonometers, GSI Lumonics Inc.). The scanning mirrors consist of galvanometric mirrors that raster scan the beam in both lateral *x* and z directions at a speed of 10 frames/s in 128x128 pixel mode, with the resulting laser raster scan pattern over the sample region shown in the inset on the top left of Fig. 3.2-1. After the scanning mirrors, a second telescope, consisting of an achromatic lens (L3) and a tube lens (L4), is used to expand the beam to match the entrance aperture of the excitation objective (EO). The tube lens (Zeiss) is designed to correct for chromic aberrations of

the objective. The tube lens used should match the objective, and should be purchased from the same manufacturer. After the second telescope, the collimated beam is transmitted through a dichroic mirror (DM1) and coupled into the excitation microscope objective (EO). The polarization optics, including a polarizer (Polarizer), half-wave plate (HWP) as well as analyzer (Analyzer), are only used for PIPO measurements, and are otherwise removed; they will be discussed in section 3.4.3.

Almost all nonlinear microscopes are constructed using commercially available refractive objectives. In experiments, two microscope objectives were used for excitation, a 0.75 and a 1.3 numerical aperture (NA) (Zeiss). They had working distances of 600 and 250 μm, respectively. Since most objectives are designed for the visible spectral range, there are only a few objectives that work optimally in the infrared region. For achieving the highest resolution specified for an objective, a high uniformity of the excitation beam across the entrance aperture of the objective is required. Overfilling the entrance aperture often helps to achieve good uniformity and the specified NA of the objective. In order to obtain a large scan area at the sample stage, a balance between scan mirror size, the mirror tilt angle, as well as the focal length of the first lens of the second telescope (L3 in Fig. 3.2-1) is required. In practice, a 7 cm focal length lens custom designed achromatic doublet was used which provided a scan area of 300x300 μm at the sample. It is recommended to test the alignment of the microscope on a regular basis by recording the spatial point spread function (PSF) of the microscope.

Testing the PSF of the microscope is a necessary step to reveal the alignment of the laser in the microscope, and to estimate the actual laser beam focal volume size. Microscope objectives are rated via numerical aperture (NA), which relates to the half cone angle θ of the focusing beam and the index of refraction n as follows:

$$NA = n\sin\theta \qquad 3.2\text{-}1$$

The theoretical PSF of objectives calculated from the NA does not always coincide with the experimental value because of differences in workmanship of the objectives, and each objective should be separately tested. The diffraction limited focusing properties of high numerical aperture microscope objectives have been approximated (Squier and Muller 2001) by assuming the paraxial approximation and using the first minima of the Rayleigh criterion as the

full width at half maximum (FWHM) of the beam, resulting in the following commonly used formula for approximating the lateral (ω_0) PSF:

$$\omega_0 = \frac{0.61\lambda}{(n)\,NA} \qquad 3.2\text{-}2$$

where λ is the vacuum laser wavelength and n is the index of refraction of the focusing medium. The axial PSF, often called the confocal parameter b is:

$$b = \frac{2\lambda}{(NA)^2} \qquad 3.2\text{-}3$$

For example, a 0.75 NA air objective has an axial PSF of 3.7 μm (assuming λ=1030nm). However, since our signals are nonlinear, they scale as the inverse j'th root for the j'th nonlinearity (aka $1/\sqrt{2}$ for SHG or $1/\sqrt{3}$ for THG) (Squier and Muller 2001) therefore, we obtain b=2.6μm for SHG, or, b=2.1μm for THG. Full diffraction theory calculations predict even smaller values for the FWHM of the focal field distributions (85% of the value) than those based on the classical theory (Squier and Muller 2001). In order to test the focusing conditions, we found that testing the axial point spread function using an air-glass interface was a fast and accurate method. By axially scanning a microscope coverglass through the focus, and detecting the resulting THG intensity at each height of the sample, we generated a curve which corresponds to the practical resolution of our microscope. This value was usually in the range 1 - 2 μm for our 1.3 NA oil objective (Zeiss) and 2 - 4 μm for the 0.75 NA air objective (Zeiss). In each case we scanned the interface on the far side of a ~150 μm microscope coverslip (CVI #1.5) because the objectives are corrected for this thickness of glass. To illustrate this point, Fig. 3.2-2 shows a typical axial THG scan (or z-scan) of a microscope coverslip using the 0.75 NA objective and 1028 nm laser. The two interfaces in Fig. 3.2-2 (a) have been normalized and enlarged in (b) and (c) respectively, and fit using a Gaussian function, revealing the PSF via full width at half maximum (FWHM) of the fit which was 4.9 μm at the first, uncorrected interface (panel (b)) which corresponds to the air-glass interface closer to the microscope objective, and 1.9 μm at the secondary glass-air interface, showing when the objective is corrected for glass its PSF is significantly narrower at the second interface.

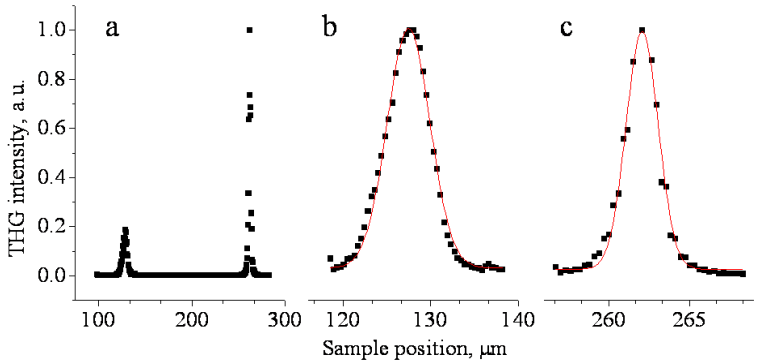

Fig. 3.2-2: THG axial scan of a blank microscope coverslip.

Panel (a) shows the entire scan where the left peak represents the first air-glass interface, and the right peak shows the second and corrected glass-air interface. The two peaks are shown in close-up in (b) and (c), respectively, and have FWHM fits (red lines) (using a Gaussian function) of 4.9 μm and 1.9 μm respectively.

Multiphoton excitation fluorescence is usually collected in the backward direction with the same objective (Fig. 3.2-1 EO) used for excitation. Epi-detection signals are separated from the fundamental laser radiation with the dichroic mirror (Fig. 3.2-1 DM1) and directed through the interference filter (F2) and partially focused by the lens (L5) into the detector (D1). Since descanned mode is not used, and the setup requires the most sensitive detection, large area photomultiplier tubes (Hammamatsu, H5783P) were used and they were set to photon counting mode. In epi-detection mode, color glass and interference filters are used for specific wavelengths depending on the emission wavelength range of the fluorophore, however, it is common to additionally use a BG39 filter (CVI Laser) in order to block the excitation beam, which often leaks through these filters. SHG can be detected in the backwards direction, in which case the filter (F2) is FF01-515/25 (Semrock) for the 1028 nm laser, or F25-400 (CVI) for the Ti:Sapphire 800 nm laser.

In contrast to fluorescence, which generally produces isotropic emission and can be efficiently collected in the epi-direction, harmonic generation is coherent, resulting in highly directed emission (Zipfel, Williams et al. 2003), mostly in the forward direction. The simplest forward detection of harmonics consists of a high NA condenser and transmitted light detector existing on some models of laser scanning confocal microscopes (Millard, Campagnola et al. 2003; Cox, Moreno et al. 2005). For the best collection efficiency, the condenser is replaced with a collection objective ((CO) in Fig. 3.2-1), which matches the NA of the excitation objective. We initially used a home-built objective I designed using Optica (Mathematica 5.0) software for

maximum transmission of harmonics from 1028 nm and 800 nm lasers, (515 and 400 nm for SHG, and 343 nm and 266 nm for THG) using two commercial 1" sapphire lenses achieving around 0.7 NA. A second objective lens was used in the recent microscope upgrade, which was designed to give 0.85 NA, with 20% higher transmission at 500nm, and had more collimated outputs free from birefringence of the lenses allowing PIPO measurements. The collimated signal radiation from the collection objective is passed through the dichroic mirror (DM2, for KGW: HT1030+515nm, HR 340nm (CVI), for Ti:Sapphire HT800+400nm, HR266 (CVI)) for separation between the second and third harmonic signals. The second harmonic is focused onto a detector (D2) by the lens (L8), after filtering by filters (F3) consisting of a BG39 (Thorlabs) and the narrow band interference filter FF01-515/25 (Semrock) for the 1028 nm laser, or F25-400 (CVI) for the Ti:Sapphire 800nm laser. The third harmonic is focused onto the detector (D3) with the lens (L7), after filtering with the interference filter (F4). For 1028 nm excitation, the filter used for THG was a F10-340 (CVI) and for 800 nm excitation, the F25-265 (CVI) filter was chosen.

A counting data acquisition (DAQ) card is used to acquire photon counts simultaneously from all three detectors (National Instruments, PCI-6602). Photon counting is synchronized with the scanning mirrors via a digital pulse train from the scanning mirrors controller (for details see section 3.3.1) rendering three simultaneously acquired images based on different nonlinear contrast mechanisms. In order to obtain optical sections at different depths, the sample is translated along the optical axis with a translation stage (PiezoJena PZ400). This renders three simultaneously acquired 3D images with different NLO contrast mechanisms. The resolution of the setup is limited by the laser wavelength, the NA of the objective and the index of refraction of the objective immersion media (Eq. 3.2-3), while the imaging depth into the sample is limited by the working distance of the focusing objective, laser radiation penetration depth, distortions of the laser beam in the sample and the attenuation of harmonic signals by the sample. The instrumentation for nonlinear microscopy was extensively described in several reviews (Squier and Muller 2001; Sun 2005; Carriles, Schafer et al. 2009; Cisek, Prent et al. 2009).

In order to find the region of interest within a microscopic sample, the microscope is equipped with white-light imaging capability. A standard white illuminator is directed through the collection objective (CO) via the flipping mirror (FM2) to illuminate the sample. The white light is collected by an imaging excitation objective (EO) and directed to the imaging camera

(CMOS) via the dichroic mirror (DM1) and the flipping mirror (FM1), and focused by the lens (L6). During laser scanning, the flipping mirrors (FM1 and FM2) are turned away to not interfere with the laser.

3.2.2 Scanning and detection systems of nonlinear optical microscopes

In order to obtain a three-dimensional image, the focal volume of the high NA objective has to be scanned across a 3D region of interest. It is possible to translate the sample with respect to the laser beam, or raster scan the beam while keeping the sample fixed. Sample translation is usually accomplished by a piezoelectric stage, with scanning speeds of several frames per second at most. Faster scanning rates were needed, and therefore, raster scanning of the beam in lateral directions using scanning mirrors was used. Galvanometric mirrors are usually employed for lateral scanning, and in the microscope 10 frames per second scanning rate galvanometers were employed. For video rate scanning, resonance scanners or rotating polygon mirrors can be used. Axial scanning is most commonly performed by translating the sample or by translating the excitation objective. Axial scanning can also be performed by changing the divergence of the beam with adaptive optics (Amir, Carriles et al. 2007). Translation of the microscope objective gives satisfactory results in epi-detection mode. For detecting the signals in transmission mode the focal point of the excitation and collection objectives must overlap; therefore, axial scanning by sample translation is preferred over translation of the objective.

Detection is a very important component of the microscope. Photomultiplier tubes, avalanche photodiodes, and charge-coupled device (CCD) cameras can be used for detection. CCD cameras can be easily interfaced with the microscope; however, if the CCD camera is not synchronized with the scanners, multiple scans are necessary to acquire one image. Scattering samples require point or line scanning synchronized with the detection. Photomultiplier tubes are usually employed for non-descanned mode due to the large area of the photocathode. Photomultipliers which had 8 mm active area (Hammamatsu, H5783P) were used. In descanned detection mode, or when stage scanning is employed, small area avalanche photodiodes or spectrometers with narrow entrance aperture can be used. Descanned mode detection has high losses due to the collection beam passing through more optical elements compared to the non-descanned configuration.

The nonlinear optical responses can be detected using integration, photon counting, or lock-in detection methods. Commercial manufactures commonly implement the signal integration approach. However, NLO signals that are emitted from microscopic samples typically generate less than one photon per excitation pulse. Therefore, it is more appropriate to use the photon counting detection method. We implemented photon counting detection mode using photomultiplier tubes operating in photon counting regime. The photomultiplier sends out a short pulse of current every time it detects a photon. This electric pulse is sent to a fast pre-amplifier (Phillips Scientific) which converts the pulse to a voltage pulse of up to 1 V. The amplified signal is subsequently converted to a digital TTL pulse, of ~4.5 V using a discriminator (Phillips Scientific). The discriminator also serves the function of filtering out noise from the pre-amplifier, by setting a minimum threshold voltage. The digital signal is subsequently transferred to a counting card which has three fast simultaneous counting transfer channels. The scanning mirrors controller provides an output pulse train which is synchronized to the position of the fast scanning mirror. The pulse train is connected to the gate function of the photon counters, enabling automatic pixilation of counts by the counting card. For further details of the position synchronization program in the scanning controller see the section 3.3.1. Although according to the manufacturer, the photon counting photomultipliers have a high signal damage threshold of 10 MHz photon counts, a signal saturation threshold occurs at about 500 kHz, above which the signal intensity is no longer linear with the count rate. This has to be taken with caution, but usually does not present a big problem because excitation laser power can be reduced, or a neutral optical density filter can be placed in front of the detector.

3.2.3 Laser sources for nonlinear microscope

A custom home-built laser oscillator was chosen for the nonlinear microscope to satisfy the special pulse energy, wavelength and repetition rate requirements of the system. The laser is based on a Yb-doped potassium gadolinium tungstate ($KGd(WO_4)_2$) crystal, pumped by a 25 W fiber coupled 980 nm wavelength laser diode (Apollo Instruments), and has 1028 nm wavelength emission (Major, Cisek et al. 2009). Initiation and sustained mode-lock is achieved by a semiconductor saturable absorber mirror (SESAM) (Keller, Weingarten et al. 1996), achieving 450 fs duration pulses with a 21 m long cavity which results in a 14.3 MHz pulse repetition rate. The optimal laser wavelength of 1028 nm was chosen in order to avoid sample damage by absorption of the laser wavelength by biological molecules (<700 nm), as well as from water

(>1400 nm). The short pulse duration was required in order to satisfy the high energy requirement of NLO responses. The optimal repetition rate was chosen based on optimizing power and minimizing sample photodamage. The benefit of the chosen low repetition rate is that the duration between pulses of 70 ns permit full relaxation of most of the excited states of molecules within the sample, reducing exciton-exciton annihilation effects and diminishing triplet state generation, which can lead to the production of singlet oxygen (Barzda, de Grauw et al. 2001; Cisek, Major et al. 2006) and subsequent photobleaching. Additionally, since the laser power was limited, the lower pulse repetition rate increased pulse energy for efficient generation of harmonics.

Several other laser choices are available for nonlinear microscopy. Ti:Sapphire lasers emitting at 800 nm, and having 80 MHz pulse repetition rate are the most popular choices for nonlinear microscopy, since they fall in the IR range, have short pulse duration near 100 fs, and appreciable average power reaching more than 1 W. Before the KGW laser was online, and while it was not working, a Ti:Sapphire laser was used for the nonlinear microscope having 780 nm or 820 nm wavelength pulses with 26 MHz repetition rate and 100 fs duration. The ~800 nm radiation induces two photon absorption autofluorescence of several major constituents of cells such as NAD(P)H (Zipfel, Williams et al. 2003) and therefore, 800 nm wavelength radiation is not optimal for imaging with harmonic generation microscopy. Additionally, THG signals from the fundamental 800 nm radiation fall in the UV region, therefore requiring special UV optics along the third harmonic detection optical path. As well, the THG is attenuated in thick biological samples due to high UV absorption. Therefore, excitation sources such as Yb:KGW and Cr:Forsterite femtosecond lasers emitting at wavelengths 1028 nm and 1230 nm, respectively, are much better choices for nonlinear microscopy (Chu, Chen et al. 2001; Major, Cisek et al. 2006). While the higher wavelength of the Cr:Forsterite laser is beneficial due to increased viability of biological samples and deeper sample penetration (Carriles, Schafer et al. 2009; Cisek, Prent et al. 2009), however the longer wavelength reduces the resolution of the microscope.

3.3 Nonlinear Optical Microscope Software

Software engineering of a nonlinear optical microscope consisted of planning, synchronizing, programming, testing and maintenance of a nonlinear microscope. All programming was performed in LabVIEW software on a single processor personal computer.

3.3.1 Laser scanning software

Laser scanning while simultaneously acquiring data and synchronizing in real time was the most complicated aspect of the microscope. A block diagram showing the electronic components involved in programming and the data flow is presented in Fig. 3.3-1. The scanning mirror electronics consist of a scan controller, two amplifiers and two galvanometric scan mirrors as well as a laser shutter (see Fig. 3.3-1). The scan controller (SC2000, GSI Lumonics, Inc.) contains memory with the scan controller program, and a processor which executes the scan and timing commands with a clock period of 240 ns (4.2 MHz). The memory on the scan controller is accessed by serial port, via text based commands. The program on the scan controller was carefully devised so that the same program could perform different scan settings to obtain different 'zoom' settings. The program consisted of three threads, one, the execution thread, which reset scanner positions and operated the laser shutter, and two execution threads; a fast thread which set the raster of the laser at an amplitude proportional to the scan area as shown by the horizontal traversal of the red line in the inset of Fig. 3.2-1, and a slow thread, which was timed to turn the slow axis of the scanning mirror corresponding to shifting down one line every time the fast axis mirror turned all the way across the area. The fast axis had timing commands that modulate a pulse train which is synchronized to the scan position by the counting card (see Fig. 3.3-1). The pulse train was only useful for positioning when the fast axis of the scanner was moving at a constant speed, so that each pixel in the image would have the same laser dwell time, and not be influenced by light induced bleaching dissimilarly in different areas of the image. To obtain a scan area with equal laser dwell times (2 – 6 μs per pixel depending on the zoom setting) throughout, at the beginning and end of each oscillation of the fast scanner axis, during acceleration/deceleration, the pulse train was turned off. The timing was manually adjusted for each zoom setting so that the pulse train was exactly 128 pulses long for each line, resulting in a scan size of 128 x 128 pixels. Furthermore, the beginning and end scan positions were adjusted so that the center of the scans were the same for different zooms, and small zoom settings could be custom positioned anywhere on the 300 x 300 μm sample region.

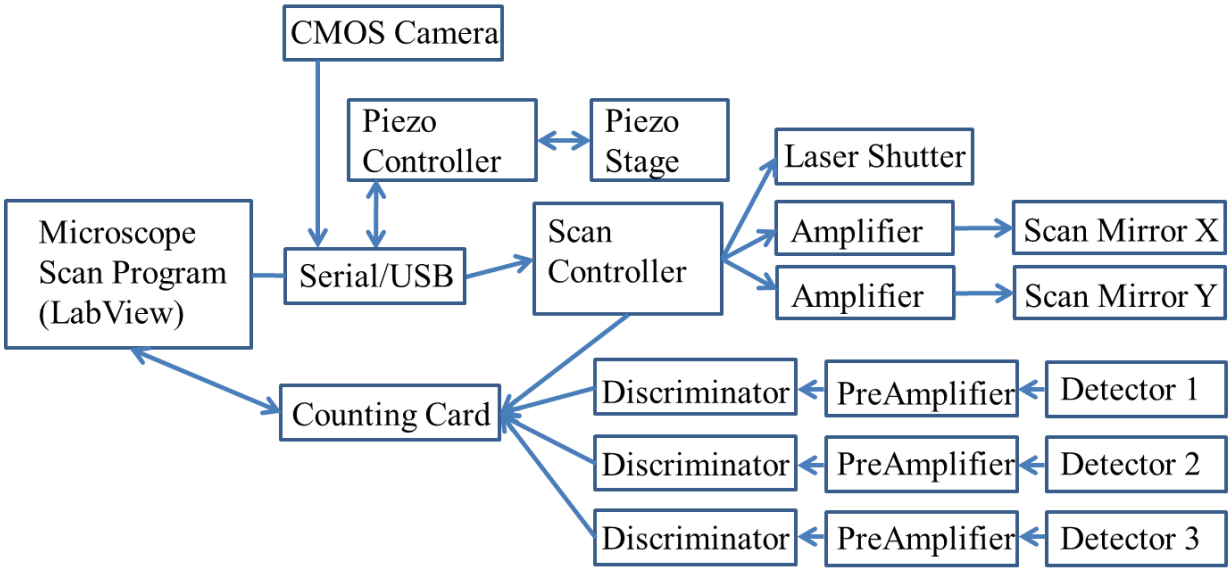

Fig. 3.3-1: Flow diagram of electronic components of the microscope involved in programming. The arrows indicate the direction of data flow.

3.3.2 Data acquisition software

Data acquisition was performed by a counting card which could use 3 direct memory access (DMA) channels, thereby allowing simultaneous acquisition of up to three data streams. The amplified and digitized output of each of the three detectors was connected to input channels of the counting card, and a program onboard the counting card was used for simultaneous detection and pixilation. Similarly to the scan controller, the counting card is a mini computer, having memory and a processor, running at 80 Mhz. Pixilation was achieved with the counting card by the use of the gated counting function, using the detectors as the source, and the scanner pulsetrain (pixel clock) as the gate signals. The card would count detection events for each of the three detectors simultaneously until it received a pulse from the pulsetrain of the scanners, at which time the counts would be saved as intensity values for the first pixel, and the counters would reset and begin acquiring the counts for the second pixel. At speeds near 10 frames per second the counting card could only hold several frames of data, therefore the LabVIEW program would use the first in first out (FIFO) buffer on the counting card to extract the data and transfer it to the computer's memory until up to 500 frames in three channels were acquired. Then the program would display the data on the scan acquisition screen, (see the screen example in Fig. 3.3-2) and save the data to a binary file on the computer. The program would then restart the scan process if more images had been requested. If images at another height (slices) were requested, during the save routine, the microscope program would adjust the position of the

piezoelectric stage (stage Fig. 3.2-1), via USB to serial connection to the piezoelectric controller, which would translate the sample along the z direction.

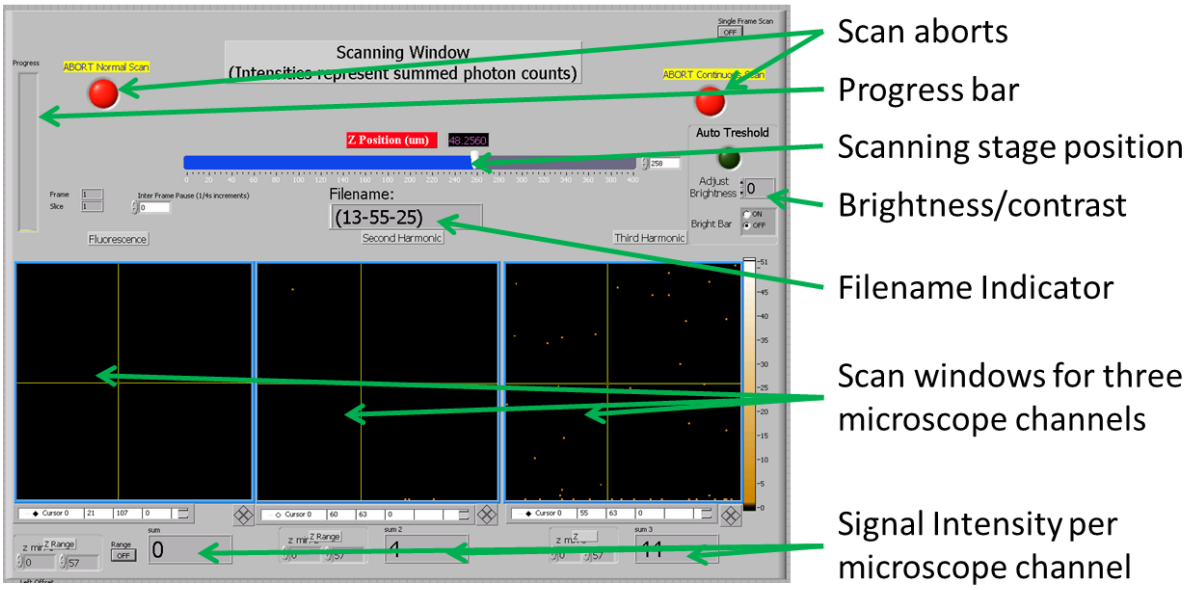

Fig. 3.3-2: The scan acquisition screen of the nonlinear multicontrast microscope program.

The microscope is capable of obtaining 3D image data with a single click. The main microscope control window is shown in Fig. 3.3-3. In the scan parameters region, the user specifies the starting axial sample position, the change in height between images, how many heights to image (slices) as well as how many images to integrate over at each height (frames). The save ON/OFF toggle is used to switch between live scanning, which shows each individual image frame without saving, in order to find the region of interest in the sample, an operator can center the window, and find the best axial sample position, all visible live through the scan acquisition window Fig. 3.3-2. The other toggle option is to save, in which case the scan acquisition window is only updated after a specified number of frames in one slice has been collected, in order to reduce the burden of collecting and saving extensive amount of data by the computer. In this setting, the data is automatically saved as the current date/time, shown in the scan acquisition window Fig. 3.3-2, as well as, in the program menu list on the main window, Fig. 3.3-3, which lists all the functions the microscope program is performing. The zoom setting is used to select scan area sizes; these range from 8x8 μm all the way to 300x300 μm. The scan position indicator allows a <150x150 μm area to be selected within the possible 300 x 300 μm to allow easy sample centering without having to physically move the sample. Intermittent scans can be repeated on a timer via the timed scan repeat control shown in Fig. 3.3-3. Finally, the

white light image control shown in Fig. 3.3-3 enables the white light function of the microscope in order to find a region of interest.

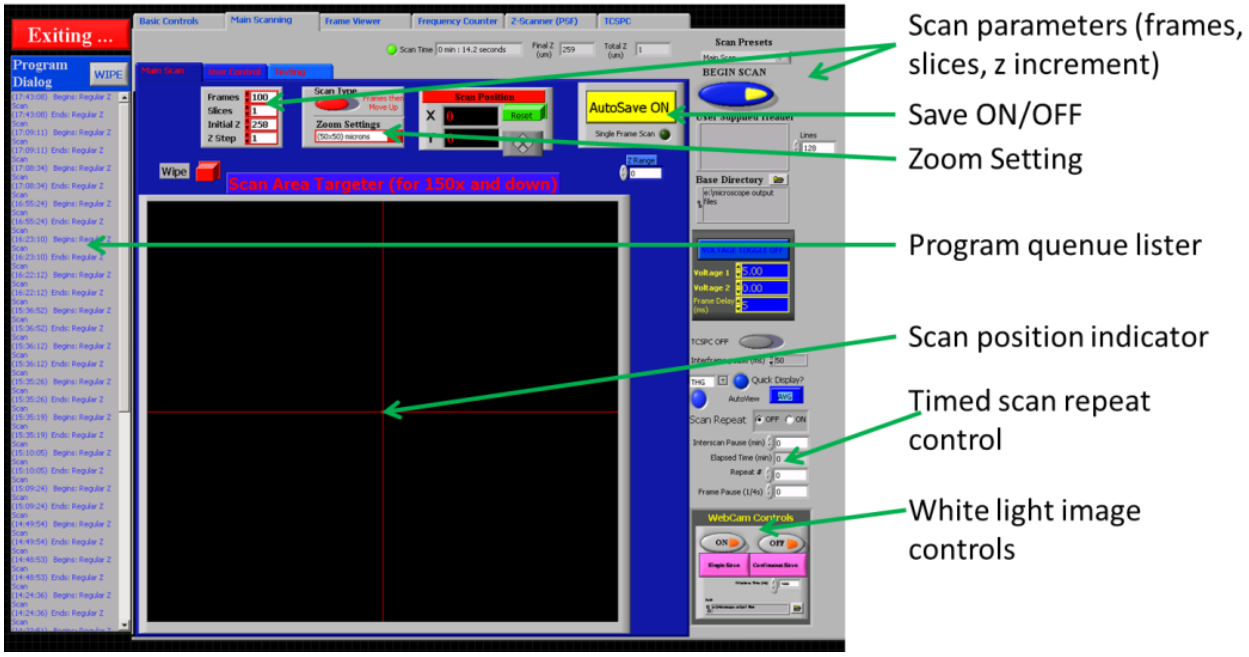

Fig. 3.3-3: Main microscope control window.

3.3.3 Image data display and analysis software

After a microscopy image is acquired data analysis software is used to analyze data and convert to standard TIFF file formats. Multiple data files can be loaded simultaneously for quick comparison of images; the current file is selected using the file indicator in Fig. 3.3-4. Since each contrast mechanism commonly has different signal intensity as well as noise, there are brightness, contrast and threshold levels for each of the three channels. Each saved microscope file can contain many slices and frames, therefore, the current frame and slice control is useful to select the desired slice and frame. Since often times, integration of all the frames at a particular height is desired, during scanning, the microscope saves this data in a separate frame integrated file. The type of file, along with many scan parameters is indicated in the data analysis software under scan information. Direct data analysis is possible within this software via using the region of interest selector, and observing the statistics for the region of interest below each image, including mean, median, mode, variance, standard deviation, the sum, the range, the number of pixels and the maximum pixel value. The region of interest selector on each image is locked to the first image, to ensure the same region is analyzed in each image. In order to convert the images to a standard file format, a convert to TIFF button exists, which conveniently converts

the images into a single TIFF stack. When images are converted to TIFF they are not altered in any way. For further data analysis using three channel structural cross correlation, a software has been written, and is described in section 3.4.2.

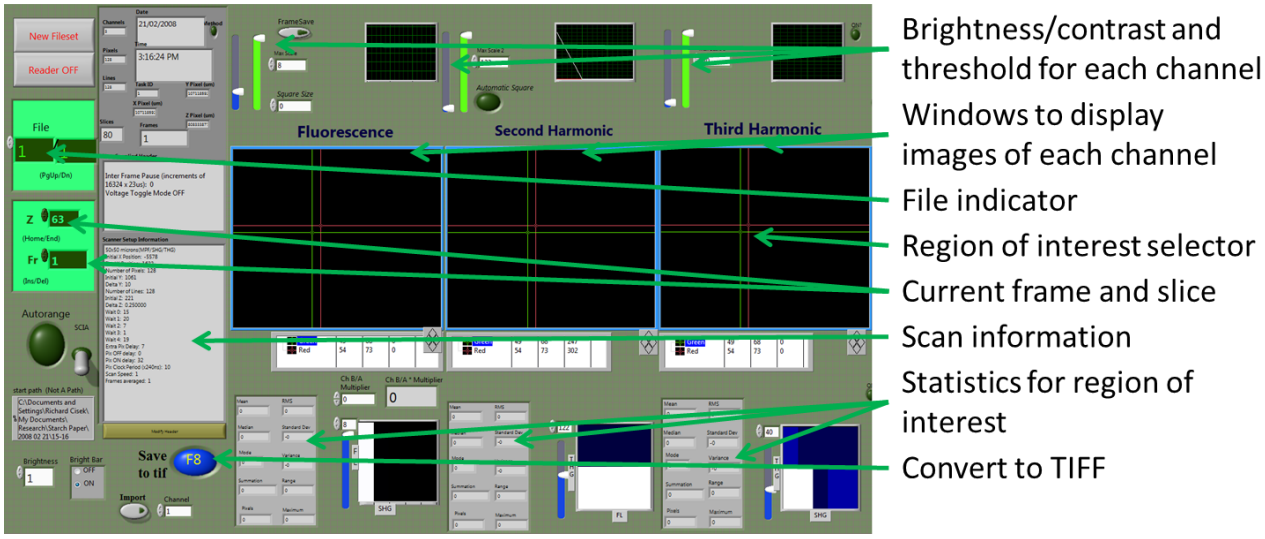

Fig. 3.3-4: Data analysis software for the three channel nonlinear microscope data files.

3.4 Nonlinear Microscopy Imaging Methods

Nonlinear microscopy requires both an imaging modality as well as a quantitative analysis tool for analyzing microscopic structures. In this section two analysis methods are presented that were developed to aid in image analysis for nonlinear microscopy. A multicontrast image correlation method which allows analysis of simultaneously recorded images from different modalities will be described, as well as, a method to quantitatively measure structural properties of samples using polarization measurements in nonlinear microscopy will be presented.

3.4.1 Multicontrast nonlinear optical microscopy measurements

Ultrafast laser pulses can simultaneously generate several nonlinear optical responses, therefore different nonlinear contrast mechanisms can be used to record images of the same structure in parallel. Multicontrast microscopes, which utilize simultaneous detection of SHG, THG, and MPF, have been developed (Chu, Chen et al. 2001; Barzda 2005; Prent, Cisek et al. 2005). Multicontrast microscopy appears to be very beneficial when different NLO responses reveal different functional structures of the same biological specimen. For example, a multicontrast SHG and MPF microscope was used to image labeled lipid vesicles (Moreaux, Sandre et al. 2000), labeled neuroblastoma cells (Campagnola, Wei et al. 1999), muscle and tubulin structures

(Campagnola, Millard et al. 2002), and labeled neurons (Moreaux, Sandre et al. 2001). Simultaneous THG and MPF detection was used for imaging of human glial cells (Barille, Canioni et al. 2001), labeled mitochondria in myocytes (Carriles, Schafer et al. 2009), while THG and SHG microscopy was used to monitor mitosis in a live zebrafish embryo (Chu, Chen et al. 2003), as well as for functional cornea imaging (Olivier, Aptel et al. 2010). All three contrast mechanisms were implemented to image mitochondria in cardiomyocytes (Barzda 2005), chloroplasts (Chu, Chen et al. 2001; Prent, Cisek et al. 2005; Cisek, Prent et al. 2009; Cisek, Spencer et al. 2009), photosynthetic bacteria and algae (Cisek, Spencer et al. 2009), photosynthetic pigment-protein complexes (Prent, Cisek et al. 2005; Cisek, Spencer et al. 2009), rhodamine stained starch granules (Cisek, Prent et al. 2009), zebrafish embryo growth (Olivier, Luengo-Oroz et al. 2010), and hematoxylin and eosin stained histological tissues (Tuer, Tokarz et al. 2010). SHG and coherent anti-Stokes Raman microscopy were used simultaneously for starch imaging (Slepkov, Ridsdale et al. 2010)

Parallel images, recorded using different contrast mechanisms, can be directly compared on a pixel by pixel basis. Although, SHG, THG and MPF images originate from the same structure, their image contrast mechanisms are fundamentally different. The comparison of images obtained with coherent and non-coherent contrast mechanisms can be very challenging because homogeneous structures cannot be visualized in SHG or THG, but might be visible in fluorescence. Additionally, differences appear for signal generation at structural interfaces, where optical properties change between two media. For THG and surface SHG, the signal maximum appears at the central position of the interface; whereas for the interface between a bulk-fluorescing and non-fluorescing structure, only ½ of the onset intensity will be reached at the interface position. The maximum two-photon excitation fluorescence (2PF) signal intensity is observed when the full focal volume is immersed in the media. Therefore, image comparisons will always have to be taken with caution.

The following sections describe the development of an image analysis method used for comparing images from different nonlinear modalities, structural image cross-correlation.

3.4.2 Structural cross-correlation image analysis of multicontrast images

Images obtained with different nonlinear contrast mechanisms can be directly compared using the method of structural cross-correlation image analysis (SCIA). The SCIA technique was

initially developed as a two-channel technique for multicontrast imaging of myocytes (Barzda 2005), and was later extended to three channels (Carriles, Schafer et al. 2009; Cisek, Prent et al. 2009). The method relies on a pixel by pixel comparison of simultaneously acquired images. The algorithm can also be applied for comparison of images recorded sequentially, as long as the scan conditions for all the images are identical. The SCIA procedure starts with a standardization of the images by applying lower as well as upper pixel intensity thresholds to remove low signal noise as well as artificially occurring high signal spikes or "glitches" in the image. Next, the images *A* and *B* are normalized to the maximum intensity and compared to each other on a pixel by pixel basis. If *x* and *y* denote the coordinates of the pixel in the image, then the cross-correlated image *I(x,y)* can be calculated as follows:

$$I(x,y) = \sqrt{A(x,y) \cdot B(x,y)} \qquad 3.4\text{-}1$$

In addition to the correlated image, the algorithm produces two uncorrelated images, $A \cap \neg B$, and $B \cap \neg A$, where $\cap$ is the logical intersection and $\neg$ is the logical not. The uncorrelated images are constructed as follows:

$$(A \cap \neg B)(x,y) = \begin{cases} A(x,y), & I(x,y) = 0 \\ 0, & I(x,y) \neq 0 \end{cases}$$
$$(B \cap \neg A)(x,y) = \begin{cases} B(x,y), & I(x,y) = 0 \\ 0, & I(x,y) \neq 0 \end{cases} \qquad 3.4\text{-}2$$

The three images are mutually exclusive and can be combined with three distinct colors into one image. The algorithm can be naturally extended to simultaneously correlate three images and results in 7 mutually exclusive images. Fig. 3.4-1 schematically illustrates 3-channel SCIA on three Venn spheres, shown in (a) (b) and (c). The three image SCIA correlation is shown (Fig. 3.4-1 (d)), and it is composed of the following correlated images: a triple correlation image $A \cap B \cap C$ (e), three partial double-correlations; $A \cap B \cap \neg C$, $A \cap C \cap \neg B$ and $B \cap C \cap \neg A$ (f), (g) and (h) as well as the uncorrelated images; $A \cap \neg B \cap \neg C$, $B \cap \neg A \cap \neg C$ and $C \cap \neg A \cap \neg B$ (i), (j) and (k). The 7 images resulting from 3 channel SCIA are mutually exclusive, so for each pixel, only one of the 7 channels will have an intensity greater than 0. This allows each image to have a unique color followed by combination into one image without any overlap, Fig. 3.4-1 (d).

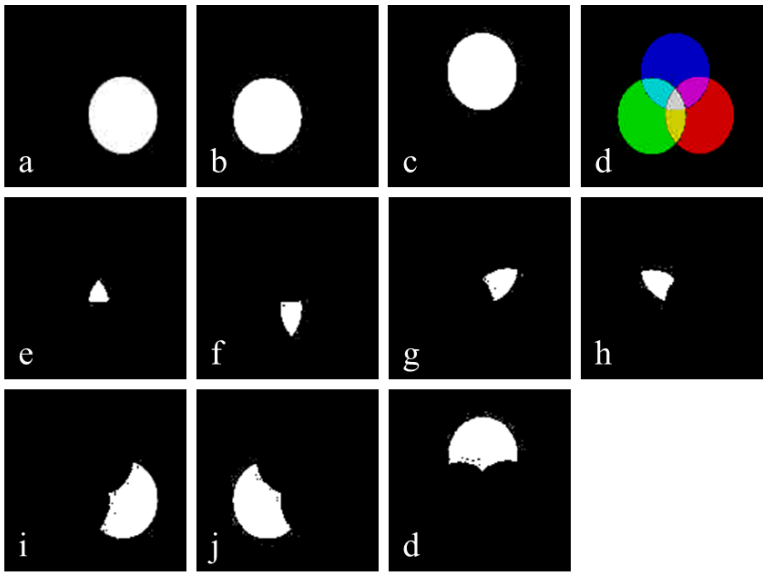

Fig. 3.4-1: Structural image cross-correlation analysis applied to a Venn diagram.
Panels (a),(b) and (c) are Venn spheres, (d): overlap of panels (a), (b) and (c), (e): A∩B∩C, f: A∩B∩¬C, (g): A∩¬B∩C, (h): ¬A∩B∩C, (i): A∩¬B∩¬C, (j): ¬A∩B∩¬C, (k): ¬A∩¬B∩C. Figure reprinted with permission from (Cisek, Prent et al. 2009).

The advantage of using SCIA is that the colors will not overlap and the combined colocalized image will reveal multicontrast information from all three channels in one image. SCIA is advantageous over a standard overlay, even in the simpler two-channel case. In overlays, when two pixels overlap, the resulting color is not unique, and depends on the colors and intensities of the two pixels, very often resulting in a confusing picture. The SCIA algorithm avoids this problem because each of the 7 resulting correlation images is assigned a unique color. For three channel correlations, overlay is typically not attempted due to the confusion of colors. The 3D correlated structures can be assembled into 3D structures if the same settings of the SCIA algorithm are used for each 3D slice. The colocalized 3D images can be reconstructed into 3D images for further rendering and image visualization. The three channel structural image cross-correlation algorithm has been achieved for multicontrast microscopy of chloroplasts (Carriles, Schafer et al. 2009) starch granules (Cisek, Prent et al. 2009), stomata, *Chlamydomonas reinhardtii*, cyanobacteria *Leptolyngbya* sp. and *Anabaena* sp. (Cisek, Spencer et al. 2009).

Three channel SCIA has been implemented using LabVIEW software. The program, shown in Fig. 3.4-2 loads three files to be correlated, either directly from the data analysis

software, or from image text files. The program is advantageous because live threshold and brightness adjustments can be made to the original images while watching the resultant correlations, an essential part of this tool. The combined correlation image, colored with the coloring scheme indicated, can be saved to TIFF along with all the double and triple correlated images.

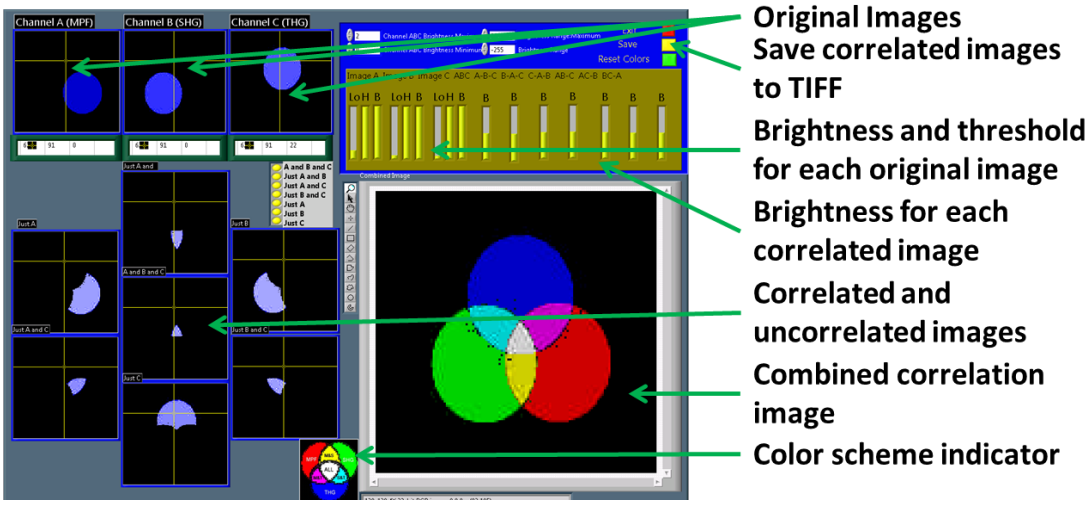

Fig. 3.4-2: The SCIA algorithm implemented in LabVIEW.

An imaging example of the 3-channel SCIA is presented in Fig. 3.4-3. Respectively, Fig. 3.4-3 (a), (b), and (c) show the MPF, SHG, and THG images of a rhodamine B–labeled potato starch granule imaged with multicontrast nonlinear microscopy. Panel (d) of Fig. 3.4-3 presents the SCIA correlation image. The panels (f-k) correspond to the individual correlations listed in the Fig. 3.4-1, while the coloring scheme is shown in panel (l) and described in the corresponding figure caption. The dye was added to starch in order to illustrate the SCIA principle with three channels, and is not required for second or third harmonic generation in starch granules. The advantage of the SCIA technique as compared to conventional image overlap analysis is that each correlation can be analyzed separately, and accordingly switched on and off to focus only on the desired correlations between the images.

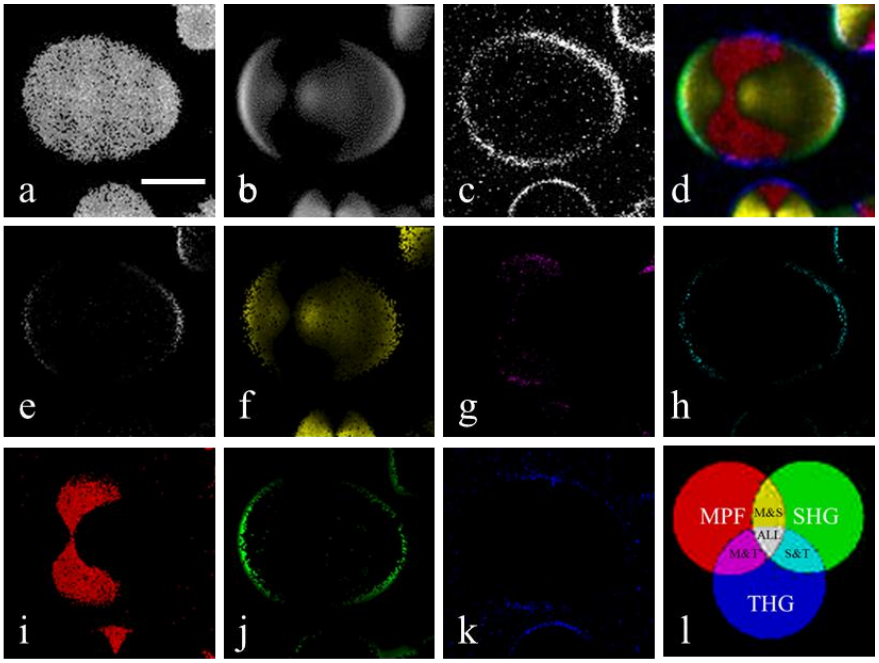

Fig. 3.4-3: SCIA of multicontrast rhodamine-B labeled starch granule images.

Three channel structural image cross-correlation analysis was applied to images of a potato starch granule labeled with rhodamine B stain and imaged with horizontally aligned linearly polarized excitation simultaneously with two photon fluorescence (shown in a), second harmonic generation (b) and third harmonic generation (c). The image (d) shows the resulting three channel correlations colored independently. White; correlation between all three channels (e). Yellow; correlation between channels A and B but not C (f). Magenta; correlation between channels A and C but not B (g). Cyan correlation between channels B and C but not A (h). Red: uncorrelated channel A (i). Green; uncorrelated channel B (j). Blue; uncorrelated channel C (k). Panel (l) shows the coloring scheme. The scale bar represents 10 µm. Panels (a) to (d) reprinted with permission from (Cisek, Prent et al. 2009).

The example in Fig. 3.4-3 shows that the THG does not correlate with the SHG (panel k) at the top and bottom edges of the starch granule, while it does at the sides (h) because SHG is mostly generated parallel to the polarization, which is horizontal in these images, while THG is still generated in the vertical orientation. Additionally, uncorrelated SHG appears on the outside edges (j) and (d) of the granule while correlated fluorescence appears inside (f) and (d), indicating the dye is not concentrated at the granule boundary. The example in Fig. 3.4-3 shows an elegant way of discriminating structures uniquely expressed by the different contrast mechanisms. SCIA can be used to discriminate different features in complex biological structures and provides an improved understanding of the spatial co-localization of the structures revealed by different nonlinear contrast mechanisms.

3.4.3 PIPO nonlinear optical microscopy measurement

Polarization-in-polarization-out (PIPO) microscopy is a novel technique that has been developed to obtain quantitative structural information based on the crystallinity and orientation of

microscopic samples. In PIPO microscopy, at each orientation of linear polarization of the laser, the polarization of the nonlinear signal is measured to reveal the susceptibility tensor elements of the crystalline structure. Since the symmetry of a crystalline structure (unit cell type and orientation) is reflected in the symmetry of the susceptibility tensor, PIPO microscopy can be used to reveal structural parameters of crystallinity and orientation of the crystalline structures in microscopic samples. PIPO measurements could be applied for basic research involving sensitive structural measurements of microscopic structures inside living biological tissue, as well as, for quick non-invasive detection of crystal uniformity and alignment of semiconductor nanostructures for quality control.

Performing PIPO measurements in a nonlinear optical microscope is possible requiring only a few changes to the microscope setup. To obtain linearly polarized light at the sample a linear polarizer (IR 1100 BC4, Laser Components Inc.) was placed just before the excitation objective in the beam (shown in Fig. 3.2-1, polarizer). To rotate the polarization of the laser we employed a half wave plate (532GR42-Comar Optics Inc.) oriented just past the polarizer but before the excitation objective (HWP in Fig. 3.2-1). The optical setup was tested via using a second duplicate linear polarizer just after the collection objective to ensure that the IR beam going through the half-wave plate and both excitation and collection objectives remained linearly polarized. One of the home-made microscope objectives induced elliptical polarization due to the crystalline sapphire lenses, chosen for their good transmission of UV wavelengths for THG detection from the Ti:Sapphire laser at 800 nm. Therefore, a new polarization insensitive home-built microscope objective with 0.85 NA was designed and used for collection of the signal in transmission mode. The dichroic mirror (DM2 in Fig. 3.2-1) was removed during PIPO measurements because it had polarization dependent transmission (albeit only <5%). During (PIPO) measurements, the half-wave plate angle was varied in 9° increments. Measuring the intensity of outgoing polarizations was accomplished by placing a linear polarizer (analyzer in Fig. 3.2-1) designed for the visible spectrum (Newport) just after the collection objective, and rotating in 18° steps. One PIPO measurement typically consisted of taking an image consisting of summed 200 frames at 10 emission polarization angles for each of 10 half-wave plate angles, resulting in emission and excitation polarization range of 0° to 180°, with a total number of 100 images. Additionally, after every 5-10 scans, the height of the sample was verified. The sample

was also scanned without an analyzer through the same range of half-wave plate orientations at the beginning and end of each scan to ensure conditions remained constant.

The PIPO technique is currently quite tedious, requiring manual rotation of a polarizer, analyzer, as well as sample alignment due to shifting, resulting in a single measurement time of several hours. Nevertheless, PIPO microscopy reveals valuable structural and orientation information in crystalline semiconductors as well as biological samples since hyperpolarizability tensor elements can be obtained and used for structural analysis of crystalline samples.

3.4.4 Data analysis of PIPO SHG images from cubic structures

Analysis of PIPO images was performed in ImageJ imaging software (Abramoff, Magalhaes et al. 2004). The 100 images obtained at different excitation and analyzer angles require alignment due to beam shifting caused by the half wave-plate. Images of nanowires (NW) (Chapter 4) were aligned automatically using an ImageJ plugin (Thevenaz, Ruttimann et al. 1998). A small region of interest was chosen on the image stack of a NW, and the ImageJ plot profile function was used to create intensity profiles of analyzer angles versus nonlinear optical signal intensity at each excitation polarization. Fig. 3.4-4 shows the SHG polarization data from a zinc blende NW as polar plots, one for each orientation of excitation polarization (red arrow) with respect to the NW axis (vertical blue line). The SHG intensity is plotted at each analyzer angle corresponding to the radius length resulting in the green line of the polar plots. It can be seen that the generated SHG is linearly polarized for each excitation polarization, as visualized in each panel of Fig. 3.4-4, in accordance with the theory (section 2.3). Additionally Fig. 3.4-4 (a) shows the SHG is oriented parallel to the NW axis when the excitation laser is polarized parallel to the NW axis and has a maximum intensity at this angle. However, the orientation and amplitude of SHG at other orientations of the laser polarization with respect to the NW is not intuitive, and depends on the particular hyperpolarizability values for the unique sample; at 60° excitation with respect to the NW, Fig. 3.4-4 (d) shows the SHG intensity is minimal, and occurs oriented along -40° with respect to the NW, while at 90° excitation (panel (f)) the SHG has a large amplitude and is oriented along -50° to the NW axis. Therefore all the polar plots shown in Fig. 3.4-4 give information as to the values of the susceptibility tensor representing this NW and should be considered to reveal the values of the hyperpolarizability for the particular sample, under the assumption that the NW is composed of a uniform crystalline phase. In order to avoid the

confusion of showing 10 graphs for one sample, the data can be summarized in a multi-curve 2D plot.

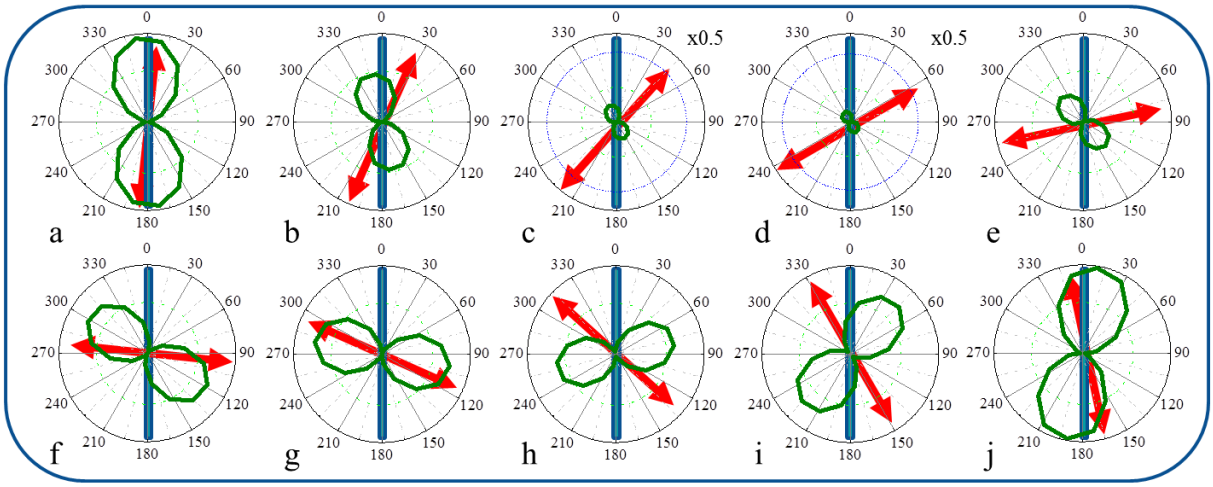

Fig. 3.4-4: Polar plots representing polarization of generated SHG from a zinc blende NW.
The NW axis is represented by the blue bar, the linearly polarized laser is oriented along the red arrow and the green curve represents SHG intensity via the radius at each analyzer angle. Data corresponds to the NWb in Fig. 4.3-2 (a).

Fig. 3.4-5 (a) shows a multi-curve 2D plot of PIPO data for a zinc blende NW, summarizing the data in the polar plots Fig. 3.4-4 into a single graph. Each curve in the 2D plot, labeled in the figure legend, corresponds to a polar plot in Fig. 3.4-4, and represents the SHG intensity as a function of the analyzer angle. The data in the 2D plot have been fit using a global fitting function (Origin 8.0), using the equation appropriate for cubic symmetry of the NW with growth direction along [1 1 1] (Eq. 2.3-9), and revealed the rotation parameter unique for this NW of $\delta=19\pm1°$. The fits (lines) to the 2D data (points) are shown in the plot of Fig. 3.4-5 (a), and match quite well with the points, which shows the use of the fitting function with cubic symmetry is a suitable model for this NW data. The plot also shows that curves at different orientations of the laser polarization with respect to the NW have maxima that are shifted from the center, which makes the fitting procedure particularly sensitive. To further reduce ambiguity in the presentation of the data, the PIPO data can be represented by a contour plot.

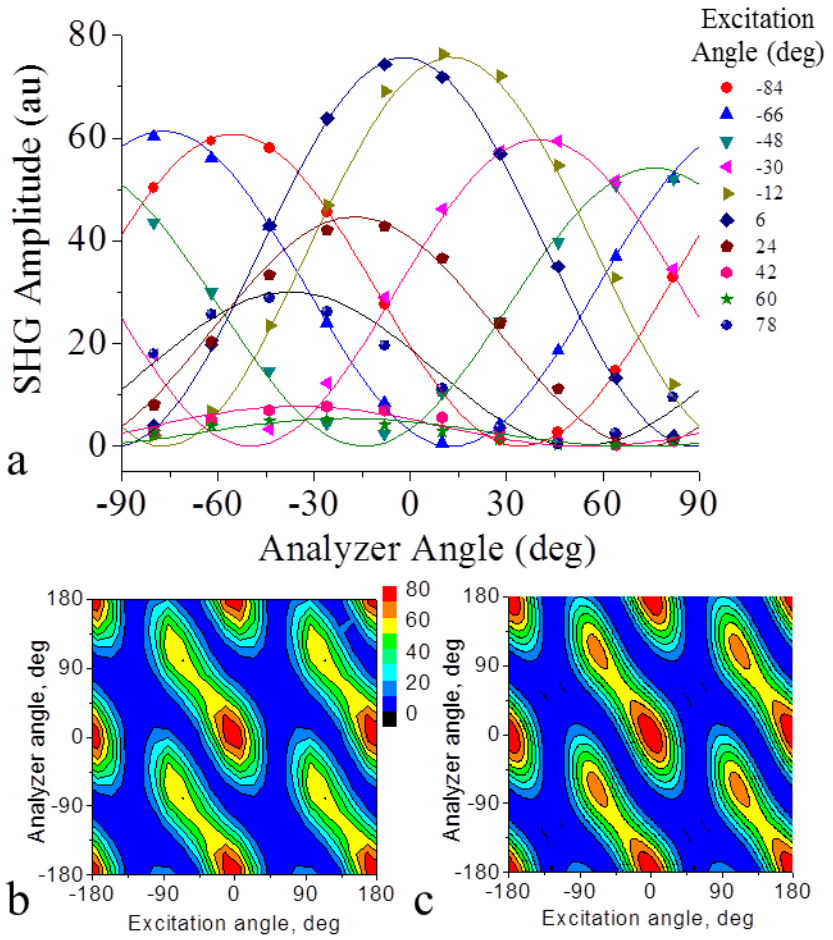

Fig. 3.4-5: PIPO SHG data from a NW.

The 2D graph (a) shows SHG intensity values at different orientations of the linearly polarized laser with respect to the NW axis, see legend, at different orientations of the analyzer with respect to the NW (x axis). The lines are fits obtained using Eq. 2.3-9, and revealed a fit parameter of δ=19±1°. The contour plot (b) shows the PIPO data at intensities as colors on a plot with orientation of the laser polarization on the x axis and orientation of the analyzer with respect to the NW on the y axis. The contour plot (c) shows the fits with the same parameters as in (a). Note that "au" in (a) represents arbitrary units.

An entire PIPO dataset can be represented by a single surface contour plot which combines all data curves, and shows the function in an intuitive way. Fig. 3.4-5 (b) shows the contour plot of the PIPO data corresponding to Fig. 3.4-5 (a), via showing SHG intensity as a color, (red maximum, black minimum), as a function of two axes; the angle between the linearly polarized laser and the NW axis (θ) is on the x axis, while the angle between the analyzer axis and the NW axis (κ) is on the y axis (for angle definitions see Fig. 2.3-1). The contour plot of PIPO data immediately enables one to discern problems in data collection if the figure is not continuous, an advantage over the 2D graphs of multiple curves, which looks rather crowded. The fit to the PIPO contour data is performed via the surface fitting tools (Origin 8.0 and

MATLAB 9), revealing the same quality fits compared to global fitting with 2D plots, and is shown in Fig. 3.4-5 (c). The fit is shown at the same color scale as the data and reveals a contour image, which has very similar shape compared with the data. A comparison of the fits Fig. 3.4-5 (a) versus (c) reveals the 2D fit of curves (a) is slightly better, especially visible at fitting the second maximum curve at -48° excitation angle; this occurs because fits of individual curves are allotted an adjusted fitting parameter for each excitation angle, and therefore provide a better fit, while the surface fit leading to the contour plot (c) does not allow for such adjustments, however the fitting parameter in both cases was the same, therefore the contour plot fit is used throughout the thesis.

Theoretical contour plots were shown in order to visualize how the function describing cubic crystals varies with the fit parameters. Fig. 3.4-6 shows theoretical contour plots (Eq. 2.3-9) of SHG intensity for a cubic crystal oriented with its [1 1 1] axis along the z axis, at different values of δ, the rotation angle of the crystal about the [1 1 1] (NW) axis is shown above each contour plot. The δ=0 was assumed to be as shown in Fig. 4.2-1 (d). As before the contour plots show SHG intensity via color as a function of the laser polarization (θ) measured from the z axis, shown on the contour plot x axis, and the analyzer angle (κ) measured from z on the y axis (for angle definitions see Fig. 2.3-1). The figure shows that the parameter of rotation in the cubic crystal around the z axis (δ) is modulo 120°. Furthermore, the PIPO contour plots show that there exists quite a variation in the PIPO plot during 60° rotation, which should enable simple differentiation between different NW rotation angles, shown by an asymmetry in the contour plot.

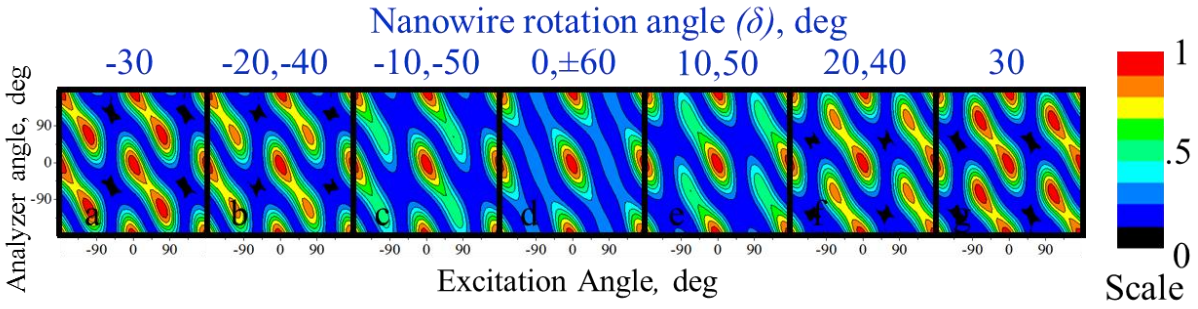

Fig. 3.4-6: Theoretical contour PIPO plots for cubic crystals.

Contour plots of Eq. 2.3-9 at different cubic crystal rotation angles δ, from -60° to 60°, modulus 120°. Each contour plot is a function of the angle between the linear polarization orientation of the laser excitation and the cubic crystal [1 1 1] axis (θ) shown on the x axis, and the orientation of the analyzer with respect to the cubic crystal axis (κ) on the y-axis, and both axes range from -180° to 180°.

3.4.5 Data analysis of PIPO SHG images from hexagonal structures

Analysis of PIPO data was performed on hexagonal structures, namely starch granules, in order to compare and contrast with the PIPO data analysis of cubic structures. Starch granule images (section 3.4.5) required manual alignment due to the changing starch granule image during rotation of the polarization optics, and could not be aligned automatically as the NWs. Similarly to NW PIPO analysis, a small region of interest was chosen on the image stack and SHG intensity profiles of analyzer angles versus NLO signal intensity at each excitation polarization are represented via polar plots in Fig. 3.4-7. The plots were produced in the same way as in the previous section 3.4.4, and reveal that the polarization of the generated SHG appears linearly polarized for each excitation polarization similarly to the NW analysis. Another similarity between the analysis of cubic and hexagonal structures is that a maximum SHG always appears when the excitation is parallel to the crystal axis (Fig. 3.4-7 (a), compare with Fig. 3.4-4 (a), however cubic structures can contain a second local SHG maximum, (see Fig. 3.4-4 (g)), but hexagonal structures do not. Additionally, the polarization of the SHG in starch granules is mostly parallel to the excitation direction, unlike in NWs it is not (see Fig. 3.4-7 versus Fig. 3.4-4). As before, the PIPO data is subsequently represented by a multi-curve 2D plot which summarizes the data.

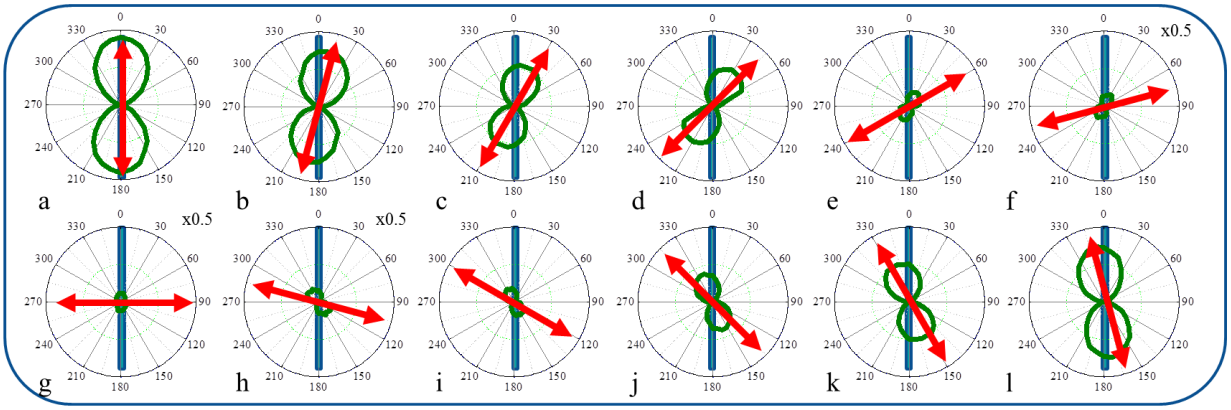

Fig. 3.4-7: Polar plots representing polarization of generated SHG from experimental data of a maize starch granule.

The starch crystal axis is represented by the blue bar, the linearly polarized laser is oriented along the red arrow and the green curve represents SHG intensity via the radius at each analyzer angle.

Fig. 3.4-8 (a) shows a multi-curve 2D plot of PIPO data for a maize starch granule, summarizing the data in the polar plots Fig. 3.4-7 into a single graph. As before, each curve in the 2D plot, labeled in the figure legend, corresponds to a polar plot in Fig. 3.4-8, and represents the SHG intensity as a function of the analyzer angle. The data in the 2D plot (points) have been fit using a global fitting function (Origin 8.0), using the equation appropriate for hexagonal symmetry of starch amylose crystals (Eq. 2.4-16), and revealed the following fitting parameters: d_{33}/d_{15}=4.2±0.3 and d_{31}/d_{15}=1.1±0.1. The fits are shown as lines in Fig. 3.4-8 (a) and reveal good agreement between the data and the fits, showing that the use of the fitting function with hexagonal symmetry is a suitable model for this starch dataset. As in the cubic NW data, the 2D plot also shows that curves at different orientations of the laser polarization with respect to the NW have maxima that are shifted from the center, which increases the sensitivity of the fitting procedure. In the next step, contour plots of the hexagonal data are shown.

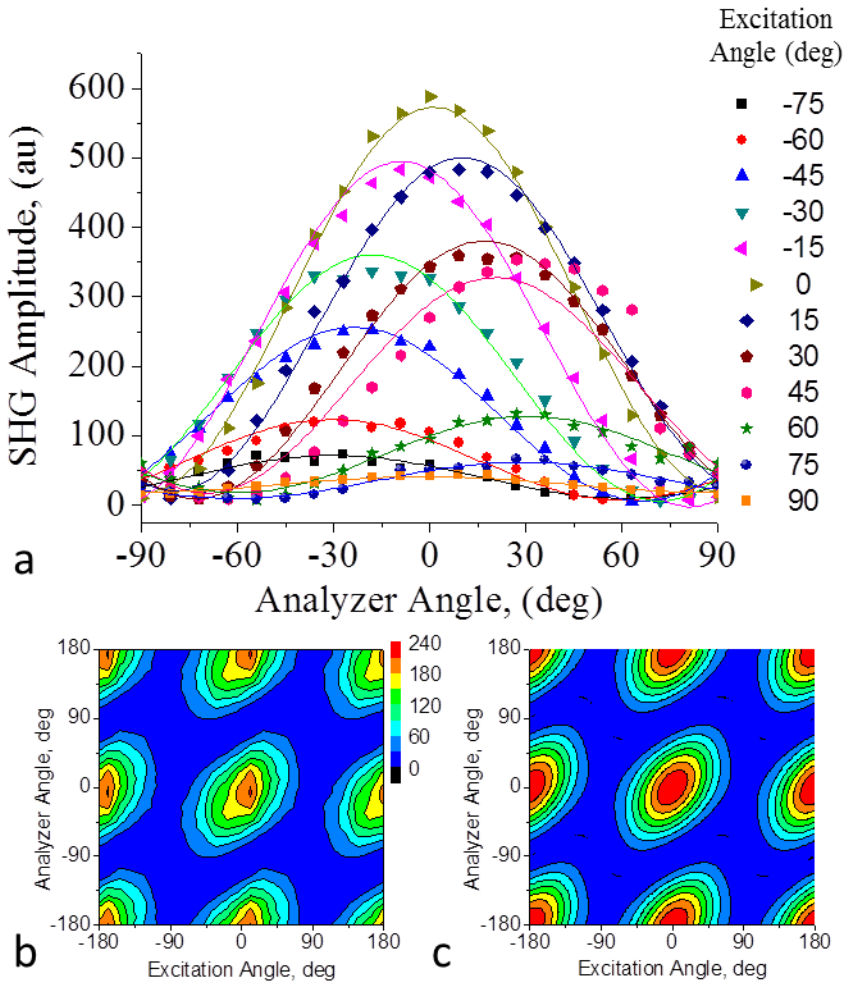

Fig. 3.4-8: PIPO data and fits of a fresh potato starch granule visualized as individual curves.
Individual SHG intensity (y axis) curves at different angles of the analyzer with respect to the helix (x axis); each plotted curve was recorded at a different position of the laser excitation with respect to the helix, indicated in the figure legend. Fit parameters are the same as Fig. 5.3-8 (b). Note that "au" in (a) represents arbitrary units.

The PIPO dataset is most conveniently represented by a single surface contour plot which combines all data curves, and shows the function in an intuitive way. Fig. 3.4-8 (b) shows the contour plot of the PIPO data corresponding to (a), by showing SHG intensity as a color, (red maximum, black minimum), as a function of two axes; the angle between the linearly polarized laser and the amylose crystal axis on the x axis, while the angle between the analyzer axis and amylose crystal axis on the y axis. The fit to the PIPO contour data is performed using Eq. 2.4-16 via the surface fitting tools (Origin 8.0 and MATLAB 9), revealing the same quality fits compared to global fitting with 2D plots, and is shown in Fig. 3.4-8 (c). The fit is shown at the same color scale as the data and reveals a contour image, which has very similar shape compared

with the data. Unlike NW data, there is always only one maximum in PIPO images of hexagonal structures, and therefore, it is worthwhile to observe how the PIPO images change by altering hyperpolarizability fit parameters.

Fig. 3.4-9 shows theoretical contour plots of SHG intensity for a hexagonal crystal corresponding to different values of the hexagonal hyperpolarizability tensor d_{33}/d_{15} and d_{31}/d_{15} ratio values. The figure shows that at d_{31}/d_{15} near 1, which is the case for materials which do not absorb at the fundamental laser or second harmonic wavelengths (see section 2.4.3), the PIPO contour plot shows marked differences allowing determination of the unique hexagonal crystallinity parameter d_{33}/d_{15}. However, in comparison to varying the fit parameter in cubic structures, the variation is not as obvious. Interestingly, at high values of d_{33}/d_{15} the sensitivity to the secondary ratio d_{31}/d_{15} is reduced. When comparing PIPO plots of hexagonal versus cubic structures, the cubic structures at rotation angles $\delta \neq 0$ are easily distinguished from hexagonal structures because they contain an asymmetry, or a second local maximum. On the other hand cubic plots at $\delta = 0$ are very similar to hexagonal plots at d_{33}/d_{31}=-2 and d_{33}/d_{15}=1, (compare Fig. 3.4-6 (d) with Fig. 3.4-9 (b2)), and good fits are needed to distinguish these structures, however it can be achieved since the central maxima lobes on the PIPO plots have different widths.

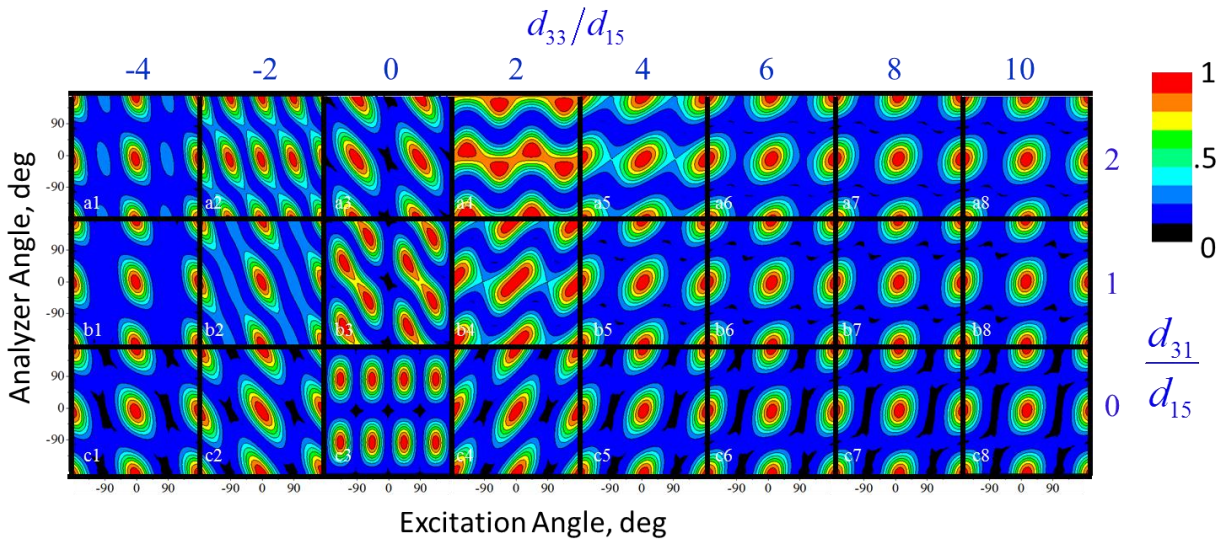

Fig. 3.4-9: Theoretical contour PIPO plots for hexagonal crystals.

Contour plots showing intensity normalized SHG intensities from Eq. 2.4-16 at different values of the hyperpolarizability ratios d_{33}/d_{15}: from -4 to 10 on the x axis, and d_{31}/d_{15} from -1 to 2 on the y axis. Each contour plot is a function of the excitation angle of laser polarization with respect to the helical axis on the x axis and analyzer angle with respect to the helical axis on the y axis, and both axes range from -180° to 180°.

For imaging hexagonal biological structures the PIPO technique is quite beneficial over the standard polarization SHG measurements currently performed. Although the pioneering measurements of the SHG from biocrystals, performed on rat tail tendon by Roth and Freund in the late 70s and early 80s recognized the importance of measuring the directionality of the polarization of SHG (Freund, Deutsch et al. 1986), recent literature in the field has not been taking this into account. Instead SHG polarization microscopy studies rely solely on the use of polarization-in data, and fitting via Eq. 2.4-13, in SHG studies of muscle, tendon and starch (Tiaho, Recher et al. 2007; Psilodimitrakopoulos, Amat-Roldan et al. 2011). Polarization-in fits rely on the width of the SHG intensity versus incident polarization curve, which results in little change at high values of the ratio d_{33}/d_{15}, visualized in the Fig. 3.4-10, which shows that model polarization-in curves, generated with $d_{31}/d_{15}=1$, at d_{33}/d_{15} ratio values of 3, 4 and 6, are difficult to distinguish, complicating the fits. In order to account for the large fitting error obtained with this method, it is common to fit all the pixels within the image of the structure, and use the best fits as representatives in pixel-histograms, which are subsequently used to predict the average values of hexagonal hyperpolarizability ratios d_{33}/d_{15} and d_{31}/d_{15} (Chen, Li et al. 2009; Psilodimitrakopoulos, Amat-Roldan et al. 2010). This method reduces the sampling resolution. Another error reduction procedure is to rely on the homogeneity of the sample and use depth-

dependent analysis for the fits (Zhuo, Liao et al. 2010). The second technique relies on good axial resolution. Both these techniques lack in sensitivity and therefore could be improved by additional collection of polarization out data. PIPO data is advantageous because it contains obvious shifts of the maximum at different excitation angles, see for example Fig. 3.4-8 (a) 15° versus -15° excitation, which is much more sensitive to the fitting parameters, and therefore yields reduced error values.

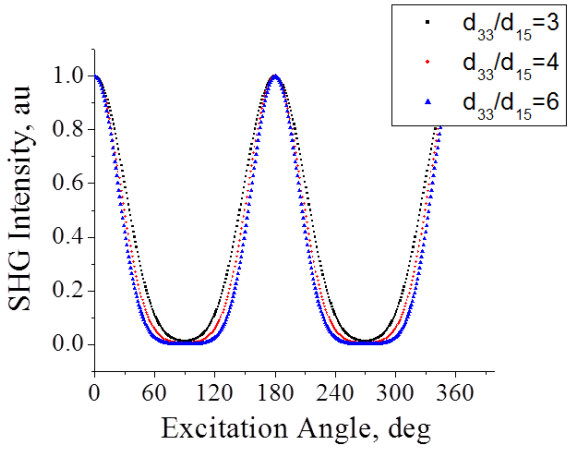

Fig. 3.4-10: Model of polarization-in SHG curves for hexagonal crystals at three values of d_{33}/d_{15}. The curves are shown normalized with d_{31}/d_{15}=1.

In summary, the analysis of PIPO SHG data has been presented. Use of contour plots was shown to give an insightful and concise summary of the PIPO data in single intuitive plots. Surface fitting of the contour plot data reveals good fits, showing the models are acceptable fits to the data. These fits can be subsequently used to estimate hyperpolarizability ratio values for hexagonal structures, or the rotational parameter for cubic structures. The advantage of the PIPO technique compared to conventional polarization-SHG was shown in the sensitivity of the PIPO plots compared with the polarization-in curves. The presented PIPO data analysis is a useful technique that can potentially yield, in a quick noninvasive manner, structural parameters of nano-sized crystalline objects inside biological organisms, and can be subsequently used to address various questions of tissue morphology and morphogenesis.

Chapter 4
Nonlinear Microscopy of ZnSe Nanowires

4.1 Introduction to Nonlinear Microscopy of Semiconductor Nanowires

Nanowires (NWs) composed of ZnSe are interesting novel nanostructures which are finding applications in optoelectronic devices such as blue LED technology, nano-sensors and optical computers (Zhang, Liu et al. 2004; Pauzauskie and Yang 2006; Ruda, Philipose et al. 2010). An investigation of ZnSe nanowires using nonlinear microscopy can be performed to reveal structural properties including the crystal composition, and the orientation of the crystal with respect to the sample plane. Knowledge of these parameters is essential to optimize optoelectronic properties such as the high frequency dielectric constant. Furthermore ZnSe NWs are an ideal model system for studying nonlinear optical properties relevant to complex biological structures because; i) they have several basic crystalline forms, similar to those in biological structures, ii) they are similar in size to single biological crystals, iii) they have a well understood structure, iv) they are robust resisting photobleaching, and v) they have a high second-order nonlinearity, ideal for SHG microscopy (Wagner, Kühnelt et al. 1998; Xia, Dai et al. 2006). The nonlinear optical microscopic signals of SHG and THG can reveal structural information about NWs since they are sensitive to the structural arrangement of atoms in different crystal lattices, determining different values of the susceptibility tensor elements (see sections 2.3.1 and 2.4.1). Many novel NW-based devices have already been demonstrated such as NO_2 sensors capable of high sensitivity down to 1 part per billion, sensors for cancer biomarkers using multiplexed antibody-functionalized NWs, as well as nano-sized field-effect transistors. Furthermore, the advancement of on-chip integration of these devices, which has also been recently demonstrated, could enable fast large-scale nanodevice production (Zhang, Liu et al. 2004; Zheng, Patolsky et al. 2005; Bryllert, Wernersson et al. 2006; Fan, Ho et al. 2008; Ruda, Philipose et al. 2010). Therefore since nonlinear optical imaging offers non-invasive fast monitoring and discrimination of different internal structures in the NWs, it could be a useful tool for quality control during assembly line production of nanodevices.

Thus far, only a handful of nonlinear microscopy studies of single semiconductor NWs have been performed. A nearfield SHG and THG microscopy study to measure single wurtzite

ZnO NWs determined the independent hyperpolarizability tensor components from measurements of polarization dependent SHG intensity (Johnson, Yan et al. 2002). Another study found SHG resonance enhancement in ZnO NWs via measurement at different wavelengths (Prasanth, Vugt et al. 2006). A large SHG anisotropy was found in polarization measurements of ZnSe NWs (Barzda, Cisek et al. 2008), and was attributed to a dielectric mismatch between the NW and its environment. An investigation of simultaneous anisotropy measurements of SHG, THG and MPF was performed showing the anisotropy depended on NW roughness, as well as on the difference between the dielectric constant of the NW and its environment (Spencer, Cisek et al. 2009; Cisek, Barzda et al. 2010). SHG from single wurtzite GaAs nanoneedles was also investigated recently, reporting a ratio of hyperpolarizability tensor values (Chen, Crankshaw et al. 2010). Se rich NWs were investigated by SHG microscopy (Ruda, Philipose et al. 2010), finding that the shape of the NWs became distorted from rod-like, clearly visible with THG microscopy. Most recently, polarization-in-polarization-out SHG microscopy was performed on zinc blende ZnSe NWs revealing, for the first time, that a measurement of the rotational orientation of the crystal lattice around the NW axis could be determined for small segments on individual NWs that have been deposited on a glass surface (Cisek, Hirmiz et al. 2011).

This chapter endeavors to present a detailed nonlinear microscopic investigation of SHG from ZnSe NWs. The structures of ZnSe NWs are reviewed in section 4.2. Section 4.3 features a detailed investigation of ZnSe NWs with SHG microscopy, characterizing different NW types including zinc blende (section 4.3.3), wurtzite and NWs with periodical twinning (section 4.3.4), by analysis with the theory in sections 2.3.3 and 2.4.3, respectively. Variations between experimental data and theoretical predictions are discussed using the phenomena of a varying dielectric constant in wurtzite NWs in section 4.3.5, with theory listed in that section, as well as from depolarization of the NW electric field due to the surface (section 4.3.6), with theory from section 2.1.3.

4.2 ZnSe Nanowires Structure

4.2.1 Introduction to the nano-scale structure of ZnSe NWs

The structure of semiconductor ZnSe NWs is described in this section. Up to now several types of nanoparticles composed of ZnSe have been synthesized which have varying morphologies:

quantum dots, coupled quantum wells, NWs as well as nanoribbons (Kumbhojkar, Mahamuni et al. 1998; Jiang, Xu et al. 2001; Philipose, Sun et al. 2007). While ZnSe quantum dots have dimensionality < 10 nm, NWs are much larger, having 50-500 nm in diameter and 3-15 μm in length, a convenient size for investigations with a nonlinear optical microscope, as well as, having a cylindrical structure similar in size to SHG active biological structures such as collagen and cellulose microfibrils. In comparison to NWs, nanoribbons are much wider structures generally containing more defects (Philipose, Sun et al. 2007). NWs on the other hand can have pure crystal phases including zinc blende and wurtzite (Xia, Dai et al. 2006) and therefore are good candidates for investigation of crystalline effects with nonlinear microscopy. Therefore, the nano-scale structure of ZnSe NWs is described in this section, beginning with a review of the evidence for two different types of ZnSe crystalline NWs: zinc blende and wurtzite.

Semiconductor NWs composed of ZnSe have interesting structural characteristics, which can be probed with nonlinear microscopy. Recently, it has become possible to produce relatively structurally uniform and defect-free ZnSe NWs by the vapor phase growth method (Xiang, Zhang et al. 2003). In this method, very pure Zn and Se are vaporized, and at high heat (500 – 1000 °C), deposited onto a silicon wafer covered with a thin layer of gold, forming NWs by self-assembly. Variation of the ratio between Zn and Se, as well as the pressure, temperature and flow rate of gas (usually argon or nitrogen) produces different morphologies of ZnSe NWs (Xia, Dai et al. 2006). These morphologies have been characterized using electron microscopy as well as photoluminescence, revealing two main molecular organizations; zinc blende and wurtzite (Xia, Dai et al. 2006; Philipose, Saxena et al. 2008). These two organizations consist of different crystal symmetries, and have dramatically different nonlinear optical properties. A third ZnSe NW morphology can also be synthesized, consisting of periodical organized zinc blende phases interrupted by wurtzite “twin” planes, known as twinned NWs.

4.2.2 Zinc blende ZnSe NWs

The structural details of the ZnSe zinc blende NWs grown by the vapor phase growth method are revealed by a combination of electron microscopy and electron diffraction. Fig. 4.2-1 (a) presents a typical zinc blende NW image, produced by low magnification transmission electron microscopy (TEM), showing a mostly uniform macrostructure. Evidence for the zinc blende cubic crystal structure is provided via diffraction pattern produced by selected area electron

diffraction (SAED), and shows a cubic structure in the inset on the top right in Fig. 4.2-1 (b). The atomic resolution scaled imaging of the NW obtained using high resolution transmission electron microscopy (HRTEM) reveals that the NW growth direction is diagonal to the cubic lattice, along the cubic [1 1 1] direction (Fig. 4.2-1 (b)), and is identified by the visualized ABC pattern, (see enlarged region in panel (b) on the top left). This ABC pattern can be identified in the crystal structure image oriented with [1 1 1] to the right direction in Fig. 4.2-1 (c). An interesting feature of the zinc blende NW is the C_3 (threefold) symmetry about the NW axis [1 1 1], visualized in Fig. 4.2-1 (d), where the NW is directed perpendicular to the page.

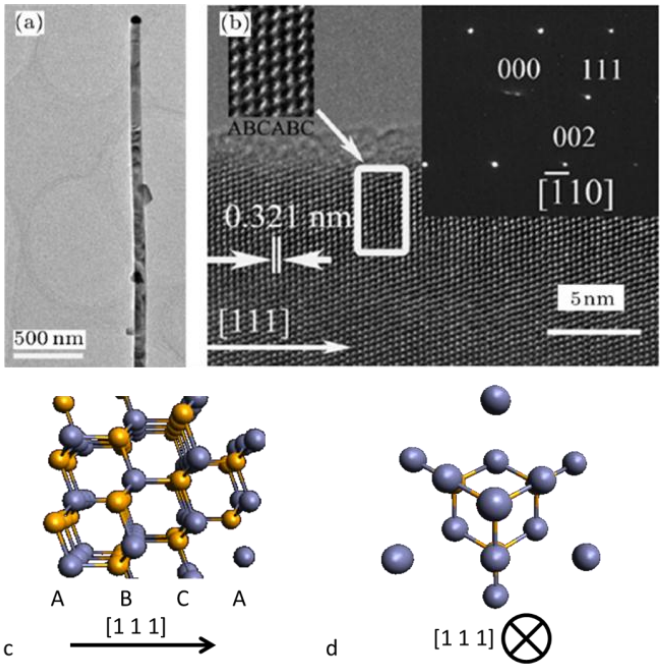

Fig. 4.2-1: Structure of zinc blende ZnSe NWs.

NWs are shown via a TEM image (a), and a HRTEM image with corresponding SAED pattern of the NW in the inset (b). The ZnSe cubic crystal unit cells are in same orientation as (b) showing ABC pattern (c), and a single ZnSe cubic crystal unit cell viewed with (1 1 1) direction into the page revealing C3 symmetry about the NW axis (d). Panels (a) and (b) reprinted with permission from (Xia, Dai et al. 2006).

4.2.3 Wurtzite ZnSe NWs

Wurtzite is an alternative lattice structure, which can occur during the vapor phase growth of ZnSe NWs (Fig. 4.2-2(a)). Wurtzite is the common name of a hexagonal mineral, commonly ZnS or FeS. Evidence for the wurtzite structure in ZnSe NWs is provided by a SAED pattern shown in the inset at the top right of Fig. 4.2-2 (b), and as well, by the distance between adjacent layers in the HRTEM image, of 0.645 nm. The left region of the HRTEM image in Fig. 4.2-2 (b) shows that the wurtzite NWs grow along the [0 0 0 1] hexagonal axis, which has a repeating AB

pattern clearly shown via the crystal structure oriented along [0 0 0 1] in panel (c). Fig. 4.2-2 (d) shows the hexagonal (C_6) symmetry around the wurtzite NW axis with a wurtzite crystal unit cell oriented perpendicular to the page. Although it is possible to obtain pure wurtzite NWs, it is common to obtain NWs that have mixed zinc blende and wurtzite morphologies, known as twinned NWs, in addition to other macroscale NW structures such as nanoribbons. Twinning can be detected by nonlinear microscopy; therefore it is further explained in the following section.

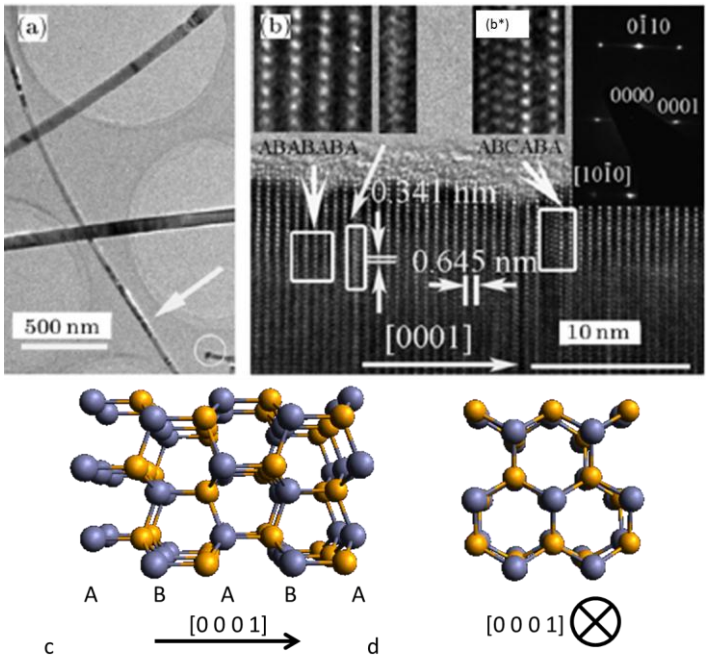

Fig. 4.2-2: Wurtzite and zinc blendestructure of a twinned ZnSe NW

A TEM is shown (a), a HRTEM image and corresponding SAED pattern of a hexagonal region of the NW (b), inset of a region containing twinning (b*), ZnSe hexagonal crystal unit cells in the same orientation as (b) showing AB pattern (c), and a single ZnSe hexagonal crystal unit cell viewed with [0 0 0 1] direction into the page revealing C6 symmetry about the NW axis (d). Panels (a) and (b) reprinted with permission from (Xia, Dai et al. 2006).

4.2.4 Twinning in ZnSe NWs

The wurtzite crystal phase of ZnSe NWs is metastable at room temperature and atmospheric pressure (Greene, Luo et al. 1995) therefore formation requires well controlled extreme conditions and can result in stacking faults and twinning (Philipose, Saxena et al. 2008). Fig. 4.2-2 (a) shows a TEM image of a twinned NW, indicated by the arrow. Twinned NWs are wurtzite NWs that contain zinc blende phases, as shown in the inset (b*) in Fig. 4.2-2 (b) by the changing pattern from zinc blende to wurtzite: ABCABA. These stacking defects can be understood from the similarity between the building blocks of zinc blende (ZB) along [1 1 1] versus wurtzite (W) along [0 0 0 1] shown in Fig. 4.2-3 (a) versus (b), to have a 60° rotational

difference between the two units. This rotation is readily visualized in the crystals of zinc blende and wurtzite along the [1 1 1] and [0 0 0 1] directions shown in Fig. 4.2-3 (c) and (d), respectively. A rotation of two zinc blende layers by 60°, termed twins for the two layers is shown explicitly in Fig. 4.2-3 (e) (Park, Cich et al. 2000), and occurs due to the presence of a single wurtzite layer sandwiched between the two zinc blende layers, and is termed a stacking fault. By adjusting the NW growth conditions, the amount of twinning can vary, in particular synthesis of NWs with stable periodic twinning has been achieved with the vapor growth method by a complicated procedure using a flux ratio of Zn:Se of 1:2 (Ruda, Philipose et al. 2010), as shown in the HRTEM images in Fig. 4.2-3 (f) and (g).

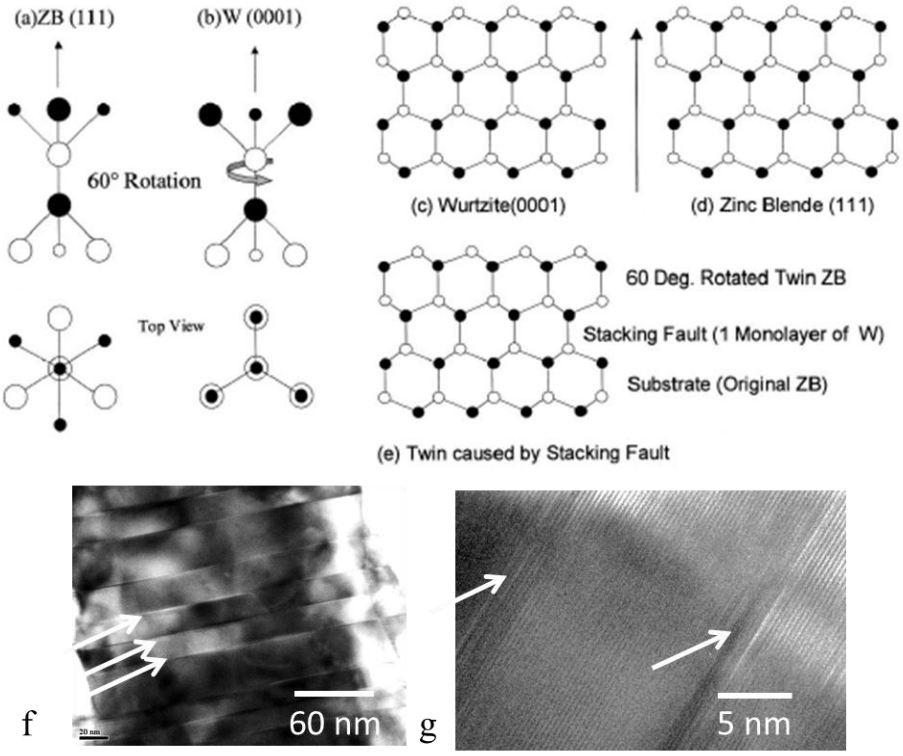

Fig. 4.2-3: Twinning explained via comparing zinc blende and wurtzite.

The basic building blocks of zinc blende (ZB) (a) wurtzite (W) (b) structures showing the 60° rotation difference, the [0 0 0 1] oriented organization of wurtzite (c) and the [1 1 1] oriented organization of zinc blende (d), the structure of the twin zinc blende formed by a stacking fault (e), and two HRTEM images of a periodically twinned ZnSe NW ((f) and (g)) with arrows showing the stacking fault regions. Panels (a)-(e) reprinted with permission from (Park, Cich et al. 2000), Copyright (2000), American Vacuum Society.

4.3 SHG Microscopy Investigation of ZnSe NWs

4.3.1 Introduction to SHG microscopy of ZnSe NWs

Nonlinear microscopic studies of ZnSe based on SHG contrast are described in this section. Although semiconductors including ZnSe were heavily studied in the past half century, before the 90s hyperpolarizability studies were focused on dispersion measurements, performed on ZnSe starting from the 60s (Chang, Ducuing et al. 1965). The dispersion of the hyperpolarizability in bulk zinc blende ZnSe was determined for the wavelength range 500 – 1250 nm, and is shown in Fig. 4.3-1 revealing a relatively flat curve at wavelengths above 1000 nm, with a hump near ~900 nm which corresponds to the first transition energy at the SHG wavelength (~2.7eV), and has a marked increase due to higher transitions starting below ~780 nm fundamental laser wavelength (Wagner, Kühnelt et al. 1998). Therefore the 1028 nm laser is not expected to induce resonantly enhanced SHG in ZnSe NWs.

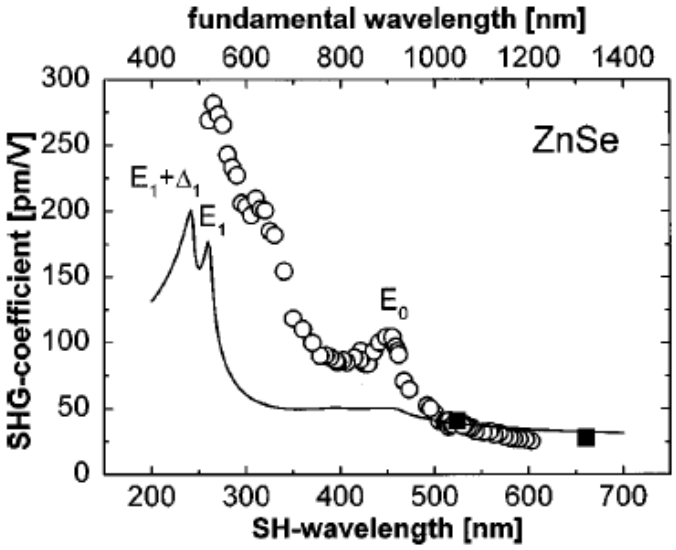

Fig. 4.3-1: Experimentally observed dispersion of the SHG coefficient k for bulk zinc blende ZnSe.
The unique ZnSe experimental hyperpolarizability coefficient (y axis) is plotted (circles), while a line of the theoretical dispersion is plotted (line). Both datasets are shown as a function of the fundamental wavelength of the laser (top axis) as well as by the SHG wavelength (bottom axis). Figure reprinted with permission from (Wagner 1998), copyright (1998) by the American Physical Society.

SHG microscopy studies of ZnSe NWs have not been performed extensively. The first nonlinear microscopy investigation ever performed was on ZnSe by Hellwarth and Christensen (1974). They studied SHG nonlinear microscopy of polycrystalline ZnSe by scattered and reflected SHG and discovered that the bulk material was made of crystal platelets about 60 μm in

diameter and 500 nm thick, with SHG emission occurring in the direction normal to the [1 1 1] orientation of the zinc blende crystal axes (Hellwarth and Christensen 1974). In another study, ZnO NWs of wurtzite structure were investigated using nearfield nonlinear microscopy with SHG intensity anisotropy. The orientation where the linear polarization of the laser was parallel with respect to the NW axis generated the largest SHG signal. This was attributed to the hexagonal crystalline lattice components of the hyperpolarizability tensor (Johnson, Yan et al. 2002). More recently studies measuring the SHG intensity anisotropy of zinc blende ZnSe NWs with different dielectric coatings were performed via conventional nonlinear multicontrast microscopy (Barzda, Cisek et al. 2008; Spencer, Cisek et al. 2009; Cisek, Barzda et al. 2010).

In this study PIPO SHG microscopy of ZnSe NWs is investigated in zinc blende, wurtzite and twinned ZnSe NWs. Discrimination between crystal lattice types of zinc blende versus wurtzite NWs is achieved. Observed deviations between theory and experiment in the PIPO data of wurtzite NWs is explained using two different theories of electric field enhancement in the nanostructures; due to variations in dielectric constant, as well as, due to a depolarization surface phenomenon.

4.3.2 NW sample preparation

ZnSe NW samples were obtained from the group of Prof. Harry Ruda, Center of Nanotechnology, University of Toronto. The NWs were synthesized by the vapor phase growth method (Philipose, Sun et al. 2007). Briefly, very pure solid Zn and Se powder is vaporized, and at high heat (500 – 1000 °C), deposited onto a silicon wafer covered with a thin layer of gold. Variation of the ratio between Zn and Se, as well as the pressure, temperature and flow rate of gas (usually argon or nitrogen) resulting in different morphologies of ZnSe NWs have been obtained (Xia, Dai et al. 2006). The silicon wafer containing NWs was sonicated in water to separate the NWs from the substrate. A drop of solution containing the NWs was placed upon a standard microscope coverslip and allowed to dry, leaving NWs on the glass surface. The wurtzite NWs as well as periodically twinned NWs were individually imaged in order to determine their crystal structure using high resolution transmission electron microscopy (HRTEM) as well as nonlinear microscopy. For HRTEM the solution containing NWs was deposited on a labeled thin gold grid of 0.5 mm thickness, which allowed localization of NW samples in two different microscopes (see Fig. 4.3-3 (a)). For subsequent scanning in the

nonlinear optical microscope, the gold grid with the NWs was placed upside down onto a standard microscope coverslip, covered with another coverslip and sealed with plastic tape.

In order to vary the relative dielectric constant between the NWs and the environment, and to prevent the NWs from bleaching, the NWs were etched to remove the oxide layer, and entire microscope slides with NWs were coated by a thin dielectric film of thickness 10–30 nm using plasma enhanced chemical vapor deposition at a temperature of 300 °C. Two coated samples were prepared, respectively, with SiO_2 and Si_3N_4 as the dielectric coating materials.

4.3.3 PIPO microscopy of zinc blende NWs

Single crystalline ZnSe zinc blende NWs were investigated by polarization-in-polarization-out (PIPO) SHG microscopy (Cisek, Hirmiz et al. 2011). To our knowledge, this is the first investigation measuring the polarization of SHG in zinc blende semiconductor NWs. The current investigation measures the polarization of the generated SHG, its dependence on the orientation of the linearly polarized laser with respect to the NW, and its relationship to the orientation of the cubic crystal lattice of the NW sample, as described in section 3.4.3. The ZnSe NWs had a zinc blende structure, and were grown along the [1 1 1] direction (see section 4.2.2), which can be characterized by a single unique nonzero hyperpolarizability component *k*, treated in section 2.3.1. The SHG intensity in such a case was found to depend on three angles illustrated schematically in Fig. 2.3-1; θ: the angle between the linearly polarized laser and the NW axis, κ: the angle between the analyzer and the NW axis and δ: the rotation of the cubic crystal lattice around the NW axis. The δ parameter occurs because the NW has a threefold symmetry perpendicular to the NW axis, which can be observed in Fig. 4.2-1 (d). The configuration corresponding to the angle δ=0 was chosen to be Fig. 4.2-1 (d), and is defined so that a positive rotation corresponds to clockwise rotation about the center of panel (d). As a result of this symmetry, PIPO data is sensitive to a range of 60° of the NW rotation, as shown in the theoretical PIPO plots of the SHG intensity equation for a cubic structure oriented along [1 1 1] in Fig. 3.4-6. Note that the PIPO data was made to correspond to the δ=0 molecular position following the assumption that a positive hyperpolarizability occurs towards the more electronegative atom, aka Zn to Se.

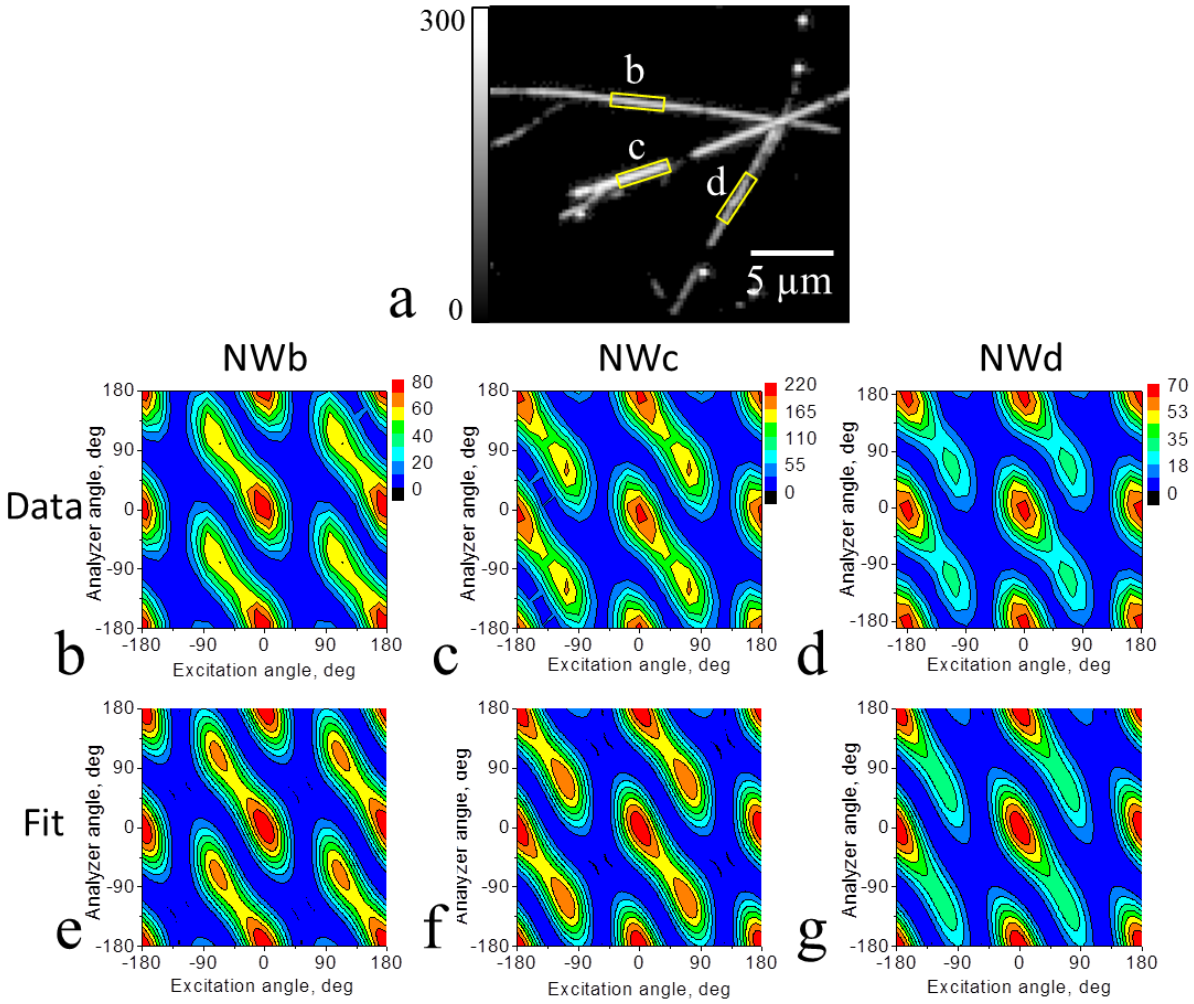

Fig. 4.3-2: PIPO SHG microscopy of zinc blende ZnSe NWs.

The ZnSe NWs are shown in the SHG image (a), showing three regions of interest that were analyzed to produce corresponding PIPO data contour plots (b), (c) and (d). Fits were performed to the PIPO data with Eq. 2.3-9, resulting in fit parameters $\delta=19\pm1°$, $\delta=-21\pm1°$ and $\delta=-9\pm1°$ for NW regions b c and d, respectively. The corresponding contour plots of the fit data for panels (b), (c) and (d) are shown in (e),(f) and (g) respectively. Panel (a) reprinted with permission from (Cisek, Hirmiz et al. 2011) © [2011] IEEE.

Fig. 4.3-2 shows PIPO SHG data for several zinc blende NWs recorded in a single image. PIPO data was recorded for each sample region totaling 100 images, with one of the images shown in Fig. 4.3-2 (a), depicting three large NWs. Fig. 4.3-2 (b), (c) and (d) reveals raw PIPO SHG data summarized into contour plots obtained from analyzing three areas with corresponding labels shown highlighted in Fig. 4.3-2 (a). Each contour PIPO plot summarizes the 100 measurements, where SHG intensity (0=blue, maximum=red) is plotted as a function of the excitation angle θ (x-axis) and the analyzer angle κ (y-axis) (for angle definitions see Fig. 2.3-1). Generation of contour plots from PIPO data is outlined in Section 3.4.4. Fitting to the PIPO data (Fig. 4.3-2 (b), (c) and (c)), was performed using the equation derived for cubic NWs (Eq. 2.3-9),

as described in section 3.4.4, and revealed good fits, shown in Fig. 4.3-2 (e), (f) and (g), respectively. The fitting parameter δ was different for each NW ((a) δ=19±1°, (b) δ=-21±1°, (c) δ=-9±1°), which is consistent with the random way the NWs are deposited onto the sample, by allowing a drop containing NWs to dry. Different regions on each of the three NWs were investigated, and resulted in similar δ values for each NW, suggesting that these NWs did not twist on a large scale. The dark regions on the NW labeled "c" in Fig. 4.3-2 (a) could not be investigated due to insufficient signal, and are attributed to regions of increased disorder.

We have shown that small regions on individual zinc blende NWs can be measured using SHG microscopy to reveal their orientation on the glass within 1° fitting error. The analysis did not consider the size and shape of the NW because a previous theoretical study showed that in the forward scattering geometry used in our setup the SHG intensity is independent of the dimensions of the particle, and only depends on the crystallographic orientation and the polarization of the fundamental electric field (Dadap 2008). This presents a great opportunity to use SHG PIPO microscopy for quality control and uniformity investigations of NWs as well as for determining the axial rotational orientation angle for the deposited NW on the surface. SHG PIPO microscopy is further applied for investigations of wurtzite type ZnSe NWs.

4.3.4 PIPO microscopy of wurtzite NWs

Wurtzite NWs made of ZnSe were investigated with SHG PIPO microscopy. Several notable publications have previously investigated the hyperpolarizability properties of wurtzite semiconductor nanostructures. A study by Johnson, Yan *et al.* (2002) measured the hyperpolarizability of wurtzite ZnO NWs using a near field microscope by modulating the linear polarization of the excitation laser with respect to the NWs, determining d_{33}/d_{15}= 2.2 in magnitude for most NWs (80-100nm wide), with a wider (~125nm) NW having d_{33}/d_{15}= 4.2 (Johnson, Yan et al. 2002). Another interesting study found the hexagonal axis orientation of GaN NWs could be determined using measurements of the intensity of the generated SHG parallel and perpendicular to the NW (Long, Simpkins et al. 2007). A more recent study used a confocal SHG microscope in epi-detection mode for investigation of wurtzite GaAs nanoneedles, which are similar in size to typical NWs, by modulating the excitation polarization and measuring the polarization of SHG generated parallel and perpendicular to the NWs, revealing the magnitudes d_{33}/d_{15} = 2.2 and d_{31}/d_{15}=0.5 (Chen, Crankshaw et al. 2010). In another

interesting study the scattering pattern of SHG has been shown to be influenced by twinning in wurtzite ZnO NWs (Liu, Zhou et al. 2008).

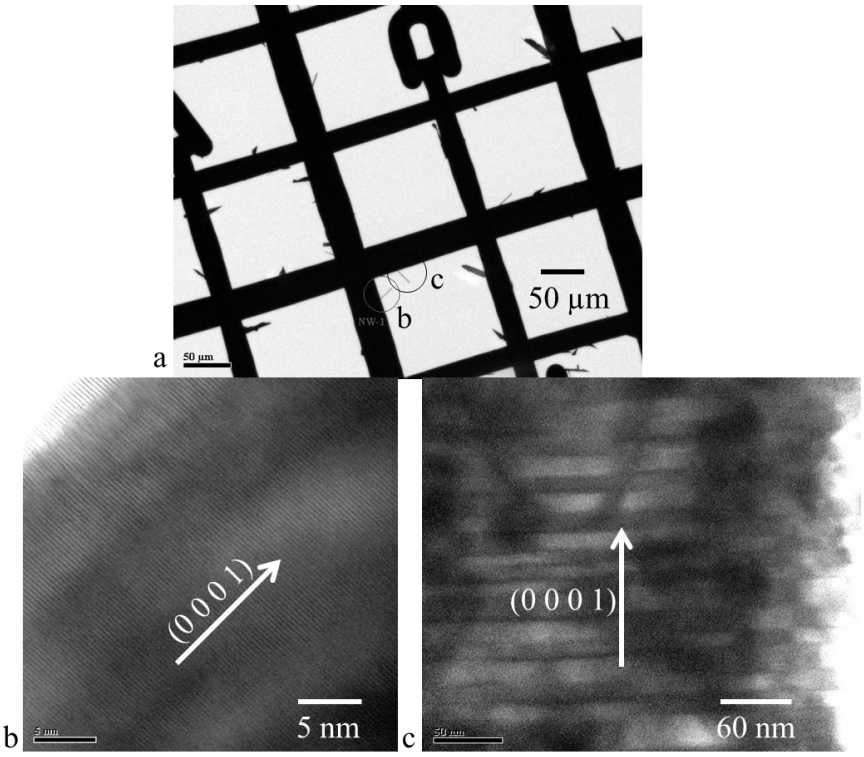

Fig. 4.3-3: HRTEM images of wurtzite NWs.

Panel (a) shows NWs on a gold grid, with circles indicating NW b and c, while (b) shows HRTEM images of a mostly pure wurtzite NW-b, (c) shows an HRTEM image of a periodically twinned NW-c. The scale bars are 50µm in (a), 5nm in (b) and 50nm in (c). Imaged by Ankur Saxena, Department of Electrical Engineering, University of Toronto.

High resolution transmission electron microscopy images of NWs were performed to determine the crystal structure of the individual NWs prior to scanning with SHG PIPO microscopy. Fig. 4.3-3 (a) shows a TEM image of a gold grid which had NWs deposited on it, and highlights two adjacent NWs, termed NW-b and NW-c which are further investigated. Detailed HRTEM imaging revealed that NW-b is single crystalline wurtzite, visualized in Fig. 4.3-3 (b). HRTEM of NW-c was also performed, revealing a periodically twinned NW, with periodicity of ~15nm, shown in Fig. 4.3-3 (c). Since the gold grid was marked it was possible to find the same sample region in the nonlinear optical microscope.

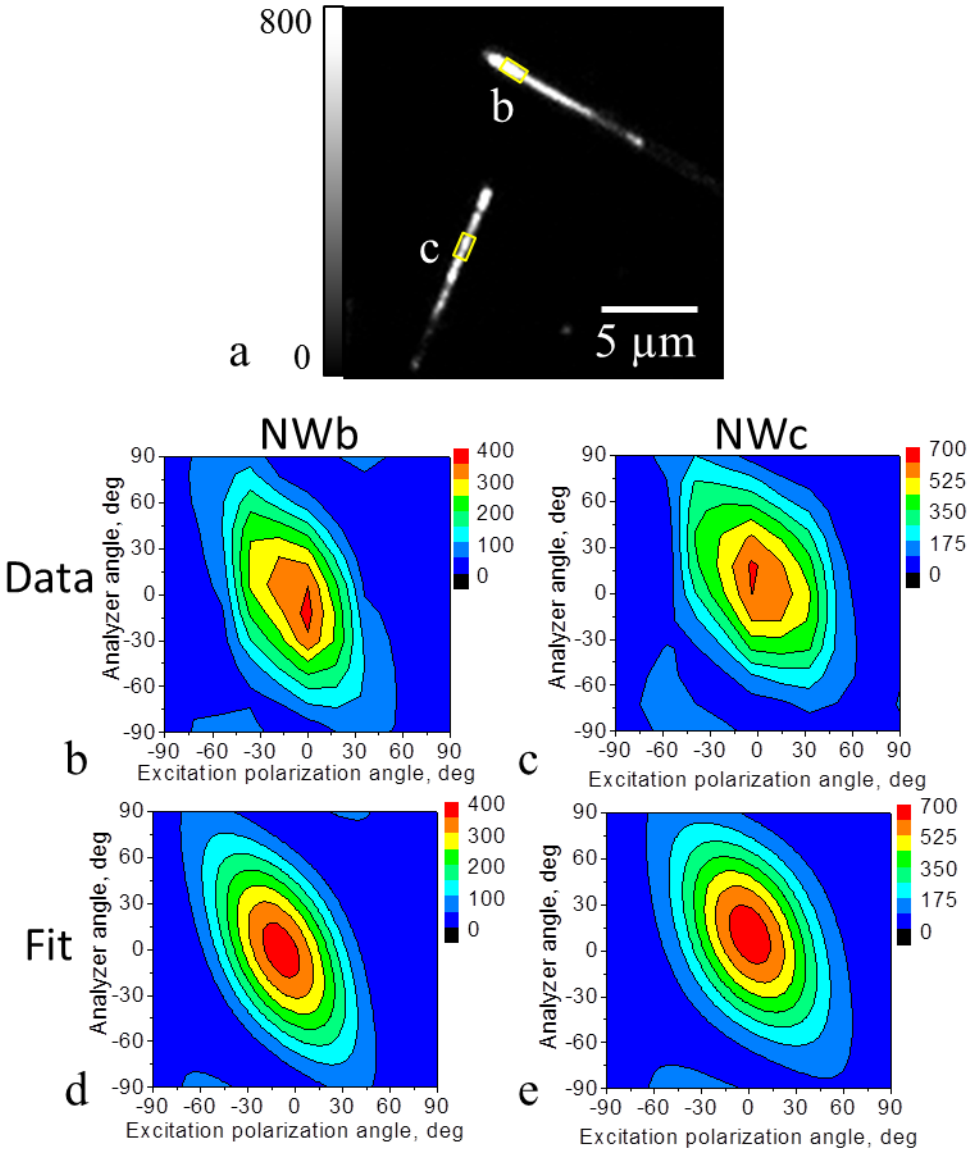

Fig. 4.3-4: PIPO SHG microscopy of wurtzite NWs.

SHG image (a) of wurtzite NW-b and NW-c from Fig. 4.3-3, showing two regions of interest that were analyzed to produce corresponding PIPO data contour plots (b,c). Fits were performed to the PIPO data with Eq. 2.4-16 assuming d_{33}/d_{15}=1 resulting in fit parameter d_{33}/d_{15}=-3.1±0.2 for (b), and d_{33}/d_{15}=-2.4±0.2 for (c). The corresponding contour plots of the fit data for (b) and (c) are shown in (d) and (e) respectively.

PIPO SHG microscopy was used to investigate wurtzite and periodically twinned NWs. An SHG image of NW-b and NW-c that were previously investigated with electron microscopy is shown in Fig. 4.3-4 (a). PIPO microscopy data was collected for the sample regions according to the procedure outlined in section 3.4.3, for the region b of NW-b and region c of NW-c indicated in Fig. 4.3-4 (a), and is shown summarized in the corresponding PIPO contour plots Fig. 4.3-4 (b) and (c). The contour plots of PIPO data from wurtzite and periodically twinned NWs Fig. 4.3-4 (b) and (c) appear symmetric about the diagonal axes, in contrast to PIPO data

from zinc blende NWs Fig. 4.3-2 for $\delta \neq 0$, in agreement with the theoretical PIPO analysis (see Fig. 3.4-9 and Fig. 3.4-6). Fitting to the PIPO data (Fig. 4.3-4 (b) and (c)), was performed using Eq. 2.4-16, as described in section 3.4.4. While the use of Eq. 2.4-16 (for hexagonal symmetry) is valid for the wurtzite NW, it is only partially valid for periodically twinned NWs since they have a severely reduced density of the NW regions containing hexagonal crystallinity, having hexagonal 'twin' planes every ~15 nm, and are therefore filled mostly (>90% volume) with the cubic crystal phase. Additionally, fitting was performed assuming $d_{31}/d_{15}=1$ since allowing this parameter to vary revealed very similar fits.

Fitting was performed with Eq. 2.4-16, and fit parameters are listed in Table 4.3-1. The fits revealed d_{33}/d_{15}=-3.1±0.3 for Fig. 4.3-4 (b) (fit shown in (d)), and d_{33}/d_{15}= -2.4±0.2 for (c) (fit shown in (e)), and had high goodness of fit parameters (see Table 4.3-1). Theoretical considerations of the hyperpolarizability tensor for a structure with cubic symmetry and growth direction along [1 1 1], reviewed in section 2.3.1, reveals that the corresponding hexagonal hyperpolarizability parameter yields d_{33}/d_{15} = -2 and d_{31}/d_{15} =1, shown in Eq. 2.3-2, and was first derived in by Robinson (1968) (Robinson 1968). The periodically twinned NW-c (Fig. 4.3-4 (a)) is composed of mostly zinc blende crystal phase mixed with periodic hexagonal defects, (see Fig. 4.2-3), and hence, it is sensible that this NW has a hexagonal hyperpolarizability fitting parameter d_{33}/d_{15} closer to -2 as compared with the purely wurtzite NW (NW-b in Fig. 4.3-4 (a)). There is a slight but significant deviation from d_{33}/d_{15}=-2, that is likely owing to the hexagonal phase, and requires explanation. The wurtzite NW-b had little or no cubic phase, and therefore, it is sensible that d_{33}/d_{15} deviated further from -2 than the periodically twinned NW. However the deviation also requires an explanation, since according to the theoretical crystallinity considerations, d_{33}/d_{15}=-2 is valid for any structure composed of cubic planes oriented along [1,1,1]. Although the literature on wurtzite ZnSe is limited, a classic study showed that the hexagonal hyperpolarizability ratio d_{33}/d_{15} is negative for bulk wurtzite ZnO (Miller and Nordland 1970) in agreement with our value. Furthermore, the hexagonal hyperpolarizability measurements in this study are similar to values obtained in recent studies of NWs for other nanostructures including ZnO NWs (Johnson, Yan et al. 2002) as well as for GaAs nanoneedles (Chen, Crankshaw et al. 2010).

NW		Cubic Model		Hexagonal Model		Hex Model with Bi	
		δ (°)	R^2	d_{33}/d_{15}	R^2	$\epsilon_\perp$	R^2
b	Pure Wurtzite	2 (±3)	0.7499	-3.1 (±0.3)	0.8509	5.2 (±0.6)	0.761
c	Periodically Twinned	0 (±2)	0.8874	-2.4 (±0.2)	0.9217	6.7 (±0.4)	0.887

Table 4.3-1: Fitting parameters for wurtzite NWs with cubic and hexagonal symmetry for Fig. 4.3-4.

The fits were performed on the NW regions shown in Fig. 4.3-4 (a). Fitting with the cubic model was performed with Eq. 2.3-9. Fitting with the hexagonal model was performed with Eq. 2.4-16, with the parameter d_{31}/d_{15}=1, and corresponds to Fig. 4.3-4 (d) and (e). Fitting with the hexagonal-birefringence model was performed assuming assuming the dielectric constant varies between parallel and perpendicular to the NW with Eq. 4.3-3, using the parameters $\epsilon_{//}$=6.6, d_{33}/d_{15}= -2 and d_{31}/d_{15}=1.

Fitting of the wurtzite and periodically twinned NWs NW-b and NW-c was also performed assuming cubic symmetry, Eq. 2.3-9, in order to further analyze the results. The fits revealed both NWs had δ=0 within error, which is sensible because hexagonal symmetric materials will always have δ=0 since the PIPO plots are symmetric (see Fig. 3.4-9), while in cubic symmetry NWs can have any δ rotation parameter between -30° and 30° depending on the particular angle each NW lands on the glass. Additionally the twinned NW has a higher goodness of fit parameter than the non-twinned NW, which indicates that the twinned NW has more cubic character.

It was demonstrated that PIPO microscopy can successfully be used to interrogate wurtzite and periodically twinned NWs. The hexagonal PIPO data fit parameter d_{33}/d_{15} can be used to differentiate between cubic, periodically twinned and non-twinned wurtzite NWs, giving SHG microscopy nanoscopic information about the lattice structure of NWs. In order to explain the discrepancy from the theoretical value of the hexagonal hyperpolarizability component ratio in wurtzite and periodically twinned NWs, we explore two phenomena which commonly occur in semiconductors; the first based on a different dielectric constant parallel and perpendicular to the NW owing to the anisotropy of hexagonal crystal structure in section 4.3.5, and another explanation, based on a changing internal electric field within the NW induced by a surface effect known as depolarization, in section 4.3.6.

4.3.5 Variation of the dielectric constant in a hexagonal NW

The difference in hexagonal hyperpolarizability values based on fitting PIPO data of twinned and purely wurtzite NWs is significantly different from d_{33}/d_{15} = -2 (see Section 4.3.4), and is here attributed to a difference in dielectric constant between the parallel and the

perpendicular orientations of the NW. While zinc blende NWs are isotropic in their linear optical properties, due to the cubic symmetry (Boyd 2008), a hexagonal NW has two optical axes, one parallel to the hexagonal axis (along the NW) and another perpendicular, and therefore can have different indices of refraction and different dielectric constants at the laser and second harmonic wavelengths. Therefore the assumption made in Eq. 2.4-15 that the material dielectric constant is uniform for different crystal directionalities does not always hold. The macroscopic electric field and the field that each atom experiences, known as the local Lorentz field, can in fact be different, and result in a field enhancement (Boyd 2008):

$$\mathbf{P}^{NLS} = \frac{\varepsilon + 2}{3}\mathbf{P}^{NL} \qquad 4.3\text{-}1$$

where $\boldsymbol{P}^{NLS}$ is the nonlinear source polarization due to the local field, $\boldsymbol{P}^{NL}$ is the usual nonlinear polarization, and ε is the relative high frequency dielectric constant of the material. Under the presumption that the relative dielectric constant along the z direction (ε_z) is different from the relative dielectric constant along the x axis (ε_x) the Eq. 2.4-15 can be rewritten:

$$\mathbf{P}_{SHG} \propto \begin{pmatrix} 2\varepsilon_x^{'} d_{15} E_x E_z \\ \varepsilon_z^{'}\left(d_{31}E_x^2 + d_{33}E_z^2\right) \end{pmatrix} \qquad 4.3\text{-}2$$

where $\varepsilon_i^{'} = \frac{(\varepsilon_i + 2)}{3}$. The derivation proceeds by calculation of the SHG intensity through Eq. 2.3-8 with the Jones matrix Eq. 2.3-7, resulting in an equation similar to Eq. 2.4-16:

$$I \propto d_{15} E^4 \left(\varepsilon_z^{'}\left(\frac{d_{33}}{d_{15}} \cos\kappa \cos^2\theta + \frac{d_{31}}{d_{15}} \cos\kappa \sin^2\theta \right) + \varepsilon_x^{'} \sin\kappa \sin 2\theta \right)^2 \qquad 4.3\text{-}3$$

This equation shows that the SHG intensity is influenced when the dielectric constants along different directions are unequal, which could occur in non-isotropic crystals such as wurtzite.

Fitting was performed on the PIPO data of Fig. 4.3-4 using Eq. 4.3-3 under the assumption that a Lorenz field exists, commonly performed in nonlinear optics (Boyd 2008). Fitting was performed with the additional parameters d_{33}/d_{15} = -2, d_{31}/d_{15} =1, and the relative high frequency dielectric constant was assigned parallel to the NWs using a literature value for bulk zinc blende ZnSe of 6.6 (Grigoriev and Meilikhov 1997). The PIPO data for wurtzite and

periodically twinned NWs of Fig. 4.3-4 reveals that the periodically twinned NW had a dielectric constant consistent with the assigned zinc blende value (6.7±0.4) which is sensible considering the twinned NW is mostly composed of a cubic phase, which by definition is isotropic and therefore should have a uniform dielectric constant. The fit of the wurtzite NW on the other hand revealed a dielectric constant significantly lower (5.2±0.6), which verifies the assumption that a lowered dielectric constant explains the apparent variation between the hexagonal hyperpolarizability ratios. The high frequency dielectric constant in wurtzite ZnSe crystals has not, to our knowledge, been previously measured, however a previous study found that in bulk wutzite ZnO crystals a variation between high frequency dielectric constants occurred between light parallel and perpendicular directions to the wurtzite axis (Ashkenov, Mbenkum et al. 2003), although with less relative amplitude compared to the current measurement. The nanoscale dimension of the NWs has until now, not been considered in the analysis, and could affect the measurement as well, resulting in deviation of the relative dielectric constant. Therefore it is investigated in the following section.

4.3.6 NW SHG from depolarization of the surface electric field

The surface effect of reduced polarization due to the transverse electric field inside a NW, or depolarization, induces another factor for the variation of the hyperpolarizability ratio d_{33}/d_{15} from the theoretical value of -2 observed in NWs. According to Eq. 2.1-1 the generation of the n'th harmonic is modulated by the magnitude of the electric field as well as the magnitude of the nonlinearity tensor, $\chi^{(n)}$. The SHG intensity Eq. 2.1-12 shows that in semiconductors such as ZnSe, which typically have $\varepsilon_r > 3$ when surrounded by air, a huge polarization anisotropy is expected since the factor before the second term is <0.03.

Evidence for SHG enhancement from electric field depolarization is presented by polarization anisotropy experiments. Zinc blende ZnSe NW were coated with SiO_2 and Si_3N_4 and SHG anisotropy was measured and compared to the uncoated samples. The angular dependence of the SHG efficiency I_{SHG} was measured by rotating the sample with respect to the excitation beam polarization and detecting the total SHG intensity at each pixel (without an analyzer). Since SiO_2 and Si_3N_4 have significantly different dielectric constants from one another, and from air, a set of ZnSe NWs with three different relative dielectric constant mismatches could be investigated to reveal the role of this important parameter in anisotropy of SHG.

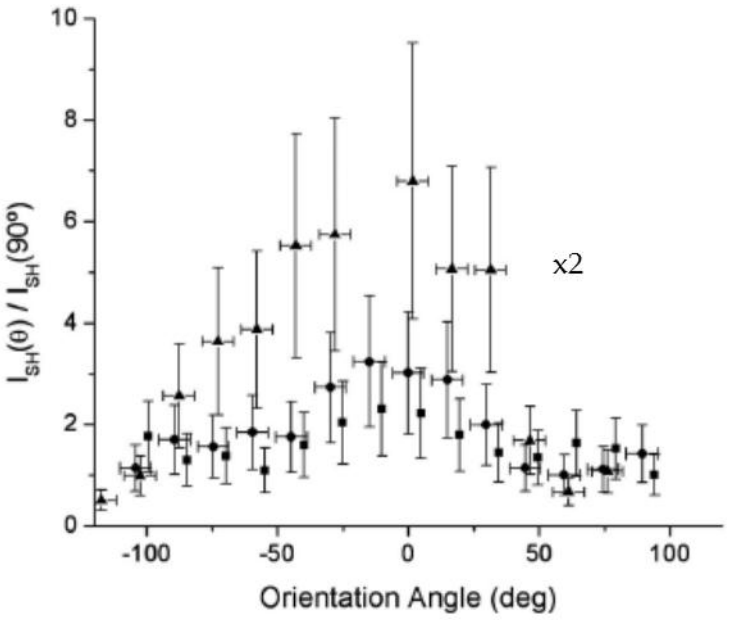

Fig. 4.3-5: NW SHG dependence on relative dielectric constant.
The dependence of linear polarization orientation with respect to the NW on the SHG intensity for an uncoated NW (triangles), a NW coated with SiO_2 (circles), and a NW coated with Si_3N_4 (squares). The data points representing the uncoated NW were compressed two times in the vertical direction. Figure reprinted with permission from (Spencer, Cisek et al. 2009), Copyright 2009, American Institute of Physics.

The experiment verified that the SHG anisotropy is related to the dielectric constant mismatch between the NW and its environment in agreement with our model, and the resulting Eq. 2.1-12, which shows a strong dependency on the dielectric mismatch between the NW and its environment characterizing this mismatch.

Fig. 4.3-5 illustrates the dependence of the SHG signal on the angle θ between the laser electric field and the NW axis (see Fig. 2.1-2 (c)) in NWs with different dielectric environments. The very large vertical error bars in the figure are due to drastic variations in the SHG signal amplitude of the different NWs on the same coverslip. For NWs in air, SiO_2, and Si_3N_4, the relative dielectric constants are ε_r=6.6±0.6, ε_r=3.1±0.3, and ε_r=1.6±0.2, respectively, where the uncertainty is related to different values of ε_r in ZnSe reported by different authors (Grigoriev and Meilikhov 1997). Therefore while the angular dependence of SHG for the samples in air has an amplitude several times larger than for the dielectric-coated samples, fitting to the data could not be performed since a large deviation from theory occurs, and is ascribed to irregularity (i.e. bending or corrugation) of the NW surface, which is discussed in the following section.

4.3.7 NW corrugation and SHG

The corrugation, or surface irregularity, of a dielectric cylinder can be taken into account by replacement θ by $\theta+\delta\theta$ in Eq. 2.1-12 where $\delta\theta$ is a small angle with Gaussian properties, and expanding the sine and cosine we obtain

$$I_{SHG}=E_0^4\left(\left(\cos\theta\cos\delta\theta-\sin\theta\sin\delta\theta\right)^4+k\left(\sin\theta\cos\delta\theta+\cos\theta\sin\delta\theta\right)^4\right) \qquad 4.3\text{-}4$$

where $k=10.3\left(\varepsilon_r-1\right)^2\Big/\left(\varepsilon_r+1\right)^4\left(1+\sqrt{\varepsilon_r}\right)^2$. Then since the angles $\delta\theta$ are small we can average over $\delta\theta$ angles to find the intensity ratio at parallel versus perpendicular polarization to the cylinder to be

$$\frac{I_{SHG}(0°)}{I_{SHG}(90°)}=\frac{1}{\dfrac{10.3\left(\varepsilon_r-1\right)^2}{\left(\varepsilon_r+1\right)^4\left(1+\sqrt{\varepsilon_r}\right)^2}+\left(\overline{\left(\delta\theta\right)^2}\right)^2} \qquad 4.3\text{-}5$$

Eq. 4.3-5 shows that corrugation of the dielectric cylinder reduces the polarization anisotropy of SHG due to surface effect depolarization (Spencer, Cisek et al. 2009; Cisek, Barzda et al. 2010). It is important to point out that the corrugation parameter $\delta\theta$ was introduced phenomenologically to understand how a variation in NW structure changes the SHG polarization anisotropy, and should not be considered an exact solution.

Corrugation, the bending or roughness of the NW surface can lead to several effects which reduce the ratio between SHG intensity obtained at parallel versus perpendicular excitation orientations of the laser with respect to the NW axis. It was found that as the corrugation parameter increased the SHG anisotropy decreased as the square of the corrugation in Eq. 4.3-5. In this context we investigated the results in Fig. 4.3-5 with an additional assumption; the corrugation varies between NWs.

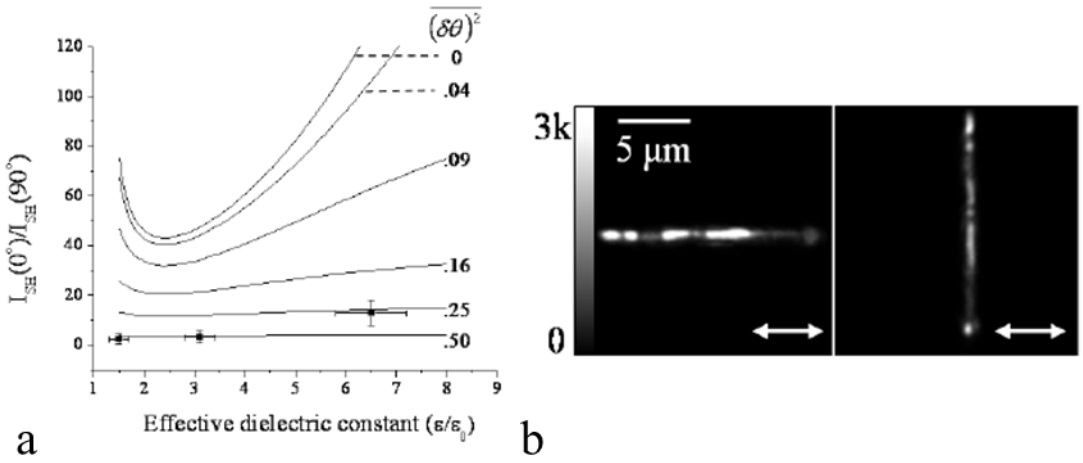

Fig. 4.3-6: Corrugation effects on SHG intensity.

The SHG intensity ratio of laser polarization parallel versus perpendicular to the NW axis (y-axis) dependence on the relative dielectric constant between the NW and its environment (x-axis) is shown in (a) with three data points; the uncoated NW, and NWs coated with SiO_2 and Si_3N_4. The solid lines represent theoretical curves obtained from Eq. 4.3-5 with corrugation value indicated near each curve. Panel (b) shows SHG images of a typical NW coated with SiO_2 at two orientations with respect to the linearly polarized excitation indicated in the bottom right. Figures reprinted with permission (Cisek, Barzda et al. 2010) © 2010 IEEE.

Fig. 4.3-6 shows three points of SHG intensity ratios $I_{SHG}(0)/I_{SHG}(90°)$ plotted as a function of the relative dielectric constant between the NW and its coating. The theoretical $I_{SHG}(0)/I_{SHG}(90°)$ ratio is also plotted on this graph for different values of the corrugation $\overline{(\delta\theta)^2}$ indicated beside each curve. The graph reveals that all the studied NWs had corrugation, and that the uncoated NW had a corrugation of about $\overline{(\delta\theta)^2} = 0.25$, while corrugation values of $\overline{(\delta\theta)^2} = 0.5$ were required for NWs coated in SiO_2 and Si_3N_4. The corrugation was expected to be larger in the coated samples since the coating procedure included a surface etching step (see section 4.3.2). Visual evidence of increased corrugation is presented in the SHG images when comparing uncoated NWs in Fig. 4.3-2 (a) with NWs coated with SiO_2 in Fig. 4.3-6 (b), showing the coated NWs have increased SHG heterogeneity. The experiment reveals that the dependency of SHG on polarization of the excitation depends on the geometrical properties of the surface and bending of the NW.

In this section the depolarization effect of the electric field due to the NW was used to explain SHG anisotropy from NWs. The polarization SHG experiment of NWs coated in different dielectrics revealed there is definitely a relationship between the relative dielectric constant and the SHG polarization anisotropy. Since optical effects in solids are caused by

electron transitions induced by the internal optical field *E*, it is evident that the polarization dependences of nonlinear optical effects are determined by the angle dependence between the light electric field *E* and the NW axis, having a relative amplitude which increases with ε_r. It is notable that the formulae we used to obtain Eq. 2.1-12 remain valid as long as the wavelength of light λ exceeds the NW radius α, which is definitely the case in our experiments, where the NWs are 80-400nm in diameter. In the aforementioned explanation quantitative fits could not be made, and the variation in anisotropy was attributed to corrugation of the NW. Therefore the deviation from the hexagonal SHG parameter $d_{33}/d_{15}=-2$ obtained from PIPO fits of wurtzite NWs could be explained by the depolarization of the electric field with accompanying corrugation.

Two explanations are discussed below to understand why the experimentally observed deviation from $d_{33}/d_{15}=-2$ occurs in PIPO data of wurtzite NWs, the variation in dielectric constant anisotropy due to the hexagonal crystal lattice, and the depolarization of the electric field due to the NW surface. In section 4.3.5 it was assumed that the variation of the dielectric constant due to the hexagonal crystal explains the deviation of the hyperpolarizability ratio in wurtzite, and the resulting fit showed that the relative high-frequency dielectric constant ε_r changed from 6.4 to 5.2 between parallel and perpendicular orientation to the crystal axis. The magnitude of the variation was previously measured in bulk ZnSe, revealing a much lower change, of $\varepsilon_r \sim 0.1$ (Ashkenov, Mbenkum et al. 2003), therefore, it points to depolarization of the NW to play a role. If depolarization is attributed a large role in wurtzite NWs however, it should also play an equal role in zinc blende NWs, since the effect is not dependent on the crystal lattice but rather on the nanostructure width being less than the wavelength of light. Since no correction was required for PIPO analysis of zinc blende NWs, see section 4.3.3, we attribute the deviation of d_{33}/d_{15} from -2 in wurtzite NWs mostly to variation in dielectric constant due to crystal lattice birefringence, which may be enhanced in the nanostructure as compared with the bulk, while the NW depolarization effect likely plays a smaller role. The differentiation of these two effects requires further investigation.

4.4 Main Conclusions

PIPO SHG microscopy was demonstrated on ZnSe NWs revealing variations of optoelectronic properties due to the crystal lattice structure and structural defects in individual NWs. By fitting of the PIPO data from zinc blende NWs the rotational orientation of the cubic lattice around the

axis of the NW could be determined. This determination could be applied for quality control of NW devices that require good alignment. Fitting SHG PIPO data from wurtzite and periodically twinned as well as zinc blende NWs allowed discrimination between the morphologies. The application of this discrimination method includes quality control for manufacturing of sensitive optoelectronic devices that contain SHG active crystalline semiconductors and require uniform crystalline morphologies.

A variation of SHG PIPO data from wurtzite and periodically twinned NWs was experimentally observed, and are influenced by two phenomena. The variation of the dielectric constant parallel versus perpendicular to the NW has the largest magnitude in wurtzite and a decreased magnitude in periodically twinned NWs. This occurs because twinned NWs have segments of cubic and hexagonal lattice, while pure wurtzite has the largest birefringence and zinc blende structure has an isotropic dielectric constant. Therefore, dielectric constant variation allowed samples with periodic twinning to be distinguished from purely wurtzite nanocrystals. The second phenomena contributing to the variation of the SHG PIPO data from the theoretical ratio d_{33}/d_{15}=-2 in wurtzite NWs was derived based on the depolarization phenomenon occurring due to surface effects in a dielectric cylinder. The equations governing SHG anisotropy due to depolarization were developed showing a dependency on the relative dielectric constant between the NW and its environment, and experimental evidence of SHG anisotropy at different relative dielectric constants was presented to prove the theory. The variation of the SHG anisotropy due to different environmental media in the experiment could not be quantitatively modeled however, and the variation was explained by differences of the NW axis corrugation in samples with different dielectric environment. Of the two phenomena, the variation of dielectric constant parallel and perpendicular to the NW was attributed to be the dominant phenomenon, while depolarization and corrugation played smaller but not insignificant roles. Further investigations would be required to quantify the relative magnitude of the two effects, for example PIPO microscopy could be performed on uniform NWs with various amounts of twinning, and coated with different dielectrics.

Nondestructive nonlinear optical measurements of NWs using PIPO SHG microscopy revealed structural information about individual NWs, which is determined by the crystal lattice, twinning, corrugation, dielectric properties of the environment, as well as, on rotational orientation with respect to the optical axis. Nonlinear optical microscopy is remarkably powerful

considering it can obtain structural information of micro sized structures quantitatively with relative speed and ease of measurement. The PIPO SHG technique could also be applied to study biological structures that produce SHG in the microscope, such as muscle, tendon, retina and starch. In the next chapter PIPO SHG microscopy will be used to investigate the hyperpolarizability of starch granules.

Chapter 5
Nonlinear Optical Microscopy of Starch Granules

5.1 Introduction to Starch Granules

Starch granules consist of highly ordered bio-polymers arranged in symmetric configurations, i.e. biocrystals, which have high nonlinear optical susceptibilities warranting sufficiently intense generation of harmonic signals that can be used for detailed quantifiable structural analysis using nonlinear optical microscopy. Nonlinear optical microscopic signals, especially SHG, are ideally suited for probing the structure of starch granules. SHG can be used as a contrast mechanism to visualize the internal structure of individual starch granules *in vivo* without special alteration of the sample or use of dyes or additives. Additionally, the polarization dependency of SHG can be investigated to reveal variations in the crystalline organization (sections 2.3 and 2.4) of the starch material, and hence can be used to reveal structural variations on a molecular scale. SHG microscopy measurements of starch granules could be used for industrial applications. Biofuels production could be optimized by monitoring the enzyme induced breakdown of starch granules during fermentation, while food sciences could benefit by monitoring decomposition rates inside individual starch granules of different plant species in order to find plant varieties with longest lasting granules to increase the duration of food storage and shelf life. Biomaterials production such as starch based biodegradable containers could be improved to make them stronger and longer lasting, using SHG for quality control by selecting granules with uniform crystalline characteristics. Additionally, starch granule types A and B, which naturally occur mixed in oat, barley and wheat, (Buleon, Colonna et al. 1998) for example, could be separated by SHG microscopy for benefit in various applications.

SHG microscopy of starch granules is a relatively new field that began in the year 2000 (Mizutani, Sonoda et al. 2000), with only a few quantitative investigations appearing in the literature. The study of the polarization modulated SHG intensity in wheat starches, measuring the hyperpolarizability tensor elements ratio values was performed for the first time in 2010 (Psilodimitrakopoulos, Amat-Roldan et al. 2010). Another quantitative publication from the same group showed how SHG intensity and polarization dependency varies on the angle between SHG active structures and the orientation of the propagation of the imaging laser (Psilodimitrakopoulos, Amat-Roldan et al. 2011). A third notable publication used polarization

modulated SHG to calculate the hyperpolarizability tensor elements of potato starch granules (Zhuo, Liao et al. 2010). The measured hyperpolarizability of wheat and potato granules by the two groups have different values, although both groups attribute the origin of the SHG to a single dominant hyperpolarizability along the helical pitch of the amylose helix. Therefore, further investigations are needed to elucidate the hyperpolarizability differences from different starch granules.

The focus of this investigation is to characterize the three-dimensional nonlinear properties of starch granules, and to investigate the origin of SHG. Additionally, variation of the hyperpolarizability between different types of starch will be elucidated based on hyperpolarizability measurements combined with *ab initio* calculations of hyperpolarizabilities of the starch constituent crystals, amylose A and B. So far published studies have not incorporated measurements of the polarization of the outgoing SHG, and instead relied on global fitting of many measurements of polarization dependent SHG intensity throughout starch images in order to establish fitting parameters with lowered uncertainties. In this study, the high precision albeit more tedious task of measuring both input as well as output polarization parameters in SHG microscopy was performed, thereby gaining more information for each small area of an individual starch granule. The PIPO method enables detailed fitting, and deduction of more accurate hyperpolarizability tensor ratio values for different regions in starch granules. Additionally, in some cases the technique allows determination of the birefringence of starch granules.

This chapter contains a detailed study of starch granules using multicontrast SHG and THG nonlinear optical microscopy. Section 5.2 reviews relevant details about the ultrastructure of starch granules. Section 5.3 describes a detailed qualitative investigation of starch granules by SHG and THG imaging nonlinear microscopy, as well as a quantitative investigation using polarization-in-polarization-out SHG microscopy. Section 5.4 describes *ab initio* calculations performed on amylose crystal residues in order to understand the molecular origin of the intense and directional SHG observed experimentally in starches. Section 5.5 gives a summary of the findings and conclusions of the chapter.

5.2 Starch Granule Structure

Starch granules are the energy storage sites inside plant cells, some algae, and chloroplasts of green plants, and have a very interesting radial biocrystalline structure that produces SHG and THG efficiently in a nonlinear optical microscope. Starch granules are an ideal model system of biocrystals to study, because they exist in several crystalline types in nature, they are extremely abundant and easy to extract fresh while also available dry, very easy to work with, resistant to degradation, and well characterized using popular analytical techniques (BeMiller and Whistler 2009). Additionally, the radial arrangement of starch granules is very convenient for polarization studies. This section will discuss the details of starch granule structure from the nano- to micro-length scales, and will attempt to give a basis for the structural studies of starches in sections 5.3 and 5.4.

5.2.1 Introduction to starch granule structure and function

Starch granules are the chemical energy storage structures in many types of plants and algae. Starch granules store glucose in polymer form, and their ultrastructure has been critically studied since they are a very important commodity product, as well as being incredibly abundant in human diet, mostly from starchy vegetables such as potato, maize, wheat, rice, as well as from fruits such as banana and apple, (see for example articles published in the Journal Starch, or, the detailed text (BeMiller and Whistler 2009)). Starch granules have a very interesting crystalline ultrastructure at several length scales. On the largest scale, typical starch granules are spherical or egg-shaped structures between 1 and 100 μm in diameter, although in general granules from different botanical sources can take on many shapes including spherical, disk, oval and others (Jane 2006). Fig. 5.2-1 panel (a) shows a typical brightfield microscopy image of a thin slice of fresh potato where starch granules are clearly visible. On the molecular scale, starch granules are a combination of glucose Fig. 5.2-1 (b) polymers in several different polymorphic states (Fig. 5.2-1 (c) and (d)) with crystalline or amorphous configurations forming double helical structures ~1 nm in diameter. On an intermediate scale, the crystalline regions form lamella of ~10 nm (Fig. 5.2-1 (e)), which in turn combine to form larger semi-crystalline regions 20-200 nm, which can be visualized with optical microscopy as starch growth rings (grey stripes in Fig. 5.2-1 (f)).

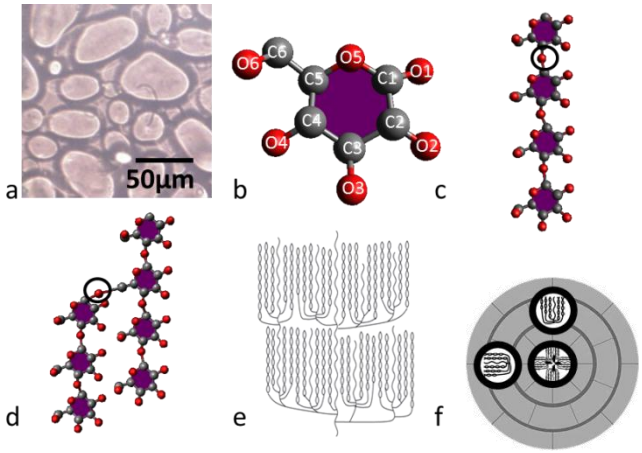

Fig. 5.2-1: Ultrastructure of starch granules.

Wide field brightfield microscopy image (a) a slice of potato with starch granules visible, (b) shows an amylose residue, (c) shows amylose residues bonded at ∝1-4 (circle) forming the starch polymer amylose, (d) shows the structure of amylopectin as two amylose chains branched at ∝1-6 (circle), (e) shows starch lamella, consisting of alternating layers of crystalline double helical amylopectin, and an amorphous branching layer, and (f) shows the macro-arrangement of starch granules depicting starch growth rings and radially oriented starch polymers in the circles, with the middle circle depicting the centrosymmetric starch hilum. Note that in (b-d) the amylose residue structure is presented flattened to clearly visualize all atoms of the molecule.

5.2.2 Molecular ultrastructure of starch granules

Two polymers of glucose form the starch molecular ultrastructure. Fig. 5.2-1 (b) shows a starch monomer; an α-D-glucose residue from amylose B (Imberty and Perez 1988), which is in a chair conformation, however, unlike the standard structure, the O5 is in front of the molecular plane, the C3 in back of the plane, O2 O3 and O4 are mostly parallel with the molecular plane, while O1 is directed backwards from the plane. In starch granules, glucose residues are in the form of branched polymers known as amylose and amylopectin. Depicted in Fig. 5.2-1 (c) is the polymer amylose, a linear polymer of α-1,-D-glucose (connecting C1 to C4 via O1/O4, see circle in (c)). The structure of amylopectin, shown in (d), consists of a branched glucose polymer of amylose strands bonded at α-1,6 (connecting C1 to C6 via O1/O6 indicated by circle). Although pure amylose is considered linear in chemical literature, starch literature uses the term a bit differently; amylose are molecules which are mostly linear but can have a little branching which is random, this form occurs inside starch granules, while the term amylopectin is reserved for amylose which is branched at regular intervals allowing neighbouring strands to form double helices (Jane 2006).

On a macromolecular scale, starch granules have a lamellar architecture, with two types of alternating layers visualized in Fig. 5.2-1 (e). Evidence for the lamella was first obtained from

small angle X-Ray diffraction on starch powders, which gives ~10 nm repeating unit (Daniels and Donald 2003). Depicted in Fig. 5.2-1 (e) are two lamella, which contain ~9 nm thick regions of parallel adjacent strands of amylopectin, which form double helices arranged regularly forming a biocrystalline layer, and a separation region of ~1 nm thick that contains the amylopectin specific branches shown circled in (d) (Yamaguchi, Kainuma et al. 1979; Copeland, Blazek et al. 2009). The growth of starch granules is complex and occurs on the granule surface in three enzyme mediated steps: (i) elongation of amylose at the surface until critical length is reached by starch synthases, (ii) creation of a branching region with starch branching enzymes and (iii) trimming and evening of the branches with starch debranching enzymes (Mouille, Maddelein et al. 1996; Buleon, Colonna et al. 1998). Therefore, the state of the surface of a starch granule is dependent on the growth cycle stage.

5.2.3 Macroscale starch granule structure

Starch granules have a very interesting macroscale structure consisting of multiple concentric layers of so called growth rings of increasing diameter, which extend from the hilum, the center of nucleation of a starch granule, outwards towards the surface of the granules. Starch granules have many macroscale characteristics, several of which are depicted in Fig. 5.2-1 (f): (i) the alternating pattern of crystalline and amorphous rings known as growth rings, (ii) the starch hilum in the center, as well as (iii) the radial architecture of amylopectin regions in the starch granules, depicted by the three circles.

Starch growth rings have been observed for more than 150 years (for classic review see (Badenhuizen 1956)), and they are particularly interesting since two different basic structural descriptions have prevailed for over 50 years, the continuous and the blocklet models, and the topic is still debated. While little is known about the amorphous growth rings (thin rings in Fig. 5.2-1 (f)), they preferentially succumb to linterization (acid treatment), which has allowed scientists to observe and investigate the semi-crystalline regions (thick rings in Fig. 5.2-1 (f)). The semi-crystalline rings, (thick regions in Fig. 5.2-1 (f)) have sizes from ~100 - 400 nm (Yamaguchi, Kainuma et al. 1979), and their ultrastructure continues to be hotly debated. These shells are highly optically active, giving intense birefringence in an optical microscope, already known in the mid-19th century (Carpenter and Smith 1856; Hogg 1867), and good X-ray diffraction patterns, observed starting from the 1930s (see (Badenhuizen 1956) and references

therein). Several theories exist on the structure of the semi-crystalline growth rings, the blocklet theory, the liquid crystal theory as well as a super-helical aggregate theory.

The blocklet theory, which was popular before 1960 (Badenhuizen 1936; Badenhuizen 1956), as hypothesized by Karl Wilhelm von Nägeli (Wilkie 1960), states that the semi-crystalline growth rings are composed of individual spherical or egg-shaped blocklets 50-400 nm in diameter. Upon the revival of the theory in the 80s and 90s, the blocklet theory was improved to state that blocklets were composed of several (2-4) side-chain clusters (bundles of 5-20 helices shown in Fig. 5.2-1 (e)), sitting in amorphous material (Gallant, Bouchet et al. 1997). The abandonment of the blocklet theory from around 1960 to 1980 occurred because it was believed the chemical and physical treatments that were performed in order to visualize blocklets, including, hot water treatments, sodium hydroxide treatments, and chromic acid treatments, were artificially creating regions in the granule that had more or less susceptibility to swelling. Hence when the treated granules would be placed in water, the differential swelling would cause cracks, enabling the visualization of so called blocklets (Badenhuizen 1956). The idea returned with the advancement of modern microscopy (Zobel 1988; Gallant, Bouchet et al. 1997). The blocklet model has been popularized by direct observations of large (>20 nm) crystalline spheroids in electron microscopy (Gallant, Bouchet et al. 1992), as well as by atomic force microscopy (AFM) in maize (Baker, Miles et al. 2001), pea (Ridout, Parker et al. 2003) and potato (Szymonska and Krok 2003). Indeed the blocklet model is once again quite popular (Tang, Mitsunaga et al. 2006), and new evidence still coming, such as from the latest observations using ultra small-angle X-ray diffraction, which found large structures in potato consistent with the blocklet model (Dündar, Turan et al. 2009).

Another theory of the macro-scale organization of starch granules is the side-chain liquid crystalline polymer (SCLCP) model (Waigh, Hopkinson et al. 1997). Side by side collections of amylopectin double helix bundles, which have lamella seen in Fig. 5.2-1 (d), are treated as single liquid crystals connected by flexible connectors, having a flexible backbone (Waigh, Kato et al. 2000). Interestingly, this model has allowed for some quantitative modeling of the distribution of orientations of crystals within the structure (Daniels and Donald 2003).

Another model exists due to Oostergetel and Vanbruggen (Oostergetel and Vanbruggen 1993) who performed a classic experiment on starch using electron diffraction. This group

observed large helical macroaggregates, with a 10 nm pitch (which are the lamella) and with a width of 20nm. In this theory the super-helices have a pore of ~8nm allowing water to pass. The main differences between this theory and the blocklet model are the large scale helicity and the pore.

The optical properties of starch granules have fascinated scientists for over a century. While starch granules do not have absorption bands in the visible spectrum, as shown by the spectrum of starch (Sigma) in Fig. 5.2-2, they have a radial architecture of amylopectin, which is thought to cause the optical effect of the Maltese cross when viewed in a wide field polarization microscope (See Fig. 5.3-4 (c)). Since nonlinear optical imaging of starch granules depicts macroscale images, it is vital to understand the radial arrangement of the amylopectin. The circles in Fig. 5.2-1 (f) depict single amylopectin side-chain clusters from three different regions of an ideal radially symmetric starch granule: The top circle depicts that amylopectin strands are oriented vertically in the region above the hilum while the left circle depicts the amylopectin strands are oriented horizontally. The center circle shows the radially arranged hilum of a starch granule, which has amylopectin fibres growing radially outwards in all three dimensions, having complete central symmetry around the hilum.

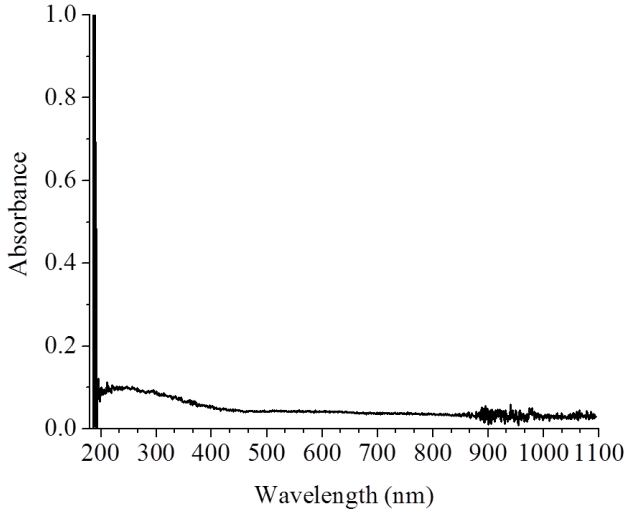

Fig. 5.2-2: The absorption spectrum of starch B powder in distilled water.

The UV–vis spectrum was obtained on an OLIS-14 (upgraded Cary-14) spectrophotometer using a 1 cm path-length SUPRASIL QS-110 quartz cuvette with OLIS Spectral Works software version 4.3 with no digital filtering, and was performed by Danielle Tokarz. The spectrum was subtracted from a baseline scanned with identical settings using the same quartz cuvette filled with distilled water. Absorbance has no units and is defined in the standard way.

5.2.4 The crystallinity of starch granules

The biocrystalline regions of starch amylopectin lamella, containing parallel double helices, visualized in Fig. 5.2-1 (d), have several interesting possible molecular arrangements. Crystallography studies of many different species of starch granules investigated thus far conform to 3 crystal polymorphs, denoted as starch A, B and C. Starch type A is mostly found in cereals including corn, type B is mostly found in tubers such as potato, while type C is mostly found in legumes such as pea and consist of a combination of polymorphisms A and B (Buleon, Gerard et al. 1998).

Scientists first recorded X-ray diffraction patterns from starch powders to identify and differentiate the two crystal types (Alsberg 1938), however these diagrams were not sufficient for 3D modelling because starch granules are not uniform crystals. In the 1950s, scientists began to agree that pure (linear) amylose can crystallize in both A and B polymorphic forms, yielding X-ray diagrams that were identical to the corresponding diffraction diagrams of A and B starches (Wu and Sarko 1978; Chen, Wu et al. 1989). These amylose crystals were subsequently used to infer the crystal structures of starches A and B by combining density data with fibre X-ray diagrams to produce the first full 3D starch crystal models (Wu and Sarko 1978; Wu and Sarko 1978). These models were subsequently refined (Imberty, Chanzy et al. 1988; Imberty and Perez 1988). Recently the structure of amylose A was further refined with X-ray microdiffraction using a synchrotron radiation source with a 10 μm beam (Popov, Buleon et al. 2009). These crystallography studies reveal structural differences between starches A and B.

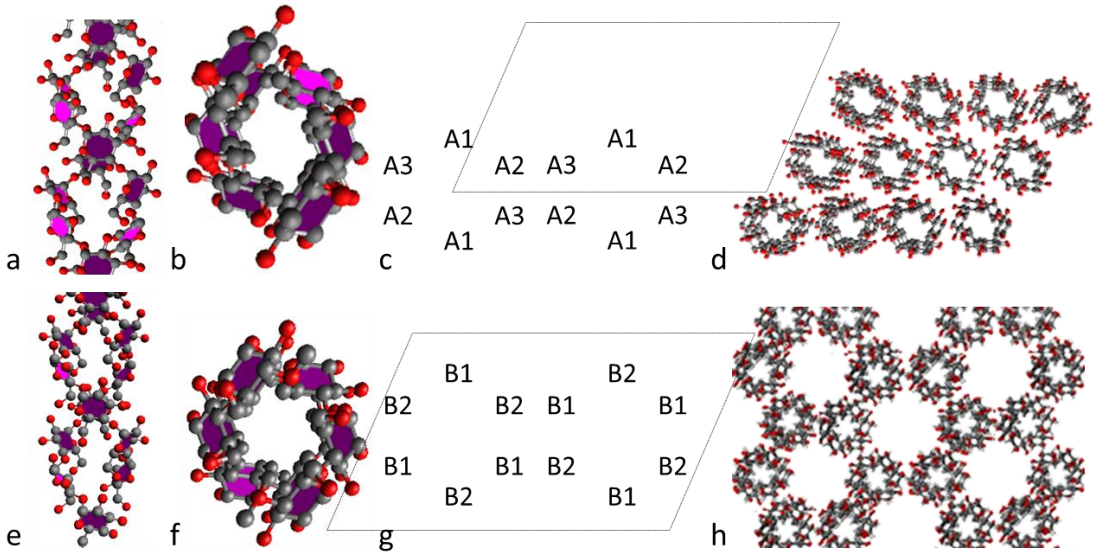

Fig. 5.2-3: The molecular arrangement of glucose residues in amylose A and B.

Amylose A (a-d) and B (e-h) crystals with helices respectively shown from the side view (a,e) look similar, but a difference is observed from the top view (b,f). Amylose A crystal symmetry is illustrated explicitly in (c) showing three unique glucose residues, A1 A2 and A3, and their arrangement in a monoclinic C_2 symmetry in the unit cell, while the ball and stick model showing the crystal arrangement is shown in (d). The hexagonal unit cell of amylose B is explicitly shown in (g), including the two unique glucose residues B1 and B2, where each helix has a C_3 symmetry around the helical axis, and the unit cell has a C_2 symmetry about the center. The ball and stick model of the amylose B crystal arrangement, showing the large open water channels, is shown in (h). Hydrogen atoms have been omitted from these images.

Amylose A and B crystals are both composed of parallel right-handed double helical strands (Fig. 5.2-3 (a) and (e), respectively), however they have different water content and crystal packing. The amylose A asymmetric unit consists of a maltotriose containing three unique glucose monomers, (depicted A1, A2 and A3 in Fig. 5.2-3 (c)), having monoclinic C_2 symmetry about the helical axis, which can also be visualized from the top view of a single starch A helix in Fig. 5.2-3 (b). The amylose A double helices are tightly packed in the unit cell with a B_2 space group, as visualized in Fig. 5.2-3 (c), and have 8 water molecules per unit cell (Imberty, Chanzy et al. 1988; Popov, Buleon et al. 2009). Amylose B on the other hand has a maltose asymmetric unit with two unique glucose molecules depicted B1 and B2 in Fig. 5.2-3 (g), with each helix having C_3 symmetry about its axis, while the crystal unit cell has C_2 symmetry about the center, giving an overall C_6 hexagonal crystal symmetry, which can be visualized as a symmetric helix from the top view in Fig. 5.2-3 (f) and via the 10 unit cells in Fig. 5.2-3 (h). The hexagonal representation has 36 water molecules per unit cell, most of which occupy the large open channels of the hexagonal crystal lattice (Imberty and Perez 1988; Takahashi, Kumano et al. 2004).

Water plays a very important role in the architecture of starch crystals. When starches have their water removed the crystalline architecture is lost (Imberty, Buleon et al. 1991; BeMiller and Whistler 2009). Completely anhydrous amylose type B for example gives no X-ray powder diffraction diagrams, requiring a minimum of 8% hydration to first observe the diffraction peaks (Imberty and Perez 1988). The positions and intensities of the diffraction peaks in amylose B vary with increasing hydration until 25-30%, afterwards the variations become small (Imberty and Perez 1988). This is supported by physical drying as well as crystallography studies which confirmed starch B crystals are 27% water by weight (Alsberg 1938; Imberty and Perez 1988). In contrast to this water filled crystal, the other polymorph, amylose A, has only 7% water content by weight (Popov, Buleon et al. 2009).

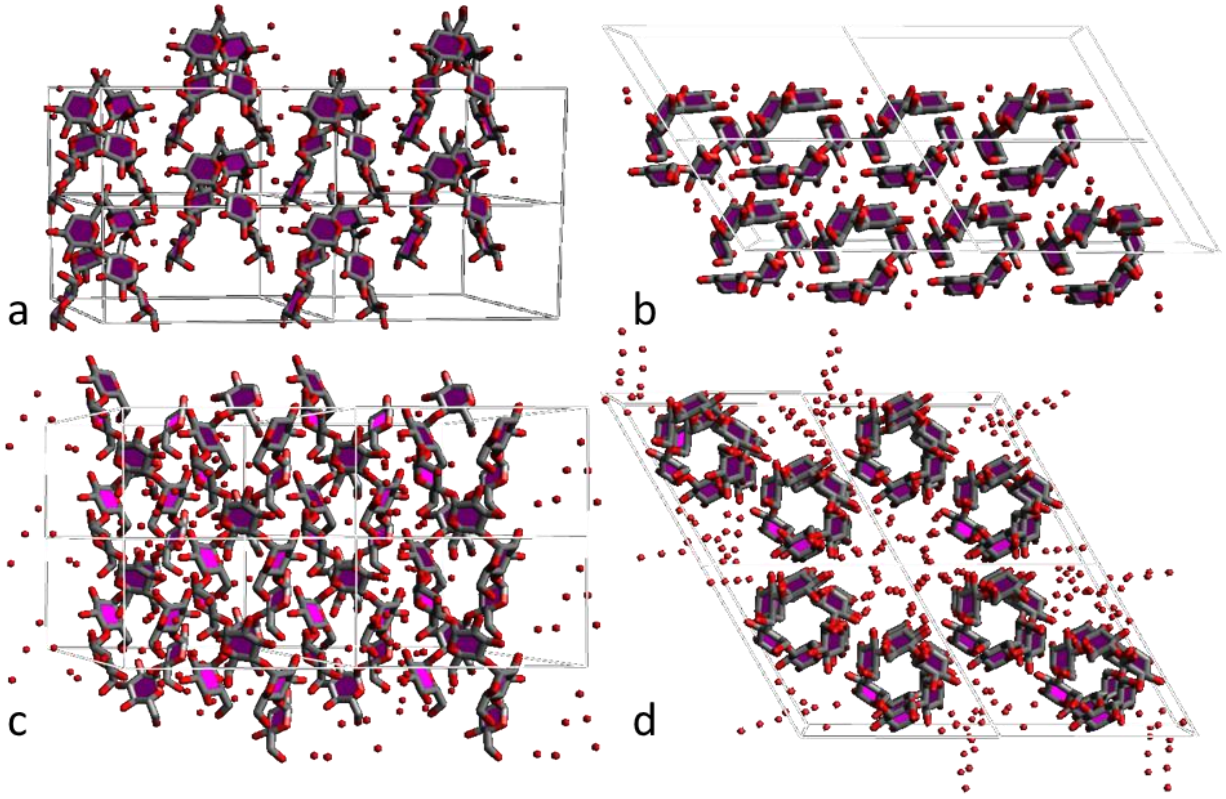

Fig. 5.2-4: Water content in amylose A and B.

Amylose A (a,b) contains less water than amylose B (c,d) as shown by four unit cells arranged sideways (a,c) and from the top (b,d). The helices are drawn as sticks, while the oxygen atoms from water are drawn as red balls, the hydrogen atoms have been omitted.

It is interesting that as compared with bulk water, the water inside starch crystals is partially immobile. The water in starch type A crystals is understood to be immobile due to the tight packing of this crystal (Imberty, Buleon et al. 1991), since the 8 water molecules per unit cell are located in distinct pockets (see Fig. 5.2-4(a) and (b)), and there is no interconnection between one pocket and another (Popov, Buleon et al. 2009). In starch B on the other hand, there is a large cavity between the helices (Fig. 5.2-3 (d)), which occurs due to the hexagonal symmetry, commonly termed an open water channel (Jane 2006), which would suggest water can freely flow in this channel. However, water is not completely free to move around, but rather is somewhat fixed in the crystallographic register (Fig. 5.2-4 (c) and (d)), as confirmed in all three major amylose B crystallographic studies based on intense X-ray diffraction peaks (Wu and Sarko 1978; Imberty and Perez 1988; Takahashi, Kumano et al. 2004), though the water is less mobile compared to bulk water, authors investigating amylose B crystals acknowledged that water molecules can statistically occupy two or more definite positions with different

probabilities. An often cited NMR study reports that only immobile water exists in starch B crystals with hydration up to 33%, while mobile, 'freezable water' exists in hydrations exceeding this amount, (Lechert 1981).

Heat treatment of starch granules has long been studied. NMR experiments of transverse magnetic relaxation time in potato starch granules have shown that starting at about 50°C a noticeable change occurs in the population of bound water (Hennig and Lechert 1977; Lechert 1981). Differential scanning calorimetry (DSC) has also been widely applied to starch granules, finding that the first endotherm of maize and potato occurs at 70.2°C and 58.3°C, respectively (Donovan 1979; Cooke and Gidley 1992). The physical process responsible for these endotherms continues to be debated, although it has been linked to loss of crystallinity, as observed by a decrease in powder X-ray diffraction intensity, as well as loss of birefringence, as observed by a decreasing intensity of the Maltese cross image when heating starch granules in a polarization microscope (BeMiller and Whistler 2009). Furthermore, the endotherm temperatures themselves are quite complex, and vary with starch moisture content and heating rate (BeMiller and Whistler 2009).

One main difference between starch crystals A and B is the nature of the interconnecting bonds between helices. When comparing the organization of the A- and B- starch crystals, it is clear that the packing of glucose residues in the A- allomorph is significantly tighter than it's B-counterpart (see Fig. 5.2-4 (b) versus (d)). While A-starch contains a number of hydrogen bonds between adjacent double helices, the B-starch has connections mainly through hydrate water bridges (Takahashi, Kumano et al. 2004; Popov, Buleon et al. 2009). The crystal cohesion and thermal susceptibility of these allomorphs is substantially different since the hydrate bridges are weaker than direct hydrogen bonds. This can be observed experimentally in two ways: (i) when amylose B is subjected to heat at low moisture it converts to type A (Vermeylen, Derycke et al. 2006), and (ii) A-amylose crystals have higher melting temperatures than the B- type at identical hydrothermal treatments (at 50% water volume fraction the melting temperatures are 130°C and 100°C for amylose A and B, respectively) (Whittam, Noel et al. 1990).

5.3 Nonlinear Microscopy of Starch Granules

5.3.1 Introduction to nonlinear microscopy of starch granules

SHG microscopy of starch granules has recently emerged as a potentially effective tool for investigating the relationship between a biocrystals structure and its nonlinear optical properties. Effective imaging of starch granules using an optical second harmonic signal in a microscope was realized in 2000 by Mizutani and coworkers (Mizutani, Sonoda et al. 2000). Since then the ability of starch granules to induce intense SHG has been observed in starch granules of various botanical sources including *Lantana camara* (Cox, Moreno et al. 2005), maize (Chu, Chen et al. 2001; Carriles, Schafer et al. 2009), potato (Carriles, Schafer et al. 2009; Cisek, Prent et al. 2009), rice (Zhuo, Liao et al. 2010), pea (Cisek, Spencer et al. 2009) and wheat (Psilodimitrakopoulos, Amat-Roldan et al. 2010). Although the role of amylose within the amylopectin crystalline double-helices is still under investigation (end of Ch. 5 in (BeMiller and Whistler 2009)), one recent study assigned the origin of intense SHG to amylopectin (Zhuo, Liao et al. 2010) based on experimental evidence that lower intensity SHG was observed in images of amylose deficient mutant rice starches compared to amylose rich mutants. The radial organization of material within starch granules is significant for SHG imaging since a linearly polarized laser shows starch SHG images with two lobes parallel to the polarization of the laser (Cox, Moreno et al. 2005), and the starch granules were shown to be very useful as probes of the orientation of linear polarization in an SHG microscope (Psilodimitrakopoulos, Amat-Roldan et al. 2008). Channels or pores, which have recently been investigated by other methods (Fannon, Shull et al. 1993; Huber and BeMiller 2000; Fannon, Gray et al. 2004; Sujka and Jamroz 2010), have, to our knowledge, not yet been demonstrated with SHG imaging. In contrast, the structure of starch hila, which is not well understood (BeMiller and Whistler 2009), and reportedly often contain voids (Huber and BeMiller 2000), have been observed by SHG imaging, revealing decrease in SHG signal attributed to poor crystalline organization or voids (Cisek, Spencer et al. 2009; Slepkov, Ridsdale et al. 2010). Additionally visualization of starch granule growth rings was recently achieved (Yu, Liao et al. 2009). A recent study measured the hyperpolarizability ratio of starch granules using polarization SHG microscopy and attributed the measured value to the helical pitch of glucose molecules within the amylose helix (Psilodimitrakopoulos, Amat-Roldan et al. 2010), presupposing that the hyperpolarizability of starch consists of a single dominant hyperpolarizability component. The periphery structure of granules has also been

investigated by SHG, and intense backwards directed SHG has been observed from the peripheries of starch granules (Psilodimitrakopoulos, Amat-Roldan et al. 2008).

Starch granules are an ideal model biological crystal system to investigate with second and third harmonic generation. Starch granules are composed of different crystals with known unit cells. Most cereal starch granules including maize contain amylose A type crystallinity, while most tuber starch granules including potato contain the amylose B type. Maize and potato starch granules are investigated, representing structures with amylose type A and B crystallinity, therefore similar to the NW analysis, differences in SHG PIPO measurements can be modeled and related to the crystalline structure of amylose A and B, and aid in the current investigation of the origin of SHG from starch granules. The macro-scale architecture of starch granules is radial, and therefore ideally suited for polarization studies using nonlinear microscopy because a single starch image scanned by linearly polarized light contains SHG emitters at every possible orientation angle to the polarization. Furthermore starch granules have suitable size for nonlinear microscopy, around 1-100 μm in diameter, and conveniently serves to model small and large microscopic structures. Additionally starch granules are complex and interesting, with several unanswered questions, which can be addressed with nonlinear microscopic measurements, such as the organization of the nucleation region of the starch granule, the structure of the starch periphery, the orientation and internal alignment of biopolymers, as well as the structure of starch growth rings (BeMiller and Whistler 2009).

In this study an investigation of starch granules is performed using nonlinear multicontrast microscopy. 2D and 3D multicontrast imaging of starch granules is investigated via second harmonic generation as well as third harmonic generation to reveal qualitative starch granule visualization characteristics. Cross polarization SHG imaging is demonstrated on starch granules as a quick and convenient method for distinguishing granules of different crystal types, and modeling of polarization dependent SHG visualization is performed to explain the observed qualitative differences in the images. PIPO SHG microscopy is used to measure the susceptibility of maize and potato starch granules, as well as to measure the effects of different hydration conditions on the PIPO SHG data. To explain the origin of experimentally observed variations in SHG susceptibility of starch granules from maize and potato, computational modeling of molecular hyperpolarizabilities is performed using *ab initio* calculations of the crystallographic structures of amylose A and B, and related to starch susceptibilities.

5.3.2 Starch granule preparation and imaging techniques

Sample preparation

Starches were imaged inside fresh plant slices, extracted from fresh samples (commercial food supplier) and immobilized in gel, as well as from commercially purchased powder (Starch Soluble, 8560-1, Caledon Laboratories Ltd.). *In vivo* starch granules were prepared by using a razor to cut a thin slice of potato (<500 μm) and sandwiched between microscope coverslips. For longer duration scans a drop of distilled water was placed upon the slice to keep it hydrated. Higher resolution images could be obtained when the fresh potato slice or maize kernel was cut and homogenized with a pestle and mortar, and the resulting liquid was diluted in distilled water by 5-10 times (by volume) and then held in polyacrylamide gel between microscope coverslips. Dried potato starch powder was imaged using several preparations: starch powders were placed upon a glass coverslip without further preparation. Starch powders were also dehydrated by subjecting to very near vacuum pressure (0.00001 atm), for a duration of 8 hours, the same technique used for obtaining molecular crystals suitable for X-ray analysis. Hydrated starch powder was obtained by placing the powder in distilled water, and followed by immobilization in polyacrylamide gel. Deuterated starch granules were obtained by placing the powder into deuterated water for 8 hours, followed by immobilization in polyacrylamide gel for scanning.

Sample immobilization in polyacrylamide gel

Immobilization of microscope samples is essential in order to reduce Brownian motion of starch granules and obtain high resolution images. Sample immobilization was used for two reasons: in order to keep the samples still during repeated scans and to keep the samples away from the glass interfaces, which induce strong THG signals that interfere with THG images of microscopic structures. First, the sample was diluted in water or buffer to obtain a desired concentration for imaging, and then the following gel components were added: 0.68 M acrylamide, 8.3 mM bisacrylamide, 0.18 mM ammonium persulfate, and 26 mM TEMED (Tetramethylethylenediamine), reaching a solid gel after 1-5 min. The gel was tested and induced no SHG, THG or MPF even at full power of the laser with the highest NA objective. In order to test whether polyacrylamide gel has significantly different optical properties from water, a sample of small, clear, polymer beads, 10 μm in diameter, was scanned in polyacrylamide gel as well as in water, resulting in identical THG signals.

Scan parameters

Typically 10-50 μm sized starch granules were chosen to keep the scanning area the same and to avoid scattering effects caused by differently sized granules. SHG images of starch granules required little laser power, only ~10 pJ of energy per pulse, or 0.1 mW average power at the sample was typically used for imaging. This is much lower than what is typically needed to scan a similar glucan, cellulose, which typically requires 5-10 nJ pulse energy. A typical starch image was obtained by integrating 200 image frames obtained at ~8 frames/s. Excitation from 800 nm as well as a 1028 nm laser sources were used. In order to obtain THG images of starches, a much higher power of up to 5 nJ pulse energy was used at the sample. During these scans an additional neutral optical density filter was placed in front of the SHG photomultiplier tube in order to keep the signal from saturating the detector.

Preparation of circularly polarized light

To obtain circularly polarized light at the microscope sample stage two techniques were employed. In the standard method, the half wave plate (HWP in Fig. 3.2-1) was replaced with a quarter wave plate (Thorlabs WPQ05M-1064) in front of the microscope objective entrance aperture. Another method was used, where the polarization optics (HWP and Polarizer) were removed before the excitation objective, and a Berek polarization compensator (5440 New Focus Inc.) was inserted before the microscope in the beam path, allowing unobstructed collection of epi-SHG. In both methods the THG signal from a glass-air interface was minimized to obtain the best circular polarization at the sample (Fittinghoff, Aus der Au et al. 2005; Cisek, Prent et al. 2009).

5.3.3 2D Visualization of starch granules with SHG microscopy

We investigated starch granules via SHG imaging of the equatorial planes of potato starches using different polarizations of incident light. Fig. 5.3-1 shows forward detected SHG images of potato starch granules recorded directly without an analyzer placed in front of the detector. Horizontal (Fig. 5.3-1 (a)) and vertical (Fig. 5.3-1 (b)) linear polarization, as well as circular polarization (Fig. 5.3-1 (c)) of the incident laser beam was used to generate the SHG images, revealing that a linearly polarized laser beam scanned across the equatorial plane of a single starch granule produces an SHG image which appears to be composed of two disjoined

lobes oriented parallel to the excitation polarization in agreement with previous studies (Mizutani, Sonoda et al. 2000; Psilodimitrakopoulos, Amat-Roldan et al. 2008). This phenomenon can be understood in the following way: since the laser beam focal volume is small compared to the granule volume, therefore it likely samples mostly parallel starch nanocrystals (as depicted in Fig. 5.2-1 (f)). Due to the radial arrangement of starch nanocrystals in the granules, at any orientation of linear polarization on the sample plane there are fibers oriented parallel to the excitation orientation, and these generate the most intense SHG because the d_{33}/d_{15} > 3 for starch, which means the helices parallel to the polarization will produce at least 9 times more SHG compared with perpendicular helices (see Eq. 2.4-13) (Zhuo, Liao et al. 2010; Psilodimitrakopoulos, Amat-Roldan et al. 2011). Indeed the directionality of the visualized lobes in a starch granule are sufficiently well ordered that an SHG image of a starch granule can be used as a probe to sample the orientation of linear polarization of the laser at the focal plane of a nonlinear optical microscope (Psilodimitrakopoulos, Amat-Roldan et al. 2008).

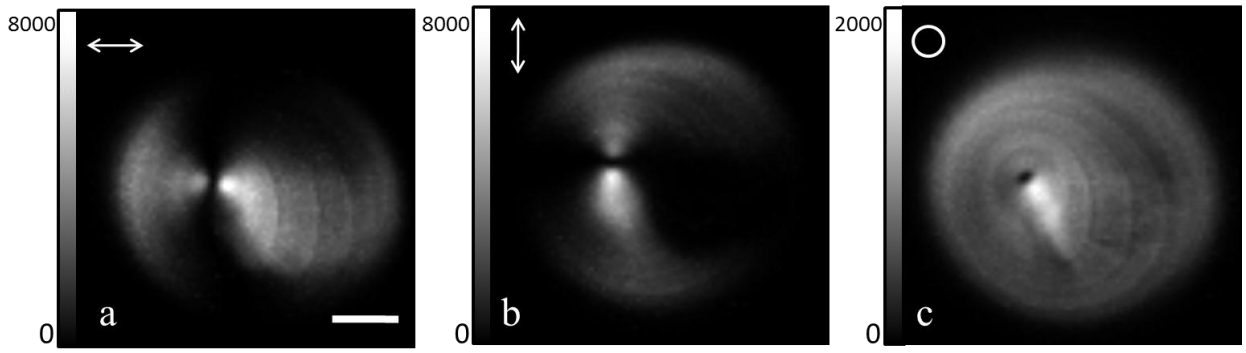

Fig. 5.3-1: High resolution polarization dependent SHG images of potato starch granules.
Panels show SHG images of the central hilum-containing optical section of the same starch granule imaged at three different polarizations of the incident laser as indicated on the top left of each image; horizontally oriented linearly polarized light (a), vertically oriented linearly polarized light (b) and circularly polarized light (c). The scale bar in (a) is 10 μm.

Circular polarized light shows the entire starch granule, visualized in Fig. 5.3-1 (c). Circularly polarized light sweeps all the lateral directions of linearly polarized light; hence it visualizes the entire starch granule and clearly reveals interesting structural starch characteristics. The intensity ratio of SHG from circular versus linearly polarized light was experimentally found to be 0.3 ± 0.1, and therefore, according to the theoretical treatment shown in section 2.4.5, using the graph Fig. 2.4-2, the potato starch granule has a d_{33}/d_{15}> 2, in agreement with (Psilodimitrakopoulos, Amat-Roldan et al. 2010). More detailed measurements of the hyperpolarizability ratio will be shown in the PIPO SHG microscopy section 5.3.9. Several

structural characteristics of starch granules can be ascertained using SHG as a contrast mechanism, since the hyperpolarizability is not only a function of concentration, but also crystalline arrangement, hence it is a useful tool to detect defects in biological crystals.

SHG detected circular dichroism of starch granules resulting from imaging with alternating right and left-handed circularly polarized light has long been used to probe the chirality terms of the hyperpolarizability (β_{ijk} where $i \neq j \neq k$) of molecules on surfaces (for a recent review see (Fischer and Hache 2005)), thus it was studied experimentally in starch granules. SHG obtained from left and right circularly polarized light showed no difference in all the starches studied, the intensities obtained with the two polarizations were always within 10% of one another, showing that anisotropic β_{ijk} tensor elements have small values compared to isotropic components. Smaller differences in SHG at opposite circular polarizations could exist, but are beyond measuring capabilities of the current imaging system. The limitation of the measurement consists of obtaining perfectly circular polarized light, which relies on the quarter wave plate axis oriented precisely along the polarizer axis. Fast polarization modulation using photoelastic modulators and lock-in detection might decrease this error sufficiently to detect the difference in left versus right circular polarization of the excitation.

Fig. 5.3-1 (c) reveals that high resolution SHG imaging of starch granules can reveal growth rings. Growth rings were easily observed in SHG images obtained using a high numerical aperture objective (1.3 oil immersion). The starch granule inner architecture is characterized by ‘growth rings’ that correspond to concentric semi crystalline shells 120 nm to microns thick, separated by thin amorphous regions (see (Glaring, Koch et al. 2006) and references therein), with ring thickness increasing towards the exterior of granules, as well with granule size. SHG microscopy has high sensitivity to structural order i.e. crystallinity and enables visualization of rings in starch granules without chemical treatment or staining. The intensity of SHG typically changes by < 1% at the growth rings, therefore it is likely that the thin amorphous regions in the granule are quite small, or, are intertwined with semi-crystalline regions in accordance with the continuous network of lamellar super-helices as hypothesized (Oostergetel and Vanbruggen 1993). Interestingly, these shells are observed (Fig. 5.3-1 (a) and (b)) to have identical polarization anisotropy to one another, signifying they are equally well aligned in the same direction and supporting the idea that some amylopectin molecules traverse the different starch

layers (see (Fannon, Gray et al. 2004) and references therein), keeping the orientation of the nanocrystallites extremely uniform from one layer to the next. Furthermore, since the SHG anisotropy appears the same, the likely origin of the signal variation between the growth rings is a change in concentration of crystalline regions, supporting the current idea that crystalline shells are interrupted by regions containing amorphous material (Glaring, Koch et al. 2006). Another recent study using simultaneous SHG and CARS microscopy was performed on potato starch granules, revealing rings were observed with both techniques (Slepkov, Ridsdale et al. 2010). The paper concluded that the SHG and CARS signal were opposite in phase, and hence, that the amorphous (less bright SHG) rings have higher density.

Several other kinds of starch granule features can be visualized with SHG. Bright regions such as in Fig. 5.3-1 (c) are visualized with SHG, and are attributed to locally higher concentration or improved crystalline order. Additionally the starch hilum is also visualized as a region containing almost no SHG intensity near the center of the granule. A more detailed discussion on the starch hilum will be presented in section 5.3.6.

In conclusion, the SHG contrast is very beneficial for starch granule imaging as it allows visualizations of many starch granule features that are commonly very difficult to observe without treatment, including growth rings, crystalline heterogeneities as well as the starch hilum. Therefore starch SHG imaging could be used to identify granules with reduced crystallinity, for quality control in food production, to pick the longest lasting foods, or to monitor starch degradation during biofuel production.

5.3.4 3D SHG imaging of starch granules

Starch granules were imaged in three dimensions in order to characterize the SHG signals generated from the entire structure of the granule.

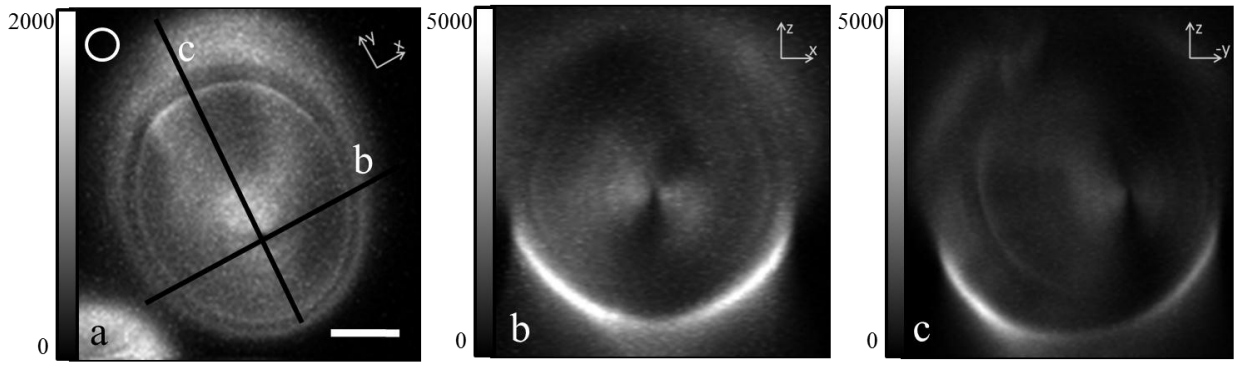

Fig. 5.3-2: SHG images of axial and lateral optical sections of a potato starch granule.
SHG image of the central hilum-containing lateral optical section is shown in (a), while (b) and (c) show axial sections, obtained by recording 2D SHG optical sections at different depths with a step size of 0.25 μm, and re-slicing the image according to the black lines indicated in (a). In (b) and (c) the laser enters the granule from below and forward SHG is detected above the image. The scale bar in (a) is 10 μm.

Fig. 5.3-2 shows results of 3D SHG imaging of a potato starch granule with circularly polarized excitation. Fig. 5.3-2 (a) shows the equatorial plane (lateral section) of a starch granule imaged with circularly polarized light, similar to Fig. 5.3-1 (c), while Fig. 5.3-2 (b) and (c) show two mutually perpendicular sections which are both parallel to the laser beam (axial section) (indicated by labeled lines in Fig. 5.3-2 (a)). 2D SHG images of lateral optical sections of the starch granule were taken every 0.25 μm to generate an image stack, which was then sliced along the lines indicated in Fig. 5.3-2 (a), using the "z-axis profile" function in image manipulation software (ImageJ 1.41) to produce the axial sections in Fig. 5.3-2 (b) and (c). SHG intensities observed in the axial slices (Fig. 5.3-2 (b) and (c)) conform to the Eq. 2.4-23, since the intensity drops off to 0 in regions where fibers are assumed to be parallel to the beam (above and below the hilum in Fig. 5.3-2 (b) and (c)), while the SHG is maximized in regions where fibers are perpendicular to the beam. SHG of starch fibers parallel and perpendicular to the beam has previously been studied for linearly polarized excitation where the same trend is observed (Zhuo, Liao et al. 2010; Psilodimitrakopoulos, Amat-Roldan et al. 2011), but was shown here with circularly polarized excitation for the first time.

Growth rings can be observed in lateral slices of starch granules Fig. 5.3-2 (b) and (c). Growth ring visualization occurs because of the difference in crystallinity between crystalline and amorphous regions, and has been discussed in section 5.3.3. Other than using SHG and CARS microscopy (Yu, Liao et al. 2009; Slepkov, Ridsdale et al. 2010), growth rings have not been observed in lateral sections of untreated starches in previous research since most

visualization techniques used to visualize growth rings, such as, differential interference contrast, atomic force microscopy and scanning electron microscopy, did not have the required optical sectioning capability (Ridout, Gunning et al. 2002; Glaring, Koch et al. 2006; Li, Guiltinan et al. 2006). Confocal microscopy has sectioning capability, however it lacks natural contrast, and requires labeling with a fluorescent dye for imaging (Chanzy, Putaux et al. 2006).

An interesting observation encountered upon 3D imaging of starch granules is bright SHG peripheries on the side of the granule located closer to the excitation objective, visualized in the bottom of Fig. 5.3-2 (b) and (c), which can be several times brighter than the granule interior. This observation has been confirmed by other labs using linearly polarized excitation (Psilodimitrakopoulos, Amat-Roldan et al. 2008) and to date has no explanation. The stronger SHG at the surface can be partially attributed to different alignment of the glucose at the surface compared to the inner part of the granule, as well as to a higher concentration of single amylose strands which is known to exist (Jane 2006).

In summary 3D SHG imaging can be performed on starch granules. The 3D imaging can visualize several characteristics in the starch granule including the starch hilum, growth rings, and an intense starch periphery. The reduction of SHG intensity observed in images off the equatorial plane of the starch granule can be explained by radially aligned amylose crystals, which increasingly point into the laser propagation orientation, where they induce no SHG, in accordance with the theory presented in sections 2.4.2 and 2.4.4 for linear and circularly polarized excitation, respectively.

5.3.5 Multicontrast nonlinear imaging of starch granules

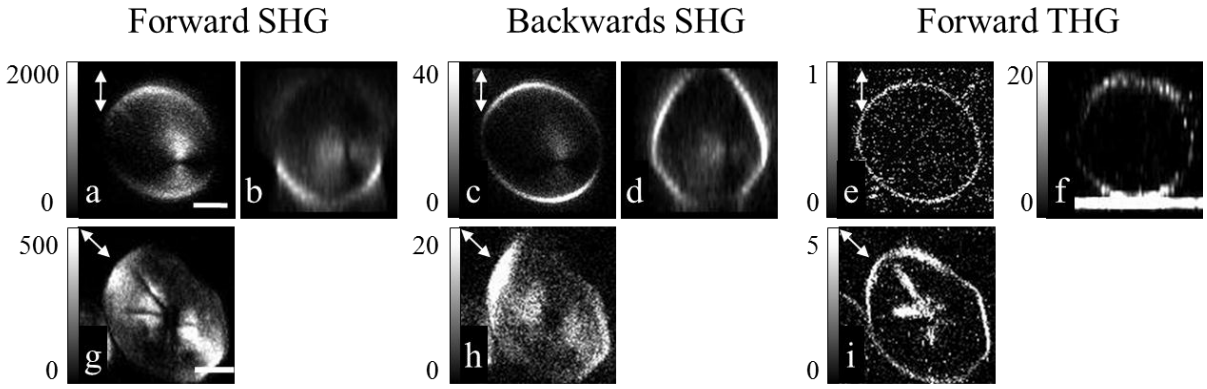

Fig. 5.3-3: Multicontrast nonlinear imaging of starch granules.

Forward detected SHG (SHG), backward detected SHG (bSHG) as well as forward detected THG of a starch granule shown via equatorial lateral section (a), (c), (e), and via axial section obtained via 3D imaging (b), (d), (f) similar to Fig. 5.3-2. The second row contains SHG, bSHG and THG images of a different starch granule containing cracks, obtained fresh from a potato. The scale bars represent 5 μm (a) and 10 μm (g).

Fig. 5.3-3 shows 3D multicontrast imaging applied to a single potato starch granule. Images of the lateral equatorial slice are shown in (a), (c) and (e), while axial images with the laser direction upwards in (b), (d) and (f), for SHG, bSHG and THG, respectively. The SHG images (a) and (b) appear similar to Fig. 5.3-2. The bSHG images are almost identical to the SHG images, especially inside the granule, and therefore, these signals are attributed to backwards scattered SHG, a phenomenon often observed in SHG imaging, for example, in tail tendon of mature rats (Williams, Zipfel et al. 2005). In forward SHG, the granule boundary on the lower half of the granule appears more intense than SHG from the bulk of the granule, while in backward SHG the granule boundary on the upper half of the granule appears more intense than SHG from the bulk. This was an interesting phenomenon observed in about half the granules. Observations of a brighter starch granule periphery in bSHG than the bulk was previously also observed by other groups in wheat starch SHG imaging (Psilodimitrakopoulos, Amat-Roldan et al. 2008). Intense backwards-directed SHG in thin samples has been shown to originate from small particles which can scatter the SHG equally in the forward and backwards directions (Cheng, Volkmer et al. 2002), as well as from small inhomogeneous structures which produce incomplete destructive interference in the backwards direction, such as small strands of fibrillar cellulose (Nadiarnykh, LaComb et al. 2007) or underdeveloped collagenous tissues (Williams, Zipfel et al. 2005; Legare, Pfeffer et al. 2007; Pfeffer, Olsen et al. 2007; Pfeffer, Olsen et al. 2008). The fact that the intense SHG at the periphery is only observed in some granules and not others is not surprising since the phenomenon likely depends on the

composition of the starch periphery, which varies depending on the stage of the granule's growth cycle (see section 5.2.2), and possibly with water content (Lechert 1981). The intense bSHG signal observed at the granule periphery could be explained by two phenomena. The concentrated amylose at the surface might behave similar to small strands of fibrillar cellulose, or, young collagenous tissues, exhibiting similar characteristics to small scatterers which scatter equally forwards and backwards (Cheng, Volkmer et al. 2002). The alternative explanation is that the observed SHG at the starch periphery could be attributed to surface SHG. Breaking of central symmetry at surfaces and resultant SHG has long been investigated due to its efficiency; indeed hyperpolarizability of the surface molecules can be measured using surface SHG experiments (Shen 1989). Measurements of the directionalities of SHG signal from starch peripheries could prove useful for determination of the surface state of starch granules.

The THG observed in the image of a lateral equatorial section Fig. 5.3-3 (e) and axial section (f) shows that signal is only generated at the granule edge. The THG signal is most intensely observed at the granule boundary where the laser propagation direction is perpendicular to the boundary interface (above and below the granule in panel (f)), similar to the phenomenon observed during imaging of polystyrene beads (Fig. 2.1-4). Note that the bright white line at the bottom of panel (f) occurred due to the presence of the interface between the glass coverslip below the granule. The lack of THG signal from the granule interior suggests that there are no interfaces where the optical material properties are abruptly changing, and hence suggests that starch granules are made of material which has spatially uniform index of refraction and third-order nonlinear susceptibility, and provides evidence that the hilum may not be empty, or small, although this will be discussed in section 5.3.6. A very high laser intensity, 7 nJ per pulse, was used for scanning in order to obtain sufficient THG for images in Fig. 5.3-3, therefore in order to obtain more details with increased THG signal a higher laser power would be necessary for scanning, however higher powers damage the sample and produce cavitation bubbles, preventing thorough structural analysis of the granules using THG.

Fig. 5.3-3 shows multicontrast imaging of a starch granule containing cracks. Equatorial lateral sections of the starch granule are shown with SHG, bSHG and THG contrasts in panels (g), (h) and (i), in a starch granule from a fresh potato. The cracks can be easily visualized inside these granules with THG contrast, having similar intensity as the THG from the granule periphery and therefore, the cracks likely contain air pockets, since the THG depends on the

change in index of refraction between the materials at the interface. SHG and bSHG also visualize the cracks in the granule with a void signal, supporting that the cracks are filled with a centrosymmetric material. This shows the possibility of using the combined signals of SHG and THG to interrogate individual starch granules for assessing their structural heterogeneity characteristics.

5.3.6 Multicontrast microscopy of the starch hilum

Most SHG images of starch granules contain a small dark central region similar in size to the microscope point spread function (PSF), located at the starch hilum. Fig. 5.3-4 shows a typical image where the location of the SHG hilum in a starch granule, shown at two orientations of linear excitation polarization (a), (b), spatially correlates with the center of the Maltese cross, as observed through crossed polarizers in the same setup (c). Since the microscope is optimized for laser scanning, but not for white light imaging, it does not provide optimal light images, especially through crossed polarizers, therefore a polarization image with software enhanced contrast using a threshold and coloring scheme is shown in Fig. 5.3-4 (c), visualizing the Maltese cross in green overlaid on a while light image of the starch granule enhanced with red coloring. Since the Maltese cross visualizes the starch hilum (Chandrashekar, Savitri et al. 1987), the observed spatial overlap between the center of the Maltese cross and the SHG dark region provides evidence that the SHG dark central regions visualize the starch hilum.

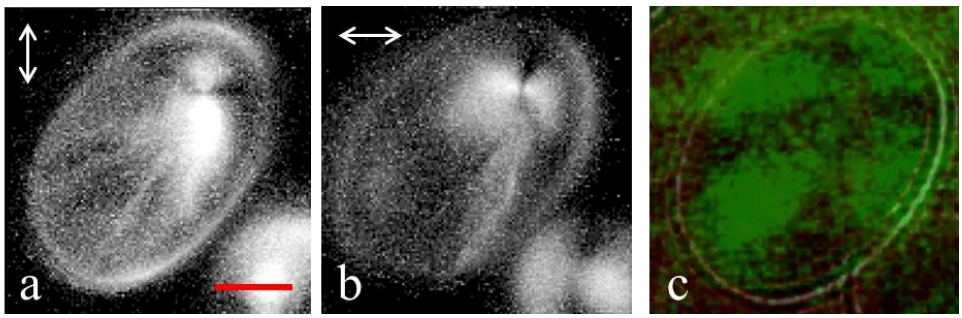

Fig. 5.3-4: SHG and polarization wide field microscopy of a starch granule.
A comparison of SHG images of a starch granule taken with linearly polarized excitations (indicated at top left in (a),(b)) and a wide field white-light image with enhanced red contrast overlaid with a cross-polarized image with enhanced green contrast, (c). The scale bar in (a) is 20 µm and was colored red for contrast.

Regardless of the polarization state of the excitation beam, SHG signal was not generated in the hilum. Examples of visualization of the starch hilum with SHG in axial sections of granules imaged with linearly polarized excitation are shown, for example, in Fig. 5.3-4 (a) and

(b), with circular polarization in Fig. 5.2-1 (c), and in lateral sections in Fig. 5.3-2 (b) and (c). This observation of an SHG dark region at the starch hilum is consistent with the hypothesis that the hilum region is arranged in a centrosymmetric configuration (see circle in middle of Fig. 5.2-1 (f)) which would render destructive interference due to SHG emission from out of phase emitters (Boyd 2008). Biologically relevant destructive interference of SHG due to oppositely aligned emitters was previously observed in oppositely aligned styryl dye molecules embedded in fused giant unilamellar vesicles as well as in oppositely aligned myosin molecules in *Drosophila melanogaster* larva myocytes (Moreaux, Sandre et al. 2000; Prent, Green et al. 2008; Carriles, Schafer et al. 2009).

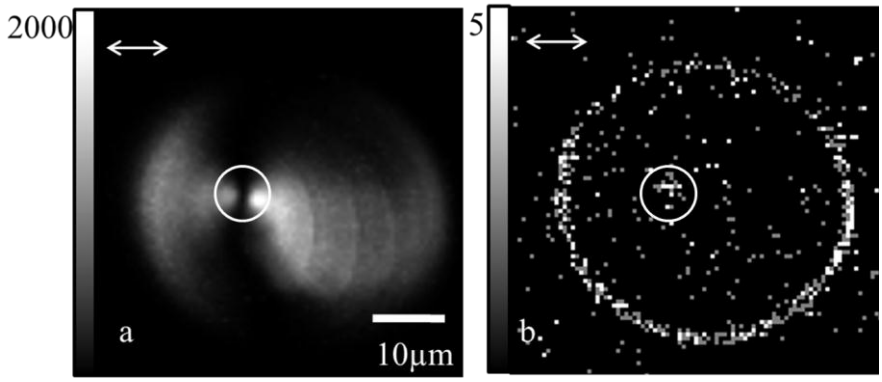

Fig. 5.3-5: Simultaneous SHG and THG showing starch hilum.
A potato starch granule immobilized in polyacrylamide gel was imaged using the 1.3 NA oil objective at 7nJ pulse energy for 200 frames to produce the SHG and THG images simultaneously. THG signal observed at the hilum of this starch granule shows it contains a hole, as indicated by the circle.

Simultaneous SHG and THG imaging was performed to investigate the hilum has an empty void. An empty hilum, filled with air, similar in size to the laser focal volume, is expected to induce a similar intensity THG signal as at the edge of the granule. For this purpose, and since no THG from the hilum is commonly observed, see Fig. 5.3-3, the laser power was maximized and the detectors were aligned for maximum efficiency. Fig. 5.3-5 shows an SHG and a THG image simultaneously obtained with the multicontrast microscope, showing that typically some starch granules do display THG at the hilum, as observed in panel (b) of Fig. 5.3-5. Many granules do not display THG at the hilum, likely since the hilum is much smaller than the laser focal volume, and may not contain air, but rather water or carbohydrates as the rest of the granule. Observations of THG from the hilum support the idea that the hilum has heterogeneous optical properties, and therefore, the hilum in this case is either empty, or contains material with different index of refraction or third-order susceptibility than the rest of the granule. A more

detailed study of THG from granules in different hydration treatments is required in order to establish if the hilum appears in THG due to swelling, due to water content, or due to randomly arranged amylose/amylopectin, or due to a void. Evidence that the hilum contains carbohydrates has been shown in another study of simultaneously scanned potato granules with SHG and CARS, where intense CARS signal of C-H vibrations was observed at the hilum (Slepkov, Ridsdale et al. 2010). Since the CARS signal depends on the concentration of carbohydrates, which are rich in C-H bonds, it therefore provides direct evidence that the starch hilum contains amylose residues. Therefore, while the hilum contains amylose, the organization of these residues is not determined, and could be arranged centrosymmetrically, in agreement with our hypothesis, or, in a disordered organization, within the size of the laser focal volume.

In conclusion, SHG microscopy can clearly visualize the starch hilum, as evidenced by the spatial overlap with the Maltese cross. The presence or absence of a small void at the hilum can be determined by THG signal. The void in the SHG signal at the hilum is attributed to centrally symmetric molecules in the vicinity of the hilum, and possibly a disordered center.

5.3.7 Cross-polarized SHG imaging of starch granules

Fig. 5.3-6 shows typical SHG images comparing maize (a,c) and potato (b,d) starch granules obtained with horizontally oriented linearly polarized laser radiation, and imaged through an analyzer oriented horizontally (a,b) and vertically (c,d) with respect to the images. Due to the radial arrangement of amylose and amylopectin helices in starch granules, at any orientation of linear polarization there are helices oriented parallel as well as perpendicular to the excitation orientation within the granule. The helices oriented parallel to the laser polarization generate an SHG component polarized parallel to the helices with intensity determined by the d_{33} hyperpolarizability component (see Eq. 2.4-16). Helices oriented perpendicular to the polarization of the excitation generate an SHG component polarized parallel to the helices which is proportional to the d_{31} hyperpolarizability component (see Eq. 2.4-16). Therefore, a crossed analyzer placed in the collection beam path before the detector will transmit the SHG generated from the helices perpendicular to the excitation, while reducing the SHG intensity of helices oriented parallel to the excitation polarization. Since, under the assumption of Kleinman symmetry ($d_{31}=d_{15}$), the d_{33}/d_{15} ratio of starch is high, >3, (Psilodimitrakopoulos, Amat-Roldan et al. 2011), the most intense SHG is generated from helices parallel to the laser polarization, and

as a result the SHG from perpendicular helices is not clearly visible in SHG images due to the high contrast, since it's intensity is at least 9 times weaker. Therefore, using a crossed analyzer increases the overall contrast of the perpendicular helices. It is interesting to compare imaging different types of granules with crossed polarizers in order to understand the variation in the d_{33}/d_{15} ratio and its consequences on SHG imaging of starches.

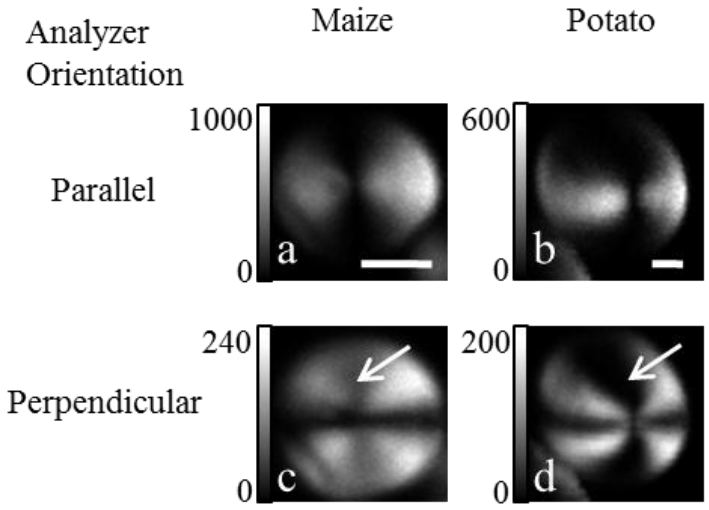

Fig. 5.3-6: SHG images of potato and maize starches using an analyzer.

Horizontally oriented linear polarization of the laser was used to induce SHG images of maize (a,c) and potato (b,d) granules. An analyzer was placed before the detector in the microscope, oriented horizontally (parallel to the excitation) (a,b) and vertically (perpendicularly to the excitation) (c,d). Visual discrimination between maize and potato starch is demonstrated in the cross polarized images (c,d) by the difference in intensity at the vertical region (arrow). The scale bars represent 5 μm.

Potato and maize granules display significantly different SHG images when an analyzer is implemented with orientation perpendicular to the excitation orientation (crossed). When the analyzer is parallel to the excitation polarization orientation, little difference is observed between different granules other than morphology. Typical SHG images obtained with crossed polarizers show a significantly brighter region for helices perpendicular to the excitation in maize granules, as compared with potato granules (see arrow in Fig. 5.3-6 (c) versus (d)). This observation suggests that the hyperpolarizability ratio d_{33}/d_{15} of maize granules is lower than the corresponding ratio for potato granules. The present analysis does not take into account the effect of birefringence, which will be investigated later in section 5.3.9. The technique of SHG imaging with crossed polarizers is useful for differentiation between maize and potato starches, and possibly, for any SHG emitting structures which have different hyperpolarizability ratios.

In conclusion, it has been experimentally shown that imaging starch granules using the cross polarized SHG technique can differentiate between different types of starch granules. Differentiation of granules via SHG imaging could be used in industry to separate starch A and B granules in plants where they are mixed, such as wheat or oat, or during heat and moisture treatment which is known to convert starch type B to the A type.

5.3.8 Modeling polarization dependent SHG visualization of starch granules

A model of SHG imaging of a starch granule is presented so that the SHG images can be better understood. A model of starch granule SHG images is formulated on the assumption that the SHG emitting biocrystals in starch are composed of radially oriented uniaxial crystals. For the case of maize, which consists of amylose A type crystalline domains, we assume the symmetry is hexagonal in order to quantify the SHG and use the Eq. 2.4-32. The basis for the assumption is the hypothesis that the crystalline blocklets, a segment of which is depicted in Fig. 5.2-1 (e), have rotational freedom around the radial starch axis. Therefore, since the laser focal spot encompasses ~1000 blocklets, assuming 65 nm sized cubic blocklets (Ridout, Gunning et al. 2002), and a cylindrical focal spot with 1.9 μm height and 0.5 μm diameter (see Fig. 3.2-2)), the monoclinic crystal symmetry of amylose A reduces to cylindrical symmetry, which is identical to hexagonal symmetry for the case of SHG (Boyd 2008). Amylose B on the other hand has hexagonal crystal unit cells known to be oriented radially in starch granules (Imberty, Buleon et al. 1991), therefore the assumption of this symmetry automatically holds.

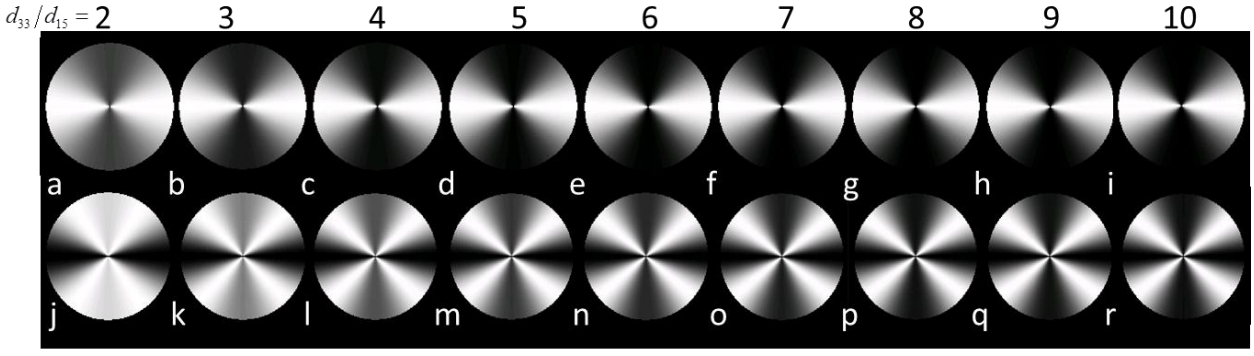

Fig. 5.3-7: Computer model of equatorial SHG starch granule images without and with a crossed analyzer at different d_{33}/d_{15} ratios.

Simulations of equatorial slices of an ideal starch granule with horizontal linear polarized excitation based on Eq. 2.4-13 (a-i) and Eq. 2.4-16 (j-r) (with κ=90°), at different values of the ratio d_{33}/d_{15} indicated above each column, modeled assuming direct SHG detection (a-i), and SHG detection through an analyzer oriented horizontally (j-r).

The SHG image of a starch granule is modeled as it would appear scanned with horizontally oriented linearly polarized light, and without an analyzer before the detector. The model was generated according to the theoretical treatment presented in sections 2.4.2 and 2.4.3, assuming radially outgrowing crystals encompassed by a laser focal volume inside a starch granule are parallel, and a spherically symmetric starch granule. In this case the relative position of the focal volume with respect to the center of the granule gives the orientation of starch crystals, as illustrated in Fig. 5.2-1 (f). The model of visualization of a starch granule is shown in the top row of Fig. 5.3-7 (a-i), at different values of the hyperpolarizability ratio d_{33}/d_{15} indicated at the top of each column, obtained via plotting Eq. 2.4-13 and visualized using LabVIEW software. The model SHG image of a starch granule (Fig. 5.3-7 (a-i)) appears to be composed of 2 separate lobes oriented parallel to the incident polarization. These images closely resemble typical images of starch granules, see for example Fig. 5.3-1 (a), where two lobes are always observed oriented parallel to the polarization orientation, showing that the model is a good description of SHG imaging of starch granules. As the value of the nonlinearity ratio d_{33}/d_{15} increases from 2 to 10, only a slight difference between the widths of the lobes is observed in (Fig. 5.3-7 (a-i)). In order to enhance the visual discrimination between different values of d_{33}/d_{15}, starch granule SHG images were modeled when SHG light is passed through a polarizer oriented perpendicular to the excitation light (crossed), located just before the detector.

Modeling of SHG imaging of a starch granule where a crossed analyzer was inserted before the detector was performed. For crossed polarization, the Jones matrix formulation is used (Eq. 2.4-16) with κ=90° (see Fig. 2.4-1), and the representative model SHG images are shown in Fig. 5.3-7 (j-r). The model images of cross polarized SHG appear to be composed of four lobes, similar to the experimental SHG images (Fig. 5.3-6 (c) and (d)) showing that the model is suitable for describing the image. A visual comparison of the model presented in Fig. 5.3-7 (j-r) with the experimentally obtained cross polarized SHG images of Fig. 5.3-6 (c) and (d), reveals the hyperpolarizability ratio appears to be in the region d_{33}/d_{15}= ~4 for maize, and d_{33}/d_{15}= ~7 for potato. The uncertainty of this technique is quite large, and is not reduced by quantitative intensity analysis because there is large heterogeneity of SHG intensity within starch granules. Additional uncertainty originates from the fact that parallel and perpendicular polarizer orientations with respect to the crystals are difficult to obtain, since real starch granules are not ideally radial. Nonetheless, the visualized difference between maize and potato starch granules

was explained in the model, showing cross polarized SHG imaging is a promising technique for visual discrimination of structures with different hyperpolarizability ratio values. However a more precise measurement of starch hyperpolarizability, including the effects of birefringence which was so far unaccounted for, is performed via detailed SHG analysis in the following section by varying the excitation polarization orientation, as well as the orientation of the analyzer using the polarization-in-polarization-out (PIPO) SHG microscopy.

5.3.9 PIPO SHG microscopy of maize and potato starch granules

PIPO measurement

Maize and potato starch granules were investigated by polarization-in-polarization-out (PIPO) SHG microscopy. To our knowledge, this is the first investigation measuring the outgoing polarization of SHG in starch granules. The current investigation measures the dependence of polarization of the emitted SHG on the orientation of the linearly polarized laser with respect to the major crystal axis, and its relationship to the crystal type of the sample, as described in section 3.4.3. For modeling we assume the hyperpolarizability of starch granules can be characterized by the unique ratio d_{33}/d_{15}, which describes SHG emitted by the uniaxial crystals, and use the Eq. 2.4-32 for analyzing the SHG PIPO measurements. For the case of maize granules, since they are composed of amylose A type crystallinity, we assume cylindrical symmetry of the biocrystallites, in order to quantify the SHG. The basis for the assumption is the popular hypothesis that the starch crystalline macrostructure consists of blocklets that have rotational freedom in the radial direction, (see section 5.3.8). Potato granules on the other hand consist of amylose B type crystallinity, which has hexagonal crystal unit cells, therefore the assumption of cylindrical symmetry automatically holds. The SHG intensity in such a case (Eq. 2.4-32) was found to depend on three angles illustrated schematically in Fig. 2.4-1; θ: the angle between the linearly polarized laser and the crystal axis, κ: the angle between the analyzer and the crystal axis and ϕ: the off the plane tilt of the crystal axis. Unlike for the analysis of NWs, ϕ was considered in the analysis because in starch the crystals are not all located parallel to the sampling plane. Additionally, the analysis does not consider the axial rotation angle δ that was introduced for the case of zinc blende NWs because of the presupposed cylindrical symmetry of starch blocklets.

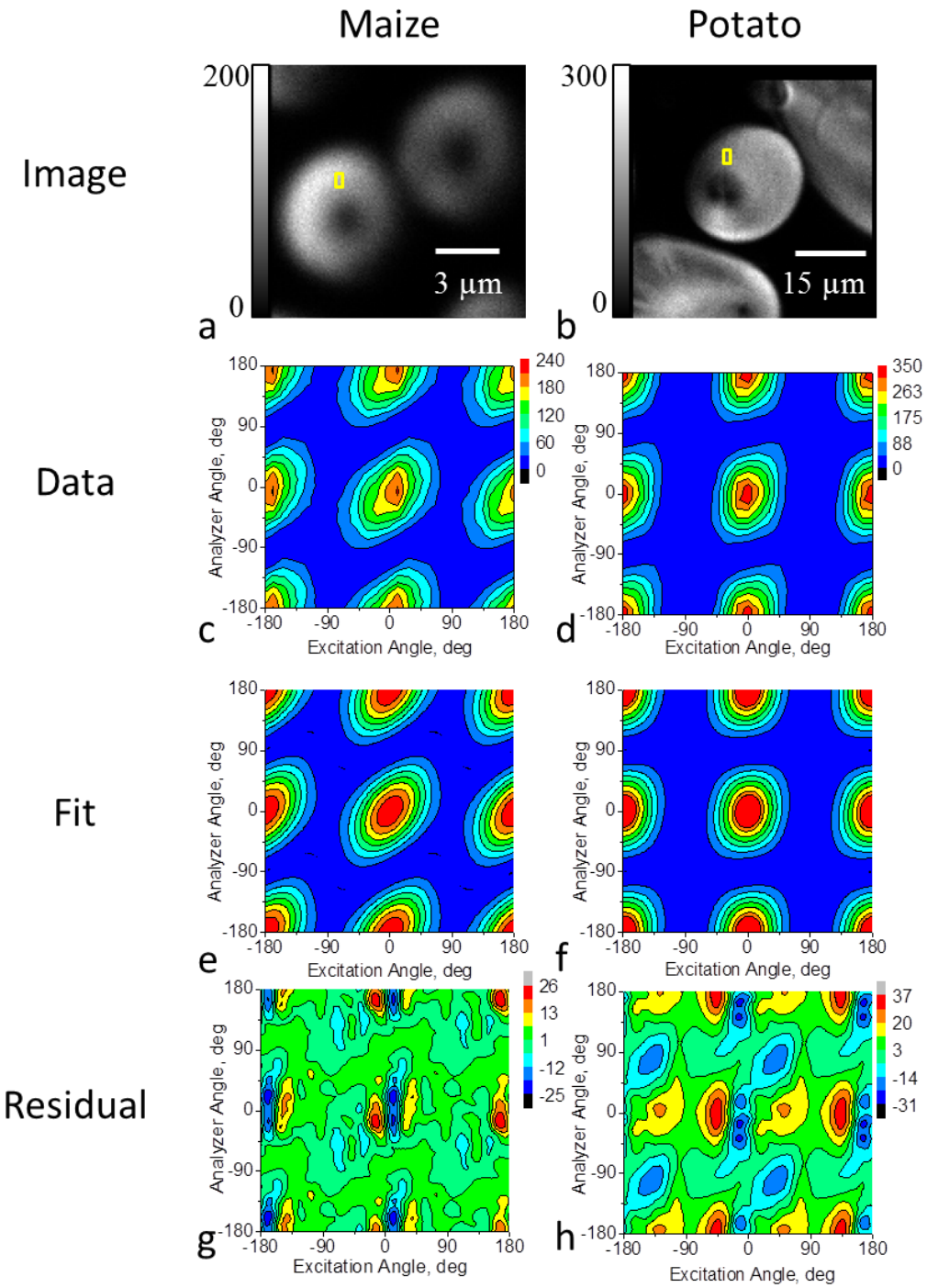

Fig. 5.3-8: PIPO SHG microscopy of maize and potato starch granules.

Representative SHG images of starch granules acquired with circularly polarized light are shown in (a) from maize and (b) from potato, however images obtained for PIPO microscopy analysis were obtained using linearly polarized light. The PIPO data for maize (c) and potato (d) is shown as contour plots (black=0, red=max) and represent data gathered from regions of interest shown as yellow squares in (a) and (b) respectively. Fits were performed to the PIPO data with Eq. 2.4-32, and are shown via contour plot in (e) and (f), and residual plots in (g) and (h), for maize and potato starch, respectively. The fit parameters are d_{33}/d_{15} = 4.2 ± 0.3 for maize and d_{33}/d_{15} = 6.4 ± 0.5 with $\Delta n = 0.009 \pm 0.002$ birefringence for potato.

Fig. 5.3-8 shows the PIPO SHG data for typical fresh potato and maize starch granules. PIPO data was recorded for small sample regions inside the granules totaling 100 images representing different incoming laser and outgoing SHG polarization orientations. The sample SHG images of the granules are shown in Fig. 5.3-8 (a) for maize and (b) for potato. Typical measured PIPO SHG data is depicted as contour plots in Fig. 5.3-8 (c) and (d) for maize and potato granules, respectively, where SHG intensity (0=black, maximum=red) is plotted as a function of the excitation angle θ (x-axis) and the analyzer angle κ (y-axis) (for angle definitions see Fig. 2.4-1) and corresponds to the regions of interest shown in panels (a) and (b). Generation of the PIPO plots is described in section 3.4.4. Fits to the PIPO data (Fig. 5.3-8 (c) and (d)) were performed using the equation derived for hexagonally symmetric crystals (Eq. 2.4-32), which takes into account birefringence of the IR as well as the SHG beam. Fitting the PIPO data was complex due to the numerous amounts of parameters, therefore Eq. 2.4-32 was first used to determine the hyperpolarizability ratios d_{31}/d_{15}, and d_{33}/d_{15} independently of the other parameters, followed by refined fitting of the equation with the remaining parameters. Fig. 5.3-8 (e) and (f) shows fits for maize and potato starch, respectively. Fits to the data were quite good, having goodness of fit parameters $R^2 > 0.95$. The residuals of the fits for maize and potato starch granules are shown in Fig. 5.3-8 (g) and (h), respectively, and show that the fits were not perfect. Deviation from the fits typically occurs near the central maximum due to several errors. Manual alignment of the starch PIPO SHG images on top of one another was likely the largest error. Images at different orientations of the HWP shift, because the HWP is wedged and because the threading on the mount is a bit loose. Although error played a higher role in starch imaging because starch images at different polarizations appear different (lobes move with polarization), and therefore, alignment with automatic algorithms could not be performed, as it was in NW PIPO data, and instead images were aligned manually. Furthermore, the error due to slightly shifting images in starch PIPO analysis is larger than in NW analysis because, starch granule are radially organized, aka different regions are oriented in different directions, while all regions in the NW point in mostly the same orientation. Fitting with $d_{33}/d_{15} \neq 1$ did not improve the fit, therefore, since starch granules do not absorb in the visible range, (see Fig. 5.2-2), $d_{33}/d_{15} = 1$ was used throughout the fits. The fitting parameter for maize $d_{33}/d_{15} = 4.2 \pm 0.3$ is much smaller as compared with $d_{33}/d_{15} = 6.4 \pm 0.5$ for potato, and is representative of typical maize versus potato granules. The hyperpolarizability ratio for maize is in agreement with SHG measurements of wheat starch (Psilodimitrakopoulos, Amat-Roldan et al. 2010), which is sensible since the small

wheat granules examined in that study reportedly contain the same type of crystallinity (amylose A) as maize (Evers 1971). The observed difference in d_{33}/d_{15} between maize and potato granules is experimentally significant, and is here attributed to variations in structure of the amylose crystals, A versus B, between the two botanical origins of the granules.

Effect of birefringence

Fits to PIPO data were examined to reveal the intrinsic birefringence of starch granules. Fitting with the birefringence parameter did not improve the fits, however, since starch granules are known to be birefringent it was used. If birefringence is neglected during the analysis of the potato granule PIPO data, the resulting fits have significantly higher perceived hyperpolarizability ratio values. For example, if birefringence is not taken into account, the fitting parameter for typical potato starch PIPO data, Fig. 5.3-8 (b) is $d_{33}/d_{15} = 12 \pm 2$, significantly different from the value of 6.4 ± 0.5 when birefringence is taken into account. Therefore birefringence is an important parameter that needs to be considered, in agreement with a polarization-SHG study of collagen, where a birefringence of $\sim\Delta n=0.003$ was found to significantly alter the results of the hyperpolarizability ratio (Aït-Belkacem, Gasecka et al. 2010). For fitting birefringence it was assumed that path lengths of the IR and SHG beams were identical, since PIPO measurements were obtained at the equatorial plane of the granules. Furthermore the Kleinman symmetry that was already determined by initial fitting of the PIPO data implies wavelength independent birefringence (Kleinman 1962; Aït-Belkacem, Gasecka et al. 2010), therefore the condition $\xi_{2\omega}=2\xi_{\omega}$ was used for fitting (Eq. 2.4-32). The retardation fit parameter for the PIPO data from potato was determined to be $\kappa = 22 \pm 5°$, corresponding to the fit Fig. 5.3-8 (f), and revealed that birefringence of potato granules is a significant factor. Taking potato starch granule size into account, and using Eq. 2.4-27, a birefringence of $\Delta n=0.009\pm0.002$ was estimated for potato granules. This value roughly corresponds to the classic birefringence values previously measured in potato of $\Delta n=0.012$-0.015 (Frey-Wyssling 1940; Frey-Wyssling 1969). The value also closely matches the more recent measurement $\Delta n=0.0083$ (Chandrashekar, Savitri et al. 1987), which also claims that the fast and slow axes are reversed in potato as opposed to cereal starches, a claim that cannot be addressed by our measurement, since the PIPO SHG intensity equation is even with respect to the birefringence orientation, see Eq. 2.4-32. These birefringence values are significantly smaller than the birefringence of stretched pure amylose B film recently measured giving $\Delta n=0.031$ (Shogren 2007), which is sensible since

stretching induces significant alignment, likely more than occurs naturally in starch granules. In this calculation the plane wave approximation was used, and further numerical calculation would be required to reveal the effects of focusing condition as well as the traversal of the focusing beam through the starch granule.

Fitting could not accurately determine the birefringence of maize granules in 3 out of 4 fits, since the birefringence parameter had little effect on the goodness of the fit. The likely cause was the small size of maize granules studied, which, if the birefringence was similar to potato, as indicated by measurement of other cereal starches (sorghum $\Delta n=0.0061$ and wheat $\Delta n=0.0081$) (Chandrashekar, Savitri et al. 1987), would only induce ~5° of phase shift. In only a single fit a retardation of $\kappa = 5 \pm 8°$ was determined, and corresponds to a similar birefringence as potato.

There were several approximations performed during the PIPO starch experiments. Starch granules were not perfectly spherical, and therefore an estimate of granule diameter was used based on an average of the observed long and short axis. Additionally the laser wave front was assumed to be unaltered by the granule. However the round shape of the starch granule, as well as the internal heterogeneity of the granules likely affects the beam wave front, and could be addressed in future investigations using a nonlinear microscope system that employs deformable mirrors to pre-compensate for induced wave front aberrations (Musikhin, Samim et al. 2011).

The birefringence of a starch granule is accounted for by fitting a polarization phase shift to the IR beam as it propagates through the granule, as well as to the SHG beam that traverses out of the starch granule. The birefringence is not straightforward to calculate, since the uniaxial crystals within the granule are aligned radially, and therefore, differ from the birefringence induced by a laser as it propagates through parallel oriented crystals, that would be calculated by Eq. 2.4-27. Instead the phase shift due to birefringence depends on the position where the laser enters the granule, see Fig. 5.3-9 (b). In order to calculate the birefringence from a starch granule, integration of the formula Eq. 2.4-27 for phase induced in the linearly polarized laser by birefringence is necessary since starch granules are not composed of parallel crystals. The apparent extraordinary index of refraction remains constant (n_e) while the apparent ordinary index (n_{ao}) depends on the angle that the starch crystals make with the laser beam, ρ (see Fig. 5.3-9 (b)) and the ordinary refractive index (n_o) in the following way:

$$\frac{1}{n_{ao}(\rho)^2} = \frac{\sin^2\rho}{n_o^2} + \frac{\cos^2\rho}{n_e^2} \qquad 5.3\text{-}1$$

At a small change in angle $\partial\rho$, the path length ∂l depends on the position where the laser enters the granule, defined by the angle ρ (see $\boldsymbol{k}$ vector in Fig. 5.3-9 (b)),

$$\partial l(\rho) = r\left(\sin(90-\rho) - \sin(90-\theta-\partial\rho)\right) \qquad 5.3\text{-}2$$

where r is the radius of the granule. In order to calculate the birefringence, Eq. 2.4-27 was numerically integrated using Eq. 5.3-1 and Eq. 5.3-2 at different values of ρ, and the results are shown in Fig. 5.3-9 (a) as ratios between the integrated phase assuming starch granule is a sphere of radial crystals, versus the phase from a slab of size r of parallel crystals. The integral was calculated assuming a birefringence of Δn=0.015. The ratio is convenient since it is independent of the granule radius, and therefore it can be easily used in combination with Eq. 2.4-27 to calculate the phase induced by the starch granule. For the birefringence calculation above, we assumed that the laser entered the granule near the hilum, ρ=10° form the hilum (Fig. 5.3-9 (b)), and therefore the factor 0.67 was used to estimate the intrinsic birefringence of the potato starch granule.

a

Beam Position (ρ, deg)	Slab/Circle Phase Ratio
0	0.66
10	0.67
20	0.70
30	0.75
40	0.80
50	0.80
60	0.91
70	0.96
80	0.99

b

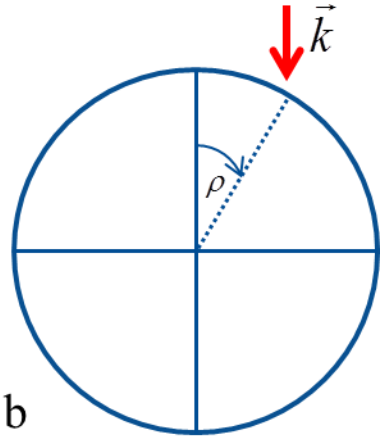

Fig. 5.3-9: Phase induced in a laser beam and SHG beam due to birefringence of a radial starch granule.

The phase induced in 1029 nm laser light traversing half the starch granule due to birefringent uniaxial crystals with Δn=0.015 as a function of the position of the entrance angle of the laser which travels along $\boldsymbol{k}$, shown in (b) as a red arrow, and represented in the chart (a) as the angle ρ. The phase is represented as the ratio between the integrated phase from uniaxial crystals from ρ in (a) to 90°, versus the corresponding phase induced assuming a slab with thickness r of parallel crystals, aka $n(\rho)=n_o$.

Structural origin of SHG

The variation in hyperpolarizability ratio data between maize and potato starch granules obtained by PIPO SHG microscopy likely originates from variations in crystal structure of amylose A and B crystalline domains. This hypothesis is supported by a recent study which showed that crystalline regions inside starch granules are responsible for the SHG, based on the observation that SHG intensity from amylopectin-rich rice granule mutants, which have high crystallinity, were observed to have higher intensity SHG than amylose rich rice mutants, which have low crystallinity (Zhuo, Liao et al. 2010).

The origin of the variation of hyperpolarizability ratio between maize and potato granules is not explained by the helical pitch hypothesis. A recent study has attributed the origin of measured hyperpolarizability ratio value of wheat starch granules according to the hypothesis that a single term dominates the starch hyperpolarizability, and is parallel to the helical pitch of the amylose crystal helices in starch granules (Psilodimitrakopoulos, Amat-Roldan et al. 2010). In that study the magnitude of the hyperpolarizability ratio d_{33}/d_{15} was attributed to the angle of the helical pitch of the amylose crystal (Psilodimitrakopoulos, Amat-Roldan et al. 2010), according to Eq. A2-1. However, the average helical pitch of amylose A is lower than the helical pitch of amylose B (by 1.8°, see Appendix 4), and hence, does not explain the observed variation in hyperpolarizability ratio between maize and potato starch granules, which would imply the helical pitch amylose B is 5° lower than A. Other than the difference in helical pitch, the crystals of amylose A and B differ by their water content (Imberty, Buleon et al. 1991). Therefore, the origin of the hyperpolarizability difference between starch A and B could be based on the variation in hydration between the two crystal types. In order to pursue this hypothesis, in the next section potato starch granules are treated with varying hydration conditions and investigated by PIPO SHG microscopy.

5.3.10 PIPO microscopy of starches at different hydration conditions

Water plays a very important role in the architecture of starch crystals. Completely anhydrous amylose type B for example gives no X-ray powder diffraction diagrams, requiring a minimum of 8% hydration to first observe the diffraction peaks (Imberty and Perez 1988). The positions and intensities of the X-ray diffraction peaks in amylose B vary with increasing hydration until 25-30%, afterwards the variations become small (Imberty and Perez 1988). Since SHG signal is

highly sensitive to the crystalline structure of the starch granules, we performed PIPO SHG investigations on potato starch granules at different hydration conditions, and also starches treated with deuterium. Dry potato starch granules (Sigma) were compared to potato starch granules treated with deuterated water for 48 hours, treated with distilled water for 48 hours, and treated with high vacuum drying at 0.01 mbar pressure for 8 hours. The sample preparation is described in more detail in section 5.3.2.

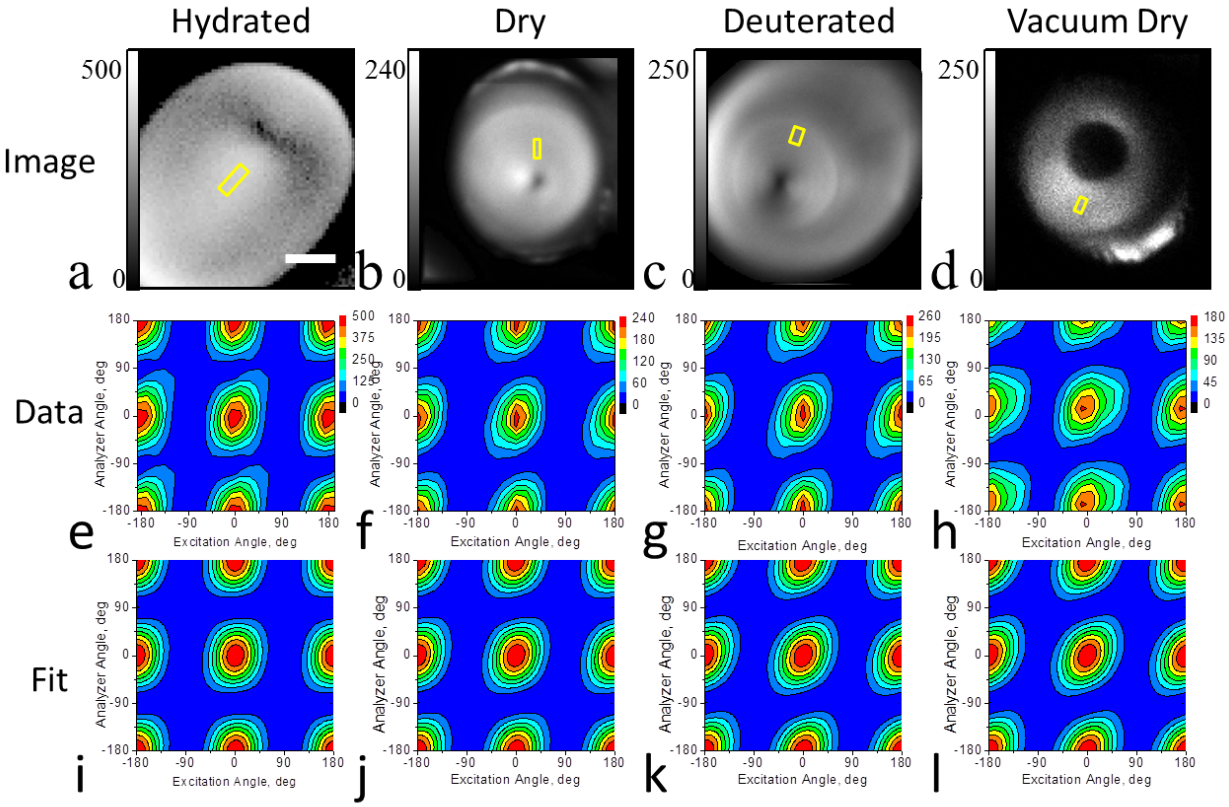

Fig. 5.3-10: PIPO SHG microscopy of potato starch granules at different hydration conditions.
A starch granule hydrated in distilled water is shown in (a), a dry untreated granule is shown in (b), a granule hydrated in D_2O is shown in (c) and a very dry granule treated with 0.01 mbar vacuum is shown in (d). Sample SHG images shown were obtained with circularly polarized light (a)-(d) and show regions of interest (yellow rectangles) that were investigated with PIPO SHG microscopy, data shown in (e) – (h). Images for PIPO microscopy were obtained with linearly polarized light. Panels (i)-(l) show corresponding fits, with parameters d_{33}/d_{15}=6±1 with birefringence Δn= 0.009 ± 0.003 for (a,e,i), d_{33}/d_{15}=5.6±0.6 with birefringence Δn= 0.010 ± 0.004 for (b,f,j), d_{33}/d_{15}=5±1 with birefringence Δn= 0.007 ± 0.003 for (c,g,k) and d_{33}/d_{15}=4.5±0.7 with birefringence Δn = 0.009 ± 0.004 for (d,h,l). The representative images (a-d) are scaled to the bar in panel (a) which represents 5 μm.

Fig. 5.3-10 reveals that variations in hydration condition of potato starch granules influences their hyperpolarizability PIPO data. Although the experimental uncertainties were large, a trend can be observed showing that typical hydrated potato starch granules Fig. 5.3-10 (a,e,i), had the highest hyperpolarizability ratio d_{33}/d_{15}=6±1, and in decreasing order were: dry

granules (b,f,j) (d_{33}/d_{15}=5.6±0.6), granules treated with D_2O (c,g,k) (d_{33}/d_{15}=5±1), and finally, granules dried under high vacuum (d,h,l) (d_{33}/d_{15}=4.5±0.7). The PIPO fit data for a typical maize granule (Fig. 5.3-8 (a,c,e)), had a d_{33}/d_{15}=4.2±0.3 value, lower than the highly dried potato starch granules. The results are in line with previous observations that B type starch granules convert to type A under low moisture and heat drying conditions (Vermeylen, Derycke et al. 2006). The hydration of B type starch, between 8% and 33% water, is known to linearly correlate to crystallinity, as measured by the intensity of the X-Ray diffraction peak (Buléon, Bizot et al. 1982; Buléon, Bizot et al. 1987). Therefore, the observed correlation between hyperpolarizability ratio d_{33}/d_{15} of B-starch and hydration is attributed to the water mediated changes in crystallinity, and therefore alignment of starch material. The birefringence parameters are likely changing, however, the change is too small to measure this effect. Birefringence is based on different indices of refraction, and does not require the material to be non-centrosymmetric or crystalline. A decrease in birefringence would indicate that alignment of helices is changing, and a changing hyperpolarizability would be expected. Birefringence may occur due to orientation of molecular chains in the amorphous starch regions (aka due to amylose) and not due to crystallinity (aka amylopectin) (Zobel 1988).

The observation that deuteration influenced the hyperpolarizability ratio of starch granules is intriguing. Deuteration via keeping potato starch powder in pure D_2O is known to exchange of hydrogens to deuterons in hydroxyl groups of the glucose residues, as well as, in all water molecules, but not in the protons of the C-H bonds (Lechert 1977). According to the fits found for the PIPO data of a potato granule treated with deuterated water, Fig. 5.3-10 (d,h,l), deuteration decreased the hyperpolarizability ratio d_{33}/d_{15} of the granule as compared to a water-hydrated granule. The variation corroborates the hypothesis that water is the source of hyperpolarizability in starch granules. The hyperpolarizability difference is not attributed to the magnitude of hyperpolarizability of light versus heavy water, since only a 1% difference was calculated with TDHF theory (Yarkony 1995). Instead the difference is attributed to the difference in orientation of D-O bonds as opposed to H-O bonds within starch. The hydroxide bonds orientation in starch crystals is determined by the hydrogen bonding network, which is expected to reorient upon deuteration. Differences between heavy and light water have recently been investigated by a combined study of neutron and X-Ray diffraction (Soper and Benmore 2008), and revealed: the angle between deuterons in D_2O is 103° as opposed to 101.4° between

hydrogens in water, D-O bonds are 3% shorter than H-O bonds and hydrogen bonds between D_2O are 4% longer than H_2O. On the basis that water forms a semi-stationary 3D hydrogen bonding network in starch granules, which has non-centrally oriented hydroxide bonds determining the hyperpolarizability of starch granules, it is no surprise that deuteration produces a re-organization of this network and results in changes in orientation of hydroxide bonds.

Several approximations were made in the preceding investigation. The variations in starch granules due to swelling as well as changes in scattering were not accounted for. Additionally the plane wave approximation was once again made, which ignores the structural irregularity of the granules including the round surface, as well as internal heterogeneity of the granules.

In conclusion, hydration of starch granules likely plays a key role in the generation of SHG based on observed variations of the hyperpolarizability ratio d_{33}/d_{15}. This observed variation is sensible since hydration has been correlated to crystallinity of B-type granules (Buléon, Bizot et al. 1987), which in turn is related to orientation of hydroxide and hydrogen bonds which likely generate SHG in starch granules. The link between crystallinity and the level of hydration has been put forth by proton NMR studies which have shown that B-type starch granules have a large population of immobile water, presumably the water that is part of the crystal, known as anisotropically bound water (Hennig and Lechert 1977). Therefore the investigation provides further evidence for the hypothesis that water molecules in starch crystals are at least partially responsible for the SHG from starch granules. To investigate this hypothesis further, the effect of heat treatment, which is known to alter the state of water in starch granules, is performed in potato starch granules.

5.3.11 Effect of heat treatment on SHG of starch granules

The effect of heat treatment has been studied in starch granules via SHG intensity imaging. The experiment was performed to determine if heat treatment, which results in breaking hydrogen bonds inside the amylose B biocrystalline shells of potato, would affect the SHG from the starch granule. Three samples of starch granules from the same fresh potato were embedded in polyacrylamide gel between microscope coverslips, and immersed in 65ºC water for 15 s, 30 s and 45 s, respectively, followed by SHG imaging using a laser with circularly polarized light. The heat treatment resulted in a dramatic SHG decrease as shown in typical granules Fig. 5.3-11

(a), (b) and (c), respectively. The heat treatment reduced the intensity below the possibility to obtain PIPO microscopy data, however the effect was studied by comparing SHG intensity of many granules at different heat exposures and the typical SHG images are shown in Fig. 5.3-11. Granules immersed in hot water of 65°C for 15 s did not result in significant intensity change (Fig. 5.3-11 (a)), but 30 s immersion produced a dramatic SHG intensity decrease, often accompanied by the emergence of channels or cracks (Fig. 5.3-11 (b)). Heat treatment of 45 s often completely destroyed the granules, but some remained with low SHG intensity, such as the granule shown in Fig. 5.3-11 (c), in agreement with a recent paper showing heat reduced SHG in starches (Slepkov, Ridsdale et al. 2010).

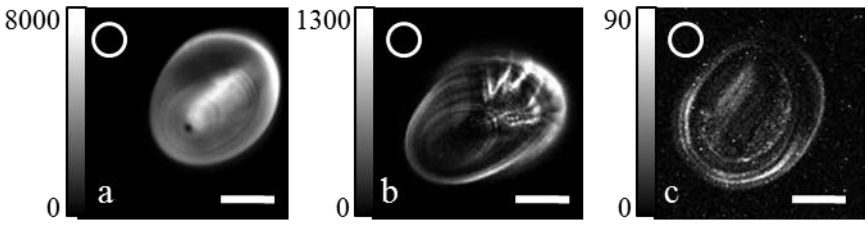

Fig. 5.3-11: SHG images of heat-treated potato starch granules.
Granules held in polyacrylamide gel between microscope coverslips were heat-treated in 65ºC water for 15 s, 30 s and 45 s, resulting in typical SHG images (a), (b) and (c) respectively. The scale bars are 5 μm.

The loss of SHG from heat treatment of starch granules provides evidence that starch granules generate SHG from oriented water molecules within starch, and/or from an oriented hydrogen bonding network mediated by the water molecules. Heat treatment at 65°C is known to reduce the hydrogen bonded population of water in amylose B crystals and in starch granules (Hennig and Lechert 1977; Lechert 1981), as observed by NMR measurements. During the heat treatment amylose and starches also loose crystallinity, as measured by decreased intensity of the X-Ray diffraction peak, which provides further evidence that the hydrogen bonding network which reinforced the crystal is severed (Imberty, Buleon et al. 1991). Therefore the SHG decrease observed during heating gives evidence that either the oriented water molecules, or the hydrogen bonding network, which previously supported the crystal via inter- and intra-helix hydrogen bonds, contributes largely to the SHG in starch granules. Additionally the observed loss of SHG could be associated with the alignment distortion of amylose helices. To address these fundamental questions the susceptibility values of starches are approximated using calculations of amylose A and B crystals with time dependent Hartree-Fock theory in the following section. The ability of SHG microscopy to monitor dynamic changes in the structure

of starch could be applied to complement starch degradation studies with amylase enzymes (Lopez-Rubio, Htoon et al. 2007) and acid (Li, Guiltinan et al. 2006), which are commonly performed for purposes of utilizing starches in industrial applications.

5.4 Theoretical Modelling the $\chi^{(2)}$ Tensor of Starch

Modeling of the hyperpolarizability tensor of starch granules was performed by calculating the hyperpolarizability of amylose crystals A and B using bond additivity as well as time dependent Hatree-Fock theory. The investigation was performed to explain the experimentally measured high hyperpolarizability ratios d_{33}/d_{15} of maize and potato starches, which ranges between 4.2 and 6.4, respectively. Amylose A consists of three unique residues and amylose B consists of two unique residues therefore, the hyperpolarizability of each residue, as well as couplings between residues was calculated in order to deduce the origin of SHG from starch.

Time dependent Hatree-Fock (TDHF) calculations were performed to determine the theoretical hyperpolarizability of amylose crystals. While quantum mechanical methods for calculating the first hyperpolarizability of molecules, such as TDHF, have long existed, the computational expense of the calculation for even a small biological molecule, with a sufficient level of theory, is not practical. Therefore, approximation methods using smaller segments, which may be more readily calculated, are often employed (Perry, Moad et al. 2005; Gualtieri, Haupert et al. 2008; Loison and Simon 2010; Tuer, Krouglov et al. 2011). In this study the hyperpolarizability of starch crystals is approximated by a sum of the hyperpolarizabilities of the individual unique glucose residues, dimers and trimers. This approximation is necessary due to the limitation of the software and computational power available, which limits the time to 48 hour durations with 32 cores, giving a maximum of 100 atoms, or 3 glucosyls per calculation. The hyperpolarizabilities of amylose residues as calculated by TDHF calculations are very sensitive to structural variations between the residues. These variations can be classified into four groupings: (i) the variations of the main residue structure, or structural deformation, which results in slight shifts of the C, O and hydrocarbon H atoms, (ii) the orientation of the residue within the helix, which demonstrates the contribution of nonlinear dipoles of the residue to d_{33} and d_{15} cylindrical hyperpolarizability components, (iii) the variations in positions of hydroxide H atoms, which are not known from the crystal structure, and could be somewhat varied, and (iv) the choice of where to cleave the residue, aka which atoms to include in a single residue,

choosing from C4', O1, O4 and O1'. TDHF calculations were performed using the 6-311++G** basis set, unless noted otherwise, with the GAMESSUS (Gordon Group, Ames Laboratory, Iowa State University) (Schmidt, Baldridge et al. 1993) software package on the SciNet supercomputing cluster at the University of Toronto.

This investigation was performed via several major steps outlined in the following sections. First the bond additivity method is used for calculating hyperpolarizabilities in order to achieve a preliminary basic understanding of the nonlinear properties of amylose residues (glucosyls). The hyperpolarizability of a generic amylose residue is calculated by the bond additivity method in section 5.4.1, and the structural deformation between residues is addressed by investigating five unique residues from amylose A and B crystals. The bonds that contribute most to the hyperpolarizability of a residue are determined. Then in section 5.4.2, the orientation of the residue in a helix is examined and nonlinear dipoles contributing to the hyperpolarizability of a helix are deduced by applying the cylindrical symmetry operation to the hyperpolarizabilities of residues oriented at a position occupied in the helical structure. In section 5.4.3, segmentation of the residue, as well as effects of residue-residue coupling are evaluated using time dependent Hartree Fock calculations. The optimal segmentation is chosen, and hydrogen and hydroxide bonds are determined to give the dominant hyperpolarizability components to the amylose helix. In section 5.4.4 hyperpolarizabilities of amylose A and B crystals are evaluated based on different choices of hydrogen and hydroxide bonds from segmented molecular hydrogen bond networks.

5.4.1 Hyperpolarizability of amylose residues from starch

The hyperpolarizability of a generic amylose residue of starch is presented, and the effects of variation in structure (deformation), between the unique residues from amylose, three in type A, (A1, A2 and A3), and two in type B (B1 and B2), are calculated. The investigation uses the bond additivity method to determine the bonds, which contribute to the hyperpolarizability of a generic amylose residue, and to determine the magnitude and direction of the change in hyperpolarizability due to deformation between the unique residues.

Bond additivity calculation of the hyperpolarizability of a generic amylose residue is presented in this section. Section 2.6.3 introduced bond additivity calculations of hyperpolarizabilities. Although the bond additivity model does not always accurately predict the

first hyperpolarizability, as bond-bond interactions should be considered (Pillai 2006), nonetheless, it has been successfully used for simple organic non-conjugated molecules (Rocha-Mendoza, Yankelevich et al. 2007; Tuer, Krouglov et al. 2011), and it is used here as a guide to understand the experimental results, as well as the results of the more complex TDHF calculations, which will be performed in sections 5.4.3 and 5.4.4. Using bond additivity for calculating hyperpolarizabilities of residues is beneficial because the effects of individual bonds can be considered to reveal the exact molecular origin of the hyperpolarizabilities in amylose residues. Since the hydroxide bond orientations are not listed within the literature of X-ray crystallographic structures of amylose A and B, they are not considered in this analysis, and their effect is studied in sections 5.4.3 and 5.4.4. The hyperpolarizabilities of each of the C-H and C-O bonds in the amylose residue, shown in three projections in Fig. 5.4-1 (a)-(c), were accounted for to calculate the hyperpolarizability of the residue, which is conveniently represented by unit spheres shown at three projections in Fig. 5.4-1 (e)-(g), respectively. The hyperpolarizability from C-C bonds of amylose residues was neglected in this approximation because they are centrosymmetric, see section 2.6.4. The calculated hyperpolarizability of a generic amylose residue reveals one dominant hyperpolarizability component, visible in Fig. 5.4-1 (e)-(g), which appears to be oriented parallel to the O3-C3 bond. The residue has only one dominant hyperpolarizability component because the remaining bonds in the residue form antiparallel bond pairs. Bond additivity calculations showed that the following bond pairs have negligible hyperpolarizability, having at most 1/5 the magnitude of the main hyperpolarizability component due to their antiparallel arrangement: from Fig. 5.4-1 it can be seen that O5-C1 is opposite to C2-O2 (a) (2.6° apart), O4-C4 is opposite to C5-O5 (a) (3.0° apart), C6-O6 is opposite C1-O1 in (b) and (c) (7.8° apart), C3-H3 is opposite to C4-H4 (b) and (c) (5.2° apart), C2-H2 is opposite to C5-H5 (b) and (c) (2.3° apart), and C1-H1 is opposite to C6-H6 (b) and (c) (8.5° apart). Two unbalanced bonds remain which are attributed to the dominant hyperpolarizability of the amylose residue, H7-C6 and C3-O3, Fig. 5.4-1 (a) and (c). These two bonds are oriented almost parallel with respect to their hyperpolarizabilities, 10.9° apart, and according to bond additivity, they constitute 97% of the total hyperpolarizability of an amylose residue (calculated by magnitude of a_i, defined below). The remaining 3% of the residue hyperpolarizability originates from the remaining bonds due to imperfect antiparallel arrangements. The dominant hyperpolarizability can be approximated by a total hyperpolarizability dipole vector $\boldsymbol{a}$, which has Cartesian components a_i, which can be calculated via:

$$a_i = \sum_j \frac{1}{3}\left(\beta_{ijj} + \beta_{jij} + \beta_{jji}\right) \qquad 5.4\text{-}1$$

where β_{ijk} are the components of the total hyperpolarizability, and the sum goes across the three Cartesian coordinates. The calculation of a_i for the generic residue reveals that the dominant hyperpolarizability is oriented roughly half way between the two dominant bonds, 4.4° from the C3-O3 bond and 3.9° from the H7-C6 bond. The average total hyperpolarizability of an amylose residue, calculated by Eq. 5.4-1 is 61.3 au.

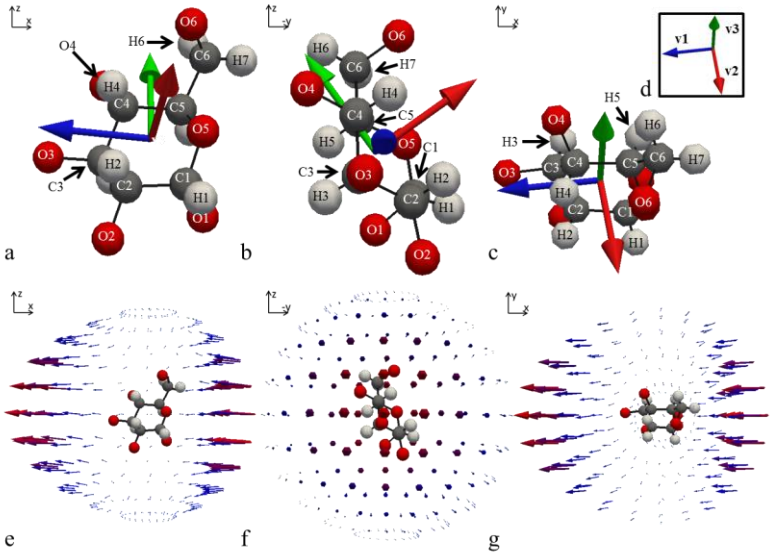

Fig. 5.4-1: Hyperpolarizability of an amylose residue calculated by the bond additivity method.
In panels (a)-(c) three projections of a glucosyl, representing a generic amylose residue, is shown with atom numbering so that all bonds can be identified. The helical direction is vertical along z, and the residue is oriented in its position within the helix. The arrows in (a) – (c) are the basis vectors defined in (d) and in the text. In (e)-(g) unit spheres of the total hyperpolarizability of a generic amylose residue are shown at three orientations, calculated by bond additivity accounting for all the C-O and C-H bonds shown in (a)-(c). Positions of atoms were obtained from (Popov, Buleon et al. 2009).

For detailed comparisons of residues, the following orthogonal basis vectors ***v1***, ***v2*** and ***v3*** are chosen (shown in Fig. 5.4-1 (a-d)); ***v1*** is along the C3-O3 bond (blue), matching the orientation of dominant hyperpolarizability in a glucosyl, ***v2*** is the vector cross product of ***v1*** and the vector joining C5 to C1, and results in a vector mostly perpendicular to the glucosyl plane (red), and ***v3*** is the cross product between ***v1*** and ***v2***, and is parallel to a line joining C1 to C5 (green).

In order to estimate the effect of residue structural differences on the hyperpolarizability, they are compared to one another by rotation of the residues to the residue A1 of amylose A (shown in Fig. 5.4-2 (a)), and alignment of the atoms C1, C2 and C3, chosen because they vary the least between the residues. The structure of residue 1 from amylose A, (A1), is shown in Fig. 5.4-2 (a) while the overlaid structures of each residue with A1 are shown in Fig. 5.4-2 (f),(k),(p) and (u) for residues A2, A3, B1 and B2, respectively. These structural overlays reveal that residues differ from one another by a slight twist in the molecular plane, see for example, Fig. 5.4-2 (p) where the circles highlight the largest deviations of O2 and O6. The hyperpolarizability of each residue is shown in two projections in columns 2 and 3, and reveals that residue deformation influences the hyperpolarizability mainly due to a slight twisting of the two bonds, C3-O3 and H7-C6, from the molecule plane, and has a small magnitude. The variations in hyperpolarizability are further revealed by unit spheres that represent the difference between each residue and residue A1, and are shown in columns 4 and 5 in Fig. 5.4-2.

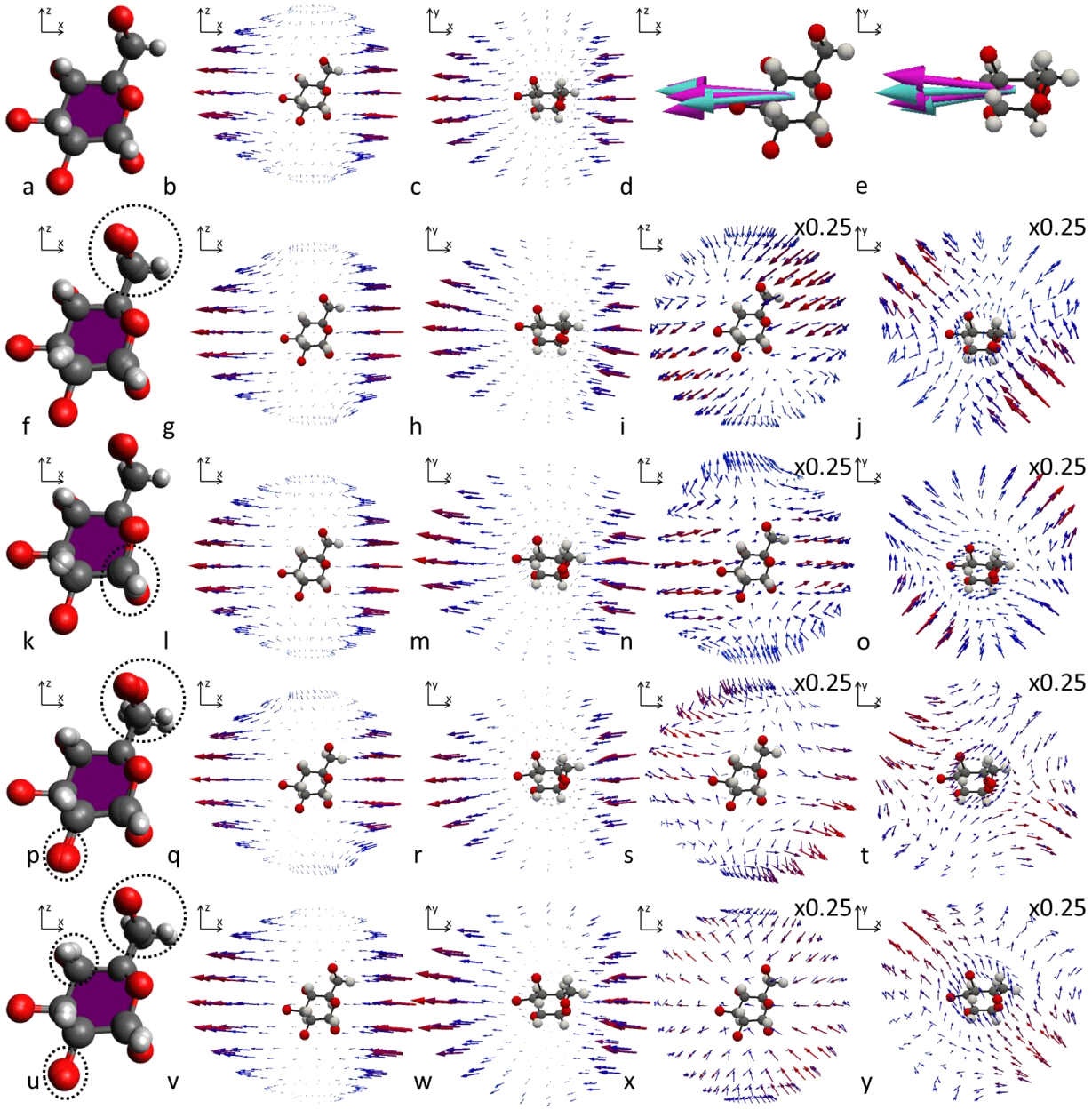

Fig. 5.4-2: Hyperpolarizability differences between residues calculated by bond additivity.

In column 1 the amylose residue A1 structure is shown in (a), while the overlaid structures of each residue with A1 is shown in (f), (k), (p) and (u), for amylose residues A2, A3, B1 and B2, respectively. Circles in (f), (k), (p) and (u) highlight visible structural variations of residues from A1. Arrows in (d) and (e) show two projections of the dominant hyperpolarizability vectors (calculated by Eq. 5.4-1) for all residues aligned to A1, magenta arrows for residues of amylose A and emerald arrows for amylose B. Starting the second row, columns 2 and 3 show two projections of unit spheres of hyperpolarizabilities of residues aligned to A1. Unit spheres representing hyperpolarizability differences between each residue with respect to residue A1 are shown in columns 4 and 5 in two projections. Changes in hyperpolarizability occur only due to deformations of the residue structure. Orientations are shown in the top left corner of each image. Residues are aligned in the helical position, with the helix along z.

A structural variation in residues has effects on the hyperpolarizability. The total hyperpolarizability, calculated by the bond additivity method, including all C-O and C-H bonds,

is shown via unit spheres in two projections in columns 2 and 3 of Fig. 5.4-2 for each residue, and shows small overall variations in total hyperpolarizability. The variations between hyperpolarizabilities of each residue are more clearly visualized by the overlay of dominant hyperpolarizability vectors ***a***, calculated by Eq. 5.4-1, shown in Fig. 5.4-2 (d) and (e) in two projections, by magenta arrows for amylose A and cyan for amylose B: each residue has a unique but similar magnitude and direction of the total hyperpolarizability vector. Interestingly, the main hyperpolarizability component, which is along the vector ***v1***, always occurs mostly perpendicular to the helical axis (Fig. 5.4-2 (d) and (e)), and hence, it only influences the perpendicular cylindrical hyperpolarizability component of the helix, while the remaining bonds, which form antiparallel bond pairs, influence both the parallel and perpendicular cylindrical hyperpolarizability components. The contribution of residues to the hyperpolarizability of a helix will be described in the next section 5.4.2. The specific hyperpolarizabilities of each unique residue of amylose A and B are described in the following subsections.

Hyperpolarizability of residue A1

The hyperpolarizability of residue A1 is dominated by a single dominant component with magnitude, calculated by vector ***a*** of Eq. 5.4-1, of 60.5 au, and direction 4.4° from ***v1***, 93.1° from ***v2*** and 93.2° from ***v3***. A1 was already investigated as the generic residue, and has a hyperpolarizability due mostly to the C3-O3 and C6-H7 bonds, which are nearly parallel to one another, and therefore the hyperpolarizability adds along their average direction. The investigation proceeds by discussing the unique hyperpolarizabilities of the remaining residues in amylose A and B compared to the hyperpolarizability of A1 in order to investigate the role of structural deformation on the hyperpolarizability of the residues.

Hyperpolarizability of residue A2

A comparison of the unit sphere projection perpendicular to the helix (Fig. 5.4-2 (c) versus (h)) reveals there is a variation of the total hyperpolarizability of residue A2 as compared with A1 due to structural deformation: the main hyperpolarizability component is horizontal in (c) and slightly inclined towards (+y) in (h). The unit spheres Fig. 5.4-2 (i,j), which represent the hyperpolarizability difference between A2 and A1, clearly show a single dipole component variation directed by 40° out of the molecular plane (j), which occurred because the angle of the total hyperpolarizability, as calculated by the vector ***a*** of Eq. 5.4-1, changed orientation by 13.0°

towards ***v1*** and 14.3° towards ***v2***. The magnitude of the hyperpolarizability vector ***a*** increased by 5.1% between A1 and A2. The percent variation in hyperpolarizability between residue A2 and residue A1, *R(A2,A1)*, due to shifts in the dominant bonds can be calculated using the following equation:

$$R(A2, A1) = \frac{\left|\mathrm{a}_{d-A2} - \mathrm{a}_{d-A1}\right|}{\left|\mathrm{a}_{d-A2} - \mathrm{a}_{d-A1}\right| + \left|\mathrm{a}_{r-A2} - \mathrm{a}_{r-A1}\right|} \qquad 5.4\text{-}2$$

where $\boldsymbol{a_{d\text{-}n}}$ and $\boldsymbol{a_{r\text{-}n}}$ are the hyperpolarizability vectors (Eq. 5.4-1) for residue *n*, and where the subscripts *d* and *r* denote consideration for only the two dominant bonds (C3-O3 and C6-H7), and only to the remaining bonds in the residue, respectively. The Eq. 5.4-2 revealed that half (50.2%) of the hyperpolarizability variation between A2 and A1 is attributed to changes in orientation of the two dominant bonds. The dominant bond C3-O3 shifted by 9.8° from ***v1*** and 9.7° from ***v2***, while C6-H7 shifted by -4.5° to ***v1*** and -5.3° to ***v2***. The remaining (49.8%) of the hyperpolarizability change between the two residues (excluding C3-O3 and C6-H7) is attributed to the reorientation of the remaining bonds with somewhat equal contributions. For variation between residues A2 and A1, the three largest contributions (having about twice the magnitude as the others) occurred due the following bond pairs: O5-C1 C2-O2, C4-O4 C5-O5, and C6-O6 C1-O1. Antiparallel bond pairs contribute two hyperpolarizability dipoles per pair, oriented at an angle ~35 and 155° from the antiparallel axis of the bonds, in the plane defined by the two dipoles. Therefore, when several antiparallel bond pairs contribute, as in the case of variation between A2 and A1 hyperpolarizability, the individual hyperpolarizability components of bonds are hard to discriminate, but one along (-z) and another along (-z,-x) is visible in Fig. 5.4-2 (i).

Hyperpolarizability of residue A3

The residue A3 varied from A1 due to partial shift of the main hyperpolarizability bonds O3-C3 by 10.7° from ***v1***, 10.0° from ***v2***, and 3.7° from ***v3***, as well as the C6-H7 bond by -4.5° from ***v1*** and -5.3° from A2. About half (*R(A3,A1)*=47.5%, Eq. 5.4-2) of the hyperpolarizability change between A3 and A1 was caused by shifting of the dominant bonds C3-O3 and C6-H6, and the rest was due to shifts in the remaining bonds. The resulting total hyperpolarizability of A3 shifted by 16.0°, and increased in magnitude only by 1%, compare Fig. 5.4-2 (c) and (m). Three distinct dipoles are visible in the difference unit sphere in Fig. 5.4-2 (n) and (o), one is due to the reduction in intensity along the main dipole due to shifts in the C3-O3 (horizontal in (n)),

while the other two occur mostly due to shifting of the antiparallel bond pairs C4-O4 C5-O5, C3-H3 C4-H4, and C2-H2 C5-H5, resulting in the two visible dipoles along (+x,+y) and (-x,+y) visible in (o).

Hyperpolarizability of residue B1

The residue B1 from amylose B has a hyperpolarizability very similar to A1, (compare Fig. 5.4-2 (b,c) to (q,r)). B1 has a total hyperpolarizability magnitude 8.3% lower than A1, and orientation shifted by 4.1° from ***v1*** and 5.0° from ***v3***. Approximately 41.4% of the hyperpolarizability change (*R(B2,A1)* in Eq. 5.4-2) occurred due to a shift in the dominant hyperpolarizability bonds: O3-C3 by 2.8° from ***v1***, -2.7° from ***v2***, and C6-H7 by -4.3° into ***v1*** and -3.5° into ***v2***. The remaining hyperpolarizability shift occurred due to antiparallel bond pairs, with the largest effects occurring from shifts in C6-O6 C1-O1, C2-H2 C5-H5 and C1-H1 C6-H6.

Hyperpolarizability of residue B2

The residue B2 was also quite similar to A1, but had a total hyperpolarizability magnitude increase of 7.9% over A1, and a shift in direction of 1.6° from ***v1***, 2.6° from ***v2*** and -5.1° from ***v3***. For B2, 33.2% of the hyperpolarizability change (*R(B2,A1)* in Eq. 5.4-2) from A1 is attributed to shifts in the dominant hyperpolarizability bonds: O3-C3 shifted 2.9° along ***v1*** and -2.7° from ***v2***, while C6-H7 shifted by 5.2° from ***v1***, 7° from ***v2*** and -2.8° from ***v3***. The remaining hyperpolarizability change between B2 and A1 is attributed to antiparallel bond pairs in the residue, with the largest effects occurring from shifts in C6-O6 C1-O1, C2-H2 C5-H5 and C3-H3 C4-H4

In conclusion two bonds, C3-O3 and C6-H7, dominate the hyperpolarizability in amylose residues. The change in magnitude of the dominant hyperpolarizability direction due to deformation of structure between the residues was on average 10%, with an average orientation change of 12°. This change in hyperpolarizability between residues due to deformation is not significantly different for residues of amylose A versus B, and does not explain the experimentally observed variation between maize and potato starches. In different residues, 30-50% of the change of the hyperpolarizability due to deformation can be attributed to shifts of the bonds C3-O3 and C6-H7, which dominate the amylose residue hyperpolarizability, while the rest occurs due to the deformation in the remaining bonds. Since the remaining bonds form six

antiparallel bond pairs, and each pair is shifted differently in each residue, and produces two resultant hyperpolarizability dipoles, the variations due to the remaining bonds are complex, with nonlinear dipole differences pointing in several directions, approaching towards an isotropic distribution.

5.4.2 Hyperpolarizability of the amylose helix based on variation of residue orientation

The variation of residue orientation and deformation within a helix is investigated to explain the experimentally observed hyperpolarizability values from maize and potato. Fig. 5.4-3 (a) shows the basis vectors that were previously defined in Fig. 5.4-1, and the definitions of the angles σ, ϱ and ρ, between each basis vector and the helical axis of amylose are shown in (b), ***v1*** (blue), ***v2*** (red) and ***v3*** (green), respectively. The three unique residues of amylose A and B are shown in the amylose helical structure (helix is vertical), in Fig. 5.4-3 (c) and (d), respectively. The orientation angles of the basis vectors of each unique amylose in the amylose helix in Fig. 5.4-1 (c) and (d) are presented in Table 5.4-1, and make a slightly different angle with respect to the helical axis, and therefore, the cylindrical hyperpolarizability of different residues is affected differently depending on the tilt of each residue in the helix.

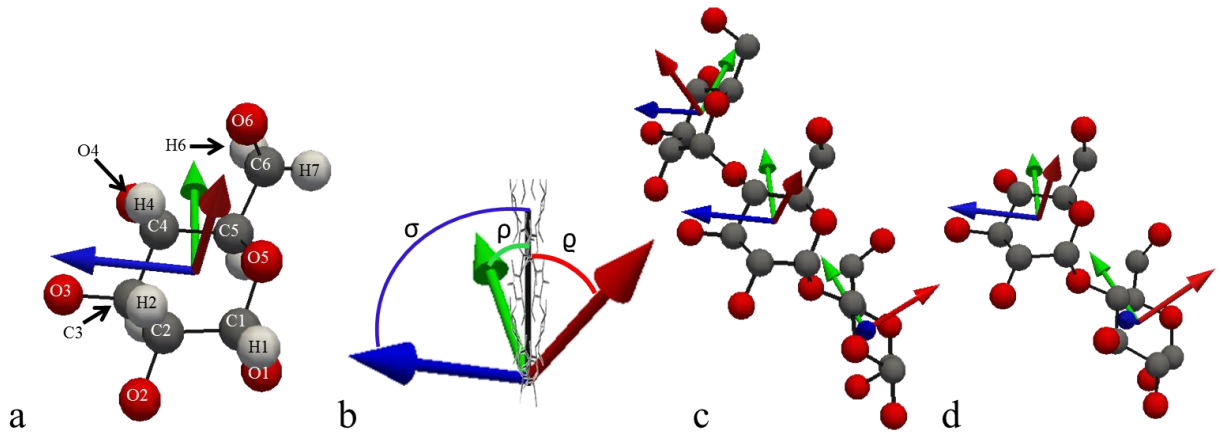

Fig. 5.4-3: The alignment of residues in amylose A and B crystals.

Panel (a) shows a generic glucose residue from amylose with the three basis orientation vectors defined in Fig. 5.4-1. In panel (b) the angles σ, ϱ and ρ represent the angle between each basis vector and the helical vertical axis, for the vectors ***v1*** (blue), ***v2*** (red) and ***v3*** (green), respectively. Panel (c) shows the asymmetric unit of amylose A crystal, consisting of three unique amylose residues, A1, A2 and A3 in a trimer, and panel (d) shows the asymmetric unit of amylose B crystal, consisting of two unique amylose residues B1 and B2 in a dimer. The helical direction is vertical in all panels. Positions of atoms were obtained from (Popov, Buleon et al. 2009) for amylose A, and (Imberty and Perez 1988) for amylose B.

For the calculation of the hyperpolarizability of a helix, two independent hyperpolarizability tensor elements, d_{33} and d_{15}, termed cylindrical elements, need to be calculated. This can be performed by imposing cylindrical symmetry in the following way: Six successive rotations of the total hyperpolarizability tensor around the helical axis every 60° are performed using the standard rotation for a rank-2 tensor, with Eq. 2.2-6, and then all the rotated hyperpolarizabilities are summed. Another equivalent method can be applied in the bond additivity method, by calculating the cylindrical hyperpolarizability components of each bond separately, and then performing a sum. For each bond with hyperpolarizability β and angle to the helical axis ς, the cylindrical components can be calculated as:

$$d_{33} = \beta \cos^3 \varsigma$$
$$d_{15} = \frac{1}{2} \beta \cos \varsigma \sin^2 \varsigma \qquad \text{5.4-3}$$

Note that cylindrical symmetry was applied to Eq. 2.4-3 to obtain the Eq. 5.4-3. In this analysis both methods were used to verify the results.

Table 5.4-1 shows the angle corresponding to the dominant hyperpolarizability, σ, which is oriented on average 84.8° and 84.2° from the helical axis, for amylose A and B, respectively. The hyperpolarizability of the amylose A and B helices based only on the bonds responsible for the dominant hyperpolarizability (C6-H7 and C3-O3) are shown in Table 5.4-1 columns 5 and 6, calculated by considering residues in the helical alignment. The values in Table 5.4-1 columns 5 have a negligible contribution to the parallel cylindrical hyperpolarizability component d_{33}, due to the large angle between the dominant bonds and the helix (σ~84.5° in column 2), see Eq. 5.4-3. These dominant bonds do however contribute to the d_{15} cylindrical parameter (Table 5.4-1 column 6), since they are aligned closer to ς=54.7°, the maximum for the d_{15} (see Eq. 5.4-3). Since the d_{33} terms are much smaller than d_{15} terms, they do not explain the experimental hyperpolarizabilities of maize and potato starches. Additionally, columns 5 and 6 in Table 5.4-1 show that d_{33} and d_{15} terms due to the dominant bonds have the same sign, similarly to the experimental results. While having d_{33} and d_{15} of the same sign occurs whenever a system has a hyperpolarizability that can be approximated by a single dominant component, it also occurs when the hyperpolarizability has two dominant components at any orientation less than 71°

apart, in addition to combinations of three or more dominant dipoles. Therefore, it is difficult to draw conclusions about the experimental results from this fact alone.

Residue	Amylose Residue Helical Tilt Angles			β of C3-O3 and C6-H7 in helix		β of all bonds in helix			β of all bonds aligned to A1	
	σ (°)	ϱ (°)	ρ (°)	d_{33} (au)	d_{15} (au)	d_{33} (au)	d_{15} (au)	d_{33}/d_{15}	d_{33} (au)	d_{15} (au)
A1	86.1	53.9	36.4	0.0	2.5	-2.7	1.1	-2.5	-2.7	1.1
A2	85.2	58.7	31.7	0.1	3.5	-6.4	2.8	-2.3	-5.9	-0.9
A3	83.1	58.4	32.6	0.3	4.8	2.0	4.7	0.4	2.4	1.2
Average A	84.8	57.0	33.6	0.1	3.6	-2.4	2.8	-0.8	-2.1	0.5
B1	84.2	54.3	36.3	0.1	3.4	-7.6	1.7	-4.6	-7.5	1.8
B2	84.1	54.5	36.1	0.1	3.3	-2.1	2.5	-0.9	-2.5	2.5
Average B	84.2	54.5	36.2	0.1	3.3	-4.9	2.1	-2.4	-5.0	2.1

Table 5.4-1: Hyperpolarizability of amylose helices by bond additivity.

Columns 2-4 show the orientation angles ρ, σ and ϱ (defined in Fig. 5.4-3) of each residue in amylose with respect to the helix. Hyperpolarizabilities (β) accounting only for the two dominant bonds C3-O3 and C6-H7 are shown in columns 5 and 6, while hyperpolarizabilities accounting for all the C-O and C-H bonds are shown in columns 7-9. Columns 10 and 11 shows the hyperpolarizabilities of residues of aligned to residue A1, in order to differentiate effects of residue tilt and deformation. All hyperpolarizabilities in the table are shown with cylindrical symmetry applied around the helical axis.

The cylindrical hyperpolarizability components of amylose A and B helices accounting for all the C-H and C-O bonds in each unique residue is shown in columns 7-9 of Table 5.4-1, and reveals the total cylindrical hyperpolarizability of amylose helices is d_{33}=-7.1 au and d_{15}=8.5 au for amylose A, and d_{33}=-9.7 au and d_{15}=4.1 au for amylose B, respectively. These values do not explain the high >3 experimentally obtained hyperpolarizability ratio d_{33}/d_{15} from maize and potato starch granules, their magnitude is lower, and their sign is opposite. Interestingly, the theoretical magnitude of hyperpolarizability ratio of amylose B was higher than type A (column 9 in Table 5.4-1) in agreement with the experiment: this was mainly due to tilt of the residue A3, which induced a higher d_{15} due to the dominant bonds C3-O3 and C6-H7 (compare Table 5.4-1 columns 6 and 8).

Columns 10 and 11 in Table 5.4-1 show the artificial situation of the cylindrical hyperpolarizability components of residues aligned to residue A1, performed to evaluate how the tilt between residues affects the hyperpolarizability of the helix. In Table 5.4-1 the similarity between the d_{33} values in columns 7 and 10 shows that the deformation and not the tilt of residues can be attributed to the d_{33} parameter in column 7. Furthermore, since the dominant hyperpolarizability bonds C3-O5 and C6-H7 have negligible effects on d_{33} due to their σ=84.5°

average angle with the helical axis (compare columns 7 and 5 in Table 5.4-1), as was mentioned earlier, it is the deformation of antiparallel bond pairs that affects the d_{33} component in amylose A and B. The tilt between amylose residues did not have a large effect from the antiparallel bonds on the cylindrical d_{33} hyperpolarizability component of amylose A and B (compare columns 7 and 10 of Table 5.4-1) because the antiparallel bond pairs can't be approximated by a single dominant dipole, but rather, a distribution, which on average has cylindrical hyperpolarizability directed downwards along the helix. On the other hand, a comparison of Table 5.4-1 columns 11 and 8 shows that the tilt between residues has a significant effect on the d_{15} cylindrical parameter of the amylose helices. The tilt of the residues with respect to the helical axis gave a significant effect on d_{15} (Table 5.4-1 columns 11 and 8) because the two dominant bonds C3-O3 and C6-H7, that significantly contribute to this d_{15} cylindrical hyperpolarizability parameter, are nearly parallel, and can be approximated by a single dipole. Interestingly, the theoretical cylindrical hyperpolarizability ratio values d_{33}/d_{15} of amylose A and B helices are negative (see column 9 in Table 5.4-1) because the two hyperpolarizabilities that dominate each residue in a helix have opposite direction with respect to the helical axis: the dominant bonds that contribute to d_{15} are oriented along the helix, since the angles of the bonds is < 90° (see column 2 in Table 5.4-1), while the remaining bonds that contribute to d_{33} have a net hyperpolarizability oriented in the opposite direction with respect to the helix.

In conclusion, the hyperpolarizability of helices from amylose residues have been accounted for, and do not explain the experimentally observed results from PIPO SHG microscopy of maize and potato starches; they have the opposite sign, and their magnitudes do not match the experimental results. The two bonds that dominate the hyperpolarizabilities of residues are oriented ~84° to the helix, and hence, while they have a minimal effect on the d_{33} cylindrical hyperpolarizability parameter, they are the dominant contribution to d_{15}, oriented along the positive orientation of the helix. The variations in helical tilt of the different residues explain the differences in the d_{15} parameter. The remaining bonds in amylose residues dominate the d_{33} cylindrical hyperpolarizability parameter, and collectively form a large distribution of hyperpolarizabilities having a net orientation in the negative helical direction. Since the hyperpolarizability of the remaining bonds is a large distribution and cannot be approximated by a single dominant dipole, it explains why tilt between the residues does not affect the d_{33} cylindrical hyperpolarizability parameter, and instead, variations of the d_{33} parameter between

residues occur due to deformations of the antiparallel bonds. While these remaining antiparallel bonds also contribute to d_{15} parameter, it is with much lower magnitude than the dominant bonds.

5.4.3 The influence of hydroxide and hydrogen bond orientations, as well as coupling between residues, on the hyperpolarizability

In this section time dependent Hartree-Fock calculations of amylose residues are performed in order to explore different factors influencing the values of the hyperpolarizability of amylose helices, which will be modeled in section 5.4.4. At first, the effects of different orientations of hydroxide bonds are investigated in a single amylose residue. Then the best residue segmentation is chosen based on minimizing the coupling between residues of a dimer. Then the hyperpolarizabilities of coupling of residues in the same helix, as well as adjacent helices is investigated. It is found that hydroxide and hydrogen bonds have by far the dominant hyperpolarizability contributions in amylose helices.

Hydroxide bonds

Hydroxide bond orientations in amylose residues are investigated by using time dependent Hatree-Fock calculations. The hydroxide bond orientation in amylose residues is not unique, since many different stable orientations can be found for each residue using optimization routines. However, there is likely a finite number of unique hydroxide bond orientations, since according to NMR evidence, water molecules have restricted mobility in starch granules (Hennig and Lechert 1977), and therefore, hydroxide bonds which orient to form hydrogen bonds between residues and with mobility restricted water molecules likely have restricted movement and defined orientations. Due to the complexity in finding optimal orientations of hydroxide bonds, they were not included in the preceding bond additivity method hyperpolarizability investigations, sections 5.4.1 and 5.4.2, in order to have a valid comparison of the effects of the residue deformation and tilt on the hyperpolarizability of the helix. In the previous sections, the hyperpolarizability of a single amylose residue in a helix was shown to have $|d_{33}| < 10$ au, therefore, since hydroxide bonds can orient into the helical axis, they could have a huge impact on the hyperpolarizability of a residue, as much as 26.6 au per each of the three hydroxide bonds. Therefore, a more robust calculation of the effects of hydroxide bonds was performed using time dependent Hartree-Fock theory for calculations of hyperpolarizabilities, as well as, for

determining possible hydroxide bond orientations. TDHF theory is beneficial since it takes into account coupling between bonds, variations in lengths of individual bonds, as well as the effects of C-C bonds, which was not considered in the bond additivity method. Details of TDHF theory as well as example calculations can be found in section 2.6.

Hydroxide bond orientations dominate the hyperpolarizabilities of amylose residues in a helix. Fig. 5.4-4 presents an amylose residue oriented such that the starch helix is directed along the z axis (vertical), with three different orientations of hydroxide bonds in (a), (f) and (k), with differences shown highlighted by circles. Differences in hydroxide bond orientations were obtained by different initial guesses of their orientation followed by geometry optimization using the TDHF calculation with the 6G-311++** basis set. The three hydroxide orientations of Fig. 5.4-4 are not unique, they were chosen because they served as good examples of the variation in hyperpolarizability of an amylose residue. In the first two rows of Fig. 5.4-4, the hydroxide bond changed orientation from being directed along (-x) direction (a), to (+x,-z) in (e), resulting in a loss of hyperpolarizability along x ((b) versus (g)), and a slight increase in +z component ((c) versus (h)). The change in one hydroxide bond orientation resulted in a small effect on the total hyperpolarizability because the hyperpolarizability of a hydroxide bond is less than 1/3 of the total hyperpolarizability of the entire amylose residue which includes all the hydroxides. The hyperpolarizability components of the residue in a helix, calculated by imposing cylindrical symmetry, and shown in column 5 of Fig. 5.4-4, show that the rotation of a hydroxide bond (compare (a) to (f)), resulted in an orientation change from perpendicular to the helical axis in (a), where it has negligible influence on the cylindrical hyperpolarizability (e), to having a large component into the helical axis in (j), which results in substantial cylindrical hyperpolarizability component d_{33}, compare (j) to (e). A single hydroxide bond significantly changes the hyperpolarizability of a residue in a helix because, as was pointed out in the previous section, amylose residues have very low cylindrical hyperpolarizabilities because their dominant hyperpolarizability is oriented 84° from the helix, and therefore, have hyperpolarizability < 10 au (see Table 5.4-1), less than half the hyperpolarizability of a hydroxide bond. The result that hydroxide bonds dominate the hyperpolarizability of residues is typical for all the residues. Another example of changing a hydroxide bond orientation in the same residue is shown in the last two rows of Fig. 5.4-4: the hydroxide bond is rotated from (+x,+y,+z) in (f) to (-x,-y,-z) in (k), which for the total hyperpolarizability resulted in reduced (-x,-z), and (-x,-y) components

seen in panels (g) versus (l), and panels (i) versus (n), respectively. Since the hydroxide orientation (f) versus (k) changed orientation with respect to the helical axis, therefore the cylindrical hyperpolarizability component of the helix d_{33} increased, (circle in (k)), further enhancing the hyperpolarizability of the helix (compare (j) versus (o)). Table 5.4-2 shows the values of the cylindrical hyperpolarizabilities of a residue with three orientations of hydroxide bonds corresponding to column 5 of Fig. 5.4-4. By changing a single hydroxide bond orientation, the hyperpolarizability ratio d_{33}/d_{15} of a single residue changed from -5.5 to nearly 250 (rows 2 and 4 in Table 5.4-2). The negative ratios in Fig. 5.4-4 occurred because to the hyperpolarizability contribution of the antiparallel bonds in the residues, which provide a net hyperpolarizability component d_{15} directed along (-z) (see section 5.4.2), while the hydrogen bonds provided hyperpolarizabilities along (+z).

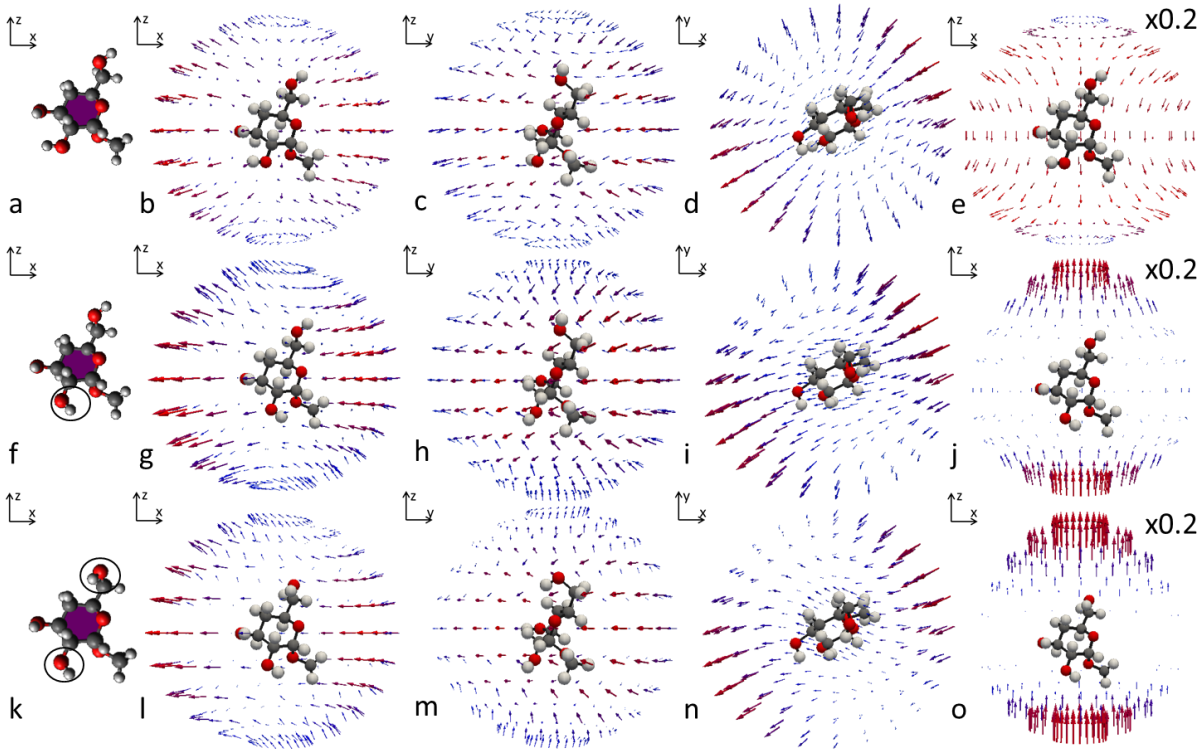

Fig. 5.4-4: Effect of hydroxyl orientations on hyperpolarizability of an amylose residue.

Results of TDHF calculations of the hyperpolarizability of a single amylose residue with three positions for hydroxide orientations (in rows) shown via the unit sphere representation. Hyperpolarizabilities are shown in three projections in columns 2-4, as indicated by the axes on the top left of each panel, and shown with cylindrical symmetry in column 5, which was scaled up by 5x to clearly visualize the arrows (indicated at top right). The hyperpolarizability values of the residue in the helix, for column 5, are shown in Table 5.4-2.

Configuration	d_{33} (au)	d_{15} (au)	d_{33}/d_{15}
1 (a-e)	1.2	-4.8	-0.2
2 (f-j)	12.0	-2.2	-5.5
(k-o)	16.7	0.1	249.9

Table 5.4-2: Hyperpolarizability of a residue in a helix at different hydroxide orientations.
Hyperpolarizability values corresponding to a residue of amylose B with hydroxide positions indicated in Fig. 5.4-4 (a), (f), and (k), and corresponds to the unit spheres (e), (j) and (o), respectively.

In conclusion, since experimental hyperpolarizability ratios d_{33}/d_{15} of starch granules are always positive, hydroxide bond orientations toward the same directions with respect to the helical axis could play the dominant role in determining the hyperpolarizability values revealed by PIPO SHG measurements. However, not all hydroxide positions are possible, due to geometry restrictions of residues in the amylose helix, and considerations of inter- and intra-double-helical hydrogen bonds, limiting the influence of hydroxide bonds to a finite number of possible configurations. Therefore, possible hydroxide bond orientations in a crystal structure are investigated in sections 5.4.4.

Segmentation of residues

TDHF calculations were used to reveal the interaction factors due to coupling between different amylose residues, and to choose the most appropriate amylose residue segmentation. The computational expense of the TDHF calculation for large molecules, with a sufficient level of theory, is not practical, therefore, approximation methods using smaller segments, which may be more readily calculated, are often employed (Perry, Moad et al. 2005; Gualtieri, Haupert et al. 2008; Loison and Simon 2010; Tuer, Krouglov et al. 2011). The choice of the optimal amylose segmentation is crucial in order to correctly approximate the total amylose hyperpolarizability. The interaction factor due to coupling between monomers in an amylose residue dimer can be calculated in the following way. If the hyperpolarizability of a monomer A1 is H(A1), and of a dimer A1A2 is H(A1A2), then the hyperpolarizability of the interaction due to coupling C(A1A2) can be calculated as (Tuer, Krouglov et al. 2011):

$$C(A1A2) = H(A1A2) - H(A1) - H(A2) \qquad 5.4\text{-}4$$

Similarly, the long range interaction due to coupling between three monomers C(A1A2A3) can be calculated, accounting for dimer coupling as follows:

$$\begin{aligned} C(A1A2A3) &= H(A1A2A3) - H(A1) - H(A2) - H(A3) - C(A1A2) - C(A2A3) \\ &= H(A1A2A3) - H(A1A2) - H(A2A3) + H(A2) \end{aligned} \qquad 5.4\text{-}5$$

Segmentation of the amylose residues played an important factor in hyperpolarizability calculations of coupling therefore, three choices were considered, shown in Fig. 5.4-5. The segmentation was chosen on the basis of minimizing the hyperpolarizability due to the interaction between monomers in a dimer, using Eq. 5.4-4. Minimizing the interaction term allows the sum of hyperpolarizabilities of the segments to better represent the hyperpolarizability of the entire amylose crystal. The residues shown in Fig. 5.4-5 (a) and (b) are segmented such that each structure contains one copy of the glycosidic bond (at C1 in (b) and at C4 in (c)), and the end carbon (C4' and C1' respectively) were saturated with hydrogens. The segment shown in Fig. 5.4-5 (c) was cleaved at the middle of the glycosidic bonds, and hydrogens were added to the terminal oxygens (O1 and O4), and for best results, the hydrogens on O1 and O4 were aligned along the same orientations as the severed O-C bonds. For segmentation configuration shown in Fig. 5.4-5 (a) calculation of the direct interaction term was performed on the dimer of amylose B, using Eq. 5.4-4, and revealed d_{33}=5.3 au, and d_{15}=-6.4 au for C(B1B2) and d_{33}=17.0 and d_{15}=-5.6 for C(B2B1). This segmentation (Fig. 5.4-5 (a)) proved to have a large interaction factor likely because the end carbon atom C4' had to be saturated, and these extra 3 hydrogen atoms gave additional hyperpolarizability. Segmentation configuration shown in Fig. 5.4-5 (b) gave very similar results to (a). Segmentation shown in Fig. 5.4-5 (c) on the other hand gave an interaction factor of d_{33}=-3.6 au and d_{15}=-1.6 au for C(B1B2) and d_{33}=2.7 au and d_{31}=-1.5 au for C(B2B1). The sum of these two interaction hyperpolarizabilities gives a relatively small result of 0.9 au and -3.1 au for d_{33} and d_{15}, respectively. Therefore the segmentation of Fig. 5.4-5 (c) was chosen for the remaining analysis. Since the correction factor was small, it was not included in the calculation of the amylose helix in section 5.4.4.

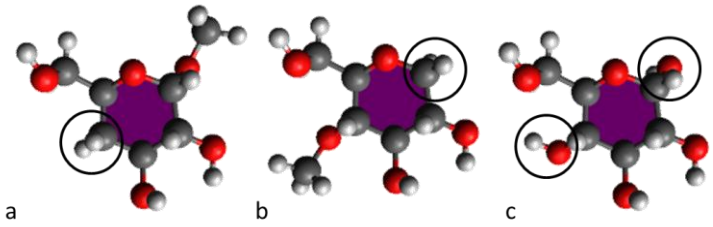

Fig. 5.4-5: Segmentation of an amylose residue.

Three possible choices for segmentation were considered, including (a) where the glycocidic link at C4 was cleaved, (b) where the glycocidic link at C1 was cleaved, and (c) where both linking oxygen atoms remain but the bonds O1-C4' and O4-C1' were severed. The circles in panels (a) – (c) indicate the cleaved bonds. Note that for this figure, the structure of the residues was flattened so that O1 is visible.

Coupling of residues

In order to visualize the interaction hyperpolarizability, and to assess its magnitude, the interaction between bonded dimers, the long range interaction between trimers, as well as, the interaction between two non-bonded but adjacent monomers is investigated. Calculations of hyperpolarizability due to coupling or interaction between residues were calculated and the results are visualized in Fig. 5.4-6. Two bonded amylose residues within a single helix, Fig. 5.4-6 (a), had a hyperpolarizabiilty due to coupling, calculated by Eq. 5.4-4, and visualized as a unit sphere in (b). Two dipole hyperpolarizability components due to coupling are visualized in Fig. 5.4-6 (b): one is directed along the bond direction between the residues (Fig. 5.4-6 (b)), and another vertical component is visible as well. The influence of hyperpolarizability of the interaction to the hyperpolarizability of the helix was calculated by applying cylindrical symmetry to the interaction hyperpolarizability, and is shown via a unit sphere in Fig. 5.4-6 (c), as well as in the Table 5.4-3. The interaction between dimers reveals a significant effect. Although this effect is smaller than the effect of a hydrogen bond, it is calculated for each dimer combination for amylose A and B, and accounted for in the hyperpolarizability calculations of section 5.4.4. For residue A, the average of the three dimer couplings are used, C(A1A2), C(A2A3) and C(A3A1), while for amylose B the average of two dimer combinations are accounted for, C(B1B2) and C(B2B1). In the hyperpolarizability calculation of a helix, one correction factor is included per residue, since each residue is bonded to the subsequent residue. Interestingly the magnitude of the interaction due to coupling changes depending on the orientations of hydroxide bonds in the residue, by over 50%, therefore it is calculated seperately for each hydroxide bond combination in section 5.4.4.

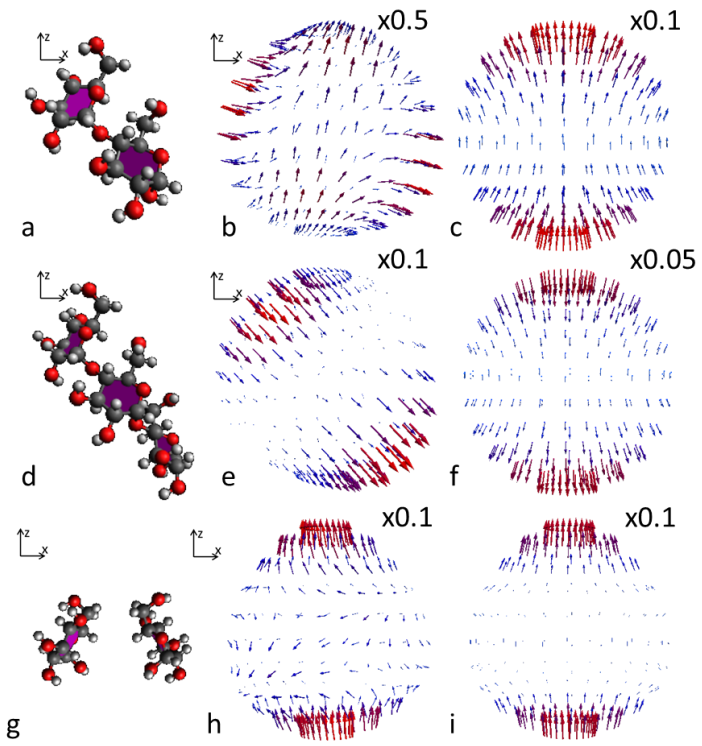

Fig. 5.4-6: Hyperpolarizability due to coupling between amylose residues.

The total hyperpolarizability of interaction due to coupling of amylose residues with orientation shown in (a,d,g) are represented by unit spheres at one projection in (b,e,h), while the cylindrical components of the hyperpolarizability of interaction, calculated via applying cylindrical symmetry, are shown in the 3rd column (c,f,i). The hyperpolarizability of interaction of the dimers in (a) and (g) were calculated by Eq. 5.4-4, while the long range interaction of the trimer was calculated via Eq. 5.4-5.

Fig. 5.4-6	**Coupling**	**d_{33} (au)**	**d_{15} (au)**
c	Dimer	3.6	1.6
f	Trimer	-1.7	-0.5
i	Non-bonded dimer	4.2	-0.8

Table 5.4-3: Cylindrical hyperpolarizability component values due to coupling between amylose residues

The cylindrical components hyperpolarizabilities due to coupling between residues were calculated via TDHF theory, using Eq. 5.4-4 for dimers and Eq. 5.4-5 for the trimer. The values correspond to Fig. 5.4-6 column 3, and only the hyperpolarizability terms that affect the helix are presented, calculated via imposing cylindrical symmetry on the total hyperpolarizability.

The hyperpolarizability of long range coupling due to three bonded amylose residues, which already accounted for coupling between dimers, was performed on the amylose trimer shown in Fig. 5.4-6 (d), via Eq. 5.4-5, with total hyperpolarizability of coupling visualized in the unit sphere in (e) and the hyperpolarizability of the interaction in a helix in (i). The TDHF calculation predicts that the hyperpolarizability due to long range coupling has mostly one dominant term oriented along the direction of coupling Fig. 5.4-6 (e), however, the magnitude of the hyperpolarizability is about 5 times less than coupling due to a directly bonded dimer. The

cylindrical components of the hyperpolarizability of the long range coupling in the trimer is less than half the magnitude as compared with the interaction of monomers in a dimer, compare Fig. 5.4-6 (c) and (f), and has hyperpolarizability of opposite sign, showing that it partially cancels with dimer coupling in this example, although this is not always the case, and depends on the orientations of hydroxide bonds, and therefore each hydroxide bond combination was separately calculated and accounted for in the calculations of amylose helices in section 5.4.4. For amylose A, the three coupling combinations were averaged, C(A1A2A3), C(A2A3A1) and C(A3A1A2), while for amylose B, the two combinations were used C(B1B2B1) and C(B2B1B2). For calculations of hyperpolarizability of the amylose helices in section 5.4.4, one long range coupling term was used for each residue. Due to computational limitations, the long range coupling was only accounted for in up to 3 amylose residues.

The Fig. 5.4-6 also shows that two residues facing each other from opposite single helices within a double helix, (g), exhibit a small coupling (h), about 5 times smaller in magnitude than coupling between a bonded dimer (b), which is sensible considering that a bond should induce more coupling. However, the hyperpolarizability Fig. 5.4-6 (h) is oriented vertically, so that even though it is 5 times smaller in magnitude, the cylindrical components of the hyperpolarizability due to adjacent coupling (i) are similar in magnitude to coupling between bonded dimers, (c). To account for coupling due to residues in adjacent helices, half this coupling is included for each residue. As for the dimer and long range couplings, the hydroxide bonds changed the coupling magnitudes, and so each hydroxide bond combination was separately considered. For amylose A, the three couplings due to residues in opposite single helices within a double helix were averaged, C(A1A1), C(A2A2) and C(A3A3). For amylose B, only a single calculated coupling had to be taken into account, C(B1B2).

In conclusion, the interaction hyperpolarizability due to coupling between residues in a dimer, the long range interaction of residues in a trimer, as well as the interaction between two non-bonded residues from opposing single helices within a double helix revealed that while the long range interaction had the lowest magnitude, all three interactions are significant to the hyperpolarizability of a helix, and are therefore accounted for in the hyperpolarizability calculations of the amylose crystal structures of section 5.4.4.

Hyperpolarizability of coupling between hydrogen bonded residues

Hydrogen bonds are an integral part of the starch crystal structure and their effect on the hyperpolarizability of amylose residues is investigated by TDHF. Hyperpolarizabilities of hydrogen bonds are commonly investigated in organic molecules using TDHF with the 6-311G basis set (Dopieralski, Panek et al. 2009; Latajka, Gajewski et al. 2009). Two types of hydrogen bonds occur in starch crystals; intra-double-helix hydrogen bonds which link two single helices of a double helix, and inter-double-helix hydrogen bonds which link neighboring double helices. Both amylose A and B crystals contain a minimum of one intra-double-helix hydrogen bond per residue, therefore, even in the simple consideration of only one double helix it is necessary to consider the effect of hydrogen bonds on the hyperpolarizability. Fig. 5.4-7 (a) and (d) show two identical glucose residues from opposing single strands within a double helix, which are linked by hydrogen bonds in opposing directions; in Fig. 5.4-7 (a) the hydrogen bond is oriented with OH-O directed along (+x,+z), while in (d) the hydrogen bond directed with OH-O along (-x,-z). The hyperpolarizability due to coupling via the hydrogen bond, shown in Fig. 5.4-7 (b) and (e), and calculated via the dimer interaction term of Eq. 5.4-4, is oriented along the hydrogen bond orientation, in the direction OH-O, and has a very large hyperpolarizability in the range 30 - 38 au, larger than the hyperpolarizability of a hydroxide bond. The magnitude of the hyperpolarizability due to the hydrogen bond orientation varied between Fig. 5.4-6 (n-c) versus (d-f); the difference occurred because the remaining hydroxide bond orientations were readjusted via an optimization routine after reversing the hydrogen bond orientation. Therefore, the hyperpolarizability of hydrogen bonds contribute largely to the hyperpolarizability of amylose, and have hyperpolarizability orientation parallel to the orientation of the hydrogen bond from H to O. We can speculate then that if the hydrogen bonding network is semi-stationary inside starch crystalline regions, and is aligned anisotropically with respect to the positive helical direction, it could be a major source of the large hyperpolarizability ratio experimentally observed in starch granules. For calculations of hyperpolarizabilites of amylose A and B crystals at different hydroxide bond combinations in the following section, all the intra-double-helix, and inter-double-helix hydrogen bonds were accounted for.

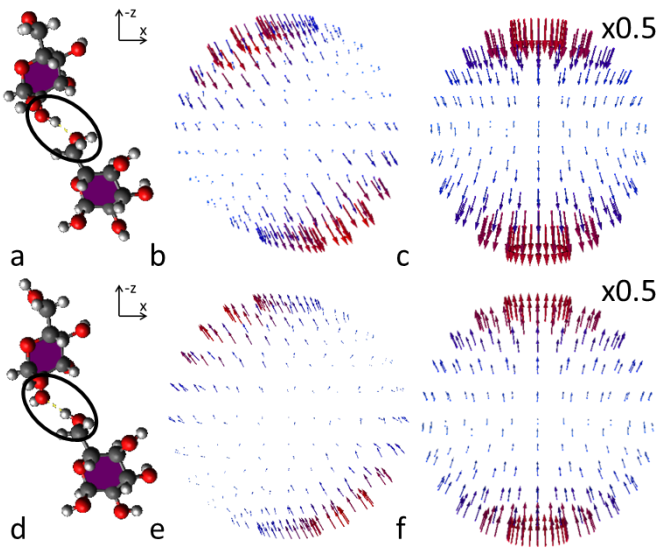

Fig. 5.4-7: The hyperpolarizability due to hydrogen bonds.

Two hydrogen bonded amylose residues are oriented with OH-O along (+x,+z) in (a) and oriented with OH-O along (–x,-z) in (d) have corresponding hyperpolarizabilites of interaction shown via unit sphere representations in (b) and (e), performed using Eq. 5.4-4. The cylindrical hyperpolarizability components are shown via the unit spheres (c), (f), and were calculated by applying cylindrical symmetry to the interaction hyperpolarizabilities (b) and (e), respectively, having values d_{33}=-25.8 au, d_{15}=-6.0 au for (c) and d_{33}=16.9 au and d_{15}=5.0 au for (f).

5.4.4 Hyperpolarizability of amylose A and B crystals

The hyperpolarizabilities of starch A and B were approximated by calculating the hyperpolarizabilities of amylose A and B crystals via the interacting segment method (Miller and Ward 1977; Sundberg 1977). The interacting segment method involved calculating the hyperpolarizability of the residues, as well as the interaction terms: dimer-dimer coupling, long range trimer coupling, the coupling between adjacent residues from two single helices within a double helix, as well as interaction due to hydrogen bonds. Critical considerations of hydroxide bond orientations and hydrogen bonding networks in the amylose crystals were taken into account for this investigation. The orientations of hydroxide bonds at O2, O3 and O6 of amylose residues were the primary concern since the influence of hydroxide bond orientations, as well as the hydrogen bond orientations were found to be the largest on the hyperpolarizability of amylose residues in TDHF calculations (see section 5.4.3). For the calculations, amylose was segmented into two and three unique monomers for amylose, A and B, respectively, according to the segmentation presented in Fig. 5.4-5 (c), and hydroxide bond orientations on the terminal residue atoms O1 and O4 were aligned along the severed bonds, since using this segmentation resulted in the lowest coupling, see section 5.4.3. For estimating orientations of hydroxide and hydrogen bonds, large portions of amylose crystal encompassing a continuous hydrogen bonding

network were selected from the crystal of amylose A and B, and were used to determine possible geometries of hydroxide bond orientations, which were subsequently used to approximate the hyperpolarizability of starch granules.

In amylose crystals literature, the orientation of hydroxyl groups are not determined. This infers that hydroxide bond orientations based on shortest oxygen-oxygen distances was complicated because an orientation ambiguity exists on each hydrogen bond pair with respect to the directionality of the bond. Therefore, it was beneficial to use large segments of a molecular network for the determination of hydrogen bond orientations. However, there is a limit to the approach since larger hydrogen bonding networks are limited in size by TDHF calculations to <100 atoms. This limit is not very critical for amylose A, which has few water molecules. However, for the amylose B water channel, which is ordered by the hydrogen bonding network, and contains 36 water molecules per one 1 unit cell thickness (see center of Fig. 5.2-4 (d)), the computational limit presents a problem. Therefore, calculations including sufficient numbers of carbon atoms from amylose B residues, and the amount of water molecules from the network, was balanced to stay within the computational limit of TDHF theory. The molecular networks used for determinations of hydroxide bond orientations are shown in Fig. 5.4-8 (a) for amylose A, and (e) for amylose B. The molecular networks were segmented based on the criteria that a continuous chain was required which contained all the unique inter-single-helix hydrogen bonds, several intra-double-helix hydrogen bonds, as well as all the hydrogen bonds between amylose residues and water. Four different hydroxide bond orientation combinations were obtained for each of amylose A (Fig. 5.4-8 (a) – (d)) and B ((e) – (h)) via different initial guesses of hydroxide orientations followed by geometry optimization. When arranging hydroxide orientations to produce differently oriented networks, directionality had to be chosen. The configurations were considered either with the hydrogen bonds directed one way from the first atom to the second, which would direct the next hydrogen bond on the second atom to the third in the network; or, the hydrogen bonds would be reversed. Upon optimization these directionalities were often preserved, showing that hydrogen bonding networks can have unidirectional long range coupled organizations. Although this observation was made only in small isolated molecular networks, it implies that in the amylose crystal inside starch granules an initial ordering of the hydrogen bonds, which could occur due to the amylose-water boundary at the edge of the granule or at the hilum, could preferentially orient the hydroxide network of the

entire crystal. Hydrogen bonds in Fig. 5.4-8 are colored in yellow and vary in the different selections of hydroxide bond orientations in the columns. Four hydroxide bond combinations were selected from each of amylose A and B because they appeared to have the most diverse geometries, but many more are possible. In the future molecular dynamics simulations could be used to determine the most probable hydroxide orientations.

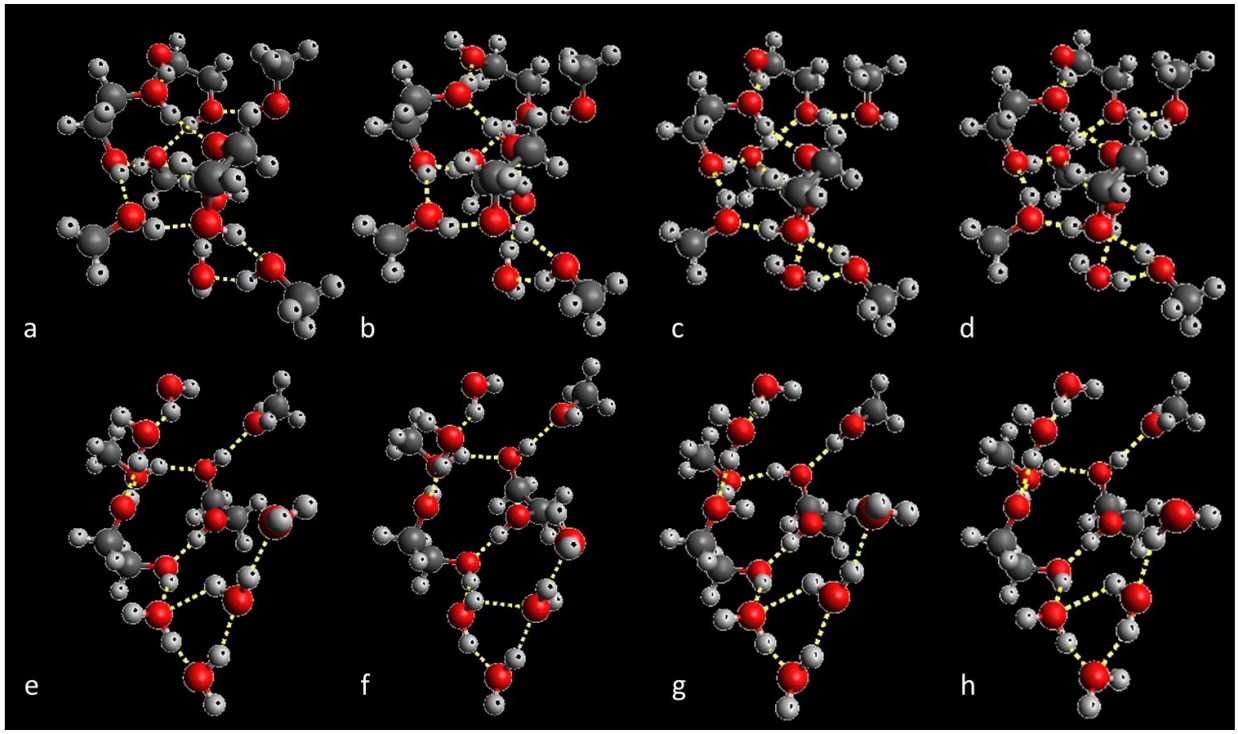

Fig. 5.4-8: Hydrogen bonding networks for optimizing hydroxide orientations.
The hydrogen bonding network chosen from amylose A is shown with four arrangements of hydroxide bonds in (a) – (d). The hydrogen bonding network from amylose B is shown with four arrangements of hydroxide bonds in (e) - (h). Hydrogen bonds are shown with yellow dotted lines. The structures are oriented with the helical direction up.

Table 5.4-4 presents cylindrical hyperpolarizability components of amylose A and B at the four different hydroxide bond orientations corresponding to Fig. 5.4-8. For all calculations shown in Table 5.4-4, cylindrical symmetry was applied so that the values represent the hyperpolarizability of the helix. Columns 2 and 3 of Table 5.4-4 show results of the average hyperpolarizabilities for the unique residues of amylose A and B, at each hydroxide bond orientation, indicated in the first column. Columns 4 and 5 of Table 5.4-4 summarize the effects of hyperpolarizabilities due to interactions of residues via hydrogen bonds, including one intra-helix hydrogen bond, one inter-helix hydrogen bond, and one residue-water hydrogen bond per residue. In Table 5.4-4 columns 6 and 7 hyperpolarizabilities due to coupling between residues are presented, including interaction due to bonded dimers within a single helix, the long range

interaction residues in a trimer and coupling due to residues in adjacent single helices of a double helix. Details of TDHF hyperpolarizability calculations can be found in the previous section 5.4.3 where calculations of residues with hydroxides, the effects of hydrogen bonds, as well as the hyperpolarizabilities of couplings are discussed.

Amylose (Fig. 5.4-8)	**Residues**		**Hydrogen Bonds**		**Coupling**		**Totals**		
	d_{33} (au)	**d_{15} (au)**	**d_{33} (au)**	**d_{15} (au)**	**d_{33} (au)**	**d_{15} (au)**	**d_{33} (au)**	**d_{15} (au)**	**d_{33}/d_{15}**
A (a)	10.4	7.7	-28.6	-16.9	3.4	-1.1	-14.8	-10.3	1.4
A (b)	-4.8	-0.9	-11.7	2.2	2.2	1.1	-14.2	2.4	-6.0
A (c)	-4.6	5.4	11.2	-3.5	-2.7	-1.4	3.9	0.4	9.0
A (d)	-3.8	5.1	13.4	-3.6	-3.0	-1.2	6.6	0.4	18.1
B (a)	-8.7	-1.6	-11.4	0.5	1.0	0.4	-19.2	-0.8	25.5
B (b)	-7.5	-1.4	-11.9	0.1	0.3	0.3	-19.1	-0.9	21.3
B (c)	-20.3	-1.1	55.8	13.3	-8.0	-0.6	27.6	11.7	2.4
B (d)	-8.8	-0.9	-14.7	0.7	2.2	1.3	-21.3	1.1	-19.4

Table 5.4-4: Hyperpolarizability of amylose A and B.

Hyperpolarizability calculations were performed on amylose A and B residues with different hydrogen positions shown in Fig. 5.4-8, referenced in column 1 of the table. The values in the table show the cylindrical components of hyperpolarizability of an amylose helix for each structure denoted in the table heading, calculated by applying cylindrical symmetry to TDHF calculations. The values in the table were scaled to be per residue.

The ordering of hydroxide bonds via different connected molecular networks in amylose A and B produces different hyperpolarizability values for each combination of hydroxide positions. Table 5.4-4 shows that residues as well as hydrogen bonds both have large contributions to the hyperpolarizability of amylose A and B helices, while the effects of hyperpolarizability due to coupling are minor in comparison. Hydrogen bonds (columns 4-5 of Table 5.4-4) had the largest contributions to the d_{33} cylindrical hyperpolarizability parameter of amylose A and B helices, because they are dominated by a single intra-double-helix hydrogen bond which is typically oriented, ~45° to the helix, giving around d_{33}=25 au, (see Fig. 5.4-7). Variations in the cylindrical hyperpolarizability components due to hydrogen bonds occurred as a result of variation of the orientation of the dominant intra-double-helix hydrogen bond, as well as, by the relative orientation of the inter-double-helix hydrogen bond, having d_{33}~8 au, and residue-water hydrogen bond, having d_{33}~5 au: the latter two hydrogen bonds were aligned antiparallel to the former in Table 5.4-4 (b), (c), (d) of amylose A and (a), (b), (d) of amylose B, in (a) of amylose A the latter two were aligned antiparallel to each other and cancelled, and in (c) of amylose B all three were aligned parallel to the helix. The cylindrical hyperpolarizability components of residues, Table 5.4-4 column 2 and 3, are dominated by hydroxide bond

orientations, which typically had similar angles from the helical axis, of around -51° for (c) in amylose B, -60° in (a), (b) and (d) of amylose B, and closer to -65° in (b), (c) and (d) of amylose A. One exception occurred at hydroxide orientation (a) in amylose A, where the hyperpolarizability was dominated by one hydroxide bond, O3-H, owing to its angle to the helical axis of ~40°, while the other two hydroxide bonds had angles >70° from the helical axis.

Table 5.4-4 columns 8-10 show the total cylindrical hyperpolarizabilities for the calculated hydroxide position combinations in amylose A and B. The experimental values for hyperpolarizability ratio d_{33}/d_{15} of maize and potato starch obtained with PIPO SHG microscopy falls into the range of possibilities found theoretically by TDHF calculations. Since cylindrical components of hyperpolarizabilities of residues without considering hydroxide positions (Table 5.4-1) cannot explain the experimental data, it is likely that hydroxide bonds and resulting hydrogen bonds that are oriented anisotropically in the amylose helices play key roles in the generation of SHG from starch granules. This is supported by variation in PIPO SHG data between dry and hydrated potato starch granules. It is also supported by the decaying SHG signal observed when starch granules were heated, which severs the hydrogen bonding network, creating an isotropic arrangement of hydroxide and hydrogen bonds. Since the experimental hyperpolarizability ratio d_{33}/d_{15} is always large and positive, it is likely that one dominant hyperpolarizability component exists, similar to hydroxide configuration (b) of amylose A, or hydroxide configuration (a) of amylose B. It could be that the effect of hydrogen bonds is in reality significantly reduced due to the dielectric water/starch environment, which in the theoretical calculations was ignored, and vacuum was assumed, which would lower the d_{33} values in column 2 of Table 5.4-4, and bring the hyperpolarizability ratio values in closer agreement to the experiment.

The residue-water hydrogen bonds in amylose B are difficult to model, but could be very important for explaining the hyperpolarizability of amylose. A self-consistent set of hydrogen positions was not found for the hydrogen bonding network of amylose B due to its large size (see Fig. 5.2-4 (d)), and because the hydroxide orientations found do not conform to the crystal register of the residues. In the cleaved molecular networks of amylose B investigated, the optimization routine more readily rotated the hydrogens on the water molecules, rather than on the residues, likely because the water molecules were only hydrogen bonded to one another, and not surrounded by a complete 3D network of hydrogen bonds of the crystal structure, which

would restrict the possible water hydroxide bond orientations, as it would be inside the ordered amylose B water channel (see Fig. 5.2-4 (d)). Therefore, the water-residue hydrogen bonds selected for amylose B are likely not diverse enough to show changes in their real effect. For these reasons, the water-water hydrogen bonds, as well as the hyperpolarizabilities of water molecules, were not included in the calculation. Since the 6 water molecules per dimer of amylose B are reportedly partially mobile (Takahashi, Kumano et al. 2004), cancelation of hyperpolarizabilities due to averaging may occur. The matter is therefore complicated, and would require the use of molecular dynamics simulation with a large water network, encompassing the entire water cavity in Fig. 5.2-4 (d) to find the high probability orientations of waters and resultant hydroxide bonds on the residues for the calculations.

The calculations of hyperpolarizabilities of amylose A and B crystals are summarized as follows. The TDHF calculations revealed that the d_{33}/d_{15} hyperpolarizability ratios of amylose A and B are largely the result of the orientation of hydroxide bonds of residues as well as the orientations of the resulting hydrogen bonds predominantly along the helical axes. In creating different choices of hydroxide bond orientations, (Fig. 5.4-8), it was observed that molecular networks can have directed hydrogen bonding networks, which could provide overall alignment to the hydroxide bonds. The hyperpolarizability ratios d_{33}/d_{15} for amylose A and B were observed in Table 5.4-4, via four choices of hydroxide orientations each, to span a range which encompassed the experimental ratio observed in PIPO SHG experiments of maize and potato starch granules. Therefore, in order to explain the experimentally derived stable and high hyperpolarizability ratios observed in maize and potato starches, we ascertain that the hydroxide bonds and possibly also the resultant hydrogen bonds are not isotropically arranged with respect to the helical axis. Further investigations on the origin of hydrogen bonding could be performed using polarization dependence of the O-H stretch vibrations with coherent anti-Stokes Raman microscopy.

5.5 Main Conclusions

Qualitative SHG and THG microscopy can be used to visualize starch granules and interrogate their structural properties. SHG images of starch granules are highly polarization dependent due to the radial arrangement of starch helices. The starch crystallinity allowed efficient generation of SHG and visualization of many starch characteristics that are commonly

very difficult to observe without treatment, including growth rings as well as crystalline inhomogeneities such as the starch hilum as well as cracks. Modeling as well as experimental evidence was shown revealing that cross polarized starch SHG imaging can be used for differentiation between starches A and B, which could lead to a quick qualitative determination for industry applications. Starch SHG imaging could be used to identify granules with reduced crystallinity and with inhomogeneities for quality control in food production, to pick the longest lasting foods, or to monitor starch degradation during biofuels production.

Quantitative SHG microscopy was performed on starch granules. The SHG intensity ratio between imaging with linearly polarized light and circularly polarized light was shown as a promising and quick method of measuring the starch hyperpolarizability ratio. The SHG PIPO microscopy technique was also demonstrated on starch granules, and proved to be sensitive enough for differentiation between starches A and B based on a large difference in hyperpolarizability ratio d_{33}/d_{15}. PIPO SHG microscopy also demonstrated that hydration influences the hyperpolarizability ratio d_{33}/d_{15} of starch granules. The variations observed in PIPO microscopy due to hydration as well as variation between maize and potato granules led to the hypothesis that hydration is a key factor in the generation of SHG from starch granules.

The theoretical approach was used to investigate the origin of the large experimentally derived difference in hyperpolarizability ratio between maize and potato starch granules, based on the differences in the published crystal structures for amylose A and B. Calculations using the bond additivity model considering only known positions of C-O and H-C bonds of residues from the crystal structures of amylose A and B revealed that starch A and B hyperpolarizability ratios were both quite small and did not explain the large experimentally observed values nor the difference between types A and B. Hydroxyl bonds were noted to have a potentially large impact on the hyperpolarizability of starch A and B, however their configuration was not predicted in the crystal structures. To check the effects of couplings between bonds and residues on the molecular hyperpolarizability, TDHF calculations were performed. TDHF calculations revealed little difference between hyperpolarizabilities of individual amylose residues, both when directly compared, and when their alignment in the helix was considered. The effects of residue-residue couplings were also considered via TDHF, and these were found to be relatively small in all cases except when hydrogen bonds existed between residues. Hydrogen bonds were found to have a significant hyperpolarizability. Additionally, it was observed that varying the orientations

of hydroxyl bond orientations also largely influenced the hyperpolarizability. In order to calculate hyperpolarizabilities of starches A and B, the orientations of hydroxyl bonds had to be defined, and since they were not known from the crystal structures, they were generated by iterative guess and hydrogen position optimization using a TDHF energy minimization routine, which produced several possible positions of the hydrogens in hydroxyl bonds. Subsequently TDHF calculations were performed for starches A and B using the optimized hydroxyl bond positions, revealing that large hyperpolarizability values could be reached at some hydroxyl configurations. In particular, the starch A hyperpolarizability ratio d_{33}/d_{15} varied from -6 to 18, and the starch B hyperpolarizability ratio varied from -19 to 26 at the different positions of hydroxyl bonds.

The combined experimental and theoretical results lead to the conclusion that in starch granules the hydroxyl bonds and resulting hydrogen bonds are oriented anisotropically with respect to the positive helical axis, and consequently, they are the source of the strong hyperpolarizability in starch granules. Therefore, SHG in starch granules is very sensitive to the water content and hydrogen bonded water network which exists between the helices, especially in starch B, and could be used to monitor changes in the association of this hydrogen bonding network. Measurements of the hydration in starches could be used in the development of granular starch composites. Starch fillers have been investigated in the plastics industry to modify properties of polymer resins, including stiffness, toughness, heat distortion, damping, permeability, electrical characteristics, density and cost (see Ch. 19 in (BeMiller and Whistler 2009)). For example, the addition of 1% starch granules by weight to polycarbonate resins results in films with reduced coefficient of static friction, higher light transmission and less haze (Carter 1983). Therefore, improved measurements of starch granule hydration properties may allow further improvement of granular starch composites leading to novel starch based materials.

Chapter 6
Nonlinear Optical Microscopy of Photosynthetic Biological Structures

6.1 Introduction

Nonlinear optical microscopy is a beneficial tool for non-invasive *in vivo* and *in situ* optical investigations of biological samples due to the possibility to visualize a diverse content of nonlinear optically active structures at the tissue, cellular and subcellular levels. In this chapter, the use of nonlinear microscopy for functional studies of complex biological structures is presented by portraying a few examples of imaging photosynthetic biological structures simultaneously with MPF, SHG and THG image contrasts.

In MPF microscopy of photosynthetic samples, laser excitation wavelengths in the range of 800 – 1200 nm can excite several photosynthetic pigments including carotenoids, chlorophylls and phycobilins. Recent studies suggest that carotenoids dominate the multiphoton absorption spectrum (Walla, Yom et al. 2000) of plant photosynthetic pigment-protein complexes, while chlorophylls do not show new two-photon absorption bands (Polivka and Sundstrom 2004). The two-photon excitation of carotenoids from the ground state $1^1A_g^-$ to the first singlet excited state $2^1A_g^-$ falls around 1000-1400 nm (double energy at 500-700 nm) for plant/green algae, and around 1100-1500 nm (double energy at 550-750 nm) for bacterial systems (see (Barzda 2008) and references therein). The low fluorescence yield of carotenoids, and the fast and efficient excitation energy transfer between carotenoids and chlorophylls leads to fluorescence emission from chlorophyll or bacteriochlorophyll in photosynthetic samples, with an almost identical emission spectrum as fluorescence from one-photon excitation (Barzda, de Grauw et al. 2001; Walla, Linden et al. 2002). Therefore imaging with MPF microscopy in photosynthetic samples is useful for localization of photosynthetic structures.

The investigation proceeds by characterizing the nonlinear signals generated in aggregates of major light-harvesting pigment-protein complex of photosystem II (PSII) from higher plants (LHCII), which serves as a model system of photosynthetic membranes. Subsequently, nonlinear imaging of different photosynthetic organisms including pea *Pisum savitum* chloroplasts, the green algae *Chlamydomonas reinhardtii,* and two strains of filamentous

cyanobacteria, *Leptolyngbya* sp. and *Anabaena* sp., are presented to compare and contrast the structural organizations warranting generation of the nonlinear signals.

6.2 Imaging Photosynthetic Structures

6.2.1 LHCII

LHCII is the most abundant light-harvesting pigment-protein complex in photosynthetic membranes of chloroplasts from green plants (Thornber 1975). The pigment-protein complexes contain chlorophyll and carotenoid molecules, which have high optical nonlinearities (Hermann and Ducuing 1974; Senge, Fazekas et al. 2007) due to their delocalized molecular electronic systems. In LHCII, these pigments are highly ordered in a non-centrosymmetric arrangement, as can be deduced from the high resolution crystal structure (Liu, Yan et al. 2004), and therefore allow efficient SHG as well as THG (Barzda 2008). LHCII can form disordered, highly ordered crystalline and multi-lamellar aggregates (Barzda, Mustardy et al. 1994; Simidjiev, Barzda et al. 1997), the latter mimicking the behavior of thylakoid membranes in grana of chloroplasts (Barzda, Garab et al. 1996). Therefore, LHCII can be used as a model system to explore the structural origin of nonlinear signals generated in photosynthetic samples.

Fig. 6.2-1 shows simultaneously acquired nonlinear images of LHCII aggregates. The heterogeneous structure of LHCII aggregates can be visualized with all three contrast mechanisms, MPF (b), SHG (c) and THG (d). The Yb:KGW laser emitting ~300 fs pulses at 1028 nm (Major, Barzda et al. 2006) predominantly excites carotenoid molecules in LHCII via two-photon excitation (Walla, Linden et al. 2002), followed by a fast excitation energy transfer from carotenoids to chlorophylls and subsequent fluorescence emission. The chlorophyll fluorescence provides information about localization of LHCII in the image Fig. 6.2-1 (b). The figure reveals heterogeneity in fluorescence intensity within the aggregates. This is in line with large variations in fluorescence lifetimes previously observed in LHCII aggregates (Barzda, de Grauw et al. 2001) and is attributed to heterogeneity in fluorescence quenching as well as singlet-singlet excitation annihilation effects (Barzda, Gulbinas et al. 2001).

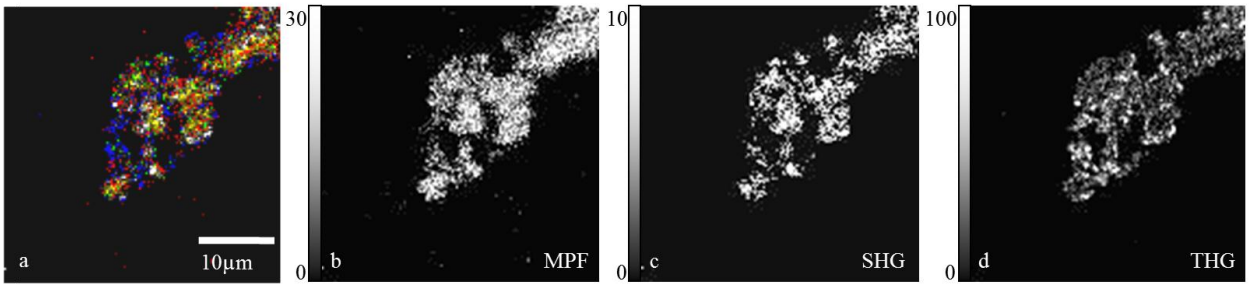

Fig. 6.2-1: Multicontrast microscopy of LHCII from pea (*Pisum savitum*)

Simultaneously recorded images of freshly isolated LHCII aggregates from pea leaves (MPF (b), SHG (c) and THG (d) are presented. The correlation image shown in (a) was colored according to the scheme presented in Fig. 3.4-3 (l). Yb:KGW femtosecond laser radiation at 1028 nm wavelength and 25 mW average power at the sample was used for excitation. 100 frames scanned at 8 frames per second were summed to produce these images. Figure reprinted with permission from (Cisek, Spencer et al. 2009).

The SHG image of LHCII aggregates, presented in Fig. 6.2-1 was simultaneously acquired with MPF, SHG and THG. Multicontrast imaging allows direct, pixel by pixel, correlation of the images. The SHG signal is generated predominantly by chlorophyll and carotenoid molecules, which are non-centrosymmetrically arranged in LHCII (Liu, Yan et al. 2004). Several aggregates in Fig. 6.2-1 (c) have high SHG intensities, stronger than fluorescence (Fig. 6.2-1 (b)). Considering that SHG emitters must be non-centrosymmetrically aligned throughout the entire focal volume, SHG efficiency depends on the relative arrangement of LHCII in the aggregate. When LHCII is aggregated in a random arrangement, it does not produce SHG. However, SHG signal is generated in non-random regions such as non-centrosymmetric lamellar formations or, aggregate edges. The highest intensity occurs when LHCII is arranged in ordered non-centrosymmetric three dimensional crystalline structures. Since a focal volume can encompass several thousand LHCII trimers, the SHG is extremely sensitive to the macro-scale organization of the pigment-protein complexes. The previous chapters of the thesis provided examples of SHG generation from crystalline arrangements such as starch granules and NWs. The correlation of MPF and SHG in the Fig. 6.2-1 (a) gives a qualitative indication where LHCII aggregates are located that generate SHG.

THG is efficiently generated in LHCII aggregates as well (Fig. 6.2-1 (d)), with higher signal strength than SHG and MPF. The THG signal also appears highly heterogeneous, revealing different structural domains. The presence of carotenoid and chlorophyll molecules with high third-order nonlinear susceptibility (Hermann and Ducuing 1974; Senge, Fazekas et al. 2007) in the heterogeneous aggregates renders strong THG. The THG domains do not always correlate with SHG and MPF, as can be observed in the correlation image (Fig. 6.2-1 (a)). While

THG is not dependent on the symmetry properties of the sample, it requires structural heterogeneity such as interfaces between two materials that have different indices of refraction or third-order nonlinear susceptibilities (Barad, Eisenberg et al. 1997; Muller, Squier et al. 1998). Additionally, THG is orientation dependent, being maximal for interfaces perpendicular to the beam (Carriles, Schafer et al. 2009).

The following structural interpretations of comparisons between the nonlinear signals in LHCII can be presented: domains with low SHG and THG are likely randomly arranged, while domains with low SHG and high THG are probably arranged into multi-lamellar structures oriented with membrane plane perpendicular to the beam. In this case, the low SHG could be due to the destructive interference caused by the flip-flop organization of LHCII trimers in the lamella, which has previously been observed (Kuhlbrandt, Thaler et al. 1983). Domains with high SHG but lower THG are well ordered into a non-centrosymmetric arrangement, however, they form continuous structures without interfaces that are larger than the focal volume, or alternatively, the interfaces are parallel to the beam. Structures with intense SHG and THG have a multi-lamellar structure perpendicular to the beam, with non-centrally organized domains. Further, macrostructural elucidation is possible by obtaining SHG and THG PIPO data. The understanding of the origin of nonlinear signals obtained by imaging LHCII aggregates can be applied to investigate other photosynthetic structures.

6.2.2 Chloroplast imaging

Nonlinear microscopy can be used to investigate chloroplast ultrastructure *in situ* and *in vivo* (Muller, Squier et al. 1998; Chu, Chen et al. 2001; Tirlapur and König 2001; Barzda 2008; Cisek, Prent et al. 2009; Reshak 2009; Reshak, Sarafis et al. 2009). Since LHCII is the most abundant pigment-protein complex in photosynthetic membranes of chloroplasts, the results obtained from LHCII aggregates in the previous section can be applied to interpret nonlinear images of chloroplasts.

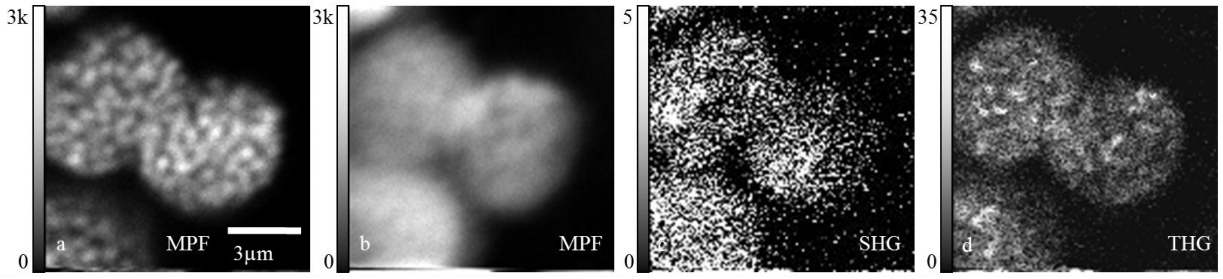

Fig. 6.2-2: Multicontrast imaging of chloroplasts from pea (*Pisum savitum*).

A 1028 nm excitation Yb:KGW laser set to record 500 frames at 0.04 mW average power was used to obtain the MPF image (a), while 200 frames of a higher intensity of 3mW was used to obtain multicontrast images, including MPF (b), SHG (c) and THG (d). The equal power-scaled maximum intensities are $3.3x10^6$, 4200, 12 and 150 for panels (a), (b), (c) and (d), respectively. Figure reprinted with permission from (Cisek, Spencer et al. 2009).

Fig. 6.2-2 presents dark adapted freshly isolated chloroplasts from pea leaves, imaged with the multicontrast nonlinear microscope. In order to avoid the intense SHG from starch granules, chloroplasts were depleted of starch by keeping plants in the dark for 12 hours prior to isolation. The femtosecond Yb:KGW laser radiating at 1028 nm (Major, Barzda et al. 2006) produced two-photon excitation of carotenoids (Walla, Linden et al. 2002) and chlorophyll fluorescence peaking at 680 nm wavelength was used for imaging. Low excitation intensity (1 pJ pulse energy) was employed to produce a MPF image of dark adapted chloroplasts (Fig. 6.2-2 (a)). The figure shows photosystem II (PSII) fluorescence of the grana and closely resembles confocal fluorescence images of chloroplasts initially observed by Van Spronsen (van Spronsen, Sarafis et al. 1989). In order to obtain harmonic generation images, more laser power is required (100 pJ). The high excitation intensity fluorescence image presented in Fig. 6.2-2 (b) shows a more homogeneous structure of the chloroplasts. At high excitation intensities, PSII fluorescence is quenched via photochemical and non-photochemical quenching (Demmig-Adams and Adams 1992; Horton, Ruban et al. 1996; Bruce, Samson et al. 1997), however, lower excitation intensity from the out of focus regions does not induce fluorescence quenching to the same extent resulting in a substantial fluorescence contribution to the overall signal. Since a confocal pinhole is not commonly used in multiphoton excitation fluorescence microscopy, the out of focus fluorescence reduces the confocality at high excitation intensities. Nonetheless, several grana can still be discerned in the image (Fig. 6.2-2 (b)).

Low intensity SHG is generated in chloroplasts (Fig. 6.2-2 (c)). The efficiency of SHG from chloroplasts is slightly lower than from isolated LHCII. The heterogeneity of SHG from within a single chloroplast can be readily observed. Grana in chloroplasts have a chiral

arrangement, which exhibits orientation dependent anomalously strong psi-type circular dichroism (Garab, Faludi-Daniel et al. 1988; Finzi, Bustamante et al. 1989; Barzda, Mustardy et al. 1994). The non-centrosymmetric organization of pigments in pigment-protein complexes that are ordered in photosynthetic membranes is expected to increase SHG if the chiral contribution to the SHG tensor is large; however, grana do not appear particularly distinct from the stroma regions as can be seen in Fig. 6.2-2 (c). The alternating arrangement of thylakoid membranes both in the grana stacks as well as in the two antiparallel stroma membranes produces a centrosymmetric arrangement of the SHG emitters. Therefore, the SHG signals from the grana and stroma membranes appear to be low. In addition, any subdiffraction sized starch granules remaining after dark treatment also could contribute to the signal.

Detailed structural characteristics can be observed in THG generated from chloroplasts (Millard, Wiseman et al. 1999; Chu, Chen et al. 2001; Prent, Cisek et al. 2005; Barzda 2008). Resonance enhancement of THG occurs due to carotenoid and chlorophyll molecules, which have high third-order nonlinearities at the laser wavelength (Marder, Torruellas et al. 1997). Since THG may be enhanced by multilayer structures (Tsang 1995), the multi-lamellar nature of the grana can amplify THG signal, compared to the unstacked thylakoids in the stroma. The multilayer effect is maximal for lamella oriented perpendicular to the laser beam; hence the face aligned chloroplasts with grana thylakoid membranes oriented perpendicular to the beam give strong THG signal. However, appreciable signal is still observed when the membranes are parallel to the beam (Barzda 2008), in that case, the THG is produced because the granum presents an interface at the boundary between the grana and the stroma.

THG signals might be sufficiently strong for PIPO THG microscopy and may reveal details of organization of the photosynthetic membrane under different physiological conditions. Fig. 6.2-3 shows multicontrast imaging of a chloroplast under osmotic shock conditions, (in buffer without mono and bivalent cations and osmoregulator sorbitol), which forced the grana to expand and form a bleb, see (d). In this image the thylakoid membrane organization is compromised leading to a different intensity than organized grana. The SHG shows a mostly random arrangement of pigments in the photosynthetic membrane, while the THG corresponds to the MPF image showing a similar map of pigment-protein complexes distributed in the bleb structure. A future investigation could use PIPO THG microscopy to measure second

hyperpolarizability elements under different physiological conditions, and could reveal the structural organization of pigment-protein complexes in chloroplast.

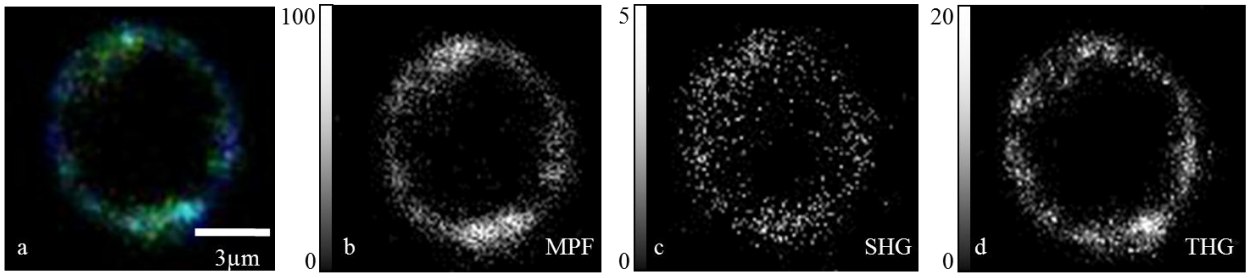

Fig. 6.2-3: Imaging osmotically shocked chloroplasts from pea (*Pisum savitum*).
A 1028 nm excitation Yb:KGW laser set to record 100 frames at 3mW average power was used to obtain multicontrast images, including MPF (b), SHG (c) and THG (d). The equal power-scaled maximum intensities are XYZ for panels (b), (c) and (d), respectively. The SCIA image is shown in panel (a).

6.2.3 *Chlamydomonas reinhardtii* imaging

The photosynthetic structure of the unicellular green alga *Chlamydomonas reinhardtii* has a different organization of thylakoid membranes as compared to higher plants. The cells have a single cup shaped chloroplast, which contains grana (Finazzi 2005) with 6 discs on average and 20 discs at maximum (Sager and Palade 1957). The organism contains several other well-ordered structures such as starch granules, which also generate strong nonlinear signals.

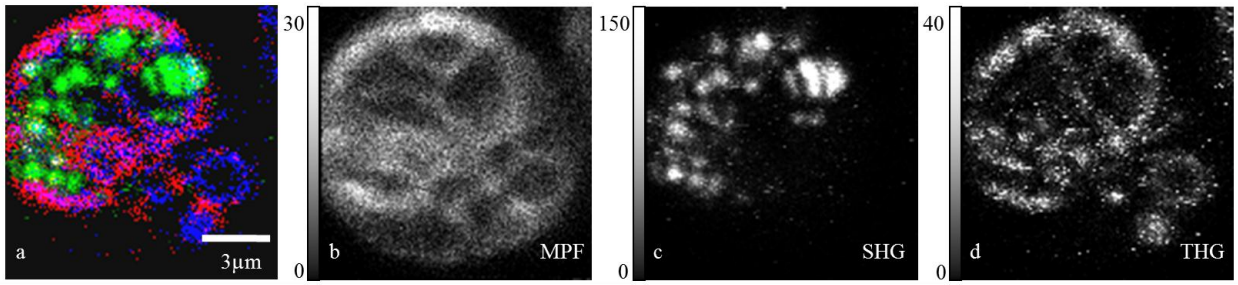

Fig. 6.2-4: Multicontrast imaging of *in vivo Chlamydomonas reinhardtii*.
Panels (b), (c) and (d) represent MPF, SHG and THG images of the alga, respectively. Panel (a) shows the correlation image, colored according to the correlation scheme shown in Fig. 3.4-3 (i). Yb:KGW laser excitation at 3 mW average power with 200 frames yielded power-scaled values 60, 300 and 150 for (b), (c) and (d), respectively. Figure reprinted with permission from (Cisek, Spencer et al. 2009).

Multicontrast imaging of *Chlamydomonas reinhardtii* is presented in Fig. 6.2-4. The MPF (Fig. 6.2-4 (b)) signal, collected between 650 and 730 nm, originates from chlorophyll molecules in the photosynthetic membrane, and clearly displays the location of thylakoids. Visible variations in fluorescence intensity originate from the heterogeneous distribution of

photosystem I and photosystem II in the photosynthetic membranes (Gunning and Schwartz 1999).

The SHG signal (Fig. 6.2-4 (c)) shows many very bright structures, which do not correlate with the intense MPF regions (green in Fig. 6.2-4 (a)). The intense SHG signal originates from starch granules, and was observed to have polarization dependency as outlined in the previous section. Mostly homogeneous SHG originating from pigment-protein complexes was also detected, and appears at the same intensity as SHG in chloroplasts, although it is not visible in the presented SHG image (Fig. 6.2-4 (c)) due to the much higher signal from starch granules and limited dynamic range of intensity values presented in the picture. Similar to the case with chloroplasts, thylakoid membranes in *Chlamydomonas* are oppositely oriented with respect to each other and loosely stacked, rendering low SHG intensity. Hence, SHG intensity variation in the regions overlapping with fluorescence provides information about the structural organization of the thylakoid membranes.

The THG signal originating from *Chlamydomonas reinhardtii* reveals several interesting structures. Most of the THG signal (Fig. 6.2-4 (c)) correlates with MPF and hence, is generated by thylakoids. Carotenoids and chlorophylls have a high second hyperpolarizability, therefore they generate a stronger and more localized THG signal. THG contrast has higher resolution than MPF due to third-order dependency on the laser intensity. Stacked thylakoids may also enhance the THG based on the number of layers in the focal volume, the packing density of pigment-protein complexes within the thylakoid layers, as well as the net orientation of thylakoid membranes, being maximal for perpendicular orientation to the laser beam. The THG intensity of thylakoids in *Chlamydomonas* is similar to the grana in pea chloroplasts (See Fig. 6.2-4 (d) and Fig. 6.2-2 (d)), even though *Chlamydomonas* have on average 6 thylakoid layers (Sager and Palade 1957) while pea grana may have 20-30 layers (Mustardy and Garab 2003). The THG intensity dependence on the number of thylakoid layers and spacing between them in both organisms requires further investigation. *Chlamydomonas* contain several other organelles which generate THG signal. On the bottom right of Fig. 6.2-4 (d) (see blue in panel (a)) two interesting structures are revealed with THG but not SHG or MPF signal. These structures are non-pigmented and present an optical interface. The characterization of these organelles will advance the application of nonlinear microscopy in research on *Chlamydomonas* allowing future nonlinear imaging with high specificity and without labeling.

6.2.4 Cyanobacteria imaging

The photosynthetic structure of prokaryotic cyanobacteria has differently organized thylakoids and different light-harvesting antenna as compared to *Chlamydomonas* and higher plants. The photosynthetic membrane progresses inside the cell as concentric stacks of 1-3 thylakoids, proximal to the plasma membrane, and uses phycobilisomes as light-harvesting antenna (Fay and Van Baalen 1987). Phycobilisomes are 25-45 nm sized (Grossman, Schaefer et al. 1993) supramolecular assemblies of phycobilliproteins, which use covalently attached phycobilins for light-harvesting. Phycobilisomes are anchored to the top exterior side of each membrane pair. In order to distinguish the nonlinear signals generated by the phycobilisomes and chlorophyll/carotenoid containing PSI and PSII, multicontrast imaging of *Leptolyngbia* was performed on cells untreated and treated with methanol to extract chlorophyll and carotenoid pigments.

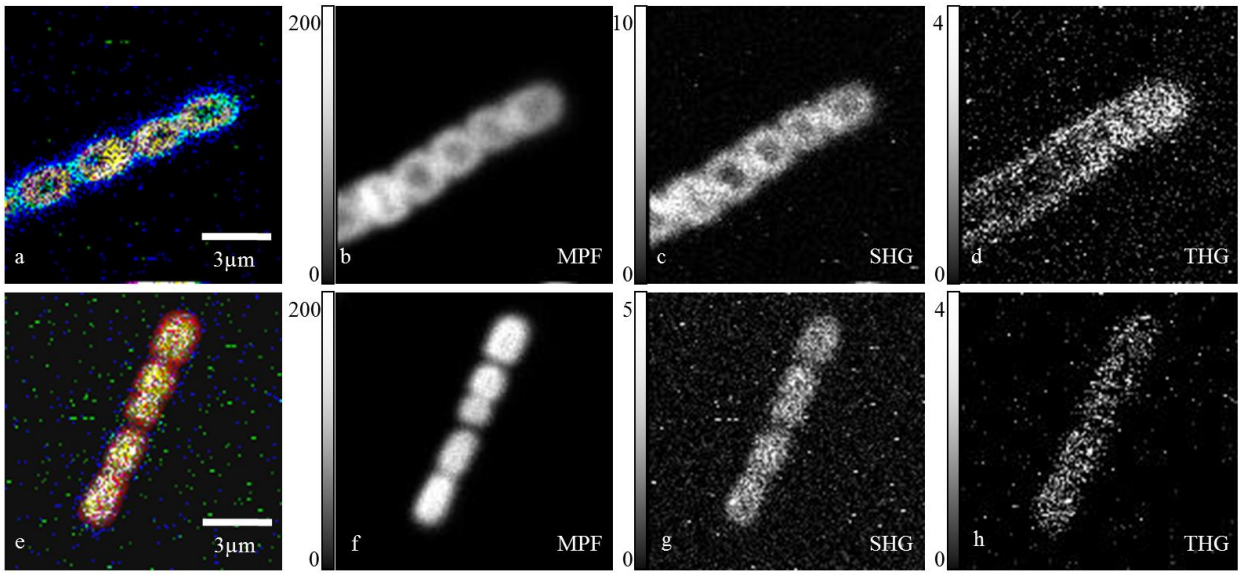

Fig. 6.2-5: Multicontrast *in vivo* images of the cyanobacterium *Leptolyngbya* sp.

Untreated *Leptolyngbya* sp. are shown in the top row, while the treated sample lacking chlorophylls and carotenoids is presented in the bottom row. Panels (b) and (f), (c) and (g), and (d) and (h), show MPF, SHG and THG images, respectively. Panels (a) and (e) show correlation images colored according to the scheme presented in Fig. 3.4-3 (j). An average Yb:KGW laser power of 3 mW was used and summing 200 frames produced the images. The power scaled count values are: 600, 50 and 10 for (b), (c) and (d), and 200, 5 and 3 for (f), (g) and (h), respectively. Figure reprinted with permission from (Cisek, Spencer et al. 2009).

Multicontrast nonlinear microscopy of *Leptolyngbya* was performed yielding strong signals of MPF, SHG and THG. The MPF image collected from phycobilins and chlorophylls in the range of 650-730 nm is presented in Fig. 6.2-5 (b), visualizes the concentric arrangement of

thylakoids. *Leptolyngbya* (Fig. 6.2-5 (c)) generates second harmonic signal, which correlates with MPF (yellow in Fig. 6.2-5 (a)) and a bit larger in intensity compared to chloroplast thylakoids. The SHG is generated by chlorophylls, carotenoids and phycobilins, which have large hyperpolarizabilities (Senge, Fazekas et al. 2007). Although the phycobilisome crystal structure is not yet fully known (Yi, Huang et al. 2005), the phycobilins pigments are likely well organized in a non-centrosymmetric organization since they generate SHG. Methanol treated thylakoids, which lack chlorophylls and carotenoids (Fig. 6.2-5 (e)) also generate SHG signal, providing evidence that second harmonic is generated not only from chlorophylls and carotenoids, but also from phycobilins. The SHG intensity from methanol treated cells was reduced probably due to extraction of chlorophylls and carotenoids as well as due to methanol induced dehydration and structural change of phycobilliproteins, which increased disorder in the system.

Leptolyngbya produces efficient THG (Fig. 6.2-5 (d)) from the periphery of the cells, (see blue in Fig. 6.2-5 (a)), which does not correlate with MPF or SHG. Cyanobacteria have a plasma membrane and a peptidoglycan layer that apparently enhances THG. Further investigations on the origin of the periphery THG could be performed by imaging gram-positive bacteria with much thicker peptidoglycan walls. The THG signal from thylakoids of *Leptolyngbya* is weak probably due to the reduced number of thylakoid layers, and lower concentration of carotenoids compared to LHCII rich chloroplasts, as well as due to the larger thylakoid spacing constrained by the presence of phycobilisomes.

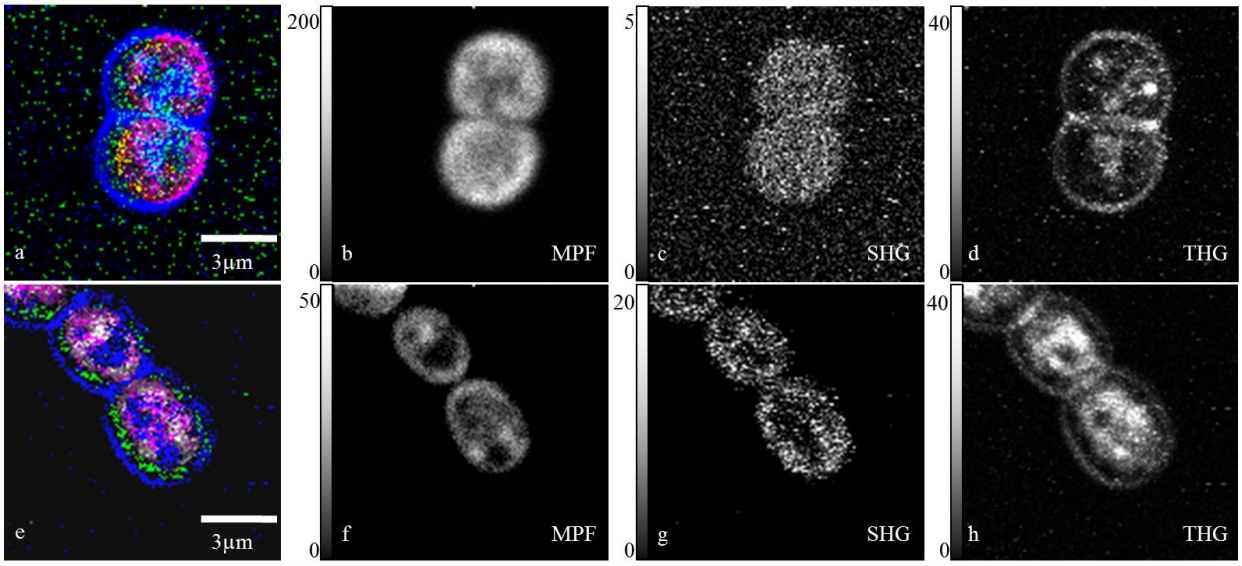

Fig. 6.2-6: Imaging *Anabaena* sp. M3 and UTCC387 with nonlinear microscopy.

Panels (b) and (f), (c) and (g), and (d) and (h) represent MPF, SHG and THG images, respectively. Panels (a) and (e) show the correlation images, colored according to the scheme presented in Fig. 3.4-3 (j). To obtain the images, 2 mW of power from the Yb:KGW laser was used and 200 frames were summed giving the following power-scaled intensities: 200, 20, 350 for (b), (c) and (d), and 700, 140, 350 for (f), (g) and (h), respectively. Figure reprinted with permission from (Cisek, Spencer et al. 2009).

Nonlinear microscopy investigations of cyanobacteria that are larger than *Leptolyngbya* were carried out on two strains of *Anabaena* sp.:M3 and UTCC387 (Fig. 6.2-6). Intense MPF collected from the phycobilins and chlorophylls localizes the thylakoid membrane, and distinguishes regions of high pigment concentration (Fig. 6.2-6 (b) and (f)). The SHG signal correlates with MPF, and therefore originates from the photosynthetic membranes. Lower SHG intensity in *Anabaena* sp. M3 (Fig. 6.2-6 (c)) as compared with UTCC387 (Fig. 6.2-6 (g)) and *Leptolyngbya* (Fig. 6.2-6 (c)) may have a morphological significance, or might just be a variation in the membrane organization due to slight differences in growth conditions. Intense THG was generated by *Anabaena* due to internal structures as well as the cell wall (Fig. 6.2-6 (d) and (h)). The THG from the periphery anti-correlates with the other nonlinear signals (see Fig. 6.2-6 (a) and (e)) supporting that THG is emitted from the layer of peptidoglycan. Most *Anabaena* contain one small structure (see bright dots in Fig. 6.2-6 8 (d)), which produced a very strong THG signal that is uncorrelated with MPF or SHG. Debarre *et. al.* found that oil droplets generate efficient third harmonic in biological structures (Debarre, Supatto et al. 2006). Since *Anabaena* sp. are known to produce phosphorous reservoirs used for the synthesis of lipids, these are likely candidates for THG enhancement. There are several other unidentified structures that produce

THG in *Anabaena*, especially visible in Fig. 6.2-6 (h). Further studies are needed to determine the origin of these structures.

6.3 Main conclusions

A study of nonlinear optical microscopy using MPF SHG and THG was performed for imaging photosynthetic organisms, readily visualizing many subcellular structures such as starch granules, pigment-protein complexes, cell walls and the photosynthetic membranes. The investigation of LHCII revealed complex signals can be obtained in SHG, THG and MPF, and further PIPO examination of these structures would potentially give more detailed information about the imaged structures. Investigations of green alga and cyanobacteria showed that these organisms are also promising candidates for investigation with nonlinear optical microscopy, and, despite their small size, the PIPO technique could be successfully applied.

Important biological information can be obtained from microscopic polarization SHG and THG studies of cellular and subcellular structures. Visualization of subcellular structures in living cells without fixing and without adding additional stains is important for biology enabling monitoring of living systems without interference form external or genetically encoded dyes, and can be performed by SHG and THG contrast mechanisms. Cellular structures can be differentiated by their signal intensity, which nonlinear signals they emit, as well as the nonlinear signal polarization response via implementation of the developed PIPO algorithm. Additionally, the use of unique molecular resonance enhancements could be used to further localize different biological molecules with SHG and THG by tuning the incident laser. Lastly, the ability to extract different structural parameters from the subcellular structures inside living cells is a tremendous benefit since biological structure and function can then be linked via a nonintrusive optical imaging method.

Summary of Main Conclusions

This thesis contains a fundamental investigation of nonlinear microscopy for obtaining structural information from *in vivo* biological samples. The motivation for the research was laid out in Chapter 1, along with a history of optical microscopy and development and applications of nonlinear optical microscopy in order to put this new technique in a historical perspective.

Chapter 2 featured theory devoted to explaining the main equations that describe the phenomena investigated in this thesis. A model for SHG polarization anisotropy due to a depolarization of the perpendicular electric field was performed. The hyperpolarizabilities for SHG from NWs with cubic crystal structures grown along the [1 1 1] direction as well as hexagonal crystal structures grown along [0 0 0 1] directions was presented. For zinc blende cubic crystals, the mathematical treatment revealed that the absolute orientation of the rotation of the NW around its own axis could be determined. For hexagonal crystals, the mathematical treatment revealed that PIPO contour images showed the possibility for discrimination between crystalline structures according to their hyperpolarizability ratio values. Birefringence of the laser excitation as well as the signal beams was accounted for in PIPO SHG analysis of hexagonal crystalline structures. In the analysis of SHG from hexagonal crystals an equation comparing SHG intensity obtained from linearly polarized excitation versus circularly polarized excitation was developed which could potentially be used for quick determinations of hyperpolarizability values.

As part of this thesis, a nonlinear multicontrast microscope was built for sample imaging, therefore Chapter 3 features a description of the instrumentation of nonlinear optical microscopy. This chapter also describes the basic parts of the nonlinear microscope as well as some software programming details. Instrumentation for polarization modulation of the excitation laser, as well as measurement of the polarization of the generated signal was described to undertake PIPO imaging. Finally, data analysis methods were described to understand the PIPO images as well as the SCIA images in this thesis. Microscopic sample preparation was also described in this chapter.

In Chapter 4 ZnSe NWs were investigated with nonlinear multicontrast microscopy. SHG anisotropy was measured and explained with the phenomenon of the depolarization of the

transverse NW electric field. Further detailed SHG analysis of ZnSe NWs was performed with the nonlinear microscope on NWs using PIPO microscopy. The SHG PIPO technique revealed the possibility to differentiate between zinc blende as well as twinned and non-twinned wurtzite NWs. In zinc blende NWs, the rotational orientation of the cubic lattice inside the NWs lying on a glass surface could be determined. PIPO SHG microscopy was shown to be a powerful tool that can be used on small sample regions of semiconductor NWs to determine their structural properties. This interesting physical phenomenon can find possible applications for novel polarization-sensitive optical devices and also opens new applications for nonlinear scanning microscopy in structural investigations of crystalline micro and nanostructures.

Chapter 5 featured an investigation of starch granules using nonlinear multicontrast microscopy. An investigation of the qualitative SHG and THG microscopy was used to visualize starch granules, revealing that SHG signals are highly dependent on the polarization of the excitation laser due to the radial arrangement of the amylose helices. The sensitivity to starch crystallinity allowed SHG to visualize many starch characteristics that are commonly very difficult to observe without treatment including growth rings as well as crystalline inhomogeneities such as the starch hilum and cracks in the granule. Mathematical modeling of the images combined with experimental evidence showed that cross polarized starch SHG imaging can be used for differentiation between starches A and B, which could lead to a quick qualitative discrimination of starch granules A and B for industry applications. Starch SHG imaging could be used to identify granules with reduced crystallinity and with inhomogeneities for quality control in food processing, to pick the longest lasting foods, or to monitor starch degradation during biofuels production.

Quantitative SHG microscopy was also performed on starch granules. The SHG intensity ratio between imaging with linearly polarized light and circularly polarized light was shown as a promising quick method of measuring the starch hyperpolarizability ratio. The SHG PIPO microscopy technique was also demonstrated on starch granules, and proved to be sensitive enough for differentiation between starches A and B based on a large difference in hyperpolarizability ratio d_{33}/d_{15}. PIPO SHG microscopy also demonstrated that hydration influences the hyperpolarizability ratio d_{33}/d_{15} of starch granules.

The theoretical approach was used to investigate the origin of the large experimentally derived difference in hyperpolarizability ratio between starches A and B, based on the differences in the published crystal structures for amylose A and B. The bond additivity model as well as time dependent Hatree-Fock calculations were used to determine the first hyperpolarizabilities of the structures. The combined experimental and theoretical results led to the conclusion that in starch granules the hydroxyl bonds and resulting hydrogen bonds are oriented anisotropically with respect to the helical axis, and consequently they are the source of the hyperpolarizability in starch granules. Therefore, SHG in starch granules is very sensitive to the hydrogen bonded water network which provides crystalline alignment for the helices, especially in starch B, and could be used to monitor changes associated with this hydrogen bonded network. Measurements of the hydration network in starches could be used in the development of granular starch composites. Starch fillers have been investigated in the plastics industry to modify properties of polymer resins, including stiffness, toughness, heat distortion, damping, permeability, electrical characteristics, density and cost (see Ch. 19 in (BeMiller and Whistler 2009)). Therefore, improved measurements of starch granule hydration properties may allow further research into granular starch composites leading to novel starch based materials.

In Chapter 6, a preliminary nonlinear microscopy study was performed for imaging photosynthetic organisms including imaging the green algae *Chlamydomonas*, two species of cyanobacteria, isolated light-harvesting pigment protein complex (LHCII) as well as chloroplasts from green plants. Visualization of many complex subcellular structures was performed *in vivo* with nonlinear optical microscopy without any labeling, visualizing subcellular structures including the cell walls, the photosynthetic membranes and the *Chlamydomonas* eyespot. Signal intensities were sufficiently high that quantitative information on the organization of complex microscopic samples is possible using PIPO harmonic generation microscopy, however it requires detailed crystallographic studies which as of now are limited, especially to understand complex *in vivo* photosynthetic structures. Nonlinear microscopy could be used to help obtain previously unknown crystallographic properties of *in vivo* samples, which is the motivation for the thesis. In the future, this work could be used to help obtain structural crystallographic information on *in vivo* samples using SHG microscopy.

Despite more than 400 years of history, the development of new microscopic imaging methods is accelerating by taking advantage of new laser sources, new optical technologies such

as adaptive optics and optical fibers, increasing sensitivity of the detectors, as well as recent advancements in computer technology, image analysis and visualization. Seeing is believing, therefore microscopic observations will always fascinate us and develop our understanding of biological structures and especially dynamic processes in living organisms.

Statement of Contributions

I built the multicontrast nonlinear laser scanning microscope described in section 3.2. The hardware I used came with LabVIEW drivers, therefore I performed implementation of all the hardware using a standard PC with LabVIEW. Microscope building from parts was performed by me, while the design was due to Prof. Barzda.

I was the main builder and programmer of the entire nonlinear multicontrast microscope. I created the program which included programming the counting data acquisition card, the scanning mirrors, the piezoelectric stage, the camera, live scanning and saving, a main control program, and a program to read back the microscope data. Nicole Prent assisted with programming the data saving routine, the data reading routine, as well as, helped program different zoom settings. I also implemented PIPO microscopy components. The microscope is still the workhorse of Prof. Barzda's lab, being used almost each day. I have upgraded the microscope several times.

I performed all the starch scans in the microscope, along with the data analysis. While I performed all the preliminary NW scans, two undergraduate students under my supervision performed additional scans and some analysis in order to gather more evidence for the polarization phenomena I observed: Leigh Spencer performed early multicontrast scans of NWs, varying the input polarization, while Nehad Hirmiz, another undergraduate, performed PIPO scans of wurtzite versus zinc blende NWs. Several of the scans of photosynthetic structures featured in section Chapter 6 were also performed by Leigh Spencer, while growth of the samples was supervised by Prof. Espie from the biology department at the University of Toronto Mississauga.

The mathematical treatments of the hyperpolarizability were important for the thesis in order to understand the SHG data. The mathematical treatment of cubic hyperpolarizability was performed by me. The circularly versus linearly polarized laser for SHG in hexagonal structures was performed with help from theorist Dr. Serguei Krouglov. Visualization of the hyperpolarizabilities was a team effort from Dr. Serguei Krouglov and initial programming was performed by myself, Adam Tuer and Danielle Tokarz. I wrote many program features to make the program user friendly, while the initial program for rotation of the SHG tensor around a

single axis was a combined effort of Adam Tuer and myself. I extended the rotation code to make the required full three angle Euler rotation for full hyperpolarizability manipulation. The idea to use arrows for the hyperpolarizability unit spheres using ParaView, which ultimately enabled the 3D unit sphere visualization, came from Daaf Sandkuijl, and the final 3D unit sphere representation was implemented by Adam Tuer.

Hyperpolarizability calculations of amylose residues were all performed by me, however, initial help of learning the GAMESS software came from Danielle Tokarz. Building of the molecular crystal segments for amylose A and B was performed by me, with data from crystal structure papers. Additionally, Dr. Popov sent me atom positions from the new crystal publication of amylose B via personal communication.

Prof. Barzda had a huge helping hand in each of the tasks above, therefore he deserves much credit.

As part of the thesis work, a book chapter, and several publications, proceedings and conference presentations were generated. The works marked with an asterisk are directly related or referenced in this thesis.

Refereed Publications

1. Tuer, A. E., S. Krouglov, N. Prent, **R. Cisek**, D. Sandkuijl, K. Yasufuku, B. Wilson and V. Barzda (2011). "Nonlinear Optical Properties of Type I Collagen Fibers Studied by Polarization Dependent Second Harmonic Generation Microscopy." The Journal of Physical Chemistry B **115**(44): 12759-12769.*
2. **Cisek, R.**, V. Barzda, H. E. Ruda and A. Shik (2010). "Nonlinear optical properties of semiconductor nanowires." Journal of selected topics in quantum electronics **17**(4): 915-921.*
3. Sandkuijl, D., **Cisek, R.**, Major, A. and Barzda, V., (2010). "Differential microscopy for fluorescence-detected nonlinear absorption linear anisotropy based on a staggered two-beam femtosecond Yb:KGW oscillator." Biomedical Optics Express **1**(3):895-901.
4. Tuer, A., Krouglov, S., **Cisek, R.**, Tokarz, D. and Barzda, V. (2010) “Three-Dimensional Visualization of the First Hyperpolarizability Tensor”, Journal of Computational Chemistry. doi: 10.1002/jcc.21694.*
5. Tuer, A., Tokarz, D., Prent, N., **Cisek, R.**, Alami, J., Dumont, D.J., Bakueva, L., Rowlands, J., and Barzda, V. (2010) "Nonlinear Multicontrast Microsopy of Hematoxylin-and-Eosin-Stained Histological Sections," Journal of Biomedical Optics **15**(2).
6. **Cisek, R.**, L. Spencer, N. Prent, D. Zigmantas, G. Espie and V. Barzda (2009). "Optical microscopy in photosynthesis." Photosynthesis Research **102**(2): 111-141.*
7. **Cisek, R.**, Prent, N., Greenhalgh, C., Sandkuijl, D., Tuer, A., Major, A. and Barzda, V. (2009) “Multicontrast Nonlinear Imaging Microscopy” in *Biochemical Applications of*

Nonlinear Optical Spectroscopy. V. V. Yakovlev ed. CRC Press, New York, Pg. 71-102.*

8. Carriles, R., D. N. Schafer, K. E. Sheetz, J. J. Field, **R. Cisek**, V. Barzda, A. W. Sylvester and J. A. Squier (2009). "Invited review article: Imaging techniques for harmonic and multiphoton absorption fluorescence microscopy." Review of Scientific Instruments **80**(8): 10364-10371.*
9. Spencer, T.L., **Cisek, R.**, Barzda, V., Philipose, U., Ruda, H.E. and Shik, A., (2009) "Orientation dependent nonlinear optical effects in ZnSe nanowires. Applied Physics Letters **94**(23): 2331191-2331193.*
10. Major, A., **Cisek, R.**, Sandkuijl, D., and Barzda, V., (2009) "Femtosecond Yb:KGd(WO4)(2) laser with > 100 nJ of pulse energy". Laser Physics Letters. **6**(4):272-274.*
11. Barzda, V., R. Cisek, T. L. Spencer, U. Philipose, H. E. Ruda and A. Shik (2008). "Giant anisotropy of second harmonic generation for a single ZnSe nanowire." Applied Physics Letters **92**(11): 31111-31113.*
12. Prent, N., Green, C., Greenhalgh, C., **Cisek, R.**, Major, A., Stewart, B. and Barzda, V. (2008) "Intermyofilament dynamics of myocytes revealed by second harmonic generation microscopy", Journal of Biomedical Optics, **13**(4):041318.
13. Greenhalgh, C., Prent, N., Green, C., **Cisek, R.**, Major, A., Stewart, B. and Barzda, V. (2007) "Influence of semicrystalline order on the second-harmonic generation efficiency in the anisotropic bands of myocytes", Applied Optics, **46**(10):1852-1859.
14. Major, A., **Cisek, R.** and Barzda, V. (2006) "Femtosecond Yb : KGd(WO4)(2) laser oscillator pumped by a high power fiber-coupled diode laser module." Optics Express **14**(25):12163-12168. *

Non-refereed Publications and Presentations

1. **Cisek, R.**, Hirmiz, N., Saxena, A., Shik, A., Ruda H. E. and Barzda, V. (2011) "Nonlinear optical properties of ZnSe nanowires investigated with SHG polarization microscopy." Nonlinear Optics Conference, Kauai, Hawaii, USA. (Conference Proceeding).*
2. **Cisek, R.**, Krouglov, S., Tuer, A., Sandkuijl, D., Major, A. and Barzda, V. (2011) "Polarization sensitive second harmonic generation microscopy of starch granules." Chemical Biophysics Symposium, Toronto, Ontario, Canada. (Poster)*
3. **Cisek, R.**, Hirmiz, N., Shik, A., Ruda, H. E. and Barzda, V. (2011) "ZnSe nanowires as harmonophores for multicontrast nonlinear microscopy." Photonics West, San Francisco, USA. (Conference Presentation)*
4. Barzda, V., **Cisek, R.** and Tuer, A. (2011) "Visualization of the first hyperpolarizability tensor elements with second-harmonic generation microscopy in biological spherocrystals." Photonics West, San Francisco, USA. (Conference Presentation)*
5. Samim, M., **Cisek, R.,** Sandkuijl, D., Musikhin S. and Barzda, V. (2011) "Three-dimensional data acquisition with aberrations correction capability for video-rate microscopy." Photonics West, San Francisco, USA. (Conference Presentation)*
6. Tokarz, D., Tuer, A., **Cisek, R.** and Barzda V., (2011) "Novel harmonophores for third-harmonic generation microscopy." Photonics West 2011, San Francisco, USA. (Conference Presentation)
7. **Cisek, R.,** Sekerka, G., Tuer, A., Tokarz, D., Prent, N., Major, A. and Barzda, V., (2010) "Second harmonic generation from Otoconia." Chemical Biophysics Symposium, Toronto, Canada. (Poster)*
8. Tokarz, D., A. Tuer, **R. Cisek**, S. Krouglov and V. Barzda (2010). "*Ab initio* calculations of the linear and nonlinear optical properties of amino acids." Journal of Physics: Conference Series **256**: 012015. (Conference Proceeding)

9. **Cisek, R.**, Tuer, A., and Barzda, V., (2010) "Origin of second harmonic generation from starch granules." Canadian Association of Physicists Conference, Toronto, Canada. (Conference Presentation)*
10. Samim, M., **Cisek, R.**, Sandkuijl, D., Musikhin, S., Prent, N., Stewart, B., Barzda, V., (2010) "Towards fast 3D microscopy: multiple depth focusing for video rate imaging." Physics in Canada. **66**(3):183-185. (Conference proceeding and poster)
11. Tokarz, D., Tuer, A., **Cisek, R.** and Barzda, V., (2010) "Ab initio calculations of the linear and nonlinear optical properties of amino acids." High Performance Computing Symposium. Toronto, Canada. (Poster)
12. Tokarz, D., Tuer, A., **Cisek, R.**, and Barzda, V. (2010) "Influence of protein secondary structure on optical second harmonic generation." Canadian Association of Physicists Congress. (Poster)
13. Tokarz, D., Tuer, A., **Cisek, R.**, and Barzda, V. (2010) "Nanoscale amorphous hemalums: harmonophores for third harmonic generation." Canadian Chemistry Conference and Exhibition. (Conference Presentation).
14. Tuer, A., Sandkuijl, D., Tokarz, D., **Cisek, R.**, Barzda, V. (2010) "*Ab Initio* calculation of collagen hyperpolarizability." Chemical Biophysics Symposium. (Poster).
15. **Cisek, R.** Prent, N., Major, A. and Barzda, V., (2009) "Starch granule crystallinity investigated with second harmonic generation microscopy." Chemical Biophysics Symposium, Toronto, Canada. (Poster)*
16. Tokarz, D., Tuer, A., **Cisek, R.**, and Barzda, V. (2009) "Harmonophores: bleach-free labels for microscopy." Chemical Biophysics Symposium. (Poster).
17. **Cisek, R.**, Prent, N., Major, A. and Barzda, V. (2008) "Direct visualization of polarization in the focal plane of a nonlinear optical microscope using starch granules." Photonics North Conference. Montreal, Canada. (Poster).*
18. **Cisek, R.**, Prent, N., Major, A. and Barzda, V. (2008) "Structural investigation of starch granules by polarization second harmonic generation microscopy." Chemical Biophysics Symposium. Toronto, Canada. (Poster)*
19. Tuer, A., Bakueva, L, **Cisek, R.**, Alami, J., Dumont, D., Rowlands, J., and V. Barzda. (2008) "Enhancement of third harmonic contrast with harmonophores in multimodal non-linear microscopy of histological sections." Multiphoton Microscopy in the Biomedical Sciences VIII; San Jose. (Conference Proceeding)
20. Prent, N., **Cisek, R.**, Greenhalgh, C., Major, A., and Barzda, V. (2007) "Investigation of mitochondria with third harmonic generation microscopy in *Saccharomyces cerevisiae*." Chemical Biophysics Symposium, Toronto, Canada. (Poster)
21. **Cisek, R.**, Major, A., Stein, G., Gyozo, G. and Barzda, V. (2007) "In vivo harmonic generation imaging of chloroplasts: determination of origins of second harmonic generation and third harmonic generation." Photosynthesis Light-Harvesting Satellite Meeting. Scotland. (Poster).*
22. Greenhalgh, C., **Cisek, R.**, Stewart, B. and Barzda, V., (2006) "Dynamic and structural visualization of muscle structure in drosophila with multimodal harmonic generation microscopy." in Biomedical Optics, Technical Digest (CD) Optical Society of America, WF6. (Conference Proceeding).
23. Prent, N., **Cisek, R.**, Greenhalgh, C., Major, A., Aus der Au, J., Squier, J., and Barzda, V. (2006) "The search for harmonophores - new labels for harmonic generation microscopy." Chemical Biophysics Symposium, Toronto ON (Poster).
24. **Cisek, R.**, Major, A., Prent, N., Greenhalgh, C., and Barzda, V. (2006) "Optimization of nonlinear excitation for reducing light-induced changes in photosynthetic systems during imaging with multimodal microscopy." Photonics North. Quebec City. Canada, vol. 6343. (Conference Presentation and Proceeding)*

25. Greenhalgh, C., Stewart, B., **Cisek, R.**, Prent, N., Major, A., and Barzda, V. (2006) "Dynamic investigation of Drosophila myocytes with second harmonic generation microscopy." Photonics North. Quebec City. Canada, **6343**. (Conference Proceeding)
26. Major, A., **Cisek, R.**, Greenhalgh, C., Prent, N., and Barzda, V. (2006) "A diode-pumped high power extended cavity femtosecond Yb:KGW laser: from development to applications in nonlinear microscopy." Photonics North. Quebec City. Canada, **6343.** (Conference Proceeding)*
27. **Cisek, R.**, Prent, N., Greenhalgh, C. and Barzda, V. (2005) "Structural investigation of stomata and proximity chloroplasts with nonlinear multimodal microscopy." Chemical Biophysics. Toronto, Ontario. (Conference Presentation)*
28. **Cisek, R.**, Musikhin, S. and Barzda, V. (2005) "Annihilation microscopy with applications in photosynthesis." Photonics North, Toronto, Canada. (Conference Presentation)*
29. Prent, N., **Cisek, R.**, Greenhalgh, C., Sparrow, R., Rohitlall, N., Milkereit, M. S., Green, C. and Barzda, V., (2005) "Application of nonlinear microscopy for studying the structure and dynamics in biological systems." **5971:**1-7. (Conference Proceeding)*
30. Greenhalgh, C., **Cisek, R.**, Prent, N., Major, A., Aus der Au, J., Squier, J. and Barzda, V., (2005) "Time and structural image analysis of microscopic volumes, simultaneously recorded with second harmonic generation, third harmonic generation, and multiphoton excitation fluorescence microscopy." **5969**:1-3. (Conference Proceeding)*
31. **Cisek, R.**, Smith, C., Aus der Au, J., Squier, J. and Barzda, V. (2004) "Heterogeneity of fluorescence lifetimes and high exciton-exciton annihilation effects in individual chloroplasts." Chemical Biophysics Conference. Toronto, Canada. (Poster)*
32. **Cisek, R.**, Aus der Au, J., Squier, J. and Barzda, V. "Fluorescence quenching and exciton-exciton annihilation effects in individual chloroplasts investigated by fluorescence lifetime imaging microscopy." in *Photosynthesis: Fundamental Aspects to Global Perspectives*, A. Van der Est, and D. Bruce, eds. (Allen Press, 2005), 776-778. (Conference Proceeding)
33. Prent, N., **Cisek, R.**, Greenhalgh, C., Aus der Au, J., Squier, J., and Barzda, V. (2004) "Imaging individual chloroplasts simultaneously with third- and second-harmonic generation and multiphoton excitation fluorescence microscopy." Photosynthesis: Fundamental Aspects to Global Perspectives. A. Van der Est and D. Bruce, eds. (Allen Press, 2005), 1037-1039. (Conference Proceeding)*
34. **Cisek, R.**, Aus der Au, J. Squier, J. and Barzda, V. (2004) "Fluorescence quenching and exciton-exciton annihilation effects in individual chloroplasts investigated by fluorescence lifetime imaging microscopy." Photosynthesis Congress. Montreal, Canada. (Poster)

References

Abbe, E. (1873). "Beitrage zur theorie des mikroskops und der mikroskopischen wahrnehmung." Schultzes Archiv fur Mikroskopische Anatomie **9**: 413-468.

Abramoff, M. D., P. J. Magalhaes and S. J. Ram (2004). "Image processing with ImageJ." Biophotonics International **11**(7): 36-42.

Aït-Belkacem, D., A. Gasecka, F. Munhoz, S. Brustlein and S. Brasselet (2010). "Influence of birefringence on polarization resolved nonlinear microscopy and collagen SHG structural imaging." Optics Express **18**(14): 14859-14870.

Alsberg, C. L. (1938). "Structure of the starch granule." Plant Physiology **13**(2): 295-330.

Amir, W., R. Carriles, E. E. Hoover, T. A. Planchon, C. G. Durfee and J. A. Squier (2007). "Simultaneous imaging of multiple focal planes using a two-photon scanning microscope." Optics Letters **32**(12): 1731-1733.

Armstrong, J. A., N. Bloembergen, J. Ducuing and P. S. Pershan (1962). "Interactions between light waves in a nonlinear dielectric." Physical Review **127**(6): 1918-1939.

Ashkenov, N., B. N. Mbenkum, C. Bundesmann, V. Riede, M. Lorenz, D. Spemann, E. M. Kaidashev, A. Kasic, M. Schubert, M. Grundmann, G. Wagner, H. Neumann, V. Darakchieva, H. Arwin and B. Monemar (2003). "Infrared dielectric functions and phonon modes of high-quality ZnO films." Journal of Applied Physics **93**(1): 126-133.

Baconnier, S. and S. B. Lang (2004). "Calcite microcrystals in the pineal gland of the human brain: Second harmonic generators and possible piezoelectric transducers." Ieee Transactions on Dielectrics and Electrical Insulation **11**(2): 203-209.

Badenhuizen, N. P. (1936). "Essays on the physical chemistry of starch and bread-preparation XXV Further observations on the block-structure of starch grain." Zeitschrift Fur Physikalische Chemie-Abteilung a-Chemische Thermodynamik Kinetik Elektrochemie Eigenschaftslehre **175**(5): 383-395.

Badenhuizen, N. P. (1956). "The structure of the starch granule." Protoplasma **45**(3): 315-326.

Baker, A. A., M. J. Miles and W. Helbert (2001). "Internal structure of the starch granule revealed by AFM." Carbohydrate Research **330**(2): 249-256.

Barad, Y., H. Eisenberg, M. Horowitz and Y. Silberberg (1997). "Nonlinear scanning laser microscopy by third harmonic generation." Applied Physics Letters **70**(8): 922-924.

Barille, R., L. Canioni, S. Rivet, L. Sarger, P. Vacher and T. Ducret (2001). "Visualization of intracellular Ca2+ dynamics with simultaneous two-photon-excited fluorescence and third-harmonic generation microscopes." Applied Physics Letters **79**(24): 4045-4047.

Barzda, V. (2005). "Visualization of mitochondria in cardiomyocytes by simultaneous harmonic generation and fluorescence microscopy." Optics Express **13**(20): 8263-8276.

Barzda, V. (2008). Non-linear contrast mechanisms for optical microscopy. Biophysical techniques in photosynthesis. T. J. Aartsma and J. Matysik. Dordrecht, Springer. **2:** 35-54.

Barzda, V., R. Cisek, T. L. Spencer, U. Philipose, H. E. Ruda and A. Shik (2008). "Giant anisotropy of second harmonic generation for a single ZnSe nanowire." Applied Physics Letters **92**(11): 31111-31113.

Barzda, V., C. J. de Grauw, J. Vroom, F. J. Kleima, R. van Grondelle, H. van Amerongen and H. C. Gerritsen (2001). "Fluorescence lifetime heterogeneity in aggregates of LHCII revealed by time-resolved microscopy." Biophysical Journal **81**(1): 538-546.

Barzda, V., G. Garab, V. Gulbinas and L. Valkunas (1996). "Evidence for long-range excitation energy migration in macroaggregates of the chlorophyll a/b light-harvesting antenna complexes." Biochimica Et Biophysica Acta-Bioenergetics **1273**(3): 231-236.

Barzda, V., V. Gulbinas, R. Kananavicius, V. Cervinskas, H. van Amerongen, R. van Grondelle and L. Valkunas (2001). "Singlet-singlet annihilation kinetics in aggregates and trimers of LHCII." Biophysical Journal **80**(5): 2409-2421.

Barzda, V., L. Mustardy and G. Garab (1994). "Size dependency of circular-dichroism in macroaggregates of photosynthetic pigment-protein complexes." Biochemistry **33**(35): 10837-10841.

Belisle, J. M., S. Costantino, M. L. Leimanis, M. J. Bellemare, D. S. Bohle, E. Georges and P. W. Wiseman (2008). "Sensitive detection of malaria infection by third harmonic generation imaging." Biophysical Journal **94**(4): L26-L28.

BeMiller, J. and R. Whistler, Eds. (2009). Starch Chemistry and Technology. Burlington, MA, Academic Press.

Bloembergen, N., R. K. Chang, S. S. Jha and C. H. Lee (1968). "Optical second-harmonic generation in reflection from media with inversion symmetry." Physical Review **174**(3): 813-822.

Bloembergen, N. and P. S. Pershan (1962). "Light waves at boundary of nonlinear media." Physical Review **128**(2): 606-622.

Bopp, M. A., Y. W. Jia, L. Q. Li, R. J. Cogdell and R. M. Hochstrasser (1997). "Fluorescence and photobleaching dynamics of single light-harvesting complexes." Proceedings of the National Academy of Sciences of the United States of America **94**(20): 10630-10635.

Boyd, R. W. (2008). Nonlinear optics. Amsterdam, Academic Press.

Brakenhoff, G. J., H. T. M. Vandervoort and N. Nanninga (1984). "High-resolution confocal scanning light-microscopy in biology." Analytica Chimica Acta **163**(Sep): 231-236.

Bruce, D., G. Samson and C. Carpenter (1997). "The origins of nonphotochemical quenching of chlorophyll fluorescence in photosynthesis. Direct quenching by P680(+) in photosystem II enriched membranes at low pH." Biochemistry **36**(4): 749-755.

Bryllert, T., L. E. Wernersson, L. E. Froberg and L. Samuelson (2006). "Vertical high-mobility wrap-gated InAs nanowire transistor." Electron Device Letters, IEEE **27**(5): 323-325.

Buléon, A., H. Bizot, M. M. Delage and J. L. Multno (1982). "Evolution of crystallinity and specific gravity of potato starch versus water ad- and desorption." Starch **34**(11): 361-366.

Buléon, A., H. Bizot, M. Madeleine Delage and B. Pontoire (1987). "Comparison of X-ray diffraction patterns and sorption properties of the hydrolyzed starches of potato, wrinkled and smooth pea, broad bean and wheat." Carbohydrate Polymers **7**(6): 461-482.

Buleon, A., P. Colonna, V. Planchot and S. Ball (1998). "Starch granules: structure and biosynthesis." International Journal of Biological Macromolecules **23**(2): 85-112.

Buleon, A., C. Gerard, C. Riekel, R. Vuong and H. Chanzy (1998). "Details of the crystalline ultrastructure of C-starch granules revealed by synchrotron microfocus mapping." Macromolecules **31**(19): 6605-6610.

Campagnola, P. J., A. C. Millard, M. Terasaki, P. E. Hoppe, C. J. Malone and W. A. Mohler (2002). "Three-dimensional high-resolution second-harmonic generation imaging of endogenous structural proteins in biological tissues." Biophysical Journal **82**(1): 493-508.

Campagnola, P. J., M. D. Wei, A. Lewis and L. M. Loew (1999). "High-resolution nonlinear optical imaging of live cells by second harmonic generation." Biophysical Journal **77**(6): 3341-3349.

Campbell, F. W. and D. G. Green (1965). "Optical and retinal factors affecting visual resolution." Journal of Physiology-London **181**(3): 576-593.

Carpenter, W. B. and F. G. Smith (1856). The microscope and its revelations. Philadelphia, Blanchard and Lea.

Carriles, R., D. N. Schafer, K. E. Sheetz, J. J. Field, R. Cisek, V. Barzda, A. W. Sylvester and J. A. Squier (2009). "Invited review article: Imaging techniques for harmonic and multiphoton absorption fluorescence microscopy." Review of Scientific Instruments **80**(8): 10364-10371.

Carter, R. P. (1983). Polycarbonate-starch compositions. USA, Mobay Chemical Corporation.

Chandrashekar, A., A. Savitri and K. Somashekar (1987). "Optical interference studies on single starch granules." Starch **39**(6): 195-197.

Chang, R. K., J. Ducuing and N. Bloembergen (1965). "Dispersion of the optical nonlinearity in semiconductors." Physical Review Letters **15**(9): 415-418.

Chanzy, H., J. L. Putaux, D. Dupeyre, R. Davies, M. Burghammer, S. Montanari and C. Riekel (2006). "Morphological and structural aspects of the giant starch granules from Phajus grandifolius." Journal of Structural Biology **154**(1): 100-110.

Chen, C., Y. Wu, A. Jiang, B. Wu, G. You, R. Li and S. Lin (1989). "New nonlinear-optical crystal: LiB3O5." J. Opt. Soc. Am. B **6**(4): 616-621.

Chen, R., S. Crankshaw, T. Tran, L. C. Chuang, M. Moewe and C. Chang-Hasnain (2010). "Second-harmonic generation from a single wurtzite GaAs nanoneedle." Applied Physics Letters **96**(5): 051110-051113.

Chen, W. L., T. H. Li, P. J. Su, C. K. Chou, P. T. Fwu, S. J. Lin, D. Kim, P. T. C. So and C. Y. Dong (2009). "Second harmonic generation chi tensor microscopy for tissue imaging." Applied Physics Letters **94**(18): 1-3.

Cheng, J.-X., A. Volkmer and X. S. Xie (2002). "Theoretical and experimental characterization of coherent anti-Stokes Raman scattering microscopy." J. Opt. Soc. Am. B **19**(6): 1363-1375.

Chu, S. W., I. H. Chen, T. M. Liu, P. C. Chen, C. K. Sun and B. L. Lin (2001). "Multimodal nonlinear spectral microscopy based on a femtosecond Cr:forsterite laser." Optics Letters **26**(23): 1909-1911.

Chu, S. W., S. Y. Chen, G. W. Chern, T. H. Tsai, Y. C. Chen, B. L. Lin and C. K. Sun (2004). "Studies of x((2))/x((3)) tensors in submicron-scaled bio-tissues by polarization harmonics optical microscopy." Biophysical Journal **86**(6): 3914-3922.

Chu, S. W., S. Y. Chen, T. H. Tsai, T. M. Liu, C. Y. Lin, H. J. Tsai and C. K. Sun (2003). "In vivo developmental biology study using noninvasive multi-harmonic generation microscopy." Optics Express **11**(23): 3093-3099.

Cisek, R., J. Aus der Au, J. Squier and V. Barzda (2005). Fluorescence quenching and exciton-exciton annihilation effects in individual chloroplasts investigated by fluorescence lifetime imaging microscopy. Photosynthesis: Fundamental aspects to global perspectives. C. R., A. Van der Est and D. Bruce. Lawrence, Allen Press. **2:** 776-778.

Cisek, R., V. Barzda, H. E. Ruda and A. Shik (2010). "Nonlinear optical properties of semiconductor nanowires." Journal of selected topics in quantum electronics **17**(4): 915-921.

Cisek, R., N. Hirmiz, A. Saxena, A. Shik, H. E. Ruda and V. Barzda (2011). "Nonlinear Optical Properties of ZnSe Nanowires Investigated with SHG Polarization Microscopy." Nonlinear Optics: 1-3.

Cisek, R., A. Major, N. Prent, C. Greenhalgh and V. Barzda (2006). "Optimization of nonlinear excitation for reducing light-induced changes in photosynthetic systems during imaging with multimodal microscopy - art. no. 634307." Photonics North 2006, Pts 1 and 2 **6343**: 71-79.

Cisek, R., N. Prent, C. Greenhalgh, D. Sandkuijl, A. Tuer, A. Major and V. Barzda (2009). Multicontrast nonlinear imaging microscopy. Biochemical applications of nonlinear optical spectroscopy. V. V. Yakovlev. New York, CRC Press**:** 71-102.

Cisek, R., L. Spencer, N. Prent, D. Zigmantas, G. Espie and V. Barzda (2009). "Optical microscopy in photosynthesis." Photosynthesis Research **102**(2): 111-141.

Cooke, D. and M. J. Gidley (1992). "Loss of crystalline and molecular order druing starch geletinization - origin of the enthalpic transition." Carbohydrate Research **227**: 103-112.

Copeland, L., J. Blazek, H. Salman and M. C. M. Tang (2009). "Form and functionality of starch." Food Hydrocolloids **23**(6): 1527-1534.

Cox, G. (1993). "Trends in confocal microscopy." Micron **24**(3): 237-247.

Cox, G., N. Moreno and J. Feijo (2005). "Second-harmonic imaging of plant polysaccharides." Journal of Biomedical Optics **10(**2): 0240131-0240136.

Dadap, J. I. (2008). "Optical second-harmonic scattering from cylindrical particles." Physical Review B (Condensed Matter and Materials Physics) **78**(20): 2053221-20532218.

Daniels, D. R. and A. M. Donald (2003). "An improved model for analyzing the small angle x-ray scattering of starch granules." Biopolymers **69**(2): 165-175.

Davidovits, P. and M. D. Egger (1969). "Scanning laser microscope." Nature **223**(5208): 831-831.

Debarre, D., W. Supatto, A. M. Pena, A. Fabre, T. Tordjmann, L. Combettes, M. C. Schanne-Klein and E. Beaurepaire (2006). "Imaging lipid bodies in cells and tissues using third-harmonic generation microscopy." Nature Methods **3**(1): 47-53.

Demmig-Adams, B. and W. W. Adams (1992). "Photoprotection and other responses of plants to high light stress." Annual Review of Plant Physiology and Plant Molecular Biology **43**: 599-626.

Denk, W., J. H. Strickler and W. W. Webb (1990). "Two-photon laser scanning fluorescence microscopy." Science **248**(4951): 73-76.

Diaspro, A. (2002). Confocal and two-photon microscopy: foundations, applications, and advances. New York, Wiley.

Dixit, R., R. Cyr and S. Gilroy (2006). "Using intrinsically fluorescent proteins for plant cell imaging." Plant Journal **45**(4): 599-615.

Donovan, J. W. (1979). "Phase transitions of the starch–water system." Biopolymers **18**(2): 263-275.

Dopieralski, P., J. Panek, K. Mierzwicki, Z. Latajka, H. Ratajczak and A. Barnes (2009). "Theoretical study on the polarizability and hyperpolarizability of hydrogen bonded complexes of nitropyridines with hydrogen fluoride." Journal of Molecular Structure: THEOCHEM **916**(1-3): 72-75.

Duncan, M. D., J. Reintjes and T. J. Manuccia (1982). "Scanning coherent anti-Stokes Raman microscope." Optics Letters **7**(8): 350-352.

Dündar, E., Y. Turan and A. E. Blaurock (2009). "Large scale structure of wheat, rice and potato starch revealed by ultra small angle X-ray diffraction." International Journal of Biological Macromolecules **45**(2): 206-212.

Ealand, C. A. (1921). The romance of the microscope, an interesting description of its uses in all branches of science, industry, agriculture, and in the detection of crime, with a short account of its origin, history & development. London, Seeley.

Erikson, A., J. Ortegren, T. Hompland, C. D. Davies and M. Lindgren (2007). "Quantification of the second-order nonlinear susceptibility of collagen I using a laser scanning microscope." Journal of Biomedical Optics **12**(4): 1-10.

Evers, A. D. (1971). "Scanning electron microscopy of wheat starch .3. granule development in endosperm." Starch **23**(5): 157-162.

Fan, Z., J. C. Ho, Z. A. Jacobson, H. Razavi and A. Javey (2008). "Large-scale, heterogeneous integration of nanowire arrays for image sensor circuitry." Proceedings of the National Academy of Sciences **105**(32): 11066-11070.

Fannon, J. E., J. A. Gray, N. Gunawan, K. C. Huber and J. N. BeMiller (2004). "Heterogeneity of starch granules and the effect of granule channelization on starch modification." Cellulose **11**(2): 247-254.

Fannon, J. E., J. M. Shull and J. N. Bemiller (1993). "Interior channels of starch granules." Cereal Chemistry **70**(5): 611-613.

Fay, P. and C. Van Baalen (1987). The Cyanobacteria. New York, Elsevier Science Pub. Co.

Feller, D. (1996). "The role of databases in support of computational chemistry calculations." Journal of Computational Chemistry **17**(13): 1571-1586.

Finazzi, G. (2005). "The central role of the green alga *Chlamydomonas reinhardtii* in revealing the mechanism of state transitions." Journal of Experimental Botany **56**(411): 383-388.

Finzi, L., C. Bustamante, G. Garab and C. B. Juang (1989). "Direct observation of large chiral domains in chloroplast thylakoid membranes by differential polarization microscopy." Proceedings of the National Academy of Sciences of the United States of America **86**(22): 8748-8752.

Fischer, P. and F. Hache (2005). "Nonlinear optical spectroscopy of chiral molecules." Chirality **17**(8): 421-437.

Fittinghoff, D. N., J. Aus der Au and J. Squier (2005). "Spatial and temporal characterizations of femtosecond pulses at high-numerical aperture using collinear, background-free, third-harmonic autocorrelation." Optics Communications **247**(4-6): 405-426.

Florsheimer, M. (1999). "Second-harmonic microscopy - A new tool for the remote sensing of interfaces." Physica Status Solidi a-Applied Research **173**(1): 15-27.

Freund, I. and M. Deutsch (1986). "Second-harmonic microscopy of biological tissue." Optics Letters **11**(2): 94-96.

Freund, I., M. Deutsch and A. Sprecher (1986). "Connective-tissue polarity - optical 2nd-harmonic microscopy, crossed-beam summation, and small-angle scattering in rat-tail tendon." Biophysical Journal **50**(4): 693-712.

Frey-Wyssling, A. (1940). "Zur optik der starkekorner." Naturwissenschaften **28**: 78-79.

Frey-Wyssling, A. (1969). "On the molecular structure of starch granules." American Journal of Botany **56**(7): 696-701.

Fricker, M., J. Runions and I. Moore (2006). "Quantitative fluorescence microscopy: From art to science." Annual Review of Plant Biology **57**: 79-107.

Frohlich, M. W. (1986). "Birefringent objects visualized by circular-polarization microscopy." Stain Technology **61**(3): 139-143.

Gallant, D. J., B. Bouchet and P. M. Baldwin (1997). "Microscopy of starch: Evidence of a new level of granule organization." Carbohydrate Polymers **32**(3-4): 177-191.

Gallant, D. J., B. Bouchet, A. Buleon and S. Perez (1992). "Physical characteristics of starch granules and susceptibility to enzymatic degradation." European Journal of Clinical Nutrition **46**: S3-S16.

Garab, G., A. Faludi-Daniel, J. C. Sutherland and G. Hind (1988). "Macroorganization of chlorophyll a/b light-harvesting complex in thylakoids and aggregates: Information from circular differential scattering." Biochemistry **27**(7): 2425-2430.

Gest, H. (2004). "The discovery of microorganisms by Robert Hooke and Antoni Van Leeuwenhoek, fellows of the Royal Society." Notes and Records of the Royal Society of London **58**(2): 187-201.

Gilroy, S. (1997). "Fluorescence microscopy of living plant cells." Annual Review of Plant Physiology and Plant Molecular Biology **48**: 165-190.

Giordmaine, J. A. (1965). "Nonlinear optical properties of liquids." Physical Review **138**(6A): 1599-1606.

Glaring, M. A., C. B. Koch and A. Blennow (2006). "Genotype-specific spatial distribution of starch molecules in the starch granule: A combined CLSM and SEM approach." Biomacromolecules **7**(8): 2310-2320.

Goldman, R. D. and D. L. Spector (2005). Live cell imaging: a laboratory manual. Woodbury, NY, Cold Spring Harbor Laboratory Press.

Gouy, C. R. (1890). "Sur la propagation anormale des ondes." Acad. Sci. Paris **110**: 1251-1253.

Greene, R. G., H. A. Luo and A. L. Ruoff (1995). "High-pressure X-ray and Raman-study of ZnSe." Journal of Physics and Chemistry of Solids **56**(3-4): 521-524.

Greenhalgh, C., R. Cisek, N. Prent, A. Major, J. Aus der Au, J. Squier and V. Barzda (2005). "Time and structural image analysis of microscopic volumes, simultaneously recorded with second harmonic generation, third harmonic generation, and multiphoton excitation fluorescence microscopy." Proceedings of SPIE **5969**(2F): 1-8.

Greenhalgh, C., N. Prent, C. Green, R. Cisek, A. Major, B. Stewart and V. Barzda (2007). "Influence of semicrystalline order on the second-harmonic generation efficiency in the anisotropic bands of myocytes." Applied Optics **46**(10): 1852-1859.

Grigoriev, I. S. and E. Z. Meilikhov, Eds. (1997). Handbook of Physical Quantities. Boca Raton, CRC.

Grossman, A. R., M. R. Schaefer, G. G. Chiang and J. L. Collier (1993). "The phycobilisome, a light-harvesting complex responsive to environmental-conditions." Microbiological Reviews **57**(3): 725-749.

Gualtieri, E. J., L. M. Haupert and G. J. Simpson (2008). "Interpreting nonlinear optics of biopolymer assemblies: Finding a hook." Chemical Physics Letters **465**(4-6): 167-174.

Gunning, B. E. S. and O. M. Schwartz (1999). "Confocal microscopy of thylakoid autofluorescence in relation to origin of grana and phylogeny in the green algae." Australian Journal of Plant Physiology **26**(7): 695-708.

Hall, A. R. (1988). "The Leeuwenhoek lecture, 1988. Antoni van Leeuwenhoek 1632-1723." Notes and Records of the Royal Society of London (1938-1996) **43**(2): 249-273.

Haugland, R. P., M. T. Z. Spence, I. D. Johnson and A. Basey (2005). Molecular probes the handbook - a guide to fluorescent probes and labeling technologies. Carlsbad, Invitrogen Corporation.

Hellwarth, R. and P. Christensen (1974). "Nonlinear optical microscopic examination of structure in polycrystalline ZnSe." Optics Communications **12**(3): 318-322.

Hennig, H. J. and H. Lechert (1977). "DMR study of D_2O in native starches of different origins and amylose of type B." Journal of Colloid And Interface Science **62**(2): 199-204.

Hepler, P. K. and B. E. S. Gunning (1998). "Confocal fluorescence microscopy of plant cells." Protoplasma **201**(3-4): 121-157.

Hermann, J. P. and J. Ducuing (1974). "Third-order polarizabilities of long-chain molecules." Journal of Applied Physics **45**(11): 5100-5102.

Hogg, J. (1867). The microscope: its history, construction, and application. London, G. Routledge.

Hooke, R. (1665). Micrographia, or, some physiological descriptions of minute bodies made by magnifying glasses, with observations and inquiries thereupon. London, Printed by J. Martyn and J. Allestry.

Horton, P., A. V. Ruban and R. G. Walters (1996). "Regulation of light harvesting in green plants." Annual Review of Plant Physiology and Plant Molecular Biology **47**: 655-684.

Huber, K. C. and J. N. BeMiller (2000). "Channels of maize and sorghum starch granules." Carbohydrate Polymers **41**(3): 269-276.

Imberty, A., A. Buleon, V. Tran and S. Perez (1991). "Recent advances in knowledge of starch structure." Starch **43**(10): 375-384.

Imberty, A., H. Chanzy, S. Perez, A. Buleon and V. Tran (1988). "The double-helical nature of the crystalline part of A-starch." Journal of Molecular Biology **201**(2): 365-378.

Imberty, A. and S. Perez (1988). "A revisit to the 3-dimensional structure of B-type starch." Biopolymers **27**(8): 1205-1221.

Jane, J.-l. (2006). "Current understanding on starch granule structures." Journal of Applied Glycoscience **53**(3): 205-213.

Jiang, Y., J. Xu, W. Wang, X. Lu, X. Liu, G. Wang and F. Li (2001). "Second-harmonic generation investigations of Zn_{1-x}Cd_{x}Se/ZnSe asymmetric coupled quantum wells." Physical Review B **63**(12): 53081-53085.

Johnson, J. C., H. Yan, R. D. Schaller, P. B. Petersen, P. Yang and R. J. Saykally (2002). "Near-field imaging of nonlinear optical mixing in single zinc oxide nanowires." Nano Letters **2**(4): 279-283.

Kaiser, W. and C. G. B. Garrett (1961). "Two-photon excitation in CaF2:Eu2+." Physical Review Letters **7**(6): 229-231.

Karna, S. P. and M. Dupuis (1991). "Frequency-dependent nonlinear optical-properties of molecules - formulation and implementation in the HONDO program." Journal of Computational Chemistry **12**(4): 487-504.

Keller, U., K. J. Weingarten, F. X. Kartner, D. Kopf, B. Braun, I. D. Jung, R. Fluck, C. Honninger, N. Matuschek and J. A. derAu (1996). "Semiconductor saturable absorber mirrors (SESAM's) for femtosecond to nanosecond pulse generation in solid-state lasers." Ieee Journal of Selected Topics in Quantum Electronics **2**(3): 435-453.

Kleinman, D. A. (1962). "Nonlinear dielectric polarization in optical media." Physical Review **126**(6): 1977-1979.

Klopsteg, P. E. (1960). "Indispensable tools of science." Science **132**(3444): 1913-1922.

Kolthammer, W. S., D. Barnard, N. Carlson, A. D. Edens, N. A. Miller and P. N. Saeta (2005). "Harmonic generation in thin films and multilayers." Physical Review B **72**(4): 1-15.

Konig, K. (2000). "Multiphoton microscopy in life sciences." Journal of Microscopy-Oxford **200**: 83-104.

Kuhlbrandt, W., T. Thaler and E. Wehrli (1983). "The structure of membrane crystals of the light-harvesting chlorophyll a/b protein complex." Journal of Cell Biology **96**(5): 1414-1424.

Kumbhojkar, N., S. Mahamuni, V. Leppert and S. H. Risbud (1998). "Quantum confinement effects in chemically grown, stable ZnSe nanoclusters." Nanostructured Materials **10**(2): 117-129.

Laclaire, J. W. (1987). "Microtubule cytoskeleton in intact and wounded coenocytic green-algae." Planta **171**(1): 30-42.

Landau, L. D. and E. M. Lifshitz (1984). Electrodynamics of continuous media. Oxford, Pergamon Press.

Latajka, Z., G. Gajewski, A. J. Barnes, D. Xue and H. Ratajczak (2009). "Hyperpolarizabilities of some model hydrogen-bonded complexes: PM3 and *ab initio* studies." Journal of Molecular Structure **928**(1-3): 121-124.

Lechert, H. (1981). Water binding on starch: NMR studies on native and gelatinized starch. Water Activity: Influences on Food Quality. L. B. Rockland and G. F. Stewart. London, Academic Press**:** 223-245.

Leeuwenhoek, A. v. (1695). Arcana naturae detecta ab Antonio van Leeuwenhoek. Delphis Batavorum, Apud H. a Krooneveld.

Legare, F., C. Pfeffer and B. R. Olsen (2007). "The role of backscattering in SHG tissue imaging." Biophysical Journal **93**(4): 1312-1320.

Levine, B. F. and C. G. Bethea (1975). "Second and third order hyperpolarizabilities of organic molecules." The Journal of Chemical Physics **63**(6): 2666-2682.

Levine, I. N. (2000). Quantum Chemistry. Upper Saddle River, Prentice Hall.

Li, J. H., M. J. Guiltinan and D. B. Thompson (2006). "The use of laser differential interference contrast microscopy for the characterization of starch granule ring structure." Starch **58**(1): 1-5.

Liu, S. W., H. J. Zhou, A. Ricca, R. Tian and M. Xiao (2008). "Far-field second-harmonic fingerprint of twinning in single ZnO rods." Physical Review B **77**(11): 1133111-1133114.

Liu, Z. F., H. C. Yan, K. B. Wang, T. Y. Kuang, J. P. Zhang, L. L. Gui, X. M. An and W. R. Chang (2004). "Crystal structure of spinach major light-harvesting complex at 2.72 angstrom resolution." Nature **428**(6980): 287-292.

Loison, C. and D. Simon (2010). "Additive model for the second harmonic generation hyperpolarizability applied to a collagen-mimicking peptide (Pro-ProsGly)10." Journal of Physical Chemistry A **114**(29): 7769-7779.

Long, J. P., B. S. Simpkins, D. J. Rowenhorst and P. E. Pehrsson (2007). "Far-field imaging of optical second-harmonic generation in single GaN nanowires." Nano Letters **7**(3): 831-836.

Lopez-Rubio, A., A. Htoon and E. P. Gilbert (2007). "Influence of extrusion and digestion on the nanostructure of high-amylose maize starch." Biomacromolecules **8**(5): 1564-1572.

Major, A., V. Barzda, P. A. E. Piunno, S. Musikhin and U. J. Krull (2006). "An extended cavity diode-pumped femtosecond Yb : KGW laser for applications in optical DNA sensor technology based on fluorescence lifetime measurements." Optics Express **14**(12): 5285-5294.

Major, A., R. Cisek and V. Barzda (2006). "Femtosecond Yb : KGd(WO4)(2) laser oscillator pumped by a high power fiber-coupled diode laser module." Optics Express **14**(25): 12163-12168.

Major, A., R. Cisek, D. Sandkuijl and V. Barzda (2009). "Femtosecond Yb:KGd(WO4)(2) laser with > 100 nJ of pulse energy." Laser Physics Letters **6**(4): 272-274.

Manten, A. A. (1969). "History of microscope and its impact on development of palynology." Review of Palaeobotany and Palynology **9**(3-4): 137-148.

Marder, S. R., W. E. Torruellas, M. BlanchardDesce, V. Ricci, G. I. Stegeman, S. Gilmour, J. L. Bredas, J. Li, G. U. Bublitz and S. G. Boxer (1997). "Large molecular third-order optical nonlinearities in polarized carotenoids." Science **276**(5316): 1233-1236.

Millard, A. C., P. J. Campagnola, W. Mohler, A. Lewis and L. M. Loew (2003). "Second harmonic imaging microscopy." Biophotonics, Pt B **361**: 47-69.

Millard, A. C., P. W. Wiseman, D. N. Fittinghoff, K. R. Wilson, J. A. Squier and M. Muller (1999). "Third-harmonic generation microscopy by use of a compact, femtosecond fiber laser source." Applied Optics **38**(36): 7393-7397.

Miller, C. K. and J. F. Ward (1977). "Measurements of nonlinear optical polarizabilities for some halogenated methanes: The role of bond-bond interactions." Physical Review A **16**(3): 1179.

Miller, R. C. and W. A. Nordland (1970). "Absolute signs of second-harmonic generation coefficients of piezoelectric crystals." Physical Review B **2**(12): 4896-4902.

Minsky, M. (1988). "Memoir on inventing the confocal scanning microscope." Scanning **10**(4): 128-138.

Mizutani, G., Y. Sonoda, H. Sano, M. Sakamoto, T. Takahashi and S. Ushioda (2000). "Detection of starch granules in a living plant by optical second harmonic microscopy." Journal of Luminescence **87-9**: 824-826.

Moad, A. J., C. W. Moad, J. M. Perry, R. D. Wampler, G. S. Goeken, N. J. Begue, T. Shen, R. Heiland and G. J. Simpson (2007). "NLOPredict: Visualization and data analysis software for nonlinear optics." Journal of Computational Chemistry **28**(12): 1996-2002.

Moad, A. J. and G. J. Simpson (2005). "Self-consistent approach for simplifying the molecular interpretation of nonlinear optical and multiphoton phenomena." The Journal of Physical Chemistry A **109**(7): 1316-1323.

Moreaux, L., O. Sandre, M. Blanchard-Desce and J. Mertz (2000). "Membrane imaging by simultaneous second-harmonic generation and two-photon microscopy." Optics Letters **25**(5): 320-322.

Moreaux, L., O. Sandre, S. Charpak, M. Blanchard-Desce and J. Mertz (2001). "Coherent scattering in multi-harmonic light microscopy." Biophysical Journal **80**(3): 1568-1574.

Moreaux, L., O. Sandre and J. Mertz (2000). "Membrane imaging by second-harmonic generation microscopy." Journal of the Optical Society of America B-Optical Physics **17**(10): 1685-1694.

Mouille, G., M.-L. Maddelein, N. Libessart, P. Talaga, A. Decq, B. Delrue and S. Ball (1996). "Preamylopectin processing: a mandatory step for starch biosynthesis in plants." The Plant Cell **8**(8): 1353-1366.

Muller, M. (2006). Introduction to confocal fluorescence microscopy. Bellingham, Wash., SPIE Press.

Muller, M., J. Squier, K. R. Wilson and G. J. Brakenhoff (1998). "3D microscopy of transparent objects using third-harmonic generation." Journal of Microscopy-Oxford **191**: 266-274.

Musikhin, S., M. Samim, R. Cisek, V. Barzda, N. Prent and D. Sandkuijl (2011). "Three-dimensional video-rate nonlinear microscopy of contracting myocytes." European Biophysics Journal with Biophysics Letters **40**: 122-122.

Mustardy, L. and G. Garab (2003). "Granum revisited. A three-dimensional model – where things fall into place." Trends in Plant Science **8**(3): 117-122.

Nadiarnykh, O., R. LaComb, P. J. Campagnola and W. A. Mohler (2007). "Coherent and incoherent SHG in fibrillar cellulose matrices." Optics Express **15**(6): 3348-3360.

Naumov, A. N., D. A. Sidorov-Biryukov, A. B. Fedotov and A. M. Zheltikov (2001). "Third-harmonic generation in focused beams as a method of 3D microscopy of a laser-produced plasma." Optics and Spectroscopy **90**(5): 778-783.

Oida, T., Y. Sako and A. Kusumi (1993). "Fluorescence lifetime imaging microscopy (flimscopy) - methodology development and application to studies of endosome fusion in single cells." Biophysical Journal **64**(3): 676-685.

Olivier, N., F. Aptel, K. Plamann, M. C. Schanne-Klein and E. Beaurepaire (2010). "Harmonic microscopy of isotropic and anisotropic microstructure of the human cornea." Optics Express **18**(5): 5028-5040.

Olivier, N., M. A. Luengo-Oroz, L. Duloquin, E. Faure, T. Savy, I. Veilleux, X. Solinas, D. Debarre, P. Bourgine, A. Santos, N. Peyrieras and E. Beaurepaire (2010). "Cell lineage reconstruction of early zebrafish embryos using label-free nonlinear microscopy." Science **329**(5994): 967-971.

Oostergetel, G. T. and E. F. J. Vanbruggen (1993). "The crystalline domains in potato starch granules are arranged in a helical fashion." Carbohydrate Polymers **21**(1): 7-12.

Oron, D., E. Tal and Y. Silberberg (2003). "Depth-resolved multiphoton polarization microscopy by third-harmonic generation." Optics Letters **28**(23): 2315-2317.

Paddock, S. W. (1999). Confocal microscopy methods and protocols. Totowa, N.J., Humana Press.

Park, Y., M. J. Cich, R. Zhao, P. Specht, E. R. Weber, E. Stach and S. Nozaki (2000). "Analysis of twin defects in GaAs(111)B molecular beam epitaxy growth." Journal of Vacuum Science and Technology B **18**: 1566-1571.

Pauzauskie, P. J. and P. Yang (2006). "Nanowire photonics." Materials Today **9**(10): 36-45.

Pawley, J. B. (2006). Handbook of biological confocal microscopy. New York, Springer.

Perry, J. M., A. J. Moad, N. J. Begue, R. D. Wampler and G. J. Simpson (2005). "Electronic and vibrational second-order nonlinear optical properties of protein secondary structural motifs." Journal of Physical Chemistry B **109**(42): 20009-20026.

Pfeffer, C. P., B. R. Olsen, F. Ganikhanov and F. Legare (2008). "Multimodal nonlinear optical imaging of collagen arrays." Journal of Structural Biology **164**(1): 140-145.

Pfeffer, C. P., B. R. Olsen and F. Legare (2007). "Second harmonic generation imaging of fascia within thick tissue block." Optics Express **15**(12): 7296-7302.

Philipose, U., A. Saxena, H. E. Ruda, P. J. Simpson, Y. Q. Wang and K. L. Kavanagh (2008). "Defect studies of ZnSe nanowires." Nanotechnology **19**(21): 1-6.

Philipose, U., P. Sun, T. Xu, H. E. Ruda, L. Yang and K. L. Kavanagh (2007). "Structure and photoluminescence of ZnSe nanostructures fabricated by vapor phase growth." Journal of Applied Physics **101**(1): 0143261-0143265.

Pillai, R. S. (2006). Third-harmonic generation from isotropic and anisotropic media using focused laser beams, University of Amsterdam. **Doctor of Philosophy**.

Plotnikov, S. V., A. C. Millard, P. J. Campagnola and W. A. Mohler (2006). "Characterization of the myosin-based source for second-harmonic generation from muscle sarcomeres." Biophysical Journal **90**(2): 693-703.

Polivka, T. and V. Sundstrom (2004). "Ultrafast dynamics of carotenoid excited states - from solution to natural and artificial systems." Chemical Reviews **104**(4): 2021-2071.

Popov, D., A. Buleon, M. Burghammer, H. Chanzy, N. Montesanti, J. L. Putaux, G. Potocki-Veronese and C. Riekel (2009). "Crystal structure of A-amylose: a revisit from synchrotron microdiffraction analysis of single crystals." Macromolecules **42**(4): 1167-1174.

Potma, E. O., W. P. de Boeij and D. A. Wiersma (2001). "Femtosecond dynamics of intracellular water probed with nonlinear optical Kerr effect microspectroscopy." Biophysical Journal **80**(6): 3019-3024.

Prasanth, R., L. K. v. Vugt, D. A. M. Vanmaekelbergh and H. C. Gerritsen (2006). "Resonance enhancement of optical second harmonic generation in a ZnO nanowire." Applied Physics Letters **88**(18): 1815011-1815013.

Prent, N., R. Cisek, C. Greenhalgh, J. Aus der Au, J. Squier and V. Barzda (2005). "Imaging individual chloroplasts simultaneously with third- and second-harmonic generation and multiphoton excitation fluorescence microscopy." Photosynthesis: Fundamental aspects to global perspectives: 1037-1039.

Prent, N., C. Green, C. Greenhalgh, R. Cisek, A. Major, B. Stewart and V. Barzda (2008). "Intermyofilament dynamics of myocytes revealed by second harmonic generation microscopy." Journal of Biomedical Optics **13**(4): 0413181-04131817.

Psilodimitrakopoulos, S., I. Amat-Roldan, D. Artigas and P. Loza-Alvarez (2011). "Three-dimensional polarization second harmonic generation (3D-PSHG) imaging: the effect of the tilted-off the plane SHG active structures." Multiphoton Microscopy in the Biomedical Sciences XI **7903**: H1-H8.

Psilodimitrakopoulos, S., I. Amat-Roldan, P. Loza-Alvarez and D. Artigas (2010). "Estimating the helical pitch angle of amylopectin in starch using polarization second harmonic generation microscopy." Journal of Optics **12**(8): 1-6.

Psilodimitrakopoulos, S., I. Amat-Roldan, P. Loza-Alvarez and D. Artigas (2010). "Optical extraction of the helical pitch angle of amylopectin in starch." Proceedings of SPIE **7715**: 7715291-7715298.

Psilodimitrakopoulos, S., I. Amat-Roldan, S. Santos, M. Mathew, A. K. N. Thayil, D. Zalvidea, D. Artigas and P. Loza-Alvarez (2008). "Starch granules as a probe for the polarization at the sample plane of a high resolution multiphoton microscope." Proceedings of SPIE **6860**: E1-E11.

Reshak, A. H. (2009). "Second harmonic generation from thick leaves using the two-photon laser scanning microscope." Micron **40**(4): 455-462.

Reshak, A. H., V. Sarafis and R. Heintzmann (2009). "Second harmonic imaging of chloroplasts using the two-photon laser scanning microscope." Micron **40**(3): 378-385.

Ridout, M. J., A. P. Gunning, M. L. Parker, R. H. Wilson and V. J. Morris (2002). "Using AFM to image the internal structure of starch granules." Carbohydrate Polymers **50**(2): 123-132.

Ridout, M. J., M. L. Parker, C. L. Hedley, T. Y. Bogracheva and V. J. Morris (2003). "Atomic force microscopy of pea starch granules: granule architecture of wild-type parent, r and rb single mutants, and the rrb double mutant." Carbohydrate Research **338**(20): 2135-2147.

Robinson, F. N. H. (1968). "Relations between the components of the non-linear polarisability tensor in cubic and hexagonal II-VI compounds." Physics Letters A **26**(9): 435-436.

Rocha-Mendoza, I., D. R. Yankelevich, M. Wang, K. M. Reiser, C. W. Frank and A. Knoesen (2007). "Sum frequency vibrational spectroscopy: the molecular origins of the optical second-order nonlinearity of collagen." Biophysical Journal **93**(12): 4433-4444.

Roth, S. and I. Freund (1981). "Optical 2nd-harmonic scattering in rat-tail tendon." Biopolymers **20**(6): 1271-1290.

Ruda, H. E., U. Philipose, A. Saxena, C. De Souza, S. Nair, J. Salfi, A. Shik, A. Othonos, E. Lioudakis, D. Tsokkou, L. Zhong and C. Fernandes (2010). "Optical response of II-VI ZnSe nanowires." ECS Transactions **28**: 193-202.

Ruda, H. E. and A. Shik (2006). "Polarization-sensitive optical phenomena in thick semiconducting nanowires." Journal of Applied Physics **100**(2): 0243141-0243146.

Saeta, P. N. and N. A. Miller (2001). "Distinguishing surface and bulk contributions to third-harmonic generation in silicon." Applied Physics Letters **79**(17): 2704-2706.

Sager, R. and G. E. Palade (1957). "Structure and development of the chloroplast in *Chlamydomonas* 1. The normal green cell." Journal of Biophysical and Biochemical Cytology **3**(3): 463-506.

Schins, J. M., T. Schrama, J. Squier, G. J. Brakenhoff and M. Muller (2002). "Determination of material properties by use of third-harmonic generation microscopy." Journal of the Optical Society of America B-Optical Physics **19**(7): 1627-1634.

Schmidt, M. W., K. K. Baldridge, J. A. Boatz, S. T. Elbert, M. S. Gordon, J. H. Jensen, S. Koseki, N. Matsunaga, K. A. Nguyen, S. J. Su, T. L. Windus, M. Dupuis and J. A. Montgomery (1993). "General atomic and molecular electronic-structure system." Journal of Computational Chemistry **14**(11): 1347-1363.

Sekino, H. and R. J. Bartlett (1986). "Frequency dependent nonlinear optical properties of molecules." The Journal of Chemical Physics **85**(2): 976-989.

Senge, M. O., M. Fazekas, E. G. A. Notaras, W. J. Blau, M. Zawadzka, O. B. Locos and E. M. N. Mhuircheartaigh (2007). "Nonlinear optical properties of porphyrins." Advanced Materials **19**(19): 2737-2774.

Shen, Y. R. (1989). "Optical 2nd harmonic-generation at interfaces." Annual Review of Physical Chemistry **40**: 327-350.

Shogren, R. (2007). "Effect of orientation on the physical properties of potato amylose and high-amylose corn starch films." Biomacromolecules **8**(11): 3641-3645.

Shotton, D. and N. White (1989). "Confocal scanning microscopy: three-dimensional biological imaging." Trends in Biochemical Sciences **14**(11): 435-439.

Simidjiev, I., V. Barzda, L. Mustardy and G. Garab (1997). "Isolation of lamellar aggregates of the light-harvesting chlorophyll a/b protein complex of photosystem II with long-range chiral order and structural flexibility." Analytical Biochemistry **250**(2): 169-175.

Simons, J. (2011). "Jack Simons Quantum Chemistry Page." from http://simons.hec.utah.edu/.

Simons, J. and J. Nichols (1997). Quantum mechanics in chemistry. New York, Oxford University Press.

Singh, S. and L. T. Bradley (1964). "3-photon absorption in napthalene crystals by laser excitation." Physical Review Letters **12**(22): 612-614.

Slepkov, A. D., A. Ridsdale, A. F. Pegoraro, D. J. Moffatt and A. Stolow (2010). "Multimodal CARS microscopy of structured carbohydrate biopolymers." Biomed. Opt. Express **1**(5): 1347-1357.

So, P. T. C., C. Y. Dong, B. R. Masters and K. M. Berland (2000). "Two-photon excitation fluorescence microscopy." Annual Review of Biomedical Engineering **2**: 399-429.

Soper, A. K. and C. J. Benmore (2008). "Quantum differences between heavy and light water." Physical Review Letters **101**(6): 0655021-0655024.

Spencer, T. L., R. Cisek, V. Barzda, U. Philipose, H. E. Ruda and A. Shik (2009). "Orientation dependent nonlinear optical effects in ZnSe nanowires." Applied Physics Letters **94**(23): 2331191-2331193.

Squier, J. and M. Muller (2001). "High resolution nonlinear microscopy: A review of sources and methods for achieving optimal imaging." Review of Scientific Instruments **72**(7): 2855-2867.

Squier, J. A., M. Muller, G. J. Brakenhoff and K. R. Wilson (1998). "Third harmonic generation microscopy." Optics Express **3**(9): 315-324.

Stoller, P., K. M. Reiser, P. M. Celliers and A. M. Rubenchik (2002). "Polarization-modulated second harmonic generation in collagen." Biophysical Journal **82**(6): 3330-3342.

Strugger, S. (1950). "Uber den bau der proplastiden und chloroplasten." Naturwissenschaften **37**(7): 166-167.

Sujka, M. and J. Jamroz (2010). "Characteristics of pores in native and hydrolyzed starch granules." Starch **62**(5): 229-235.

Sun, C. K. (2005). "Higher harmonic generation microscopy." Microscopy Techniques **95**: 17-56.

Sundberg, K. R. (1977). "A group--dipole interaction model of the molecular polarizability and the molecular first and second hyperpolarizabilities." The Journal of Chemical Physics **66**(1): 114-118.

Supatto, W., D. Debarre, E. Farge and E. Beaurepaire (2005). "Femtosecond pulse-induced microprocessing of live *Drosophila* embryos." Medical Laser Application **20**: 207-216.

Szymonska, J. and F. Krok (2003). "Potato starch granule nanostructure studied by high resolution non-contact AFM." International Journal of Biological Macromolecules **33**(1-3): 1-7.

Takahashi, Y., T. Kumano and S. Nishikawa (2004). "Crystal structure of B-amylose." Macromolecules **37**(18): 6827-6832.

Tang, H., T. Mitsunaga and Y. Kawamura (2006). "Molecular arrangement in blocklets and starch granule architecture." Carbohydrate Polymers **63**(4): 555-560.

Thevenaz, P., U. E. Ruttimann and M. Unser (1998). "A pyramid approach to subpixel registration based on intensity." Image Processing, IEEE Transactions on **7**(1): 27-41.

Thornber, J. P. (1975). "Chlorophyll-proteins: Light-harvesting and reaction center components of plants." Annual Review of Plant Physiology and Plant Molecular Biology **26**: 127-158.

Tiaho, F., G. Recher and D. Rouede (2007). "Estimation of helical angles of myosin and collagen by second harmonic generation imaging microscopy." Optics Express **15**(19): 12286-12295.

Tinoco, I., W. Mickols, M. F. Maestre and C. Bustamante (1987). "Absorption, scattering, and imaging of biomolecular structures with polarized-light." Annual Review of Biophysics and Biophysical Chemistry **16**: 319-349.

Tirlapur, U. K. and K. König (2001). "Femtosecond near-infrared lasers as a novel tool for non-invasive real-time high-resolution time-lapse imaging of chloroplast division in living bundle sheath cells of Arabidopsis." Planta **214**(1): 1-10.

Tsang, T. Y. F. (1995). "Optical third-harmonic generation at interfaces." Physical Review A **52**(5): 4116-4125.

Tuer, A., S. Krouglov, R. Cisek, D. Tokarz and V. Barzda (2010). "Three-dimensional visualization of the first hyperpolarizability tensor." Journal of Computational Chemistry **32**(6): 1128-1134.

Tuer, A., D. Tokarz, N. Prent, R. Cisek, J. Alami, D. J. Dumont, L. Bakueva, J. Rowlands and V. Barzda (2010). "Nonlinear multicontrast microscopy of hematoxylin-and-eosin-stained histological sections." Journal of Biomedical Optics **15**(2): 0260181-0260189.

Tuer, A. E., S. Krouglov, N. Prent, R. Cisek, D. Sandkuijl, K. Yasufuku, B. Wilson and V. Barzda (2011). "Nonlinear Optical Properties of Type I Collagen Fibers Studied by

Polarization Dependent Second Harmonic Generation Microscopy." The Journal of Physical Chemistry B **115**(44): 12759-12769.

Ulrich, V., P. Fischer, I. Riemann and K. Konig (2004). "Compact multiphoton/single photon laser scanning microscope for spectral imaging and fluorescence lifetime imaging." Scanning **26**(5): 217-225.

Vacha, F., F. Adamec, J. Valenta and M. Vacha (2007). "Spatial location of photosystem pigment-protein complexes in thylakoid membranes of chloroplasts of *Pisum sativum* studied by chlorophyll fluorescence." Journal of Luminescence **122**: 301-303.

van Oijen, A. M., M. Ketelaars, J. Kohler, T. J. Aartsma and J. Schmidt (1999). "Unraveling the electronic structure of individual photosynthetic pigment-protein complexes." Science **285**(5426): 400-402.

van Spronsen, E. A., V. Sarafis, G. J. Brakenhoff, H. T. M. Vandervoort and N. Nanninga (1989). "3-dimensional structure of living chloroplasts as visualized by confocal scanning laser microscopy." Protoplasma **148**(1): 8-14.

Verbiest, T., S. Van Elshocht, M. Kauranen, L. Hellemans, J. Snauwaert, C. Nuckolls, T. J. Katz and A. Persoons (1998). "Strong enhancement of nonlinear optical properties through supramolecular chirality." Science **282**(5390): 913-915.

Vermeylen, R., V. Derycke, J. A. Delcour, B. Goderis, H. Reynaers and M. H. J. Koch (2006). "Structural transformations during gelatinization of starches in limited water: Combined wide- and small-angle X-ray scattering study." Biomacromolecules **7**(4): 1231-1238.

Wagner, H. P., M. Kühnelt, W. Langbein and J. M. Hvam (1998). "Dispersion of the second-order nonlinear susceptibility in ZnTe, ZnSe, and ZnS." Physical Review B **58**(16): 10494-10501.

Waigh, T. A., I. Hopkinson, A. M. Donald, M. F. Butler, F. Heidelbach and C. Riekel (1997). "Analysis of the native structure of starch granules with X-ray microfocus diffraction." Macromolecules **30**(13): 3813-3820.

Waigh, T. A., K. L. Kato, A. M. Donald, M. J. Gidley, C. J. Clarke and C. Riekel (2000). "Side-chain liquid-crystalline model for starch." Starch - Stärke **52**(12): 450-460.

Walla, P. J., P. A. Linden, K. Ohta and G. R. Fleming (2002). "Excited-state kinetics of the carotenoid S-1 state in LHC II and two-photon excitation spectra of lutein and beta-carotene in solution: Efficient car S-1 -> Chl electronic energy transfer via hot S-1 states?" Journal of Physical Chemistry A **106**(10): 1909-1916.

Walla, P. J., J. Yom, B. P. Krueger and G. R. Fleming (2000). "Two-photon excitation spectrum of light-harvesting complex II and fluorescence upconversion after one- and two-photon excitation of the carotenoids." Journal of Physical Chemistry B **104**(19): 4799-4806.

Wang, X. D., Y. J. Pang, G. Ku, X. Y. Xie, G. Stoica and L. H. V. Wang (2003). "Noninvasive laser-induced photoacoustic tomography for structural and functional in vivo imaging of the brain." Nature Biotechnology **21**(7): 803-806.

Ward, J. F. and G. H. C. New (1969). "Optical third harmonic generation in gases by a focused laser beam." Physical Review **185**(1): 57-72.

Whittam, M. A., T. R. Noel and S. G. Ring (1990). "Melting behavior of A- type and B-type crystalline starch." International Journal of Biological Macromolecules **12**(6): 359-362.

Wilkie, J. S. (1960). "Naegeli's work on the fine structure of living matter II - The immediate reception of Naegeli's work." Annals of Science **16**(3): 171 - 207.

Williams, R. M., W. R. Zipfel and W. W. Webb (2005). "Interpreting second-harmonic generation images of collagen I fibrils." Biophysical Journal **88**(2): 1377-1386.

Wu, H. C. H. and A. Sarko (1978). "Packing analysis of carbohydrates and polysaccharides .8. Double-helical molecular-structure of crystalline B-amylose." Carbohydrate Research **61**(Mar): 7-25.

Wu, H. C. H. and A. Sarko (1978). "Packing analysis of carbohydrates and polysaccharides .9. Double-helical molecular-structure of crystalline A-amylose." Carbohydrate Research **61**(Mar): 27-40.

Xia, D. Y., L. Dai, W. J. Xu, L. P. You, B. R. Zhang, G. Z. Ran and G. G. Qin (2006). "Synthesis and PL properties of ZnSe nanowires with zincblende and wurtzite structures." Chinese Physics Letters **23**(5): 1317-1320.

Xiang, B., H. Z. Zhang, G. H. Li, F. H. Yang, F. H. Su, R. M. Wang, J. Xu, G. W. Lu, X. C. Sun, Q. Zhao and D. P. Yu (2003). "Green-light-emitting ZnSe nanowires fabricated via vapor phase growth." Applied Physics Letters **82**(19): 3330-3332.

Yamaguchi, M., K. Kainuma and D. French (1979). "Electron-microscopic observations of waxy maize starch." Journal of Ultrastructure Research **69**(2): 249-261.

Yang, S. Y. and M. Tsuboi (1999). "Polarizing microscopy of eyespot of *Chlamydomonas*: *In situ* observation of its location, orientation, and multiplication." Biospectroscopy **5**(2): 93-100.

Yarkony, D. R., Ed. (1995). Modern electronic structure theory part II. River Edge, World Scientific Publishing Co.

Yelin, D. and Y. Silberberg (1999). "Laser scanning third-harmonic-generation microscopy in biology." Optics Express **5**(8): 169-175.

Yi, Z. W., H. Huang, T. Y. Kuang and S. F. Sui (2005). "Three-dimensional architecture of phycobilisomes from *Nostoc flagelliforme* revealed by single particle electron microscopy." Febs Letters **579**(17): 3569-3573.

Yu, J. Y., C. S. Liao, Z. Y. Zhuo, C. H. Huang, H. C. Chui and S. W. Chu (2009). "A diffraction-limited scanning system providing broad spectral range for laser scanning microscopy." Review of Scientific Instruments **80**(11): 37041-37045.

Zhang, D., Z. Liu, C. Li, T. Tang, X. Liu, S. Han, B. Lei and C. Zhou (2004). "Detection of NO_2 down to ppb levels using individual and multiple In_2O_3 nanowire devices." Nano Letters **4**(10): 1919-1924.

Zhang, H. F., K. Maslov, G. Stoica and L. H. V. Wang (2006). "Functional photoacoustic microscopy for high-resolution and noninvasive in vivo imaging." Nature Biotechnology **24**(7): 848-851.

Zheng, G., F. Patolsky, Y. Cui, W. U. Wang and C. M. Lieber (2005). "Multiplexed electrical detection of cancer markers with nanowire sensor arrays." Nat Biotech **23**(10): 1294-1301.

Zhuo, Z. Y., C. S. Liao, C. H. Huang, J. Y. Yu, Y. Y. Tzeng, W. Lo, C. Y. Dong, H. C. Chui, Y. C. Huang, H. M. Lai and S. W. Chu (2010). "Second harmonic generation imaging - A new method for unraveling molecular information of starch." Journal of Structural Biology **171**(1): 88-94.

Zipfel, W. R., R. M. Williams and W. W. Webb (2003). "Nonlinear magic: multiphoton microscopy in the biosciences." Nature Biotechnology **21**(11): 1368-1376.

Zobel, H. F. (1988). "Molecules to granules - a comprehensive starch review." Starch **40**(2): 44-50.

Zumbusch, A., G. R. Holtom and X. S. Xie (1999). "Three-dimensional vibrational imaging by coherent anti-Stokes Raman scattering." Physical Review Letters **82**(20): 4142-4145.

Appendix 1: List of Abbreviations

2-D	two-dimensional
2PF	two-photon excitation fluorescence
3-D	three-dimensional
AFM	atomic force microscope
CARS	coherent anti-Stokes Raman spectroscopy
CCD	charge coupled device
CPU	central processing unit
DAQ	data acquisition
FIFO	first in first out
FWHM	full width at half maximum
GFP	green fluorescent protein
HRTEM	high resolution transmission electron microscopy
IR	infrared
LED	light emitting diode
LHCII	light-harvesting pigment-protein complex associated with photosystem II
MPF	multi-photon excitation fluorescence
NA	numerical aperture
NLO	nonlinear optical
NMR	nuclear magnetic resonance

NW	nanowire
PIPO	polarization-in-polarization-out
PSF	point spread function
SAED	selected area electron diffraction
SCF	self-consistent field
SCIA	structural cross-correlation image analysis
SHG	second harmonic generation
SNR	signal to noise ratio
TDHF	time dependent Hartree-Fock
TEM	transmission electron microscope
THG	third harmonic generation
UV	ultraviolet
XRD	X-ray diffraction

Appendix 2: Single Dominant Hyperpolarizability Component and Helical Pitch

Under the assumption that the hyperpolarizability has a single dominant component, oriented an angle υ away from the unique axis of a uniaxial crystal, then the hyperpolarizability ratio d_{33}/d_{15} corresponds to (Plotnikov, Millard et al. 2006):

$$\cos^2 \upsilon = \frac{\frac{d_{33}}{d_{15}}}{\frac{d_{33}}{d_{15}} + 2} \qquad \text{A2-1}$$

Such a situation can occur in a helix, where molecules are aligned along the helical pitch. In that case the angle υ in Eq. A2-1 would correspond to the helical pitch angle, γ, defined in the Fig. A2-1 (a).

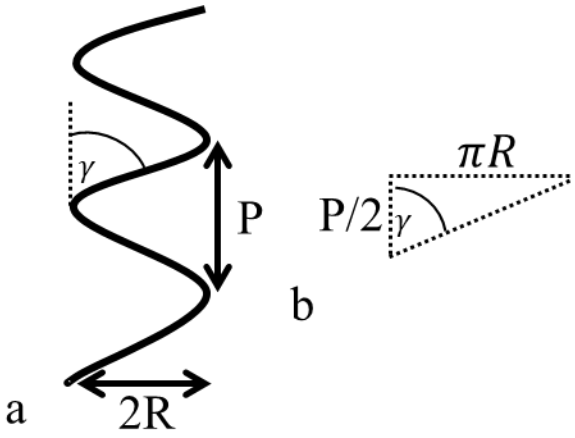

Fig. A2-1: Definitions of parameters describing a helix.
A single helix is shown in (a) having a pitch P, a radius R, and a helical pitch angle γ. The triangle used to calculate the helical pitch angle is explicitly shown in (b).

Assuming that the helical pitch angle γ is near 90°, it can be approximated by:

$$\tan \gamma = \frac{2\pi R}{P} \qquad \text{A2-2}$$

where R is the radius of the helix, and P is the pitch (height) of a repeating helical unit (see Fig. A2-1). The side opposite to the angle γ in Fig. A2-1(b) is calculated by approximating that the distance is equal to half a circumference (Tiaho, Recher et al. 2007).

The helical pitch angles for helices of amylose A and B can be calculated from experimental X-Ray data of amylose crystal structures (Imberty, Chanzy et al. 1988; Popov, Buleon et al. 2009) using Eq. A2-2, with parameter definitions shown in Fig. A2-1 (Tiaho, Recher et al. 2007). For amylose A, the pitch was P=21.2 Å and the radius (R), taken as the average distance between three unique pairs of glycosidic oxygens (O1 in Fig. 5.2-1), was R=2.72 Å, which gives a helical pitch angle of 39.4°. The helical pitch angle of amylose-B was calculated in a similar way with P=20.8 Å and R=2.90 Å, giving 41.2°.